Forces in the Shoulder Joint

On validation of musculoskeletal shoulder models

Forces in the Shoulder Joint
On validation of musculoskeletal shoulder models

Proefschrift

ter verkrijging van de graad van doctor
aan de Technische Universiteit Delft,
op gezag van de Rector Magnificus prof. ir. K.C.A.M. Luyben,
voorzitter van het College voor Promoties,
in het openbaar te verdedigen op
maandag 20 juni 2011 om 15.00 uur

door

Ali ASADI NIKOOYAN
Master of Science in Biomedical Engineering
Amirkabir University of Technology, Tehran, Iran
geboren te Shemiran, Iran

Dit proefschrift is goedgekeurd door de promotoren:
Prof.dr. F.C.T. van der Helm
Prof.dr. H.E.J. Veeger

Samenstelling promotiecommissie:

Rector Magnificus,	voorzitter
Prof.dr. F.C.T. van der Helm,	Technische Universiteit Delft, promotor
Prof.dr. H.E.J. Veeger,	Technische Universiteit Delft, promotor
Prof.Dr.-Ing. G. Bergmann,	Charité - Universitätsmedizin Berlin
Prof.dr.ir. N.N.J Verdonschot,	UMC Radboud Nijmegen
Prof.dr. R.G.H.H. Nelissen,	Leids Universitair Medisch Centrum
Prof.dr.ir. C.A. Grimbergen,	Technische Universiteit Delft
Dr. K. Meijer,	Universiteit Maastricht
Prof.dr. J. Dankelman	Technische Universiteit Delft, reservelid

This research was funded by Technology Foundation STW project number 07345

ISBN 978-90-8891-296-2

Keywords: Force, EMG, shoulder joint, validation, instrumented endoprosthesis.

Printed in the Netherlands

Table of Contents

Chapter 1

Introduction

1.1. Background

Detailed information about muscle function and muscle forces in the human musculoskeletal system is demanded for several applications. Among these are the improvement of the design and preclinical testing of endoprostheses, a more detailed description of muscle- or joint-injuries, and design and improvement of the treatments of motor disorders. Nevertheless, measuring the muscle forces *in-vivo* is hardly possible by noninvasive methods. This explains why biomechanical models of the neuromusculoskeletal system have been invented to estimate muscle forces based on external measurements. To date, biomechanical models are still the only means for the estimation of muscle forces, certainly outside laboratory conditions. In the last few decades, a variety of models of the entire human musculoskeletal system from simple two-dimensional (2D) to complex three-dimensional (3D) models, have been developed (Erdemir et al, 2007; Garner and Pandy, 2001).

The shoulder joint, also sometimes called *shoulder mechanism* (Figure 1.1), is the most complex while the most moveable joint in the human body. It provides a range of motion of about 2/3 of a sphere (Engin and Chen, 1986). The shoulder complex is composed of the thorax (partly), the clavicle, the scapula, and the humerus (or the upper arm) as well as a number of muscles and ligaments. It comprises a closed-chain mechanism consisting of the thorax, the clavicle, and the scapula. The clavicle is connected to the thorax and the scapula through the sternoclavicular and the acromioclavicular joints, respectively. The scapula is constrained to glide over the thorax. To do so, it requires the combined action of at least two muscles that together press the scapula onto the thorax surface. Most important pairs are the m. serratus anterior on the lateral side and the m. rhomboideii and m. trapezius on the medial side of the thorax.

As in all joints, changes in structure will affect function. In the shoulder, more than in other joints, joint integrity and joint function is dependent on the accurate function and coordination of muscles: the glenohumeral joint derives its stability to a larger extent from muscular control, while, scapular motion is highly dependent on the coordinated activation of (although wrongly defined) antagonist scapulothoracal muscles. When coordination is disturbed, complications such as impingement syndrome, or scapular dyskinesia and ultimately chronic defects such as rotator cuff tears or arthritis might develop.

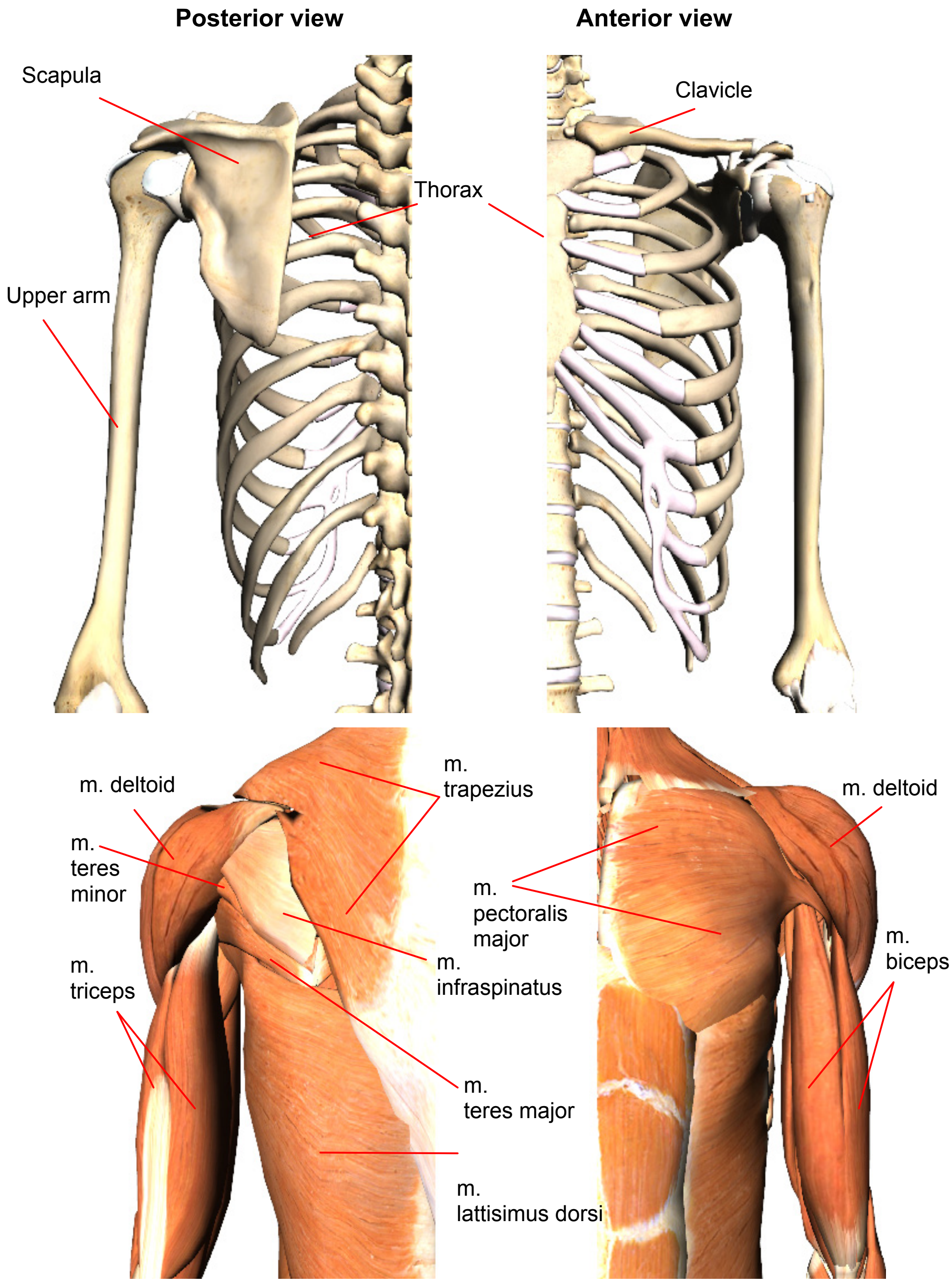

Figure 1.1. Schematic drawings of the shoulder mechanism. The screenshots are taken from Google Body Browser.

It is clear that the kinematic structure of the upper limb is rather complex. The interaction between the many degrees-of-freedom of the shoulder girdle limit the usefulness of simple 2D models of the upper extremity and lead to complex 3D models. These models should be complex enough to realistically replicate the behavior of the musculoskeletal system. Few complex 3D upper extremity models have been developed such as the Swedish model (Karlsson and Peterson, 1992; Makhsous et al, 1999), the Newcastle shoulder model (Charlton and Johnson, 2006), and the Delft Shoulder and Elbow Model.

The musculoskeletal model mainly used in this thesis will be the Delft Shoulder and Elbow Model (the DSEM). This model was developed in the Man-Machine Systems and Control Group at the Faculty of Mechanical Engineering, Delft University of Technology. Since its first introduction in 1994 (van der Helm, 1994a) the model has been extensively developed. To date, the DSEM has been used in a variety of clinical and biomechanical applications such as studies on the glenohumeral loads in weight lifting and wheelchair propulsion, tendon transfer, goal-directed arm movements, massive rotator cuff tears, stability of cementless glenoid prostheses, etc. In Chapter 2 of this thesis, one can find a detailed description about the DSEM developments and the different simulation architectures available in the model as well as a comparison between the DSEM and the other available complex models of the shoulder.

1.2. Problem definition

A major concern in biomechanical modeling of the human body musculoskeletal system is the model validity. We use the biomechanical models because we cannot directly measure the muscle forces. On the other hand, to validate a model we need to compare its predictions to real measured muscle forces. This conflict (Figure 1.2) makes the model validation the most challenging issue in the area of musculoskeletal modeling.

Up to date, all studies aiming to validate the biomechanical models of the shoulder have followed two main approaches:

- The first validation approach is to compare the model “strength” to externally, *in-vivo*, measured forces. In this approach the maximum force which the model is capable of producing is compared with the maximum force that a subject can exert on the handle connected to a force sensor. The major drawback of this method is that only few muscles in very specific (maximum isometric) tasks can be evaluated. Also, information about the *in-vivo* measured individual muscle forces and force distribution is actually not available.
- The second and the most frequently used approach is the force-Electromyography (EMG) comparison. In this approach the model-estimated force-time curves are compared to measured EMG signals. This method has been used to evaluate the predictions of the DSEM (van der Helm, 1994b). However, the agreement between force patterns and EMG

can only be seen as a qualitative validation since this agreement does not give information on the magnitude and accuracy of predicted force levels.

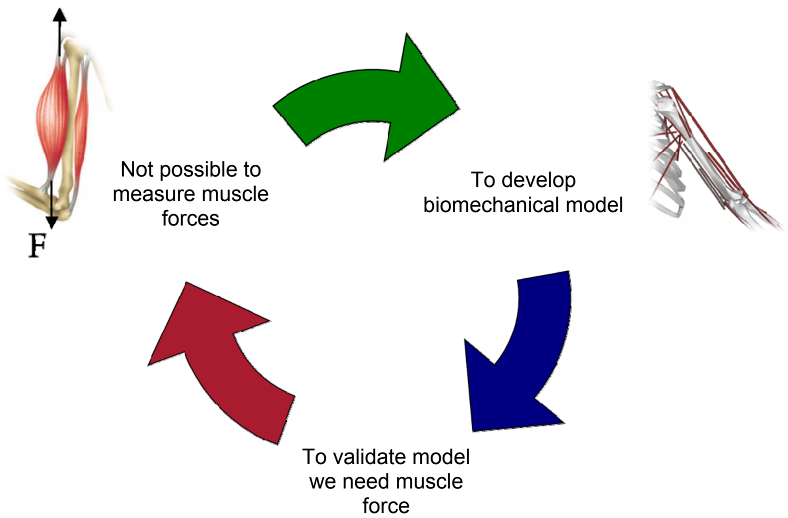

Figure 1.2. The conflict of model validation

Recently, an implantable instrumented shoulder endoprosthesis has been developed that is capable of measuring contact forces and moments in the glenohumeral joint *in-vivo* (Figure 1.3, see reference (Westerhoff et al, 2009) and Chapter 3 for a detailed description). The endoprosthesis has been tested and implanted in a number of patients. Although direct measurement of muscle forces is still not possible by this instrumented implant, it does allow for a general validation at the level of the summed muscle forces around the glenohumeral joint.

1.3. Aim and scope

The aim of this thesis is to validate the Delft Shoulder and Elbow Model at the levels of kinematic and dynamic models.

At the level of kinematic model, different methods for approximation of the glenohumeral joint rotation centre will be compared and validated based on the closeness of their estimation to the rotation centre determined on the subject-specific CT data.

Regarding the dynamic model, the different modelling simulation architectures available in the model will be represented and evaluated. The validity of a major stability constraint in the model will also be (experimentally) evaluated using the *in-vivo* measured glenohumeral joint reaction forces for a wide range of motion of shoulder movements.

Most importantly, the *in-vivo* measured glenohumeral joint reaction forces and moments in the shoulder joint using an instrumented endoprosthesis will be used to quantitatively validate the model at the level of summed muscle forces around the glenohumeral joint.

Finally, the reasons for the possible differences between the model predictions and the experimental data will be explored which helps to modify and individualize the model in order to find a closer match between model and experiment.

The scope of this thesis fits very well in the developments sketched in an Editorial published by Cutti and Veeger (2009) on shoulder biomechanics in which it was concluded that there is a need for the general biomechanical (upper extremity) models to be more thoroughly validated and tested.

Figure 1.3. The instrumented shoulder endoprosthesis. Picture courtesy of the Julius Wolff Institut, Charité - Universitätsmedizin Berlin (http://jwi.charite.de)

1.4. Outline of the thesis

This thesis concerns about model validity at different modeling levels (i.e. kinematic and dynamic models).

Firstly, all the DSEM developments since its first introduction are reviewed and described in Chapter 2. In this chapter, the different simulation architectures available in the DSEM are also extensively discussed and qualitatively validated following a force-EMG comparison approach. Moreover, the different biomechanical models of the shoulder are briefly introduced and compared.

In Chapter 3, the instrumented shoulder endoprosthesis is introduced. Also, a complete description of all measured patients and the ethics statement, data recordings, and image processing is given. This chapter represents the first time *in-vivo* shoulder joint loads measured by the instrumented shoulder implant transferred to the glenoid side. The outcomes of this chapter will be used to validate an important stability assumption in the musculoskeletal models of the shoulder.

The thesis is followed by quantitative validations.

In Chapter 4, the different methods for the *in-vivo* estimation of the glenohumeral joint rotation centers are evaluated for patients with shoulder hemiarthroplasty. Each method is validated based on the closeness of its estimated rotation center to the one determined on the subject-specific CT scans.

Chapter 5 deals with the first time quantitative validation of the DSEM by using the *in-vivo* measured glenohumeral joint reaction forces from the instrumented shoulder endoprosthesis. Both the magnitude of the resultant force and the direction of the force vector toward the glenoid cavity will be compared between the model and the experiment. The validation will be carried out for the generic model as well as the uniformly scaled model.

The remainder of the thesis is dedicated to model adaptations and improvements. The idea is to explore the reasons for the differences between the model predictions and the experimental data and to adapt and modify the model in order to find a closer match between model and experiment.

To account for possible antagonist muscle co-contraction in patients with arthroplasty, an EMG-driven version of the DSEM is developed in Chapter 6. In that model, the measured EMG signals will be normalized and included as input in the modeling process. The newly developed model will also be evaluated for a selection of patient data.

The subject of Chapter 7 is to identify the adjustable parameters of an energy-based muscle load sharing cost function that has been shown to be promising previously (Praagman et al, 2006) and which adjusting may result in a closer match between the model and the experiment.

In Chapter 8, the effect of including *in-vivo* measured friction-induced moments as measured with the instrumented shoulder endoprosthesis on model predictions is studied. In that chapter, the Coulomb friction coefficient in an artificial shoulder joint will be estimated using the *in-vivo* measured forces and frictional moments.

The final chapter (Chapter 9) evaluates progress and new challenges resulting from the undertaken research and will of course highlights the main findings of the thesis. Some guidelines are also suggested and areas for future research are recommended.

1.5. References

Charlton, I.W., Johnson, G.R., 2006. A model for the prediction of the forces at the glenohumeral joint. Proceedings of the Institution of Mechanical Engineers part H-Journal of Engineering in Medicine 220 (H8), 801-812.

Cutti, A.G., Veeger, H.E.J., 2009. Shoulder biomechanics: today's consensus and tomorrow's perspectives. Medical and Biological Engineering and Computing 47 (5), 463-466.

Engin, A.E., Chen, S.M., 1986. Statistical data base for the biomechanical properties of the human shoulder complex - I: kinematics of the shoulder complex. Journal of Biomechanical Engineering-Transactions of the ASME 108, 215-221.

Erdemir, A., McLean, S., Herzog, W., van den Bogert, A.J., 2007. Model-based estimation of muscle forces exerted during movements. Clinical Biomechanics 22 (2), 131-154.

Garner, B.A., Pandy, M.G., 2001. Musculoskeletal model of the upper limb based on the visible human male dataset. Computer methods in biomechanics and biomedical engineering 4 (2), 93-126.

Karlsson, D., Peterson, B., 1992. Towards a model for force predictions in the human shoulder. Journal of Biomechanics 25 (2), 189-199.

Makhsous, M., Hogfors, C., Siemien'ski, A., Peterson, B., 1999. Total shoulder and relative muscle strength in the scapular plane. Journal of Biomechanics 32 (11), 1213-1220.

Praagman, M., Chadwick, E.K.J., van der Helm, F.C.T., Veeger, H.E.J., 2006. The relationship between two different mechanical cost functions and muscle oxygen consumption. Journal of Biomechanics 39 (4), 758-765.

van der Helm, F.C.T., 1994a. A finite element musculoskeletal model of the shoulder mechanism. Journal of Biomechanics 27 (5), 551-553.

van der Helm, F.C.T., 1994b. Analysis of the kinematic and dynamic behavior of the shoulder mechanism. Journal of Biomechanics 27 (5), 527-550.

Westerhoff, P., Graichen, F., Bender, A., Rohlmann, A., Bergmann, G., 2009. An instrumented implant for in vivo measurement of contact forces and contact moments in the shoulder joint. Medical Engineering & Physics 31 (2), 207-213.

Modified from: A.A. Nikooyan, H.E.J. Veeger, E.K.J. Chadwick, M. Praagman, F.C.T. van der Helm, "Development of a comprehensive musculoskeletal model of the shoulder and elbow", under revision.

Chapter 2

A comprehensive musculoskeletal model of the shoulder and elbow

The Delft Shoulder and Elbow Model (DSEM), a three-dimensional musculoskeletal model of the shoulder and elbow has been extensively developed since its introduction in 1994. Extensions cover both model structures and anatomical data focusing on the addition of an elbow part and muscle architecture parameters. The model was also extended with a new inverse-dynamics optimization cost function and combined inverse-forward-dynamics models. This chapter is an update on the developments of the model over the last decade including a qualitative validation of the three simulation architectures available in the DSEM. To validate the model, a dynamic forward flexion motion was performed by one subject, of which the motion data and surface EMG-signals of 12 superficial muscles were measured. Patterns of the model-predicted relative muscle forces were compared with their normalized EMG-signals. Results showed relatively good agreement between forces and EMG (mean correlation coefficient of 0.74). However, for some cases (three out of twelve muscles) no force was predicted while EMG activity had been measured (false-negatives). In this chapter, the DSEM is also compared to the other existing comprehensive models of the shoulder.

Nomenclature

l_f	Fiber length
l_s	Sarcomere length
l_{opt}	Optimal fiber length
θ	Reference joint angle
$\dot{\theta}$	Reference joint angular velocity
$\ddot{\theta}$	Reference joint angular acceleration
L_m	Muscle length
M	Net joint moment
$\sigma_{\max}$	Maximum muscle stress
F_m	Predicted muscle force
$PCSA$	Muscle physiological cross sectional area
F_{min}	Minimum permissible muscle force in the inverse optimization
F_{max}	Maximum permissible muscle force in the inverse optimization
e	Excitation dynamics
u	Hypothetical neural input of the forward muscle model
a	Active state
L_{ce}	Length of contractile element (CE)
M_c	Correction moment
θ_c	Calculated joint angle
$\dot{\theta}_c$	Calculated joint angular velocity

2.1. Introduction

Biomechanical models can give insight into the mechanical basis of musculoskeletal function. In the last few decades, a variety of models of the entire human musculoskeletal system, from simple two-dimensional (2D) to complex three-dimensional (3D) models, have been developed. However, of all these models, not many describe the upper extremity. A major reason for this is the complex kinematic structure of the upper limb. The many degrees-of-freedom (DOF) of the shoulder girdle limit the usefulness of simple 2D models and lead to complex 3D models.

For clinical applications, sophisticated models are needed. Such models should be complex enough to realistically replicate the behavior of the human musculoskeletal system. Few complex upper extremity models have been developed such as the Swedish model (Karlsson and Peterson, 1992; Makhsous et al, 1999) based on the model of Hogfors *et al* (1991; 1987), the Newcastle shoulder model (Charlton and Johnson, 2006), the shoulder part of the AnyBody Modeling System (Damsgaard et al, 2006), the Stanford model implemented in SIMM (Holzbaur et al, 2005), and the Delft Shoulder Model which is the core of this study.

The Delft Shoulder Model (DSM) as first described in 1994 (van der Helm, 1994a) is a comprehensive 3D inverse-dynamic model of the shoulder complex in which the recorded motions of the bony segments and external loads are used as input to the model and muscle and joint contact forces, muscle lengths, and moment arms are calculated as model outputs through an inverse-dynamics analysis. To qualitatively validate the model, estimated force-time curves were compared to measured EMG signals (van der Helm, 1994b) which showed good agreement in the timing of muscle activations. Data for the original model were taken from references (van der Helm et al, 1992; van der Helm and Veenbaas, 1991; Veeger et al, 1991). Later, elbow data were added based upon a follow-up cadaver study (Veeger et al, 1997); consequently the model was renamed to the Delft Shoulder and Elbow Model (hereinafter the DSEM).

Following a detailed cadaver study on the shoulder (Klein Breteler et al, 1999) and elbow (Minekus, 1997), information about muscle architecture and optimal fiber length was additionally obtained. It was expected that this addition would lead to improvements in the prediction of muscle forces and better insight into the functioning of specific muscles since force-length and force-velocity relationships could be implemented. By including the muscle dynamics, some modifications and extensions were carried out in the model. Firstly, the inverse-dynamics model was modified in such a way that the muscle dynamics were taken into account as constraints on the maximum permissible muscle force during the inverse optimization. Secondly combined inverse-forward-dynamics versions of the DSEM (Chadwick and Van Der Helm, 2003; van der Helm and Chadwick, 2002) could be developed. Thirdly, a new muscle load sharing cost function for inverse optimization namely the energy-based criterion (Praagman et al, 2006) was introduced and implemented in the model. This new cost function is based on the energy consuming processes in a muscle needed to produce a contraction.

Although the DSEM has been widely used in a number of studies, it was not individually addressed in the literature. The aim of this chapter is to provide all aspects and developments of the model since its original introduction in 1994, including a qualitative validation of the three different simulation architectures available in the DSEM (inverse dynamics optimization - IDO, inverse-forward-dynamics optimization - IFDO, and inverse-forward-dynamics optimization with controller - IFDOC). The model simulations will be based on a new anatomical dataset and the application of an energy-based load sharing cost function enabled by the addition of the muscle architecture parameters. The DSEM will also be compared briefly to the other available biomechanical models of the shoulder.

2.2. Materials and Methods

2.2.1. Anatomical data

The geometrical data for the DSEM were taken from studies on the shoulder (Klein Breteler et al, 1999) and elbow (Minekus, 1997) from the same specimen, a 57 years old muscular male cadaver. In these studies a total number of 31 muscles/muscle parts of the shoulder (23 muscles) and elbow (8 muscles) were divided into 139 elements. Joint surfaces and other bony contours were digitized for modeling using geometrical forms. Muscle architecture parameters including tendon length, physiological cross-sectional area (PCSA), pennation angle, and the fiber length (l_f) were measured. The sarcomere lengths (l_s) were also measured using a laser-diffraction technique (Young et al, 1990). Assuming an optimal sarcomere length of 2.7 μm (Walker and Schrodt, 1974), the optimal fiber length (l_{opt}) for a muscle was calculated as:

$$l_{opt} = 2.7 \frac{l_f}{l_s} \tag{1}$$

Since the elbow data have not yet been published other than in an internal report (Minekus, 1997), these data are partly presented in Appendix A. These data include the position of bony landmarks, bony contours for muscle wrapping, the values of the muscle parameters (PCSA, mass and optimal fiber length), and the relative muscle force-sarcomere length curves. A brief description of the measurement methods is also given in Appendix A.

2.2.2. Kinematics

The DSEM is a finite-element model which has been implemented by building on the software packet SPACAR (van Soest et al, 1992) for the analysis of spatial multi-body mechanisms. For detailed descriptions of model kinematics and implementation in SPACAR see reference (van der Helm, 1994a).

The total number of DOF of the model is 17, namely 6 for the thorax (which is considered as the moving base), 3 for the shoulder girdle, 3 for the glenohumeral-joint, 2 for the elbow and 3 for the wrist.

There are several options to provide input to the model among which using the joint angles is the most popular.

To calculate the glenohumeral-joint rotation center, which is necessary for reconstruction of the local coordinate system of the humerus, the instantaneous helical axes method (Veeger, 2000; Woltring et al, 1994) is mostly used, although alternatives such as the use of regression equations (Meskers et al, 1998) or the SCoRE method (Ehrig et al, 2006; Monnet et al, 2007) are also possible in the DSEM (see Chapter 4 for a detailed description about the different methods).

For the definition of the clavicular orientation only two landmarks are generally available, thus, the axial rotation of the clavicle is estimated by minimizing the rotations in the acromioclavicular joint (van der Helm and Pronk, 1995).

The shoulder girdle is a closed-chain mechanism and the motions are constrained by such factors as the shape of the thorax over which the scapula glides, the length of the conoid ligament, the length of the clavicle, and the size of the scapula. As such, the motions of the shoulder girdle of a measured subject cannot be exactly reproduced by the model due to differences in the geometry between subject and model. To ensure that all positions input to the model can actually be assumed by the model, the measured angles are adjusted slightly to fit the constraints of the model by minimization of the following cost function (de Groot, 1998):

$$J = W_1\left((dC_x)^2 + (dC_y)^2 + (dC_z)^2\right) + W_2\left((dS_x)^2 + (dS_y)^2 + (dS_z)^2\right) \tag{2}$$

Where dC_x and dS_x are the differences between the measured and optimized angles for the clavicle and scapula around the x-axis, respectively. A similar definition is applied for angles around the y- and z- axes. W_1 and W_2 are weight factors, and were set at 1, resp. 2. For detailed description of the optimization procedure see Appendix B.

2.2.3. The Inverse-Dynamics Optimization (IDO)

In the original model (DSM), the inertial forces and moments were included but muscle dynamics were not. In the modified inverse dynamics model (IDO, Figure 2.1a) the muscle dynamics has been taken into account as constraint on the maximum permissible muscle force ($F_{max,i}$) in the inverse optimization process. The joint angles (θ_i) and external loads are used as the model inputs. The outputs of the model include muscle and joint reaction forces (F_i), muscle and ligament lengths, and muscle power.

The filtering and differentiation routines of Woltring (the GVC method) (1986) have been implemented to calculate velocities ($\dot{\theta}_i$) and accelerations ($\ddot{\theta}_i$) from the inputs.

The load-sharing problem is solved using a nonlinear optimization process in which a cost function is minimized. The stress cost function (SCF) which is based on minimization of the squared muscle stress (Crowninshield and Brand, 1981), was originally implemented in the DSM as the default objective function, but recently a new energy-based cost function (ECF) (Praagman et al, 2006) has been implemented. In the energy-based cost function, the energy consumption due to calcium pumping and cross-bridge function is taken into account (see Chapter 7 for a detailed description).

The calculated forces in the optimization process for each muscle element (m) are bounded by the inclusion of muscle force-length relation where minimum force is taken as zero and the maximum force is a function of maximum muscle stress ($\sigma_{\max}$), $PCSA$, and sarcomere length (l_{sm}):

$$F_{\max}(l_{sm}) = f(l_{sm}).PCSA_m.\sigma_{\max} \tag{3}$$

where $\sigma_{\max}$ is taken as 100 N/cm^2 (An et al, 1989). $f(l_{sm})$ is the normalized muscle force–length relationship defined as a Gaussian-type shape function (see reference (Winters and Stark, 1985) for a detailed description).

The model stability is defined as being maintained when the joint reaction force vector is directed inside the rim of the glenoid fossa, modeled by an ellipse.

2.2.4. The Inverse-Forward-Dynamics Optimization (IFDO)

The combination of an inverse dynamic optimization approach with inclusion of the muscle dynamics by a forward dynamic muscle model (IFDO) is an efficient way to obtain dynamically feasible muscle forces and neural inputs. Happee and van der Helm (1994; 1995) showed that inclusion of the muscle dynamics in the inverse optimization had considerable effects on the model-estimations of the neural inputs and individual muscle forces during performing goal-directed tasks.

The muscle models are required in order to account for the effect of muscle electromechanical delays and force-velocity relationship in an inverse-dynamic optimization. In the IFDO (Figure 2.1b) both forward and inverse muscle models are used. As for muscle model, a three-component Hill type model (Winters, 1990; Winters and Stark, 1985) consisting of a second-order activation dynamics part and a first-order contractile dynamics part is being used (for a detailed mathematical formulation of the muscle model see Appendix C).

At each time-step (i, Figure 2.1b) the calculated optimal muscle forces are constrained by maximum ($F_{max,i}$) and minimum ($F_{min,i}$) permissible values of the muscle forces estimated by a forward muscle model with use of the muscle states of the previous time-step (e_{i-2}, $a_{i,-1}$, $L_{ce,i-1}$). At the same time-step (i), an inverse muscle model is used to estimate the neural inputs (e_{i-1}, a_i, $L_{ce,i}$) that will be used as the inputs to the forward muscle model in the next step (i+1). The starting position is assumed to be quasi-static in which the initial vales of u, e, a, and L_{ce} are estimated through a steady-state equilibrium condition. During the next time steps, the states are updated in a dynamic optimization procedure. The values of e, a, and L_{ce} are updated iteratively while u is estimated analytically.

2.2.5. The Inverse-Forward-Dynamics Optimization with Controller (IFDOC)

Due to discretization errors and possibly an unstable system, the motions calculated by the forward-dynamic part in the IFDO will not be exactly the same as the recorded motions which were input to the inverse dynamics part. Therefore, the IFDO was modified in such a way that the difference in position and velocity will be fed back to the inverse-dynamic model. The modified model is called the IFDO with controller or simply the IFDOC (Figure 2.1c) (Chadwick and Van Der Helm, 2003). At each time step, the feedback controller will adjust the neural input signal in the next time step by calculating a correction moment (M_c) using the errors in angle and angular velocity. Therefore, a forward-dynamic simulation will be carried out which should result in exactly the same motion as the recorded motion. In the forward dynamics part of the model (Figure 2.1c), the forward musculoskeletal model developed by van der Helm and Chadwick (van der Helm and Chadwick, 2002) was implemented. For integration of the motion equations in forward dynamics analysis, two different algorithms namely the Adams-Moulton and Euler algorithms have been implemented in the model. The forward dynamics simulation based on the Euler method is up to four times faster than the Adams-Moulton algorithm, but less stable.

In contrast to the IDO model in which each time step is considered to be independent of the preceding time steps, in the IFDO and IFDOC analysis each time-step is coupled to the following time-steps through sets of differential equations.

2.2.6. Biomechanical applications of the model

The DSEM has frequently been applied. It was used to study goal directed movements (Happee and Van der Helm, 1995), wheelchair propulsion (Van Drongelen et al, 2005b; Veeger et al, 2002), rotator cuff tears (Steenbrink et al, 2009), tendon transfers (Magermans et al, 2004a; Magermans et al, 2004b), loads on the arm (Praagman et al, 2000; Steenbrink et al, 2009), rotator cuff changed following scapular neck fracture (Chadwick et al., 2004), effect of rotator cuff dysfunctions on wheelchair propulsion (Van Drongelen et al, 2005a), weight transfers in wheelchair users (Van Drongelen et al, 2006), and stability of cementless glenoid prostheses (Suarez et al, 2009).

2.2.7. Evaluation of the DSEM

To qualitatively validate the three different simulation architectures available in the DSEM (i.e. IDO, IFDO, and IFDOC), we compared EMG signals with model-predicted muscle forces. To this end, one patient (male, 64 yr, 163 cm, 85 kg) with shoulder hemi-arthroplasty was measured after giving informed consent. Measurements included the recording of pose and EMG. The subject was asked to perform a typical standard shoulder dynamic task (i.e. forward flexion motion) up to maximum possible arm elevation angle. The speed of movement was about 0.1 Hz.

For motion recordings, marker clusters on bony segments, including thorax, scapula, upper arm, and forearm, were measured using four Optotrak camera bars (Northern Digital Inc., Canada, nominal accuracy 0.3 mm) at a sampling frequency of 50 Hz. Considering the limited range of motion of the patient we used an acromion sensor (Karduna et al, 2001) for scapular motion tracking. Local coordinate systems of the segments were defined according the ISB standardization protocol (Wu et al, 2005).

EMG signals of 12 superficial muscles were measured using Ambu N-00-S ECG bipolar surface EMG electrodes and recorded by a 16-channels Porti system (TMS International, Enschede, The Netherlands) at the sampling frequency of 1000 Hz. The measured muscles included the trapezius ascendens, transversum, and descendens, the infraspinatus, the deltoid anterior, medialis, and posterior, the pectoralis major clavicular and thoracic parts, the biceps short head, the triceps medialis, and the brachioradialis. The SENIAM recommendations (Merletti et al, 1999) were followed for the EMG sensor positioning. We visually checked the measured signals for possible crosstalk. To determine the maximum EMG values, maximum voluntary contractions (MVCs) were also performed.

From the segment poses, joint angles were calculated based upon the ISB-standard and were used to run the three models. The ECF was used in all models to solve the muscle load sharing problem in the inverse dynamic optimization. To guarantee the stability of the forward dynamics simulations in the IFDOC, the Adams-Moulton algorithm with an integration time-step of 0.005s was used. The individual muscle forces as well as the glenohumeral joint reaction forces were estimated as the outputs of the model. The calculated muscle forces were normalized (relative muscle force) to the maximum muscle force (Equation 3).

Measured EMG’s were high-pass filtered, rectified, and subsequently low-pass filtered. For high- and low- pass filtering, second order Butterworth filter with cut-off frequencies of, respectively, 25 and 2 Hz were used. For each muscle, the measured EMG was normalized with respect to the maximum value found for that muscle during MVCs.

To evaluate the model, the time series of the relative forces and normalized EMG’s were compared. For each muscle, the comparison was carried out for the muscle element which was the closest to the position of the EMG electrodes on the subject’s body. Since the time series of forces and EMG were compared, we used the bivariate two-tailed Pearson correlation coefficient (R) as indicator of goodness of fit. Moreover, the resultant glenohumeral joint reaction force was compared between different modeling architectures.

2.3. Results

The simulation times for the IDO, IFDO, and IFDO were 43.3s, 68.2s, and 423.12s, respectively.

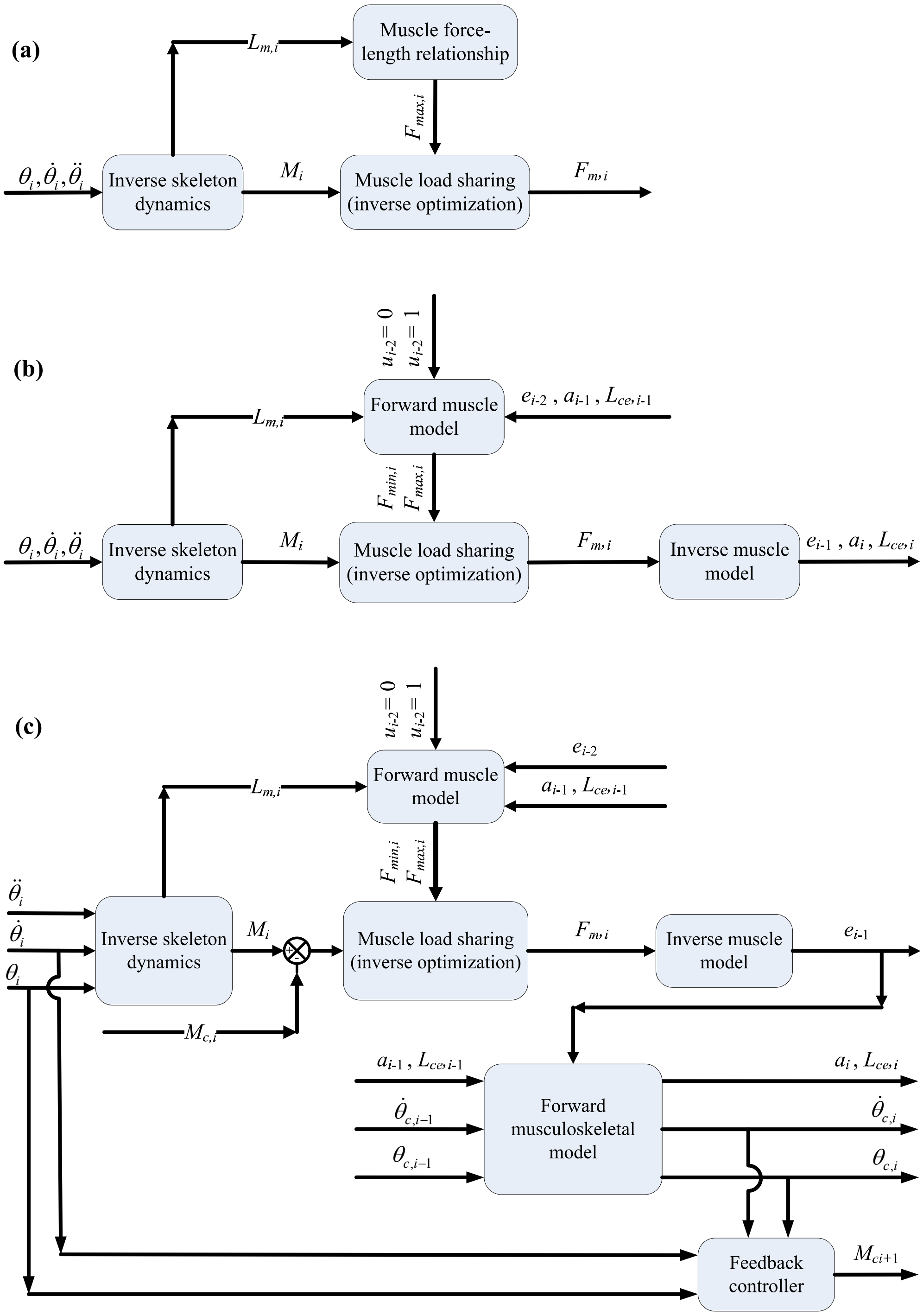

Figure 2.1. Schematic of the (a) IDO, (b) IFDO, and (c) IFDOC simulation architectures.

2.3.1. EMG-force comparison

For most conditions, the predicted forces (Figure 2.2) followed (mean R ~ 0.74) the pattern of the EMG signals (Figure 2.3). The IDO and IFDO showed almost the same but noticeably different results from IFDOC. In a few cases false-negatives were found in which no muscle force (Figure 2.2) was calculated by the model while EMG showed activity for that muscle (Figure 2.3). For IDO and IFDO models, the false-negatives occurred for trapezius descendens, deltoid posterior, and pectoralis major thoracic muscles. For IFDOC model, the false-negatives were related to biceps, pectoralis major thoracic, and triceps medialis. Except for false-negatives, three models followed the pattern of EMG signals. A very high correlation (R ~ 0.97) was found between the IDO and IFDO estimated force-time curves with the EMG signal of trapezius transversum, deltoid anterior, and triceps medialis. The correlation between the IFDOC predictions and the EMG was relatively high (R > 0.80) for trapezius ascendens, trapezius descendens, deltoid anterior, and infraspinatus muscles.

The results of comparing the estimated muscle force-time curves to measured EMG signals during forward flexion motion in the current study are comparable to the ones in the study by van der Helm (van der Helm, 1994b). In the study by van der Helm, the comparison was performed for the inverse dynamics model and by using the DSM original anatomical dataset and the SCF for inverse dynamics optimization. In both studies the false-negatives occurred for deltoid posterior and pectoralis major thoracic part (for humeral elevation ≤ 100º). A very similar pattern was observed in two studies for the predicted muscle forces of infraspinatus and deltoid anterior muscles.

2.3.2. Glenohumeral joint reaction force comparison

The IFDOC predicted considerably higher (~ 26%) reaction force in the glenohumeral joint at the peak elevation angle as compared with the IDO and IFDO (Figure 2.4).

2.4. Discussion

This chapter aimed to, first, report about all developments of the DSEM since its early introduction, second, to compare the force-time curves with the EMG signals in order to qualitatively evaluate the three simulation architectures available in the DSEM, and third to compare the DSEM with currently available large-scale musculoskeletal models of the shoulder.

2.4.1. Evaluation of the DSEM

The qualitative validation was carried out for the generic model for one subject performing a typical dynamic shoulder task (i.e. forward flexion). The model was not scaled to subject’s geometry. Main reasons for this are the difficulties related to scaling in general, but also the choice to present the model as currently and up till now mostly used, which is not scaled, but with scaled (optimized) kinematics.

Results (Figures 2.2 and 2.3) showed a relatively good agreement between the model-predicted normalized forces and measured EMG of individual muscles, although a few cases of false-negatives were observed. The IDO and IFDO showed very similar patterns but quite different patterns from IFDOC. The predicted glenohumeral joint reaction force by the IFDOC was also considerably higher in comparison to the other two models (Figure 2.4).

As discussed earlier, the original DSM was previously validated by comparing the estimated muscle force-time curves to measured EMG signals (van der Helm, 1994b). That comparison was performed using the DSM original anatomical dataset and the SCF for inverse dynamics optimization, while the specific muscle force-length relationship was not included in the model. In this study, the new anatomical dataset and optimization criterion (the ECF) were used and validation was performed for the three modeling architectures (IDO, IFDO, and IFDOC). In the modified IDO model used for the current study, the muscle force-length relationships were also considered in the inverse optimization.

Praagman *et al* (2006) compared the model predicted muscle forces to measured muscle oxygen consumption. They used elbow isometric contractions and applied both the SCF and ECF. They concluded that the ECF led to fewer false-negatives and a higher correlation between predicted muscle forces and measured oxygen consumption. In a more recent study (Steenbrink et al, 2009), it was shown that comparing to the SCF using the ECF makes a better consistency between the experimentally measured and model estimated so-called Principal Action. The results of these studies suggest that the ECF would be the preferred optimization criterion for the DSEM. Therefore, in the current study the ECF was used in the process of model evaluation.

The IDO and IFDO predicted similar forces. Therefore, the effects of considering the muscle force-velocity relationship in case of low-speed motions (in our case ~ 0.1 Hz) are not remarkable. One would expect the muscle force-velocity relationship to be more of influence during high-speed shoulder movements like throwing a ball in baseball. However, the IFDOC predictions of the relative muscle forces as well as the glenohumeral joint reaction force were considerably different from those of the other two models. This difference between models may relate to the forward-dynamics optimization and/or the feedback controller which may lead to calculation of noticeably different neural inputs and/or corrected moment (Figure 2.1c). As Heckathorne and Childress (1981) concluded, the amplitude of the surface EMG is affected by muscle length. Therefore, the measured surface EMG can only be applied for qualitative model validation. Nonetheless, the relative muscle forces close to one as predicted by IFDOC for trapezius ascendens, trapezius transversum, and deltoid anterior do not seem to be realistic.

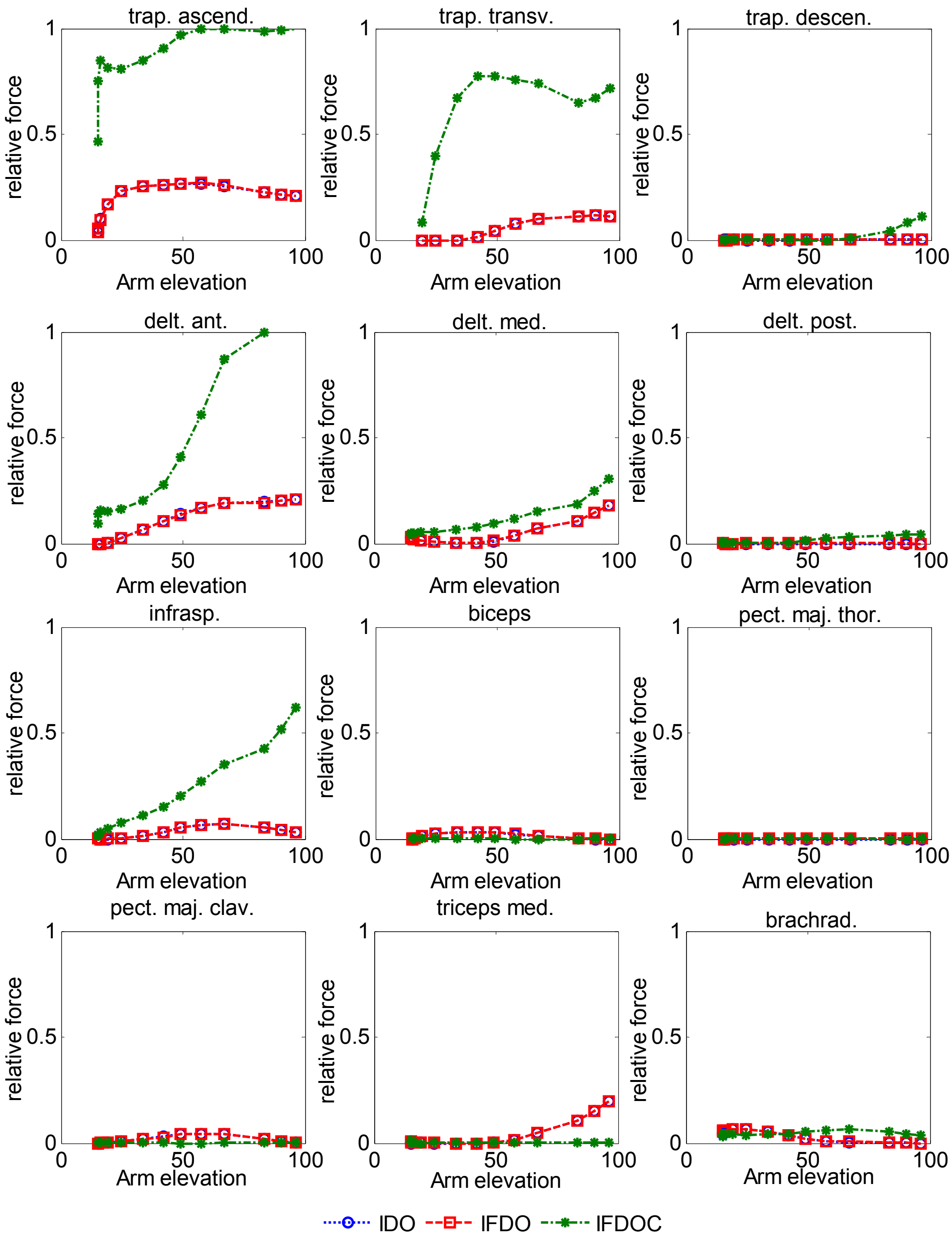

Figure 2.2. The relative muscle forces for 12 muscles (muscle parts) during forward flexion motion. The simulations from three modeling architectures (IDO, IFDO, and IFDOC) are compared. The forces are plotted against arm elevation angles (in degrees).

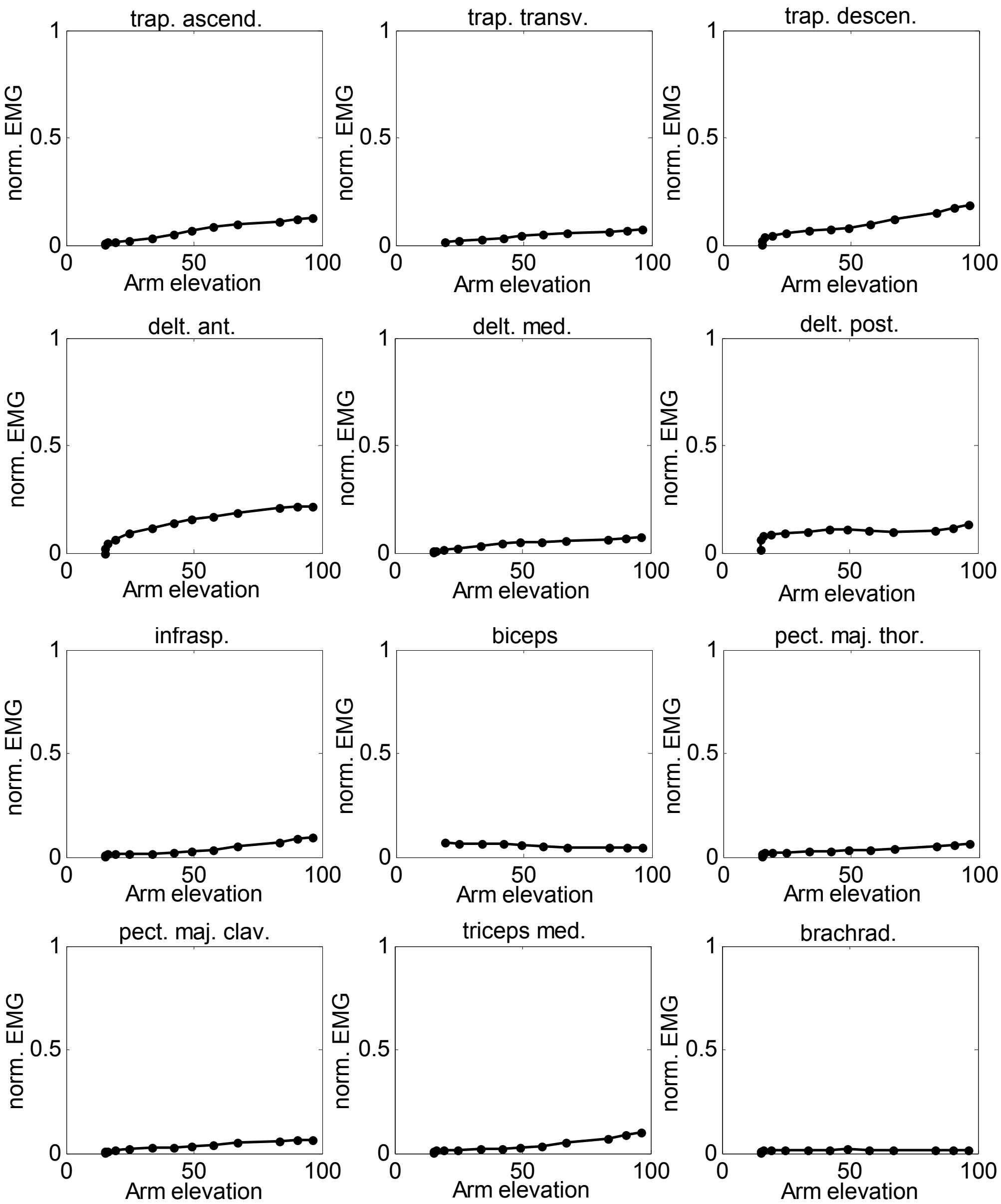

Figure 2.3. The normalized EMG for 12 muscles (muscle parts) during forward flexion motion. The EMGs are plotted against arm elevation angles (in degrees). (trap. ascen.: trapezius ascendens, trap. transv.: trapezius transversum, trap. descen.: trapezius descendens, infrasp.: infraspinatus, delt. ant.: deltoid anterior, delt. med.: deltoid medialis, delt. post.: deltoid posterior, pect. maj. thor.: pectoralis major thoracic, pect. maj. clav.: pectoralis major clavicular, biceps: biceps short head, triceps med.: triceps medialis, and brachrad.: brachioradialis)

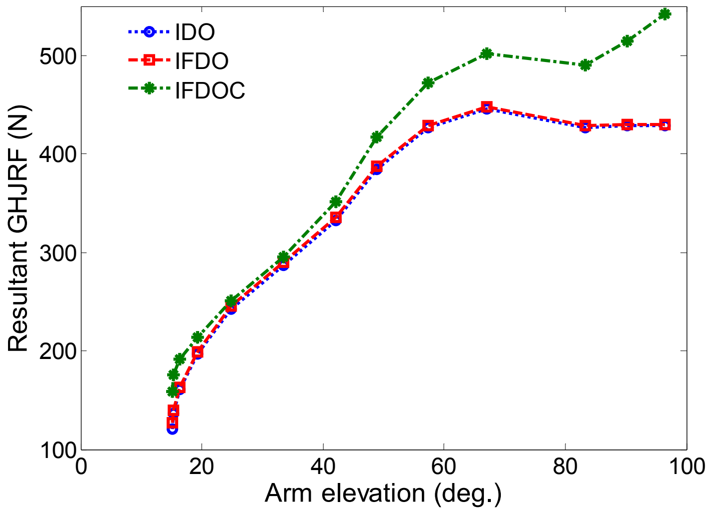

Figure 2.4. The predicted resultant reaction force in the glenohumeral joint (GH-JRF) by the IDO, IFDO, and IFDO models versus arm elevation angle during forward flexion motion.

On the other hand, in a recent study (Nikooyan et al, 2010) and in an attempt to quantitatively validate the DSEM, the glenohumeral-joint reaction forces estimated by the IDO model were compared to those simultaneously measured by the instrumented shoulder implant (Westerhoff et al, 2009). The results of that study (see also Chapter 5) showed that the generic IDO model generally underestimates the glenohumeral-joint reaction forces during standard dynamic tasks such as abduction and forward flexion. According to the results of the current study, the IFDOC predicts higher glenohumeral joint reaction forces during dynamic motions like forward flexion compared with the IDO. This means that the IFDOC can potentially be a better candidate for modeling dynamic tasks. However, we still cannot trust the IFDOC predictions of individual muscle forces. Therefore a rigorous validation of the IFDOC model is still required for a decisive conclusion. Moreover, one should note that the IFDOC needs much more (i.e. 10 times more) simulation time than the IDO.

2.4.2. Comparing different models

When the DSEM is compared to other sophisticated shoulder models (Table 2.1) some differences can be discerned:

In contrast to the DSEM in which the motions of the scapula and clavicle are used as inputs, the Swedish Shoulder Model (SSM), Newcastle shoulder model (NSM), and the SIMM model use the ‘shoulder rhythm’ as input for scapular motions. While this is practical since kinematic data collection is highly simplified, the downside of that option is the limitation of their use to applications where scapular motion is not disturbed.

For optimization most models use the quadratic cost function, although the SSM also uses the so-called soft-saturation criterion (Siemienski, 1992). The AnyBody and Delft models use also the min/max (Rasmussen et al, 2001) and energy-based criteria, respectively, as optimization cost function.

For the SSM, the predicted forces and the normalized EMG patterns of four muscles of the shoulder have been compared (Jarvholm et al, 1989; Jarvholm et al, 1991). Most importantly, results showed significant differences above 60 to 90 degrees humeral elevation during abduction.

The Newcastle shoulder model (NSM) is based to a large extent on the same data as the DSM, but also includes data from reference (Johnson et al, 1996). Although the muscle force predictions from NSM have been compared with those of DSM and SSM, there is no individual report on validation of the model.

The AnyBody shoulder model uses the original anatomical dataset of the DSEM but its structure is slightly different: the scapulothoracic-gliding plane and wrapping contours for the deltoid muscle have differently been modeled. The validation of the model was performed for wheelchair propulsion (Dubowsky et al, 2008).

Comparing to the other models, the SIMM model (Holzbaur et al, 2005) is rather simplified since it accounts for only 9 muscles of the shoulder. The number of muscles is similar (=16) for the other models except for the model by Graner and Pandy (2001) (the subclavius is also included in that model).

The relatively new developed model by Blana *et al* (2008) uses the new DSEM anatomical dataset and optimization criterion, but the SIMM algorithms for calculating muscle wrapping paths rather than those of SPACAR. The model can be used in both inverse and forward dynamics analyses, and was evaluated by force-EMG comparison for standard dynamic and activity of daily living tasks using a similar method to that described here.

Despite all its advantages, the DSEM does not offer any Graphical User Interface (GUI). Although there is a MATLAB routine to plot the model outputs, no visual interface exists for modeling purposes like the one in the commercial simulation environments like AnyBody and/or SIMM.

2.5. Conclusions

This study was an update on the developments of a sophisticated musculoskeletal model of the entire shoulder and elbow, the Delft Shoulder and Elbow Model, over the last decade including a qualitative validation of the three simulation architectures (IDO, IFDO, and IFDOC) available in the model. The DSEM was also compared to the other existing comprehensive models of the shoulder. Following conclusions can be drawn from this study:

Table 2.1. Comparing different sophisticated musculoskeletal shoulder models

Shoulder model		**Anatomical data**	**No. muscles**	**Scapular/clavicular kinematics**	**Load sharing criteria**
Delft model	(van der Helm, 1994a)	(Klein Breteler et al, 1999)	16	scapular/clavicular rotations as model inputs	- quadratic - energy-based
Swedish model	(Karlsson and Peterson, 1992)	(Hogfors et al, 1987)	16	regression model for shoulder rhythm	- quadratic - soft saturation
Austin model	(Garner and Pandy, 2001)	Visible Human Male Project Dataset	17	scapular/clavicular rotations as model inputs	-
SIMM model	(Holzbaur et al, 2005)	(Langenderfer et al, 2004)	9	regression model for shoulder rhythm	- quadratic
Newcastle model	(Charlton and Johnson, 2006)	(Johnson et al, 1996; van der Helm et al, 1992)	16	regression model for shoulder rhythm	- quadratic
AnyBody Model	(Damsgaard et al, 2006)	(van der Helm et al, 1992)	16	regression model and/or scapular/clavicular rotations as inputs	- quadratic - min/max
Cleveland model	(Blana et al, 2008)	(Klein Breteler et al, 1999)	16	regression model for shoulder rhythm	- energy-based

The developed model has capability of inverse-, forward-, and combined inverse-forward dynamics analysis and has potential to be recruited in different clinical and biomechanical applications.

- For more realistic predictions, it is recommended to use the new anatomical dataset and the new developed (energy-based) load sharing cost function.
- A relatively good agreement was found between model-predicted forces and measured EMG signals.
    - The IDO and IFDO predicted similar forces. Therefore, the effects of considering the muscle force-velocity relationship in case of low-speed motions were not remarkable.
    - The IFDOC predictions were considerably different from those of the other two models. The IFDOC can potentially be a better candidate for modeling dynamic tasks. However, a rigorous validation of the IFDOC is still required for a decisive conclusion.
- The DSEM is one of the most comprehensive existing shoulder models.

2.6. References

An, K.N., Kaufman, K.R., Chao, E.Y.S., 1989. Physiological considerations of muscle force through the elbow joint. Journal of Biomechanics 22 (11-12), 1249-1256.

Blana, D., Hincapie, J.G., Chadwick, E.K., Kirsch, R.F., 2008. A musculoskeletal model of the upper extremity for use in the development of neuroprosthetic systems. Journal of Biomechanics 41 (8), 1714-1721.

Chadwick, E.K.J., Van Der Helm, F.C.T., Combined inverse/forward dynamic optimization of a large-scale biomechanical model of the shoulder and elbow, presented at IX International Symposium on Computer Simulation in Biomechanics, Sydney, Australia, 2003.

Charlton, I.W., Johnson, G.R., 2006. A model for the prediction of the forces at the glenohumeral joint. Proceedings of the Institution of Mechanical Engineers part H-Journal of Engineering in Medicine 220 (H8), 801-812.

Crowninshield, R.D., Brand, R.A., 1981. A physiologically based criterion of muscle force prediction in locomotion. Journal of Biomechanics 14 (11), 793-801.

Damsgaard, M., Rasmussen, J., Christensen, S.T., Surma, E., de Zee, M., 2006. Analysis of musculoskeletal systems in the AnyBody Modeling System. Simulation Modelling Practice and Theory 14 (8), 1100-1111.

de Groot, J.H., 1998. The shoulder: a kinematic and dynamic analysis of motion and loading. PhD Thesis, Delft University of Technology, Delft.

Dubowsky, S.R., Rasmussen, J., Sisto, S.A., Langrana, N.A., 2008. Validation of a musculoskeletal model of wheelchair propulsion and its application to minimizing shoulder joint forces. Journal of Biomechanics 41 (14), 2981-2988.

Ehrig, R.M., Taylor, W.R., Duda, G.N., Heller, M.O., 2006. A survey of formal methods for determining the centre of rotation of ball joints. Journal of Biomechanics 39 (15), 2798-2809.

Engin, A.E., Chen, S.M., 1986. Statistical data base for the biomechanical properties of the human shoulder complex - I: kinematics of the shoulder complex. Journal of Biomechanical Engineering-Transactions of the ASME 108, 215-221.

Garner, B.A., Pandy, M.G., 2001. Musculoskeletal model of the upper limb based on the visible human male dataset. Computer methods in biomechanics and biomedical engineering 4 (2), 93-126.

Happee, R., 1994. Inverse dynamic optimization including muscular dynamics, a new simulation method applied to goal directed movements. Journal of Biomechanics 27 (7), 953-960.

Happee, R., Van der Helm, F.C.T., 1995. The control of shoulder muscles during goal directed movements, an inverse dynamic analysis. Journal of Biomechanics 28 (10), 1179-1191.

Heckathorne, C.W., Childress, D.S., 1981. Relationships of the surface electromyography to the force, length, velocity, and contraction rate of the cineplastic human biceps. American Journal of Physical Medicine 60 (1), 1-19.

Hogfors, C., Peterson, B., Sigholm, G., Herberts, P., 1991. Biomechanical model of the human shoulder joint--II. The shoulder rhythm. Journal of Biomechanics 24 (8), 699-709.

Hogfors, C., Sigholm, G., Herberts, P., 1987. Biomechanical model of the human shoulder--I. Elements. Journal of Biomechanics 20 (2), 157-166.

Holzbaur, K.R.S., Murray, W.M., Delp, S.L., 2005. A model of the upper extremity for simulating musculoskeletal surgery and analyzing neuromuscular control. Annals of Biomedical Engineering 33 (6), 829-840.

Jarvholm, U., Palmerud, G., Herberts, P., Hogfors, C., Kadefors, R., 1989. Intramuscular pressure and electromyography in the supraspinatus muscle at shoulder abduction. Clinical Orthopaedics and Related Research (245), 102-109.

Jarvholm, U., Palmerud, G., Karlsson, D., Herberts, P., Kadefors, R., 1991. Intramuscular pressure and electromyography in four shoulder muscle. Journal of Orthopaedic Research 9 (4), 609-619.

Johnson, G., Spalding, D., Nowitzke, A., Bogduk, N., 1996. Modelling the muscles of the scapula morphometric and coordinate data and functional implications. Journal of Biomechanics 29 (8), 1039–1051.

Karduna, A.R., McClure, P.W., Michener, L.A., Sennett, B., 2001. Dynamic measurements of three-dimensional scapular kinematics: A validation study. Journal of Biomechanical Engineering 123, 184-190.

Karlsson, D., Peterson, B., 1992. Towards a model for force predictions in the human shoulder. Journal of Biomechanics 25 (2), 189-199.

Klein Breteler, M.D., Spoor, C.W., Van der Helm, F.C.T., 1999. Measuring muscle and joint geometry parameters of a shoulder for modeling purposes. Journal of Biomechanics 32 (11), 1191-1197.

Langenderfer, J., Jerabek, S.A., Thangamani, V.B., Kuhn, J.E., Hughes, R.E., 2004. Musculoskeletal parameters of muscles crossing the shoulder and elbow and the effect of sarcomere length sample size on estimation of optimal muscle length. Clinical Biomechanics 19, 664-670.

Magermans, D.J., Chadwick, E.K.J., Veeger, H.E.J., Rozing, P.M., van der Helm, F.C.T., 2004a. Effectiveness of tendon transfers for massive rotator cuff tears: a simulation study. Clinical Biomechanics 19 (2), 116-122.

Magermans, D.J., Chadwick, E.K.J., Veeger, H.E.J., van der Helm, F.C.T., Rozing, P.M., 2004b. Biomechanical analysis of tendon transfers for massive rotator cuff tears. Clinical Biomechanics 19 (4), 350-357.

Makhsous, M., Hogfors, C., Siemien'ski, A., Peterson, B., 1999. Total shoulder and relative muscle strength in the scapular plane. Journal of Biomechanics 32 (11), 1213-1220.

Merletti, R., Wallinga, W., Hermens, H., Freriks, B., *Guidelines for reporting SEMG data*: Roessingh Research and Development, 1999.

Meskers, C.G.M., van der Helm, F.C.T., Rozendaal, L.A., Rozing, P.M., 1998. In vivo estimation of the glenohumeral joint rotation center from scapular bony landmarks by linear regression. Journal of Biomechanics 31 (1), 93-96.

Minekus, J., "Kinematical model of the human elbow," Leiden University, Leiden 1997.

Monnet, T., Desailly, E., Begon, M., Vallee, C., Lacouture, P., 2007. Comparison of the SCoRE and HA methods for locating in vivo the glenohumeral joint centre. Journal of Biomechanics 40 (15), 3487-3492.

Nikooyan, A.A., Veeger, H.E.J., Westerhoff, P., Graichen, F., Bergmann, G., van der Helm, F.C.T., 2010. Validation of the Delft Shoulder and Elbow Model using in-vivo glenohumeral joint contact forces. Journal of Biomechanics 43 (15), 3007-3014.

Praagman, M., Chadwick, E.K.J., van der Helm, F.C.T., Veeger, H.E.J., 2006. The relationship between two different mechanical cost functions and muscle oxygen consumption. Journal of Biomechanics 39 (4), 758-765.

Praagman, M., Stokdijk, M., Veeger, H.E.J., Visser, B., 2000. Predicting mechanical load of the glenohumeral joint, using net joint moments. Clinical Biomechanics 15 (5), 315-321.

Pronk, G.M., Van der Helm, F.C.T., 1991. The Palpator: an instrument for measuring the positioning of bones in three dimensions. J Med Eng Tech 15 (1), 15-20.

Rasmussen, J., Damsgaard, M., Voigt, M., 2001. Muscle recruitment by the min/max criterion -- a comparative numerical study. Journal of Biomechanics 34 (3), 409-415.

Siemienski, A., "Soft saturation - an idea for load sharing between muscles. Application to the study of Human locomotion," in *Biolocomotion: A Century of Research Using Moving Pictures*, A. Cappozzo, M. Marchetti, and V. Tosi, Eds. Rome, 1992, pp. 293-303.

Steenbrink, F., de Groot, J.H., Veeger, H.E.J., van der Helm, F.C.T., Rozing, P.M., 2009. Glenohumeral stability in simulated rotator cuff tears. Journal of Biomechanics 42 (11), 1740-1745.

Steenbrink, F., Meskers, C.G.M., van Vliet, B., Slaman, J., Veeger, H.E.J., De Groot, J.H., 2009. Arm load magnitude affects selective shoulder muscle activation. Medical & Biological Engineering & Computing 47 (5), 565-72.

Suarez, D.R., Valstar, E.R., Linden, J.C., Van Keulen, F., Rozing, P.M., 2009. Effect of rotator cuff dysfunction on the initial mechanical stability of cementless glenoid components. Medical & Biological Engineering & Computing 47 (5 SPEC. ISS.), 507-514.

van der Helm, F.C.T., 1994a. A finite element musculoskeletal model of the shoulder mechanism. Journal of Biomechanics 27 (5), 551-553.

van der Helm, F.C.T., 1994b. Analysis of the kinematic and dynamic behavior of the shoulder mechanism. Journal of Biomechanics 27 (5), 527-550.

van der Helm, F.C.T., Chadwick, E.K.J., A forward-dynamic shoulder and elbow model, presented at 4th meeting of the International Shoulder Group, Cleveland, OH, USA, 2002.

van der Helm, F.C.T., Pronk, G.M., 1995. Three-dimensional recording and description of motions of the shoulder mechanism. Journal of Biomechanical Engineering 117, 27-40.

van der Helm, F.C.T., Veeger, H.E.J., Pronk, G.M., Van der Woude, L.H.V., Rozendal, R.H., 1992. Geometry parameters for musculoskeletal modelling of the shoulder system. Journal of Biomechanics 25 (2), 129-144.

van der Helm, F.C.T., Veenbaas, R., 1991. Modelling the mechanical effect of muscles with large attachment sites: Application to the shoulder mechanism. Journal of Biomechanics 24 (12), 1151-1163.

Van Drongelen, S., Van Der Woude, L.H., Janssen, T.W., Angenot, E.L., Chadwick, E.K., Veeger, D.H., 2005a. Glenohumeral contact forces and muscle forces evaluated in wheelchair-related activities of daily living in able-bodied subjects versus subjects with paraplegia and tetraplegia. Archives of Physical Medicine and Rehabilitation 86 (7), 1434-1440.

Van Drongelen, S., Van Der Woude, L.H., Janssen, T.W., Angenot, E.L., Chadwick, E.K., Veeger, D.H., 2005b. Mechanical load on the upper extremity during wheelchair activities. Archives of Physical Medicine and Rehabilitation 86 (6), 1214-1220.

Van Drongelen, S., Van Der Woude, L.H.V., Janssen, T.W.J., Angenot, E.L.D., Chadwick, E.K.J., Veeger, H.E.J., 2006. Glenohumeral joint loading in tetraplegia during weight relief lifting: A simulation study. Clinical Biomechanics 21 (2), 128-137.

van Soest, A.J., Schwab, A.L., Bobbert, M.F., van Ingen Schenau, G.J., 1992. SPACAR: A software subroutine package for simulation of the behavior of biomechanical systems. Journal of Biomechanics 25 (10), 1219-1226.

Veeger, H.E.J., 2000. The position of the rotation center of the glenohumeral joint. Journal of Biomechanics 33 (12), 1711-1715.

Veeger, H.E.J., Rozendaal, L.A., van der Helm, F.C.T., 2002. Load on the shoulder in low intensity wheelchair propulsion. Clinical Biomechanics 17 (3), 211-218.

Veeger, H.E.J., Van Der Helm, F.C.T., Van Der Woude, L.H.V., Pronk, G.M., Rozendal, R.H., 1991. Inertia and muscle contraction parameters for musculoskeletal modelling of the shoulder mechanism. Journal of Biomechanics 24 (7), 615-629.

Veeger, H.E.J., Yu, B., An, K.-N., Rozendal, R.H., 1997. Parameters for modeling the upper extremity. Journal of Biomechanics 30 (6), 647-652.

Veldpaus, F.E., Woltring, H.J., Dortmans, L.J.M.G., 1988. A least-squares algorithm for the equiform transformation from spatial marker co-ordinates. Journal of Biomechanics 21 (1), 45-54.

Walker, S.M., Schrodt, G.R., 1974. I segmental lengths and thin filament periods in skeletal muscle fibres of the rhesus monkey and human. Anatomical Record 178, 63-82.

Westerhoff, P., Graichen, F., Bender, A., Rohlmann, A., Bergmann, G., 2009. An instrumented implant for in vivo measurement of contact forces and contact moments in the shoulder joint. Medical Engineering & Physics 31 (2), 207-213.

Winters, J.M., "Hill based muscle models: a systems engineering perspective," in *Multiple muscle systems: biomechanics and movement organization*, J. M. Winters and S. L.-Y. Woo, Eds. New York: Springer, 1990, pp. 70-93.

Winters, J.M., Stark, L., 1985. Analysis of fundamental human movement patterns through the use of in-depth antagonistic muscle models. IEEE T Bio-Med Eng 32, 826-839.

Winters, J.M., Stark, L., 1988. Estimated mechanical properties of synergistic muscles involved in movements of a variety of human joints. Journal of Biomechanics 21 (12), 1027-1041.

Woltring, H., 1986. A FORTRAN package for generalized, cross-validatory spline smoothing and differentiation. Adv Eng Softw 8, 104–113.

Woltring, H.J., Long, K., Osterbauer, P.J., Fuhr, A.W., 1994. Instantaneous helical axis estimation from 3-D video data in neck kinematics for whiplash diagnostics. Journal of Biomechanics 27 (12), 1415-1425.

Wu, G., van der Helm, F.C.T., Veeger, H.E.J., Makhsous, M., Van Roy, P., Anglin, C., Nagels, J., Karduna, A.R., McQuade, K., Wang, X., Werner, F.W., Buchholz, B., 2005. ISB recommendation on definitions of joint coordinate systems of various joints for the reporting of human joint motion--Part II: shoulder, elbow, wrist and hand. Journal of Biomechanics 38 (5), 981-992.

Young, L.L., Papa, C.M., Lyon, C.E., George, S.M., Miller, M.F., 1990. Comparison of microscopic and laser diffraction methods for measuring sarcomere lengths of contracted muscle fibers of chicken pectoralis major muscle. Poultry Science 69, 1800-1802.

2.7. Appendix A – Parameters of the elbow

2.7.1. Measurement of the geometrical parameters

All muscles of the elbow were dissected from the cadaver after they were divided in multiple parts. The elbow muscles which pass through the hand were cut at the level of the retinaculum flexorum and extensorum. The geometrical parameters including the origins and insertions of the muscles and ligaments, the shape and position of the bony contours, the rotation centers of the joints, and the position of the anatomical landmarks (Figure A1, Table A1) were measured using a 3-D digitizer (Pronk and Van der Helm, 1991). Before dissection, at least four metal screws were put in all segments of the specimen and the positions of all these screws were measured in the intact body. From those measurements the global coordinate system and relative orientations of all segments were obtained. In subsequent measurements with the digitizer, the positions of the geometrical parameters were determined in their local coordinate systems as defined with the aforementioned screws and subsequently transformed from the local to the global coordinate system. The shape and position of the bony contours which determine the wrapping objects for the muscles (Table A2) were estimated by a least squares method. The flexion and pronation axes (Table A3) were calculated on the basis of screw axes. To determine the flexion axis, the orientation screws of the humerus (fixed to a frame), and ulna were measured at different elbow flexion angles. The rotation matrices and axes for each set of measurements were calculated by using the method in reference (Veldpaus et al, 1988). The averaged rotation axis was then used as the elbow flexion axis. For the pronation axis, the radius was fixed to a frame and the orientation screw of the ulna and radius were measured at different pronation angles. Similar calculations as for the flexion axis were used to determine the pronation axis.

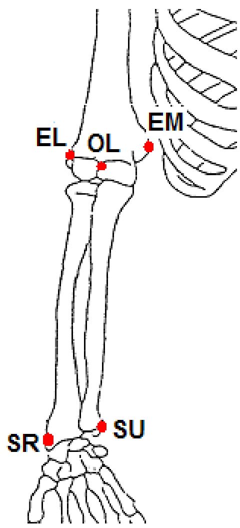

Figure A1. Palpable anatomical landmarks on the humerus, ulna and radius.

Table A1 - Positions of palpable bony landmarks (BL) on the Humerus, Ulna, and Radius in the global coordinate system defined in reference (Klein Breteler et al, 1999)

BL	*X* (cm)	*Y* (cm)	*Z* (cm)
Epicondyle medialis (EM)	15.66	-30.79	10.56
Epicondyle lateral (EL)	21.53	-30.21	7.15
Olecranon (OL)	18.97	-30.23	10.58
Styloideus Ulnae (SU)	21.54	-55.71	3.39
Styloideus Radii (SR)	17.29	-55.01	0.01

Table A2 - Bony contours. [d_x d_y d_z] is the direction of the central axis of the cylinder; [P_x P_y P_z] is the coordinate of an arbitrary point on the central axis of the cylinder; R is the radius. All values are in cm.

Wrapping object	Bony structure	P_x	P_y	P_z	d_x	d_y	d_z	R
Cylinder 1	Radius	19.92	-35.32	5.79	0.0993	0.9003	0.4239	0.92
Cylinder 2	Ulna	19.36	-30.80	9.02	0.8531	0.0183	-0.5108	1.90
Cylinder 3	Ulna	19.36	-30.80	9.02	-0.8531	-0.0183	0.5108	1.50
Cylinder 4	Radius	19.79	-43.87	3.87	0.0186	0.9767	0.2136	0.90
Cylinder 5	Ulna	20.77	-51.88	3.88	-0.1157	0.9547	0.274	0.70
Cylinder 6	Radius	19.28	-40.60	3.49	-0.1481	-0.8839	-0.4436	0.71

Table A3 – The position ([P_x P_y P_z]) and orientation ([d_x d_y d_z]) of the functional axes of rotation of the elbow. All values are in cm.
Flex.: Flexion, Ext.: Extension, Pro.: Pronation, Sup.: Supination

Rotation axis	Bony structure	P_x	P_y	P_z	d_x	d_y	d_z
Flex./Ext.	humerus-ulna	19.36	-30.80	9.02	0.8531	0.0183	-0.5108
Pro./Sup.	ulna-radius	20.11	-32.27	6.87	-0.0604	0.9874	0.1465

2.7.2. Measurement of the muscle parameters

2.7.2.1. Sarcomere length

Sarcomere length was measured by the laser diffraction method. In this method, light is diffracted due to passing of the laser through the muscle fiber. The laser tube is positioned at a fixed distance from the wall on which the sarcomere length can be read from the calibrated scale. Measurement samples of the muscle fiber bundles with 1cm length were prepared. At each cross-section, about 10 fibers were selected. The samples were thin enough to let the laser light to shine through them. Before starting the measurements, it was checked that as long as the measuring sample is not pulled during the measurement, the sample preparation does not affect the sarcomere length. Considering the variations of the sarcomere length through the muscle fiber (up to about 0.2µm), the sarcomere length was measured at different places over the muscle fiber where the average value was used as the mean sarcomere length. The number of sarcomere was then calculated by dividing the measured muscle fiber length by the calculated mean sarcomere length.

The relative maximum forces as well as the actual sarcomere length of each muscle element were calculated at five flexion postures from 0 to 120º with the step of 30º while forearm was supinated. The relative force-sarcomere length curves of all elements of the biceps breve and anconeus muscles are, respectively, shown in Figures A2 a and b.

2.7.2.2. Muscle length, mass, and PCSA

For each muscle element, the length (l_m) between the two markers put at the origin and insertion was measured. From each muscle element, three fiber bundles were dissected and their lengths (l_f) were measured. The tendon length (l_t) was calculated as the difference between the total muscle length and the fiber length:

$$l_t = l_m - l_f \tag{A1}$$

The mass of the muscle bellies without the tendons was measured as the muscle mass (m). The specific density of the muscles (δ) were previously measured by (Klein Breteler et al, 1999). Considering that the volume of the muscles remains constant during the contractions, the physiological cross sectional area ($PCSA$) was calculated as follows:

$$PCSA = \frac{m}{\delta . l_{opt}} \tag{A2}$$

Where, l_{opt} is the optimum fiber length.

The measured muscle parts of the elbow and their origins and insertions are summarized in Table A4. In Table A5, the muscle parameters of all elbow muscle elements including PCSA, mass and optimum fiber length are also given.

Table A4 - Measured muscle parts of the elbow and their origins and insertions

Muscle	No. elements	Origin	Insertion
m. biceps caput longum (BL)	1	humerus	radius
m. biceps caput breve (BB)	2	scapula	radius
m. triceps caput longum (TRL)	4	scapula	ulna
m. triceps caput mediale (TRM)	5	humerus	ulna
m. triceps caput laterae (TRLT)	5	humerus	ulna
m. brachialis (BR)	7	humerus	ulna
m. brachioradilais (BRD)	3	humerus	radius
m. anconeus (ANC)	5	humerus	ulna
m. supinator ulna-rad (SUP)	5	ulna	radius
m. pronator quadratus (PQ)	3	ulna	radius
m. pronator teres hum-rad (PT hum)	1	humerus	radius
m. pronator teres ulna-rad (PT uln)	1	ulna	radius

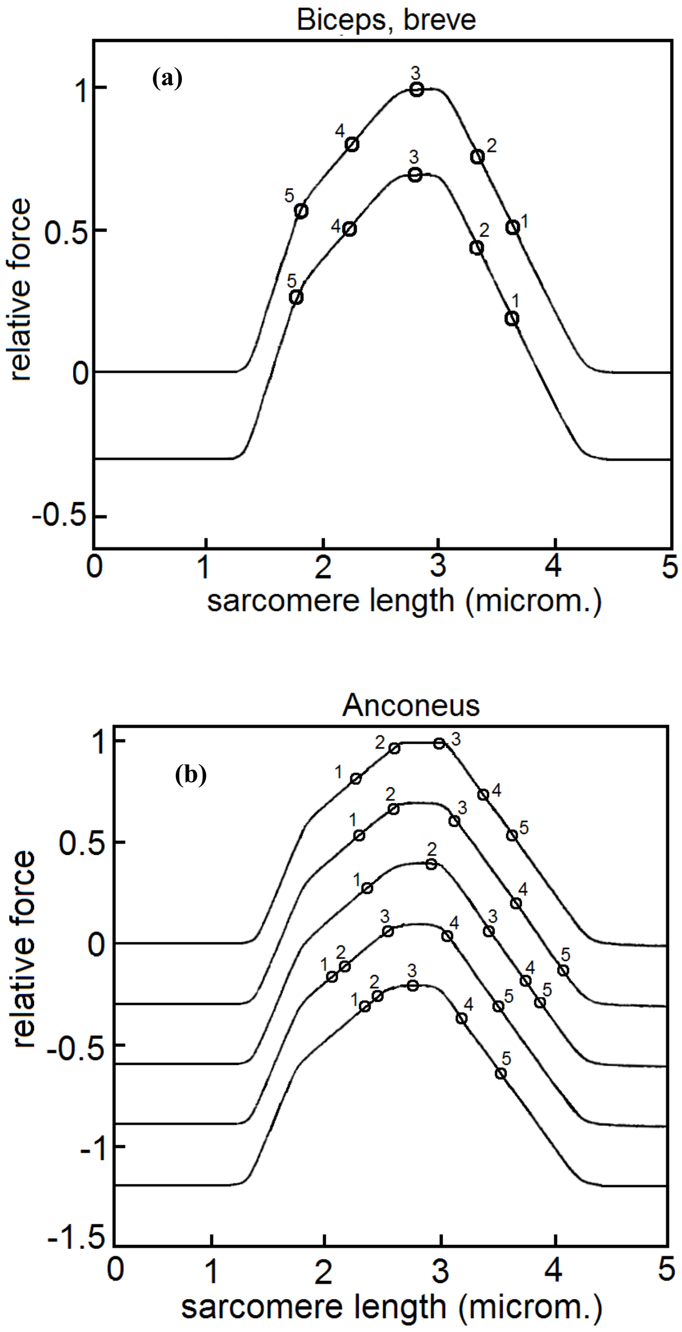

Figure A2 - Relative maximum forces vs. sarcomere length in all elements of the (a) biceps caput breve and (b) anconeus muscles. The numbers 1 to 5 on each subfigure stand for the positions during flexion from 0 to 120 degrees (with step of 30 degrees) while the forearm is supinated.

Table A5 - Muscle parameters including PCSA, mass, and optimum fiber length

Muscle	Element no.	PCSA (cm^2)	Mass (gr)	Opt. fiber length (cm)
BL	1	3.47	66.20	12.92
BB	1	1.73	20.79	11.70
	2	3.22	31.07	11.49
TRL	1	2.23	26.97	10.08
	2	2.96	29.55	8.81
	3	2.83	29.64	11.83
	4	3.27	32.03	12.26
TRM	1	2.63	18.40	8.07
	2	2.56	17.65	7.73
	3	2.40	11.95	6.02
	4	2.11	13.95	7.46
	5	1.07	7.70	8.07
TRLT	1	1.53	12.50	7.58
	2	4.10	33.20	7.66
	3	2.19	15.20	6.56
	4	2.75	16.20	6.38
	5	0.87	5.85	6.38
BR	1	3.14	29.10	8.76
	2	1.58	15.90	9.53
	3	1.57	14.65	8.70
	4	0.87	7.00	7.58
	5	1.01	6.60	6.19
	6	1.04	4.10	4.72
	7	1.18	6.50	6.21
BRD	1	0.30	4.70	16.13
	2	0.82	14.00	16.13
	3	0.52	5.97	10.66
ANC	1	0.31	0.83	2.52
	2	0.70	1.50	2.02
	3	0.25	0.60	2.28
	4	1.18	2.20	2.70
	5	1.18	3.33	2.66
SUP	1	0.47	0.84	2.67
	2	2.32	3.64	1.48
	3	1.26	3.36	2.52
	4	1.48	2.96	2.63
	5	2.85	6.76	2.74
PQ	1	0.73	1.63	3.77
	2	1.78	3.47	3.86
	3	2.19	4.93	3.52
PT hum	1	5.10	27.50	5.10
PT uln	1	1.41	4.33	3.91

2.8. Appendix B – Kinematic optimization

The morphology of the cadaver from which the geometrical parameters of the model were obtained may differ from the morphology of a measured subject. Important factors are the size of the scapula and clavicle, the shape of the thorax over which the scapula glides, and the length of the conoid ligament. If the model is not scaled to subject-specific geometrical parameters, the measured (Cardan) angles of the scapula and clavicle (with respect to the thorax) from the measured subject may result in model positions where the medial border of the scapula and the surface of the thorax do not fit and also the conoid ligament may have a non-physiological length. Therefore, there is a need to find the optimal model input angles which not only fit the model constraints but also have the smallest difference with the actually measured angles.

In the model, the clavicle is defined by the rotation centers of the sterno-clavicular (SC) and the acromio-clavicular (AC) joints and the origin of the conoid ligament. Four points including the trigonum spinae (TS) angulus inferior (AI), the AC, and the insertion of the conoid ligament define the scapula. Using the measured orientation of the scapula and clavicle, the constraints of the closed-chain mechanism are met and the differences between the subject's and model orientation are minimized. These constraints include:

- the distance between the surface of the thorax (which is modeled as an ellipsoid, see reference (Klein Breteler et al, 1999)) and the points TS and AI must remain constant

- the length of the conoid ligament (= 18.33 mm) must remain constant.

The position of the shoulder girdle is determined by minimizing the differences (d) between measured and optimized angles for the scapula and clavicle around the global x- (dS_x and dC_x), y- (dS_y and dC_y), and z- (dS_z and dC_z) axes as follows:

$$J = W_1\left(\left(dC_x\right)^2 + \left(dC_y\right)^2 + \left(dC_z\right)^2\right) + W_2\left(\left(dS_x\right)^2 + \left(dS_y\right)^2 + \left(dS_z\right)^2\right) \qquad \text{(B1)}$$

Where W_1 and W_2 are weight factors. The choice of the relative weight factors is subjective. The accuracy of estimation of the clavicular or scapular angles depends on these weight factors. de Groot (1998) concluded that using W_1 =1 and W_2 = 2 resulted in a slight improvement on the average scapular angles and notable improvement on the average axial rotation of the clavicle, when compared with actually measured angles.

2.9. Appendix C – The muscle model

The muscle model (Figure C1) consists of different parts as follows.

1) The *activation dynamics* part (Figure C1b) is a second-order system and includes the neural excitation (u) and calcium dynamics. The excitation (e), is analogous to the pulse transmissions along the nerves or action potentials along the muscle fibers (EMG) and is defined as the input to the model (assumed to be constant in each time-step) while the outputs of the model are the spatial positions of the bony segments. The excitation dynamics (e) is related to the neural excitation (u) through a first-order relation as follows:

$$\dot{e} = \frac{u - e}{\tau_{ne}} \tag{C1}$$

where τ_{ne} (~ 0.04 s) is the neural excitation time-constant. Values of both u and e are restricted to the interval (0, 1).

The activation (a), which physiologically is interpreted as the calcium flow through the muscle membrane, is modeled by two first-order systems including muscle activation (calcium in-flow) and deactivation (calcium out-flow):

$$\dot{a} = \frac{e - a}{\tau} \tag{C2}$$

where τ is the time constant which can be either used for muscle activation (τ_{act} ~ 0.01 s) or deactivation (τ_{deact} ~ 0.05 s).

2) The *contractile dynamics* part (Figure C1b) defining the muscle-tendon complex is a nonlinear first-order system and consists of a contractile element (the muscle fibers, CE) in series with an elastic element (a spring-like tendon, SE). The muscle force-length and force-velocity relationships have been implemented in the CE.

2.1. force-length relationship (F_{lCE})

The normalized force-length relationship is described by a Gaussian equation as follows:

$$F_{lCE}\left(l_{CE}\right) = \cos(\alpha).\exp\left(-\frac{l_{CE} - l_0}{l_{CEsh}}\right) \tag{C3}$$

Where:

α is the pennation angle which is function of the length of the contractile element (l_{CE}):

$$\alpha = \sin^{-1}\left(\frac{d_0}{l_{CE}}\right) \tag{C4}$$

(a)

(b)

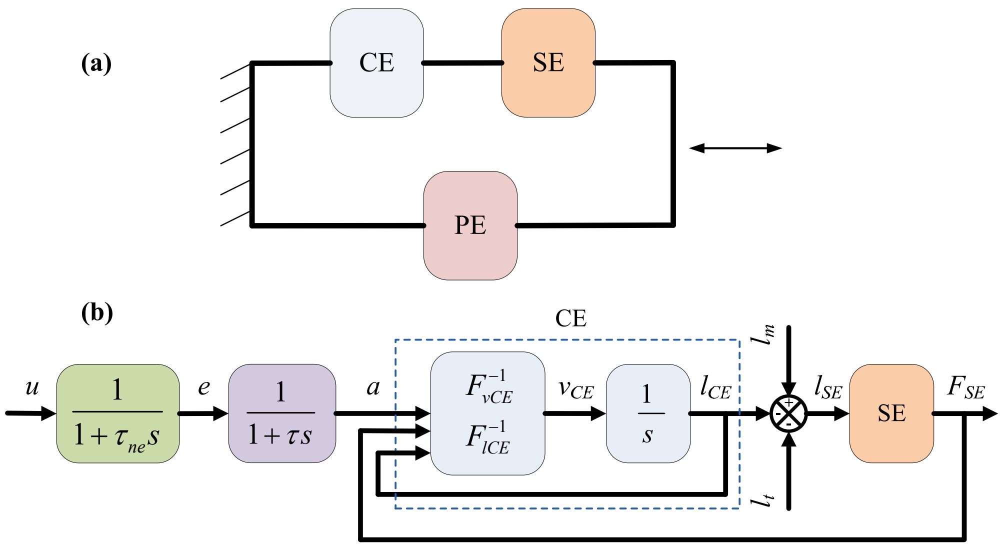

Figure C1 – (a) Schematic of the muscle model (reproduced from reference (Engin and Chen, 1986)), and (b) the activation and contraction dynamics parts of the muscle model. CE: contractile element, SE: series-elastic element, PE: parallel viscoelastic element

The bipennate muscle architecture is modeled with a constant d_0 as:

$$d_0 = l_0 \sin \alpha_0 \tag{C5}$$

l_0 is the optimum fiber length (optimum length of the CE).

l_{CEsh} is the shape parameter determining the width of the force-length curve.

Having the lengths of the CE (l_{CE}) and tendon (l_t), the length of the SE (l_{SE}) can be calculated as:

$$l_{SE} = l_m - \cos(\alpha)\, l_{CE} - l_t \tag{C6}$$

Where l_m is the muscle length.

2.2. force-velocity relationship (F_{vCE})

$F_{vCE}(a,\ l_{CE}\ ,\ v_{CE}\ )$ is the normalized force from the force-velocity relationship. In the muscle model, the contraction velocity of the CE (v_{CE}) is derived by inverting the force-velocity curve:

$$v_{CE} = \begin{cases} \dfrac{V_{sh} v_{\max} \left(F_{vCE}\left(a, l_{CE}, v_{CE}\right) - 1\right)}{F_{vCE}\left(a, l_{CE}, v_{CE}\right) + V_{sh}} & 0 \le F_{vCE} < 1 \\ \dfrac{-V_{sh} V_{sl} v_{\max} \left(F_{vCE}\left(a, l_{CE}, v_{CE}\right) - 1\right)}{F_{vCE}\left(a, l_{CE}, v_{CE}\right) + V_{exsh}} & 1 < F_{vCE} \le F_{mf} \end{cases} \tag{C7}$$

Where

V_{sh} (= 0.25) is the Hill shape parameter of the force-velocity curve.

V_{sl} is the shape parameter of the lengthening curve.

V_{exsh} and v_{max} are calculated as follows:

$$V_{exsh} = -1-(1+V_{sh}V_{sl})(V_{mf}-1) \quad \text{(C8)}$$

and

$$v_{max} = V_{vm}\left(1-V_{er}+V_{er}aF_{lCE}\left(l_{CE}\right)\right) \quad \text{(C9)}$$

Where

V_{vm} (~ 25 rad/s) is the initial value of the maximum contraction velocity, and

V_{er} is scaling parameter.

The muscle force produced in the contractile part (F_{SE}) is calculated as follows:

$$F_{SE} = F_{CE} = K_{SE1}\left(\exp\left(K_{SE2}l_{SE}\right)-1\right) \quad \text{(C10)}$$

The SE element is modeled with a non-linear spring in which:

$$K_{SE1} = \frac{F_{max}}{\exp\left(SE_{sh}-1\right)} \quad \text{(C11)}$$

and

$$K_{SE2} = \frac{SE_{sh}}{SE_{xm}} \quad \text{(C12)}$$

Where

SE_{sh} (= 3) is the shape parameter of the curvature of the exponential slope, and

SE_{xm} (~ 0.0201 m) is the stretch of the SE element with maximum isometric force.

3) The *parallel viscoelastic element* (PE)

The force produced in the PE element (F_{PE}) is a function of the muscle length and velocity and is calculated in a similar way to F_{SE} as follows:

$$F_{PE} = K_{PE1}\left(\exp\left(K_{SE2}\right).2^{\left(l_m-l_{PE0}\right)}-1\right) \quad \text{(C13)}$$

where

$$K_{PE1} = \frac{F_{max}}{\exp\left(PE_{sh}-1\right)} \quad \text{(C14)}$$

and

$$K_{PE2} = \frac{PE_{sh}}{PE_{xm}} \tag{C15}$$

PE_{sh} is the shape parameter,

PE_{xm} is the maximum extension of the PE element,

l_{PE0} is the muscle rest length (maximum length when $F_{PE} = 0$)

2.9.1. The input variables

The values for time-constants (τ_{ne}, τ_{act}, τ_{deact}) and the other parameters (V_{sh},V_{vm}, SE_{sh}, SE_{xm}) were adopted from the studies by Winters and Stark (1985; 1988).

The real muscle inputs are the pulse trains for different motor units. Nevertheless, it is not possible to record all these pulse trains. Therefore, a neural input (u) is defined representing the relative muscle force with respect to the maximum possible force during an isometric contraction. A measured EMG signal normalized to its maximum can be used as an average neural excitation (e) across different muscle fibers.

At each time-step, the neural excitation is calculated in an iterative procedure from the neural inputs at the previous step. The initial values are estimated in the quasi-static position and through the steady-state equilibrium process.

Chapter 3

In-vivo measured glenohumeral contact forces on the glenoid

This chapter aims to represent the *in-vivo* measured contact forces in the shoulder joint on the glenoid. A recently developed instrumented shoulder endoprosthesis allows for the *in-vivo* measurement of the glenohumeral joint contact forces on the humeral head. However, these contact forces were measured in the implant-based coordinate system. In this study, *in-vivo* measured forces were transferred from the instrumented implant to the glenoid. Motion data and external loads as well as the *in-vivo* glenohumeral joint contact forces of six patients with an instrumented shoulder hemiarthroplasty were recorded while performing loaded and unloaded dynamics tasks (including abduction and forward flexion), quasi-static force tasks, and activity of daily living tasks (including washing axilla and perineal care). The processed motion data and patient-specific CT-images were used to calculate the transformations needed to transform force data from the implant-based local coordinate system (in which the forces were originally measured) to a glenoid-based system. The trajectory of the glenohumeral joint reaction force vector through the articular surface of the glenoid was estimated from the transferred forces. Except for few cases, the force trajectory was inside the glenoid rim for most (~ 86 %) of the measured patients and tasks. Large interindividual differences were observed for the trajectory of the glenohumeral joint reaction force inside the glenoid. The results support the validity of the stability assumption in the biomechanical models of the shoulder upon which the joint reaction force is constrained inside the glenoid rim. The 14% situations where the force points outside the glenoid can only be explained by errors in the image processing and/or motion recordings. The magnitude of the resultant glenohumeral joint reaction force for each subject was also normalized with respect to the body weight (BW). The results of a one-way repeated analysis of variance (ANOVA) showed a significance effect of shoulder movement on the magnitude of the resultant joint reaction force.

3.1. Introduction

Shoulder joint is the most moveable while one of the most complex joints in the human body. It allows for a wide range of motion. As properly phrased by Veeger and van der Helm (2007) the shoulder joint is "a perfect compromise between mobility and stability". Clinically, instability is equal to joint dislocation. A spherical ball-and-socket joint like the glenohumeral (shoulder) joint is clinically defined as 'stable' when the humeral head (the ball) is compressed in the glenoid cavity (the socket). Glenohumeral joint stability is preserved by the muscles and ligaments surrounding the joint.

Accurate estimation of muscle function and related forces in the human musculoskeletal system is essential for improving implant design and testing. The force data could also be useful to advise patients and medical staff as to what motions are suited for training during the rehabilitation process or should better be avoided. To date, biomechanical models are the only means for the estimation of the muscle forces due to our inability to *in-vivo* measure these forces.

In the biomechanical models of the shoulder (Damsgaard et al, 2006; van der Helm, 1994a), glenohumeral joint stability is maintained by constraining the direction of the glenohumeral joint reaction force vector inside the rim of the glenoid fossa which is usually modeled by an ellipse. This constraint is applied as a nonlinear inequality in the inverse dynamics optimization (muscle load sharing) process.

Other than the magnitude of the loads on the shoulder joint, the direction of the reaction force vector is of great importance. Resultant forces will be mechanically the same in magnitude on both the humeral and glenoid side of the glenohumeral joint. The force direction, however, is an important factor for the possible development of the complications of the glenoid component in the shoulder arthroplasty. One of these complications is the "Rocking Horse Effect" (Franklin et al, 1988). In the rocking horse glenoid, contact forces which are applied in the periphery of the glenoid surface, mostly resulting from rotator cuff tears, produce a superior displacement of the humeral head. Franklin *et al* (1988) showed a close correlation between superior migration of the humeral head and the degree of glenoid loosening.

Several studies have focused on the measurement of contact pattern in the glenohumeral joint. To determine the contact patterns during abduction up to 90º arm elevation, Warner *et al* (1998) observed in a cadaver study that the contact area was limited to the central glenoid with a slight posterior shift. A number of studies have tried to measure the glenohumeral joint contact pattern *in-vivo*. In those studies, the glenohumeral joint contact patterns have been estimated by combining the glenohumeral joint motion measured from the biplane X-rays and the subject-specific CT-images. In that technique, at each time-step of the measurement, the point on the humeral head which has the minimum distance to the articular surface of the glenoid is estimated and assumed to be the contact point. Boyer *et al* (2008) studied the contact pattern in five healthy subjects during performing static

abduction (at 0º, 45º, and 90º) combined with maximal external/internal rotation. They found large interindivual differences for contact points inside the glenoid fossa. Bey *et al* (2010) also used bi-planar fluoroscopy to *in-vivo* measure the glenohumeral joint contact pattern on patients with repaired and/or contralateral shoulders during abduction up to 120º arm elevation. Although these studies could successfully represent the contact points in the glenohumeral joint, they did not provide any information about either the magnitude or direction of the contact forces.
A recently developed instrumented shoulder endoprosthesis (Westerhoff et al, 2009a) now allows for *in-vivo* measurement of the glenohumeral joint contact forces. However, the *in-vivo* forces are measured in the local coordinate system of the humeral head. The goal of the current study was to transfer the *in-vivo* measured forces from the instrumented implant to the glenoid. Synchronously captured motion data and patient–specific CT images were used for this transformation.

The importance of representing the measured joint contact forces on the glenoid is threefold:

- First, a stability assumption in the biomechanical models of the shoulder upon which the joint reaction force is constrained inside the glenoid rim (see Chapter 2) is evaluated using *in-vivo* measured forces.
- Second, the stability of the shoulder joint can be assessed during different shoulder motions within normal physiological range.
- Third, transferred forces can be used in the validation process of the biomechanical models of the shoulder (see Chapter 5).

3.2. Materials and Methods

3.2.1. Ethics Statement

The ethical committee of the Freie Universität Berlin and Charité-Universitätsmedizin Berlin gave permission for clinical studies using the instrumented endoprosthesis as well as related patient CT-images. Before surgery, patients were informed on the aims and procedures of all measurements after which they agreed by signing an informed consent to participate and having their images published.

3.2.2. Subjects

Six patients (Table 3.1) with an instrumented shoulder hemiarthroplasty (Westerhoff et al, 2009a) participated. Implantation was based upon the diagnosis of osteoarthritis with no serious rotator cuff damage. The surgical approach was deltopectoral and no nerve was damaged during the operation.

Table 3.1. Detailed information for the measured subjects. (F: female; M: male)

Subj.	Sex	Age (yr.)	Height (cm)	Weight (kg)	Implant side	Implant head radius (mm)
S1	F	73	168	72	Left	24.0
S2	M	64	163	85	Right	22.0
S3	F	83	152	52	Right	22.0
S4	F	68	163	107	Right	24.0
S5	M	69	173	93	Right	24.0
S6	M	74	173	83	Right	25.0
Mean (SD)	-	71.8 (6.6)	165.3 (7.9)	82.0 (18.7)	-	23.5 (1.1)

3.2.3. CT-imaging

Before and after joint replacement, 3D CT-scans of the subjects' upper extremity were obtained using a 64-slice CT scanner (Toshiba Aquilion 64, TMSE, The Netherlands) with slice thickness of 0.5 mm. Subject S3 (Table 3.1) was the only exception for whom only pre-operative CT data were obtained. The CT-imaging was carried out in Charité Department of Radiology CCM, Berlin. All CT scans were taken in a supine position.

3.2.4. Motion and force data collection

Motion recordings were performed at the VU Amsterdam, department of Human Movement Sciences. Measurements comprised the collection of motion data and external loads as well as *in-vivo* glenohumeral joint reaction forces (GH-JRF).

The measured tasks consisted of standard Range-of-Motion recordings that comprised unloaded and loaded (with a 2.4 kg dumbbell) abduction-adduction and forward flexion (and returning to normal position), quasi-static force tasks, and activity of daily livings (ADL) including washing axilla and perineal care. The patients warmed up prior to measurements. They were also trained to perform the tasks for several times and in case of dynamic motions to elevate their arms up to maximum possible range (α_{max}, Table 3.2).

To perform the force tasks, subjects were asked to hold a handle attached to the force sensor and isometrically apply forces in up-down, forward-backward, and latero-medial directions. An AMTI 6-DOF force sensor (Advanced Mechanical Technology, Inc., USA, nominal accuracy 0.1 N) was used to measure external forces and moments.

In the calibration process, the spatial positions of anatomical landmarks on bony segments (Table 3.3) were recorded relative to technical marker clusters on those segments. The anatomical landmark selection was based on the ISB standardization protocol for upper extremity (Wu et al, 2005). The glenohumeral joint rotation center, which was necessary for reconstruction of the local coordinate system of the humerus but could not be palpated *in-vivo*, was estimated using the Instantaneous Helical Axes (IHA) method (see Chapter 4 for detailed descriptions about this method).

Table 3.2. The maximum recorded arm elevation angle (α_{max}) for the measured subjects during performing unloaded and loaded abduction (Abd and AbdL) and forward flexion (FF and FFL) motions. All values are in degrees. (L: loaded)

Subj.	Abd	FF	AbdL	FFL
S1	85	115	70	75
S2	120	130	110	120
S3	85	95	50	50
S4	85	85	65	65
S5	60	60	45	40
S6	115	120	110	120
mean (SD)	92 (22)	101 (26)	75 (29)	78 (34)

Table 3.3. The palpated anatomical landmarks in the calibration process.

Bony segment	Palpated landmark	Abbreviation
Thorax	Incisura Jugularis	IJ
	Processus Xiphoideus	PX
	Processus Spinosus of the 7th cervical vertebra	C7
	Processus Spinosus of the 8th thoracic vertebra	T8
Clavicle	Most ventral point on the sternoclavicular joint	SC
	Most dorsal point on the acromioclavicular joint	AC
Scapula	Angulus Acromialis	AA
	Trigonum Spinae	TS
	Angulus Inferior	AI
	Most ventral point of processus coracoideus	PC
Humerus (upper arm)	Most caudal point on medial epicondyle	EM
	Most caudal point on lateral epicondyle	EL
Forearm	Most caudal–lateral point on the radial styloid	SR
	Most caudal–medial point on the ulnar styloid	SU

During motion recordings, marker clusters on bony segments were measured using four Optotrak (Northern Digital Inc., Canada, nominal accuracy 0.3 mm) camera bars at a sampling frequency of 50 Hz. Each cluster marker was built of three markers. Considering the limited range of motion of the patients (Table 3.2) we used cluster markers on the acromion (scapula-sensor) (Karduna et al, 2001; van Andel et al, 2008), for scapular motion tracking.

To measure the forces in the glenohumeral joint, a BIOMET Biomodular shoulder hemi-prosthesis was equipped with 6 strain gages, a 9-channel telemetry, and a coil for inductive power supply (Figure 3.1a) (Westerhoff et al, 2009a). The *in-vivo* measured contact forces were transferred to the external measuring equipment (Figure 3.1b). The *in-viv*o measured forces were synchronized and re-sampled with the motion recording frequency (i.e. 50 Hz) to allow for further processing. For synchronization, the trigger signal from the Optotrak system was used.

3.2.5. CT-image processing

Subject-specific CT images were used to calculate inter-coordinate transformations. Mimics medical image processing software (version 13.1, Materialise, Leuven, Belgium) was used to process the CT-Scan images.

Image processing was performed manually. To calculate the accuracy of manual point positioning on the CT images in Mimics, a set of six anatomical landmarks (IJ on the thorax, AA, TS, and AI on the scapula, EM and EL on the humerus) were pointed on the CT images based on the information provided in the ISB standardization proposal (Table 3.3). This procedure was performed twice. The differences between the corresponding landmarks in the two sessions were calculated and the maximum value across all subjects (0.83 mm) was defined as the accuracy.

The implant-based coordinate system (Westerhoff et al, 2009a) (Figure 3.1a) was reconstructed on the post-operative CT scans of all subjects except S3.

The local coordinate systems of the humerus (Figure 3.2a) and scapula (Figure 3.2b) were reconstructed following the ISB standardization protocol definitions. To this end, anatomical bony landmarks on the humerus (Figure 3.2a) including EL and EM as well as scapula (Figure 3.2b) including AA, AI, and TS were located on the images.

The position of the glenohumeral joint rotation center (GH) which is needed to determine the local coordinate system of the humerus was determined on the CT scan images using the method proposed and used in (van der Helm et al, 1989). To this end, approximately 50 points on the glenoid surface were determined on the segmented glenoid for each subject. A sphere with the fixed radius of the implant head (see Table 3.1) was fitted to the obtained data points on the glenoid surface by applying a least square criterion (Veeger, 2000). The center of the fitted sphere was defined as the anatomical center of rotation (see section 4.2.4, Chapter 4, for more detailed description).

(a)

(b)

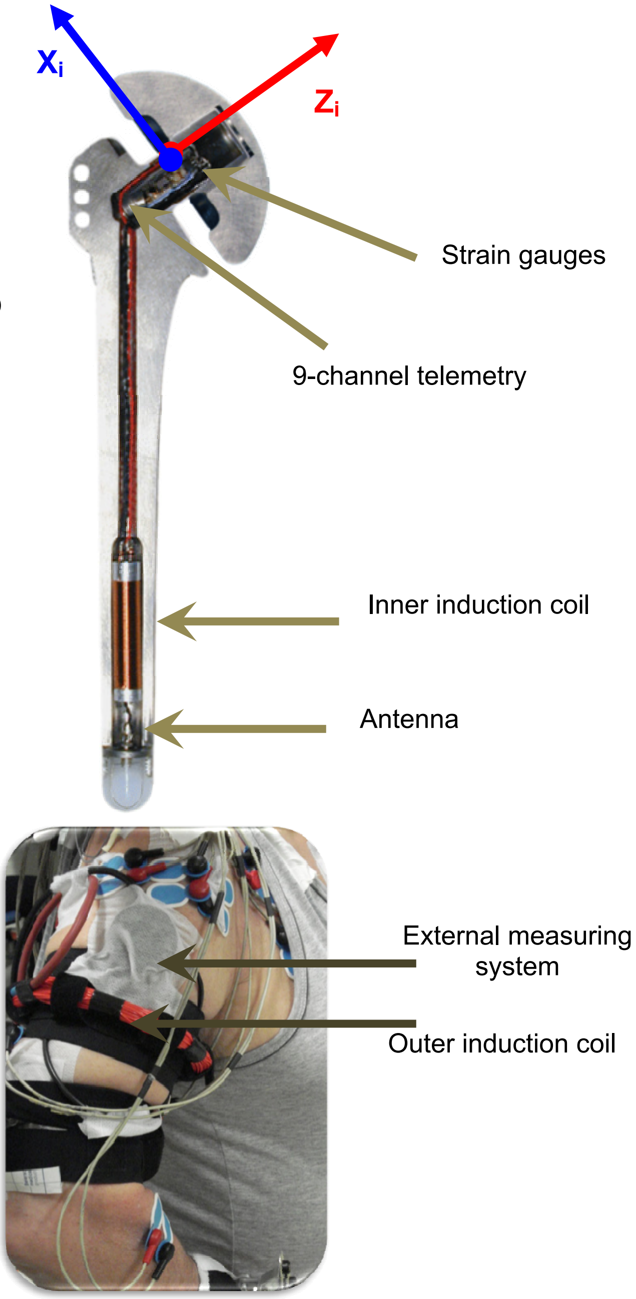

Figure 3.1. The instrumented shoulder hemiarthroplasty (a) the cross-sectional view of the internal measuring system (Picture courtesy of the Julius Wolff Institut, Charité - Universitätsmedizin Berlin) (b) the external measuring equipment.

To determine the local coordinate system of the glenoid, an ellipse was fitted to the data points obtained from the rim of the glenoid by using the method developed by Andrew *et al* (1999). The minor and major axes of the fitted ellipse were defined to be respectively the *x*- and *y*- axis of the local coordinate system of the glenoid (Figure 3.2c). The *z*-axis was consequently defined by using the *x*- and *y*- axes.

For S1, who has an endoprosthesis in her left shoulder (Table 3.1), all raw measured data were mirrored with respect to the sagittal plane and subsequently treated as a right shoulder.

3.2.6. Transformations

The *in-vivo* GH-JRFs are basically measured in the implant-based coordinate system (Figure 1a). To represent the measured forces in the local coordinate system of the glenoid (Figure 2c), three steps of inter-coordinate transformations were carried out as follows:

1. Rotations between the implant-based and the humeral coordinate system (${}^{h}R^{i}$), were obtained from the subject specific post-operative CT-image processing (see section 2.2) and formulated as follows:

   $$ {}^{h}R^{i} = {}^{h}R^{g} \cdot {}^{g}R^{i} = \left({}^{g}R^{h}\right)^{T} \cdot {}^{g}R^{i} \qquad (1) $$

   Where ${}^{g}R^{h}$ and ${}^{g}R^{i}$ are, respectively, the orientations of the humerus and the implant in the global (i.e. CT-image) system.

   For subject S3 for whom the post-operative CT-data were not available, the retroversion angle (= 30º) mentioned in the surgical report was used.

2. Rotations between the humeral and the scapular coordinate system (${}^{s}R^{h}$) were calculated in each time-frame (*t*) by kinematic analysis of the recorded motion data from the technical markers on the humerus and scapula and formulated as follows:

   $$ {}^{s}R^{h}(t) = {}^{s}R^{g}(t) \cdot {}^{g}R^{h}(t) = \left({}^{g}R^{s}(t)\right)^{T} \cdot {}^{g}R^{h}(t) \qquad (2) $$

   Where ${}^{g}R^{s}(t)$ and ${}^{g}R^{h}(t)$ are, respectively, the orientations of the scapula and humerus in the global (i.e. lab) system at each measured time-frame (*t*).

   The local coordinate system definitions of the humerus and scapula were determined following the ISB standardization protocol definitions.

3. Rotations between the scapular and the glenoid coordinate system (${}^{gl}R^{s}$) were obtained from the subject specific CT-image processing (see section 2.2.) and formulated as follows:

   $$ {}^{gl}R^{s} = {}^{gl}R^{g} \cdot {}^{g}R^{s} = \left({}^{g}R^{gl}\right)^{T} \cdot {}^{g}R^{s} \qquad (3) $$

   where ${}^{g}R^{gl}$ and ${}^{g}R^{s}$ are, respectively, the orientations of the glenoid and scapula in the global (CT-images) system.

Using the three above-mentioned rotations, the final rotation matrix (${}^{gl}R^{i}(t)$) at each measured time-frame (t) was defined to rotate the measured forces from the implant-based (F_i) to the glenoid (F_{gl}) coordinate system as follows:

$$ {}^{gl}R^{i}(t) = {}^{gl}R^{s} \cdot {}^{s}R^{h}(t) \cdot {}^{h}R^{i} \tag{4} $$

$$ F_{gl} = -{}^{gl}R^{i} \cdot F_{i} \tag{5} $$

where the negative sign in Equation 5 means that the transferred force is the "reaction force" acting on the glenoid component.

The intersection points of the GH-JRF vector through the articular surface of the glenoid were estimated from the compressive and shear components of the transferred forces on the glenoid.

3.2.7. Statistical analysis

The magnitude of the measured resultant GH-JRF was normalized with the respect to the body weight (BW) for each subject. The normalized forces were averaged across all subjects and compared between different shoulder tasks (Figure 3.3). To evaluate the effect of shoulder movement on the significance of the differences in the magnitude of the resultant GH-JRF, a one-way repeated analysis of variance (ANOVA) was used. The significance level was set to $\alpha = 0.05$.

3.3. Results

3.3.1. Direction of the GH-JRF vector

Expect for few cases (i.e. S2 abduction, S4 abduction, S1 washing axilla and perineal care, S4 washing axilla, and S3 perineal care), for most (~ 86%) of the patients and shoulder tasks, the trajectory of the GH-JRF vector stayed inside the glenoid rim (Figures 3.4 to 3.7).

For all shoulder tasks, a large variability was observed among different patients for the trajectory of the GH-JRF vector inside the glenoid fossa (Figures 3.4 to 3.7). In case of dynamic tasks, however, a good agreement was found between the force trajectories in loaded and unloaded motions for individual subjects (Figures 3.4a and 3.4b, 3.5a and 3.5b).

3.3.2. Magnitude of the resultant GH-JRF

On average across all subjects, the magnitude of the normalized resultant GH-JRF was the smallest (= 0.44 BW) for the ADL tasks but the largest (= 1.50 BW) for the force tasks (Figure 3.3).

For dynamic motions (both loaded and unloaded), the maximum GH-JRF occurred at the peak abduction angle (Table 3.2) for all measured subjects.

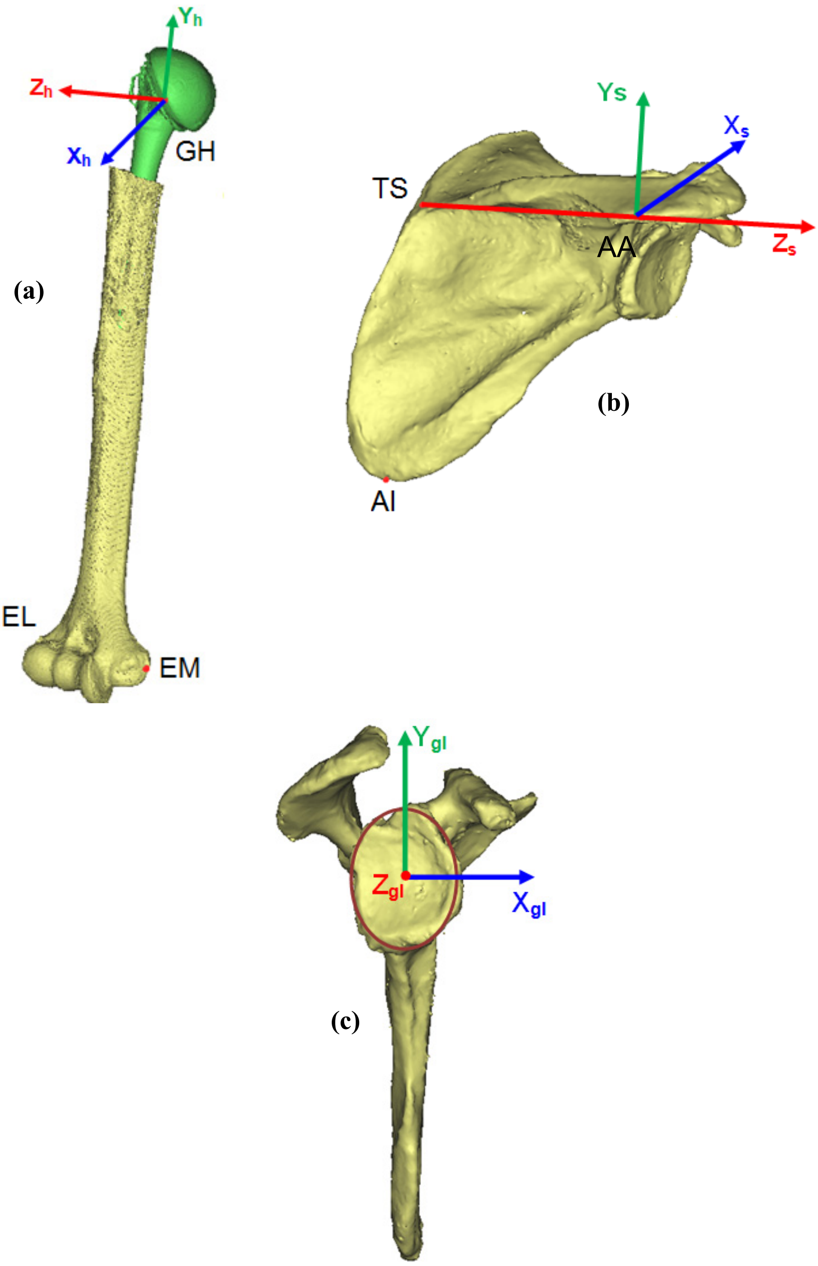

Figure 3.2. The local coordinate system of the (a) humerus, (b) scapula, and (c) glenoid, on the CT-images.

The results of the statistical analysis revealed a significant effect of shoulder movement on the magnitude of the resultant GH-JRF ($F_{6,30} = 10.26$, $p < 0.01$). As can be appreciated from Figure 3.3, the GH-JRF for the ADL tasks (Wash and Peri) were smaller than the other tasks. For the dynamic tasks (Abd, and FF), the GH-JRFs were lower than their loaded counterparts (AbdL and FFL). The highest GH-JRF was found for FT. No remarkable difference was observed between the following pairs of shoulder tasks: unloaded abduction and forward flexion, loaded abduction and forward flexion, and loaded dynamic and force tasks (Figure 3.3).

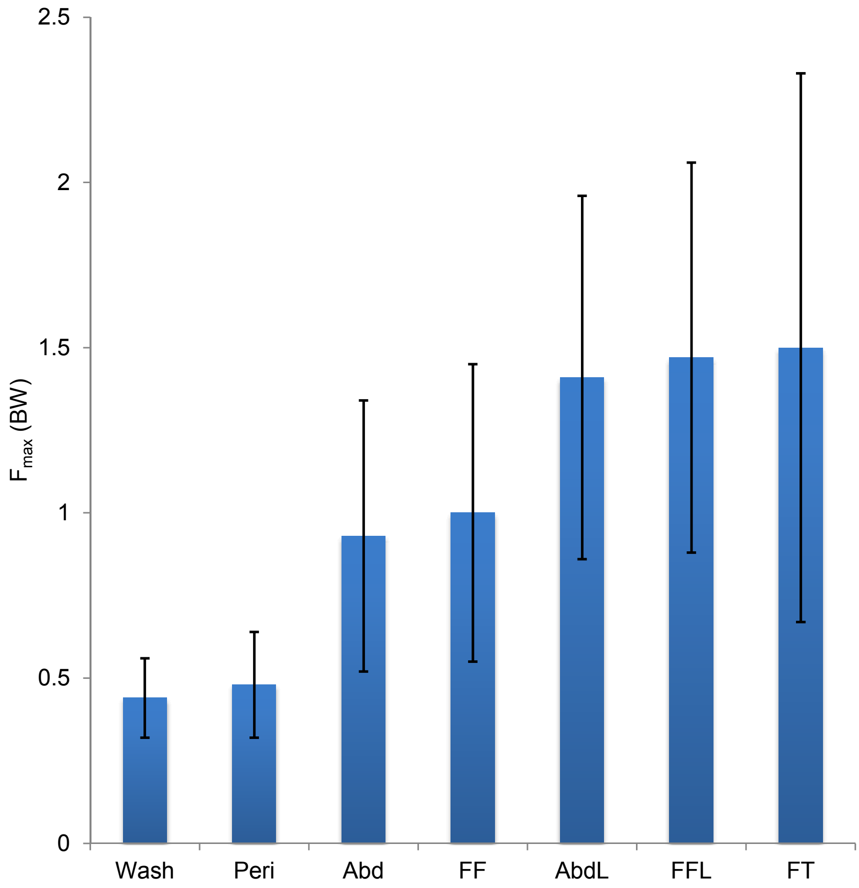

Figure 3.3. The maximum recorded resultant GH-JRF (F_{max}) with respect to the body weight (BW) averaged across all measured subjects during performing different shoulder tasks given in Body Weight (BW) (Wash: ADL washing axilla, Peri: ADL perineal care, Abd: abduction unloaded, FF: forward flexion unloaded, AbdL: abduction loaded, FFL: forward flexion loaded, FT: force task).

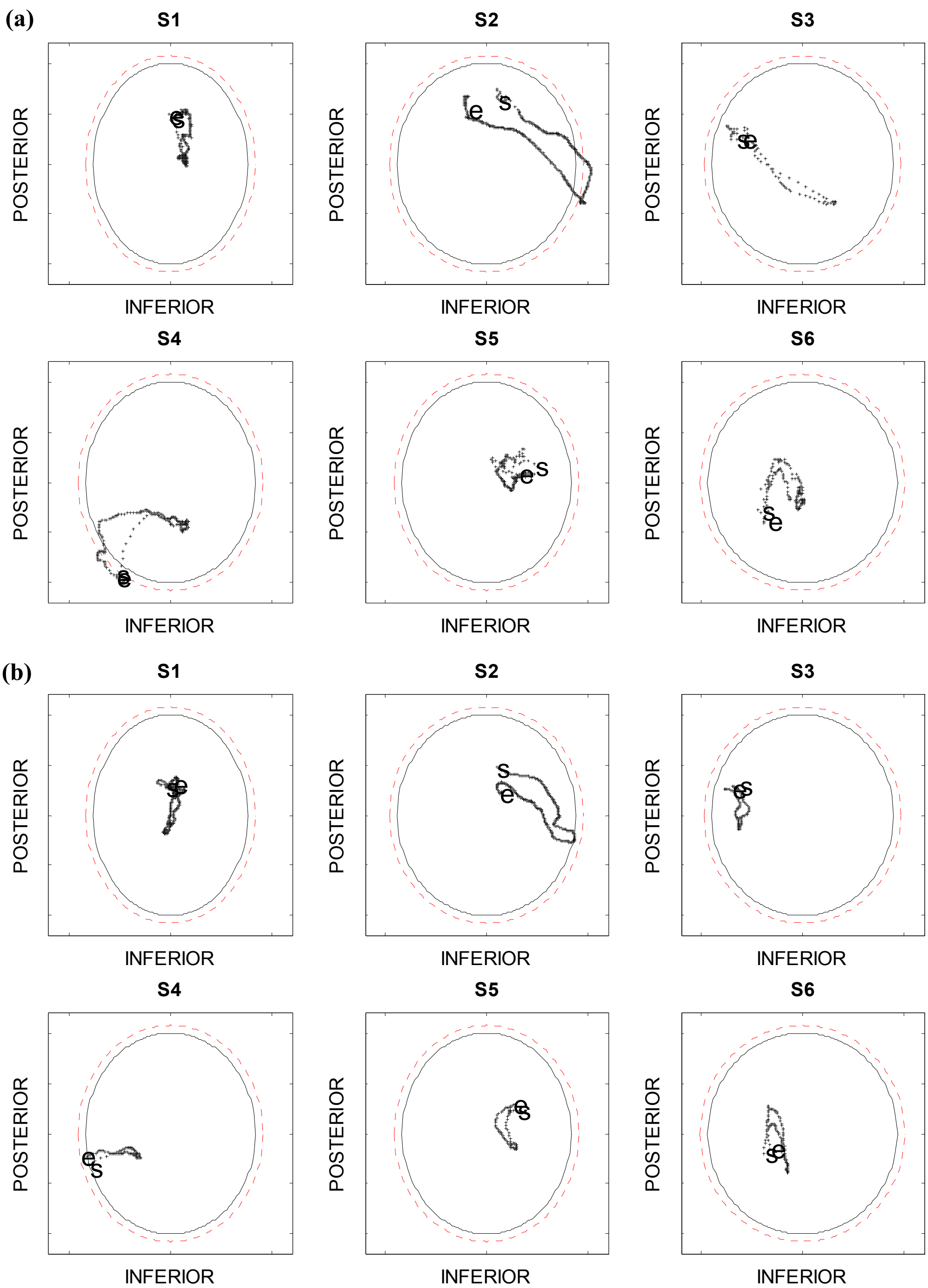

Figure 3.4. The trajectory of the GH-JRF vector inside the glenoid fossa for six measured subjects during (a) unloaded and (b) loaded abduction-adduction motion. s: starting point, e: ending point. solid ellipse: glenoid rim without labrum, dashed ellipse: glenoid rim + labrum

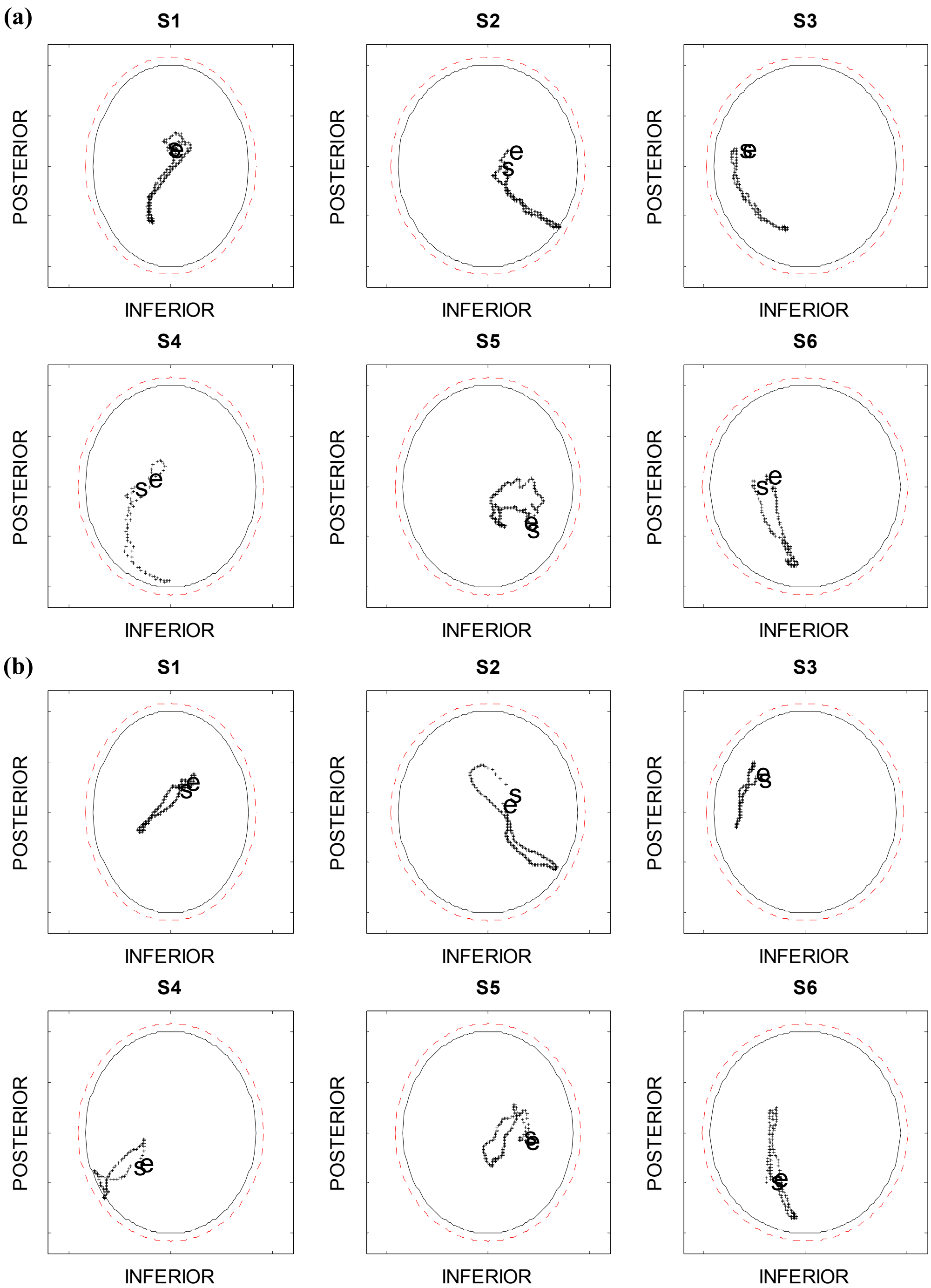

Figure 3.5. The trajectory of the GH-JRF vector inside the glenoid fossa for six measured subjects during (a) unloaded and (b) loaded forward flexion and backing to normal position.

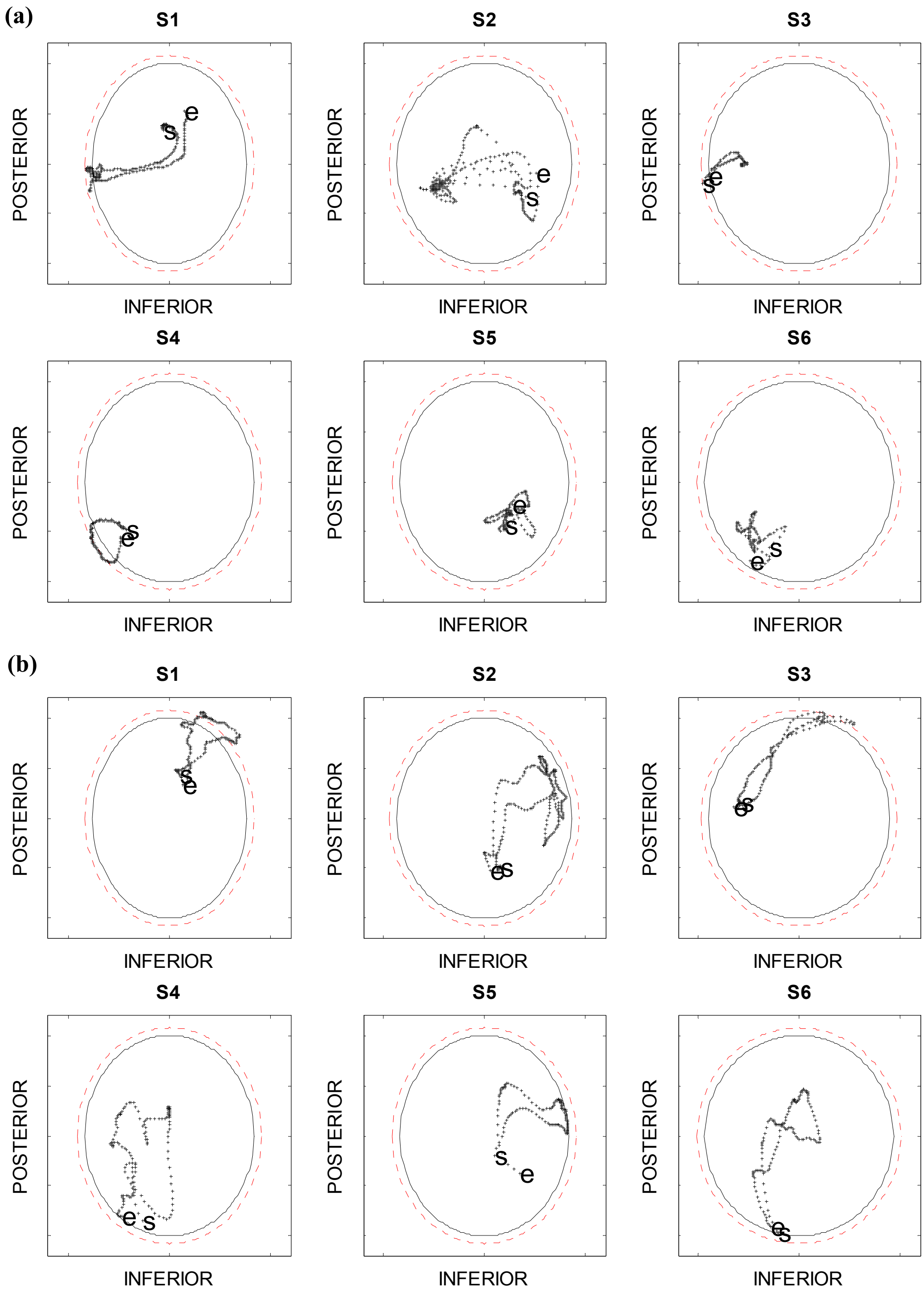

Figure 3.6. The trajectory of the GH-JRF vector inside the glenoid fossa for six measured subjects during (a) washing axilla and (b) perineal care.

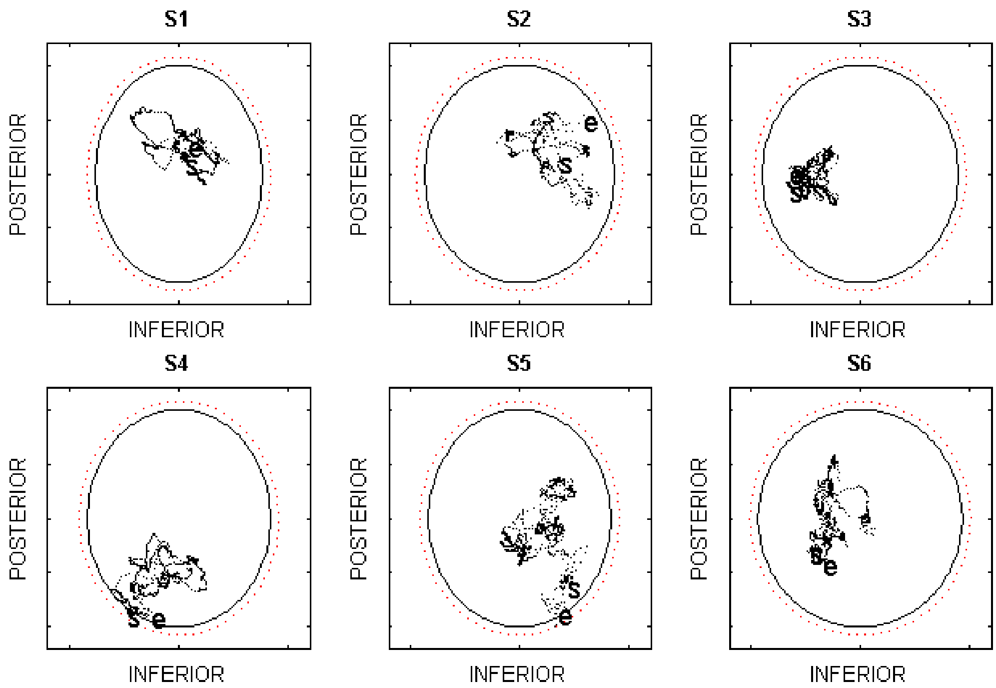

Figure 3.7. The trajectory of the GH-JRF vector inside the glenoid fossa for six measured subjects during static force tasks in up-down, for-backward, and lateral-medial directions.

3.4. Discussion

In this study, the *in-vivo* measured contact forces in the glenohumeral joint were represented on the glenoid. The trajectory of the glenohumeral joint reaction force vector through the articular surface of the glenoid was estimated from the transferred forces.

3.4.1. Direction of the GH-JRF vector

Except for few cases, the GH-JRF vector pointed towards the glenoid cavity for most of the patients and subjects (Figures 3.4-3.7). These findings support the stability assumption according to which the direction of the GH-JRF should be constrained inside the glenoid fossa to maintain the joint stability.

No physical interpretation exists for intersection points lying outside the glenoid rim as was observed for few cases in Figures 3.4a and 3.6. Theoretically, this should lead to a dislocation of the joint. Dislocation of the humeral head is not incorporated in the kinematic model in which the recorded forces in the implant are being transformed to forces in the glenoid. If the humeral head is dislocated and only connects to the glenoid rim, a joint reaction force will still exist. However, the orientation of this joint reaction vector is biased towards the center of the glenoid, and could not explain any orientation outside the glenoid. The only remaining explanation could be measurement errors in the procedure to calculate the glenoid joint reaction force vector. Considering that three sets of transformation from implant to glenoid coordinate system were used, there is possibility for errors in any of transitional stages:

Error in image processing and/or educational guess in case of lack of CT data could be a potential source of observed behavior. An example is subject S3 for whom the post-operative CT data was not available and the angle of retroversion of the humeral (implant) head was assumed to be equal to the one stated in the surgical report. We can show the sensitivity of the position of the intersection of the GH-JRF vector and the glenoid fossa to the variation in retroversion angle during performing a standard task like forward flexion (Figure 3.8a). As can be appreciated from Figure 3.8a, a plus/minus 10º variation in the retroversion angle shifts the force trajectory supero-anteriorly/infero-posteriorly inside the glenoid. Another example is the effect of potential error in estimating the rotation angles between the scapula and the glenoid in case of subject S2. For this subject only the post-operative CT data was available. Due to the high contrast of the implant it was difficult to segment the posterior part of the glenoid. Figure 3.8b shows that ±10º variation in glenoid tilt angle could bring the force trajectory completely inside the glenoid rim or pushes it more toward outside the glenoid rim. Except for these examples, the chance of large errors in our image processing is very low and potential errors are likely not to exceed 10 degrees.

Errors may also occur during either motion recording or in estimating the rotation angles between humerus and scapula for which the local coordinate systems are based on bony landmarks. We have compared (see Chapter 4) two different methods for the estimation of the glenohumeral joint rotation centers (including IHA and SCoRE). The results revealed that, although, the estimated glenohumeral joint rotation center by the IHA method was significantly closer to the one obtained from CT-data compared to the SCoRE method, however, still an average Euclidian distance of about 15 mm existed between the estimated and the geometric center of rotation (see Table 4.2, Chapter 4). Such error may cause difference in the orientation of the humeral head derived from measured bony landmarks and the ones determined on the CT images and consequently can affect the position of the intersection of the GH-JRF vector and the glenoid cavity. The potential errors are, however, likely not to exceed few degrees.

As mentioned before (section 3.2.5), to determine the local coordinate system of the glenoid, we fitted an ellipse to the data points obtained from the rim of the glenoid. However, one should note that the labrum was not included in that fitting. Therefore, it is likely that including the labrum (dashed ellipses in Figures 3.4-3.7) can potentially increase the mechanical contact area and help to solve the problem in case of for example S1 and S4 during washing axilla (Figure 3.6a) or S3 during perineal care (Figure 3.6b).

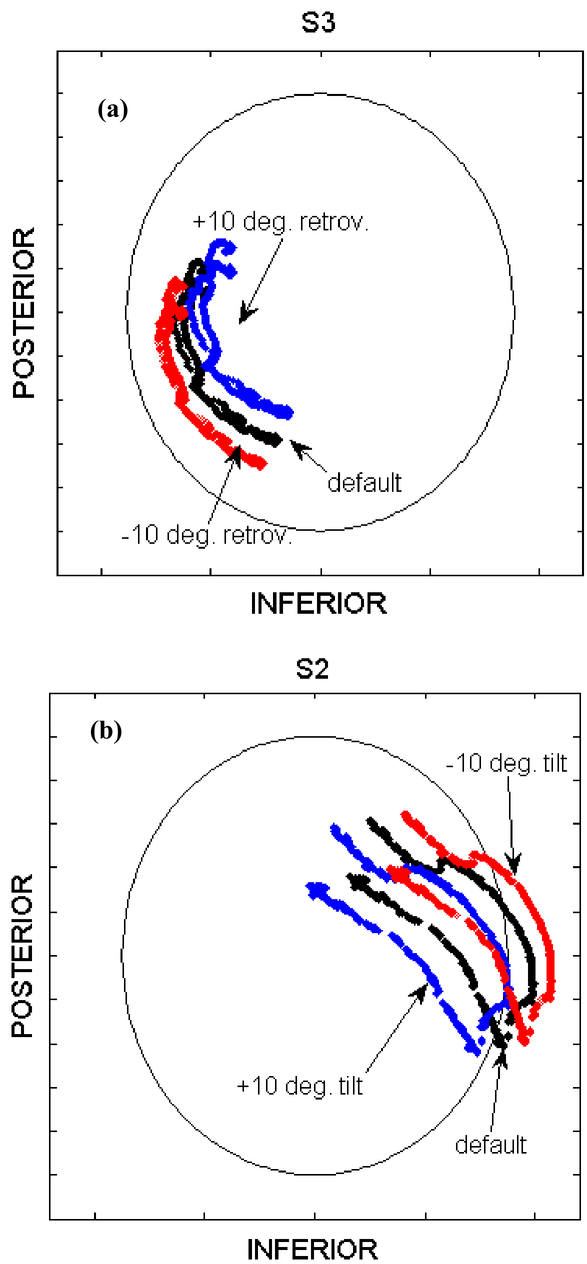

Figure 3.8. The effect of variations in the rotation angles on the position of force trajectory inside the glenoid (a) S3 during unloaded forward flexion and (b) S2 during unloaded abduction. retrov.: retroversion angle. The positive rotation is counterclockwise and the negative one is clockwise.

Although the instrumented endoprosthesis has reported to be well calibrated (nominal accuracy ~ 0.02 N) (Westerhoff et al, 2009a) and *in-vivo* measured contact loads by this implant are used as our 'golden standard' for model validation throughout this thesis. However, one may still give, even small, chance to potential errors in measuring the contact forces *in-vivo*, especially at low forces in the resting position. This could be the case for S4 during unloaded abduction (Figure 3.4a) where the contact points in resting positions lye outside the glenoid area. For this subject the measured force in the humeral coordinate system had a very small (close to zero) Y-component (Figure 3.2a) compared with the other two components. This causes a close to zero Z-component (Figure 3.2c) in the glenoid coordinate system in resting position which pushes the force trajectory outside the glenoid rim.

Interindividual variability

For all tasks, a large variability for the GH-JRF pattern inside the glenoid was observed in this study (Figures 3.4 to 3.7). At this moment, few explanations do exist for such phenomenon. Interindividual variability in bony and muscular anatomy seems to be a potential source of the observed variability. Such variability can also be seen in other studies. Assuming the point of application of the joint contact force to be the same as the contact point between the articular surfaces of the proximal and distal segments, one will be able to compare the results of different studies. Using modeling simulations, van der Helm (1994b) showed that the intersection of the GH-JRF vector and the articular surface of the glenoid should be close to the anterior border of the glenoid rim during unloaded abduction while it should be more posterior during unloaded forward flexion motion (Figure 3.9a). Nevertheless, the position of the contact points was found to be close to center of the glenoid in the cadaver study by Warner *et al* (1998). The glenohumeral contact pattern during abduction, in contrast to what van der helm reported, was completely posterior (Figure 3.9b) in the *in-vivo* study by Bey *et al* (2010). However, their observation of the effect of the humeral elevation angle on the superior-inferior contact position agrees with that by van der Helm. Similar to our observations in this study, Boyer *et al* (2008) found a large interindividual variability for the contact pattern in five measured healthy subjects. The contact point at 90º humeral elevation angle during performing abduction was all over the place inside the glenoid (e.g. middle inferior, middle, middle posterior, anterior-inferior, and superior-posterior) in five different subjects.

The dispersion of the points of application of the GH-JRF inside the glenoid fossa can be related to the range of motion. As illustrated in Figures 3.4 and 3.5, the most scattered force trajectory during unloaded abduction motion is related to S2 who showed the largest range of motion (Table 3.2) while S5 with the smallest range of motion showed the most concentrated force trajectory during both unloaded abduction and forward flexion. By comparing the loaded and unloaded motions for each subject (Figure 3.4a and b, 3.5a and b), one can also see that the force trajectory inside the glenoid was less scattered when performing a loaded task compared with an unloaded one. This is because subjects generally had a smaller range of motion during loaded motions (Table 3.2). Nonetheless, this hypothesis cannot explain some other observations: for example, the maximum arm elevation for S4 is about 70% of the corresponding value for S2 and S6 during forward flexion motion while a more dispersed force pattern inside the glenoid is observed for S4 (Figure 3.5).

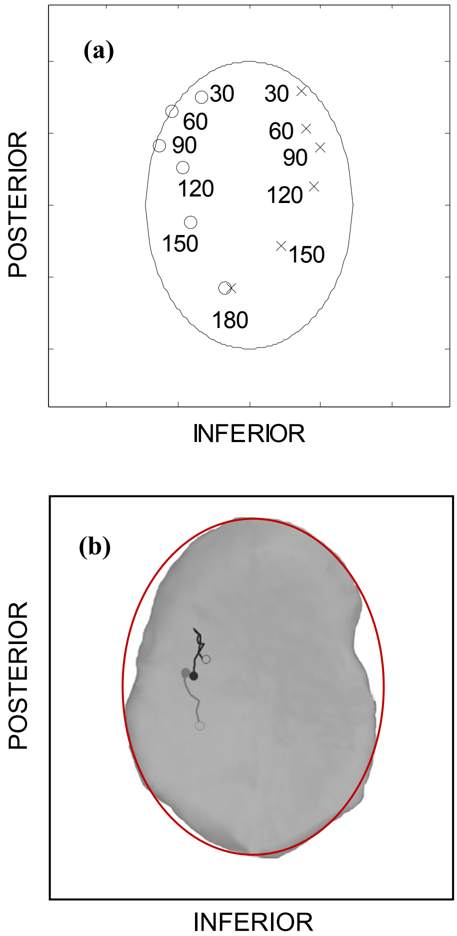

Figure 3.9. (a) Intersection of the GH-JRF vector and the articular surface of the glenoid for unloaded (x) abduction and (o) forward flexion at different humeral elevation angles, reproduced from reference (van der Helm, 1994b). (b) The glenohumeral joint contact pattern for repaired and contralateral shoulder during unloaded abduction motion, adopted (and modified) from reference (Bey et al, 2010)

3.4.2. Magnitude of the resultant GH-JRF

The measured force magnitudes (Figure 3.3) were in the range of previously *in-vivo* measured dynamic (Bergmann et al, 2007) and ADL (Westerhoff et al, 2009b) tasks. The results of the current study showed that the glenohumeral stability does not depend on the magnitude of the net joint reaction force acting on the glenoid. The maximum measured GH-JRF during unloaded forward flexion reached 1.83 BW (~ 1500 N) on patient S6 which was about than 4 times larger than the one for S3 (~ 400 N). However, both subjects showed almost the same force trajectory inside the glenoid fossa. The same is also true for the quasi-static force tasks. This means that when the magnitude of the resultant GH-JRF increases, only the compressive component of the GH-JRF vector is notably increases to preserve the joint stability.

The results of this study (Figure 3.3) showed that standard dynamic tasks like abduction and forward flexion motions were relatively heavy-duty for patients with shoulder implant compared with ADL tasks like washing axilla. This may, partly, explain the limited range of motion (Table 3.2) of the shoulder during performing abduction and/or forward flexion in our patients.

In contrast to some model calculations (Poppen and Walker, 1978; Terrier et al, 2008), the joint load still increased after exceeding the horizontal plane (i.e. arm elevation angle > 90º) in both abduction and forward flexion motions (see also Chapter 5). However, this could only be seen in some patients (i.e. S1, S2, and S6) due to the limited range of motion in our patients (Table 3.2). Increasing the measured GH-JRF above the horizontal plane may have been caused by antagonist muscle co-contraction in order to provide the joint stability in arm elevations above 90°, where the arm behaves like an inverted pendulum.

The transformations used in the current study to represent the *in-vivo* measured contact forces in the glenoid cavity can also be used to transfer the measured contact moments. Besides the measurement of forces, the instrumented shoulder implant is also capable of measuring (friction-induced) moments on the implant. These moments, together with the contact forces presented in the glenoid system can be used to estimate the friction coefficient in the artificial joint (see Chapter 8).

3.5. Conclusions

The first time, *in-vivo* shoulder joint loads were represented on the glenoid side. Following conclusions can be drawn from this study:

- Within a wide range of motion of the shoulder movements, the direction of the GH-JRF vector pointed towards the glenoid cavity for most of the patients and shoulder movements. One may conclude form this that the stability assumption according to which the direction of the GH-JRF should be constrained inside the glenoid fossa to maintain the joint stability, is a valid assumption. The 14% situations where the GH-JRF points outside the glenoid cannot be explained mechanically.

- Large interindividual differences were observed for the trajectory of the glenohumeral joint reaction force inside the glenoid. Such variability has also been seen in other studies. Interindividual variability in bony and muscular anatomy seems to be a potential source of the observed variability.
- In contrast to previous model simulations, the magnitude of the resultant GH-JRF still increased after exceeding the horizontal plane during performing standard dynamic tasks. This may be caused by muscle co-contraction to preserve the joint stability for humeral elevation above 90°.
- The transformations used in the current study can also be used for some future applications:
    - Validation process of the biomechanical models of the shoulder,
    - Transfer of the measured contact (friction-induced) moments in the instrumented shoulder implant which together with the contact forces presented in the glenoid system can be used to estimate the friction coefficient in the artificial joint.

3.6. References

Andrew, W., Fitzgibbon, M.P., Robert, B.F., 1999. Direct least-squares fitting of ellipses. IEEE Transactions on Pattern Analysis and Machine Intelligence 21 (5), 476-480.

Bergmann, G., Graichen, F., Bender, A., Kaab, M., Rohlmann, A., Westerhoff, P., 2007. In vivo glenohumeral contact forces-Measurements in the first patient 7 months postoperatively. Journal of Biomechanics 40 (10), 2139-2149.

Bey, M.J.B., Kline, S.K., Zauel, R., Kolowich, P.A., Lock, T.R., 2010. In vivo measurement of glenohumeral joint contact patterns. EURASIP Journal on Advances in Signal Processing vol. 2010, Article ID 162136, 6 pages.

Boyer, P., Massimini, D., Gill, T., Papannagari, R., Stewart, S., Warner, J., Li, G., 2008. In vivo articular cartilage contact at the glenohumeral joint: preliminary report. Journal of Orthopaedic Science 13 (4), 359-365.

Damsgaard, M., Rasmussen, J., Christensen, S.T., Surma, E., de Zee, M., 2006. Analysis of musculoskeletal systems in the AnyBody Modeling System. Simul Model Pract Th 14 (8), 1100-1111.

Franklin, J.L., Barrett, W.P., Jackins, S.E., Matsen, F.A., 1988. Glenoid loosening in total shoulder arthroplasty. Association with rotator cuff deficiency. Journal of Arthroplasty 3 (1), 39-46.

Karduna, A.R., McClure, P.W., Michener, L.A., Sennett, B., 2001. Dynamic measurements of three-dimensional scapular kinematics: A validation study. Journal of Biomechanical Engineering 123, 184-190.

Poppen, N.K., Walker, P.S., 1978. Forces at the glenohumeral joint in abduction. Clinical Orthopaedics and Related Research 135, 165-170.

Terrier, A., Vogel, A., Capezzali, M., Farron, A., 2008. An algorithm to allow humerus translation in the indeterminate problem of shoulder abduction. Medical Engineering & Physics 30, 710–716.

van Andel, C.J., Wolterbeek, N., Doorenbosch, C.A.M., Veeger, D., Harlaar, J., 2008. Complete 3D kinematics of upper extremity functional tasks. Gait & Posture 27 (1), 120-127.

van der Helm, F.C.T., 1994a. A finite element musculoskeletal model of the shoulder mechanism. J Biomech 27 (5), 551-553.

van der Helm, F.C.T., 1994b. Analysis of the kinematic and dynamic behavior of the shoulder mechanism. Journal of Biomechanics 27 (5), 527-550.

van der Helm, F.C.T., Pronk, G.M., Veeger, H.E.J., van der Woude, L.H.V., 1989. The rotation center of the glenohumeral joint. Journal of Biomechanics 22 (10), 1092.

Veeger, H.E.J., 2000. The position of the rotation center of the glenohumeral joint. Journal of Biomechanics 33 (12), 1711-1715.

Veeger, H.E.J., van der Helm, F.C.T., 2007. Shoulder function: The perfect compromise between mobility and stability. Journal of Biomechanics 40 (10), 2119-2129.

Warner, J.J.P., Bowen, M.K., Deng, X.H., Hannafin, J.A., Arnoczky, S.P., Warren, R.F., 1998. Articular contact patterns of the normal glenohumeral joint. Journal of Shoulder and Elbow Surgery 7 (4), 381-388.

Westerhoff, P., Graichen, F., Bender, A., Halder, A., Beier, A., Rohlmann, A., Bergmann, G., 2009b. In vivo measurement of shoulder joint loads during activities of daily living. Journal of Biomechanics 42, 1840–1849.

Westerhoff, P., Graichen, F., Bender, A., Rohlmann, A., Bergmann, G., 2009a. An instrumented implant for in vivo measurement of contact forces and contact moments in the shoulder joint. Medical Engineering & Physics 31 (2), 207-213.

Wu, G., van der Helm, F.C.T., Veeger, H.E.J., Makhsous, M., Van Roy, P., Anglin, C., Nagels, J., Karduna, A.R., McQuade, K., Wang, X., Werner, F.W., Buchholz, B., 2005. ISB recommendation on definitions of joint coordinate systems of various joints for the reporting of human joint motion--Part II: shoulder, elbow, wrist and hand. Journal of Biomechanics 38 (5), 981-992.

Modified from: A.A. Nikooyan, F.C.T. van der Helm, P. Westerhoff, F. Graichen, G. Bergmann, H.E.J. Veeger, 2011, "Comparison of two methods for *in-vivo* estimation of the glenohumeral joint rotation center of the patients with shoulder hemiarthroplasty", PLoS ONE 6(3): e18488.

Chapter 4

Glenohumeral joint rotation center for the patients with implant

Determination of an accurate glenohumeral-joint rotation center (GH-JRC) from marker data is essential for kinematic and dynamic analysis of shoulder motions. Previous studies have focused on the evaluation of the different functional methods for the estimation of the GH-JRC for healthy subjects. The goal of this chapter is to compare two widely used functional methods namely the instantaneous helical axis (IHA) and symmetrical center of rotation (SCoRE) methods for estimating the GH-JRC *in-vivo* for patients with implanted shoulder hemiarthroplasty. The motion data of five patients were recorded while performing three different dynamic motions (circumduction, abduction, and forward flexion). The GH-JRC was determined using the CT-images of the subjects (geometric GH-JRC) and was also estimated using the two IHA and SCoRE methods. The rotation centers determined using the IHA and SCoRE methods were on average 1.47±0.62 cm and 2.07±0.55 cm away from geometric GH-JRC, respectively. The two methods differed significantly (two-tailed *p*-value from paired t-Test ~ 0.02, post-hoc power ~ 0.30). The SCoRE method showed a significant lower (two-tailed *p*-value from paired t-Test ~ 0.03, post-hoc power ~ 0.68) repeatability error calculated between the different trials of each motion and each subject and averaged across all measured subjects (0.62±0.10 cm for IHA vs. 0.43±0.12 cm for SCoRE). It is concluded that the SCoRE was a more repeatable method whereas the IHA method resulted in a more accurate estimation of the GH-JRC for patients with endoprostheses.

4.1. Introduction

According to the International Society of Biomechanics (ISB) recommendation for the upper extremity (Wu et al, 2005), the glenohumeral joint rotation center (GH-JRC) is needed to define the local coordinate system and longitudinal axis of the humerus. The GH-JRC is impossible to palpate *in-vivo* and, thus, needs to be estimated.

A variety of methods have been developed for the estimation of the kinematic joint rotation centers of ball joints (Ehrig et al, 2006). For estimation of the GH-JRC, various methods have been introduced and used such as regression models (Campbell et al, 2009; Meskers et al, 1998a), spherical-fit (Halvorsen et al, 1999), instantaneous helical axis (IHA) (Veeger, 2000; Woltring et al, 1985; Woltring et al, 1994), symmetrical center of rotation (SCoRE) (Ehrig et al, 2006; Monnet et al, 2007), bias compensated (Halvorsen, 2003), and least-square methods (Chang and Pollard, 2007; Gamage and Lasenby, 2002). Nevertheless, there is disagreement about either "repeatability" or "accuracy" of those methods for approximation of the kinematic GH-JRC. The first indicates the interindividual repeatability of a method for different trials of a specific arm motion. The "accuracy" of a method has been defined as the closeness of the estimated rotation center to a reference which is mostly considered as the geometrical center of rotation.

As for repeatability, Stokdijk *et al* (2000) applied three methods, including a linear regression model, a spherical-fit, and the IHA method to calculate the GH-JRC *in-vivo*. They concluded that the sphere-fit and IHA methods gave almost identical results, but different to the regression method. They preferred the IHA over the spherical-fit due to its shorter calculation time. Monnet *et al* (2007) used the SCoRE method for *in-vivo* estimation of the GH-JRC and compared it with the IHA method and concluded that SCoRE was a more repeatable method.

The studies who evaluated the accuracy of the different methods may be divided into the *in-vitro* and *in-vivo* studies:

The *in-vitro* studies have been carried out on cadavers. Veeger (2000) compared the kinematic and geometric GH-JRC based on a cadaver study. He showed that the calculated GH-JRC using the IHA method was very close (≤ 2 mm) to the geometric center of rotation which was defined as the center of the sphere fitted to the glenoid surface with the radius of the humeral head (van der Helm et al, 1989).

In the *in-vivo* studies (Campbell et al, 2009; Lempereur et al, 2010), the geometric (anatomical) GH-JRC determined on the subject specific CT/MRI-images were used as the reference for evaluation of the accuracy of the functional methods for estimation of the kinematic GH-JRC. Campbell *et al* (2009) used MRI images to evaluate a newly developed regression model. In the most comprehensive study (Lempereur et al, 2010), five different functional methods including IHA, SCoRE, bias compensated and two least square methods were compared based on the Euclidian distance between the kinematic GH-JRC and the geometrical GH-JRC pointed on the MRI images. Based on the results of reference (Lempereur et al, 2010), the SCoRE method approximated the geometrical GH-JRC more accurate than the IHA method. However, in contrast to the results of study by Monnet *et al* (2007), the IHA method was the method which showed higher repeatability.

All the aforementioned *in-vivo* studies were carried out on healthy subjects. Nevertheless, based on our best knowledge, no functional method for *in-vivo* estimation of the GH-JRC has yet been evaluated for patients with endoprostheses for whom the displaced rotation centers may occur. In the current study we will focus on the two recently most debated methods i.e. the IHA and the SCoRE. The aim of this chapter is to evaluate the repeatability as well as the accuracy of the IHA and SCoRE methods for *in-vivo* estimation of the kinematic GH-JRC for the patients who carry the shoulder hemi-endoprosthesis. The repeatability of each method will be accessed across different motion trials for each subject. To evaluate the accuracy, the geometric GH-JRC determined on the post-operative CT-scan images of the patients will be used as the reference of comparison.

4.2. Materials and Methods

4.2.1. Subjects

Five subjects with instrumented shoulder hemi-arthroplasty (S1, S2, S3, S5, and S6, Table 3.1, Chapter 3) participated in the experiments. For the Ethics Statement and detailed descriptions about the participants see sections 3.2.1 and 3.2.2, Chapter 3.

4.2.2. CT-imaging

For the detailed description about the CT imaging see section 3.2.3, Chapter 3.

4.2.3. Motion data collection

Measurements included calibration, static, and dynamic trials. The dynamic tasks included circumduction, abduction-adduction, and forward flexion (arm elevation and return to the initial position).

The speed of the movements on average across all subjects was about 0.17 Hz (one cycle every 6 s). The subjects were asked to perform the abduction and flexion tasks up to maximum possible arm elevation. However, the measured subjects showed relatively limited elevation capacity (see Table 3.2, Chapter 3).

For the detailed description about the motion data recordings see section 3.2.4, Chapter 3.

4.2.4. Geometric GH-JRC

A cross-platform image processing software, namely the Delft Visualisation and Image processing Development Environment (DeVIDE version 9.8., Delft, the Netherlands) (Botha and Post, 2008), was used to process the post-operative CT-Scan images.

To calculate the accuracy of point positioning on the CT images in DeVIDE, a set of six anatomical landmarks (incisura jugularis on the thorax, angulus acromialis, trigonum spinae, and angulus inferior on the scapula, epicondyle medialis and lateralis on the humerus) were pointed on the CT images based on the information provided in the ISB standardization proposal (Wu et al, 2005). In the next step, the software was reloaded and the same bony landmarks as the last step were re-pointed on the CT scan images. Finally, the differences between the corresponding landmarks in the two sessions were calculated and the maximum value across all subjects (0.621 mm) was defined as the accuracy.

The image processing was performed manually. The anatomical bony landmarks on scapula including Angulus Acromialis (AA), Angulus Inferior (AI), and Trigonum Spinae (TS) were located on the images. The ISB standardization proposal was used for definition of the anatomical bony landmarks as well as the local coordinate definitions.

Alternative image processing software namely Mimics (version 13.1, Materialise, Leuven, Belgium) was also used for positioning of the anatomical landmarks. Since Mimics is more user-friendly and segmentation is easier controllable, we wanted to be certain that the originally used method (DeVIDE) provided trustable data. So, this process might probably be called a check on the reliability of segmentation and landmark identification. The maximum differences between the results in the two software (DeVIDE and Mimics) across all subjects did not exceed 2 mm. The landmarks identified in DeVIDE were used for further processing.

The geometric GH-JRC was determined on the CT scan images by using the method proposed and used in references (van der Helm et al, 1989; van der Helm et al, 1992). van der Helm *et al* (1989) showed that the surfaces of the glenohumeral joint are two concentric spheres and defined the center of sphere fitted to the glenoid using a constant radius equal to the radius of the humeral head. This definition was also used to determine the geometric GH-JRC in references (Meskers et al, 1998a; van der Helm et al, 1992). The method by van der Helm *et al* is, however, slightly different from previous studies (Campbell et al, 2009; Lempereur et al, 2010) in which the geometric GH-JRC was considered to be the center of the sphere fitted to the congruent surface of the humeral head. If the glenoid and humerus surfaces are congruent and in close contact, there should be no difference between both methods.

In order to find the radius of the humeral in previous studies (Campbell et al, 2009; Lempereur et al, 2010; van der Helm et al, 1992), the positions of some points were determined on the caput humeri and subsequently a sphere was fitted to the data points using the least square method. However, in case of our patients, the radius of the humeral head will be equal to the radius of the implant head. Therefore, having the values of the implant head radius (Table 3.1, Chapter 3), about 50 points on the glenoid surface (including the labrum) were determined on the segmented CT images of each subject. A sphere with the fixed radius of the implant head was fitted to the obtained data points on the glenoid surface by applying a least square criterion (Veeger, 2000). The center of the fitted sphere was defined to be the geometric GH-

JRC. The fitted sphere was also visualized on the CT images in the Mimics software (Figure 4.1) to check the correctness of the mathematical calculations.

In contrast to subjects S1, S2, S5, and S6, for subject S3 the pre-operative CT data were used since post-operative images worked out to be unobtainable. For this subject, the rotation center was determined using the known geometry of the humeral head and the shape of the glenoid, assuming a tight contact between the two. As a check, we compared the segmented glenoid on the pre- and postoperative images for subjects S1, S5, and S6 and did not observe any changes in the shape of the glenoid and/or scapula.

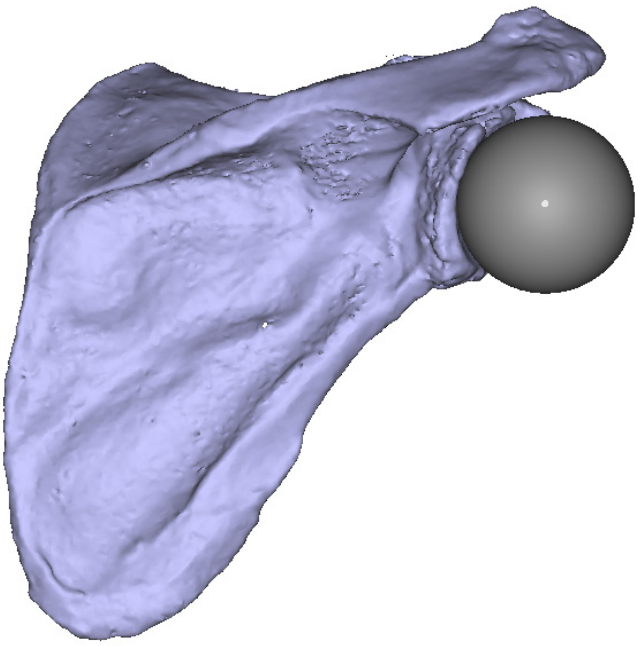

Figure 4.1. Visualization of the sphere fitted to the glenoid in Mimics software for S6.

4.2.5. Kinematic GH-JRC

4.2.5.1. The IHA method

In the IHA method (for details see references (Woltring, 1990; Woltring et al, 1985; Woltring et al, 1994)), at each time frame of the data recording, the position vector (**p**) of an instantaneous helical axis (Figure 4.2) is calculated using the relative position vector (**s**) as well as the angular velocity vector (**ω**) of the markers on the upper arm with respect to the markers on the scapula as follows:

$$\mathbf{s} = \mathbf{p} + \boldsymbol{\omega} \times \frac{\dot{\mathbf{p}}}{\sqrt{\boldsymbol{\omega}^{\mathbf{T}}\boldsymbol{\omega}}} \tag{1}$$

Where ω is calculated from the rotation matrix (**R**) of the upper arm with respect to the scapula and its numerical derivative ($\dot{\mathbf{R}}$) as follows:

$$\mathbf{w} = \frac{1}{2}\left[\dot{\mathbf{R}}\mathbf{R}^{\mathbf{T}} - \mathbf{R}\dot{\mathbf{R}}^{\mathbf{T}}\right],$$
$$\boldsymbol{\omega} = \begin{bmatrix} \mathbf{w}(3,2) \\ \mathbf{w}(1,3) \\ \mathbf{w}(2,1) \end{bmatrix} \tag{2}$$

The optimal pivot point (i.e. P_{opt}, Figure 4.2) which is the closest point to all calculated helical axes is estimated by using the least squares optimization method developed by Woltring (1990). The estimated pivot point is defined as the kinematic joint rotation center.

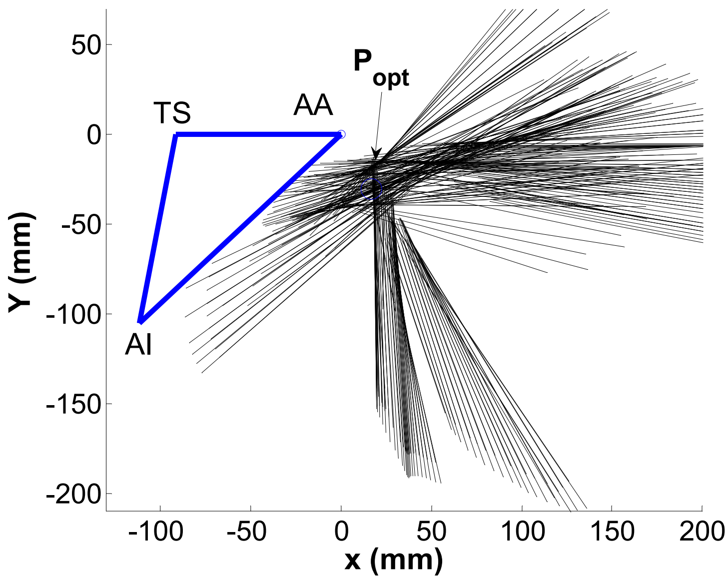

Figure 4.2. Typical example of the calculated instantaneous helical axes for Cir, Abd, and FE motions in the xy-plane.

4.2.5.2. The SCoRE method

The SCoRE method (for details see references (Ehrig et al, 2006; Monnet et al, 2007)) is based on the assumption that the position of the joint rotation center should remain constant relative to the distal and proximal segments during performing a joint movement. As for the GH-joint, such assumption will mathematically result to the following linear least square problem:

$$\begin{bmatrix} \mathbf{R}_{h,1} & -\mathbf{R}_{s,1} \\ . & . \\ . & . \\ . & . \\ \mathbf{R}_{h,n} & -\mathbf{R}_{s,n} \end{bmatrix} \begin{bmatrix} \mathbf{rc}_h \\ \mathbf{rc}_s \end{bmatrix} = \begin{bmatrix} \mathbf{p}_{s,1} - \mathbf{p}_{h,1} \\ . \\ . \\ . \\ \mathbf{p}_{s,n} - \mathbf{p}_{h,n} \end{bmatrix} \tag{3}$$

Where:

$\mathbf{R}_{h,i}$ and $\mathbf{R}_{s,i}$ are, respectively, the rotation matrices of the upper arm (humerus) and scapula in the global coordinate system at time frame *i*.

$\mathbf{p}_{h,i}$ and $\mathbf{p}_{s,i}$ are, respectively, the position vector of the humerus and scapula in the global coordinate system at time frame *i*.

$\mathbf{rc}_h$ and $\mathbf{rc}_s$ are the position vector of the joint rotation center in the local coordinate system of the humerus and scapula, respectively.

4.2.5.3. Estimation of the kinematic GH-JRC

The kinematic rotation center was calculated using both IHA and SCoRE methods. The position of the marker clusters on scapula and upper arm while performing dynamic trials were used. Similar to the previous studies who compared the IHA and SCoRE methods (Lempereur et al, 2010; Monnet et al, 2007) and in line with recommendations of Begon *et al* (2007) for estimation of kinematic rotation center of the hip joint, three sets of kinematic data were used to find the joint rotation center as follows:

- Dataset 1 (Cir): one trial of arm circumduction motion
- Dataset 2 (FE/Abd): combination of one trial forward flexion (arm elevation and backing to the initial position) and one trial arm abduction/adduction
- Dataset 3 (FE/Abd/Cir): combination of one trial forward flexion, one trial abduction/adduction, and one trial circumduction

For each dataset, six trials were measured and used.

All kinematic data were filtered using a second order low-pass digital Butterworth filter with cutoff frequency of 3 Hz (~18 times larger than the speed of movement). Due to the sensitivity of the IHA method to the angular velocity (ω, Equation 2), only the angular velocities more than 10% of peak angular velocity (ω_{max}, the highest norm angular velocity in the signal) were applied.

4.2.6. Repeatability of the methods

The repeatability of the methods was evaluated in the same way as in references (Lempereur et al, 2010; Monnet et al, 2007) based on the repeatability error (i.e. *e*, Table 4.1). The location of the GH-JRC in the space (*x*, *y*, *z*) was calculated with the two methods. For each type of motion dataset (1, 2, or 3) and each subject, the repeatability error (*e*) was defined as follows:

$$e = \left(\sum_{i=x,y,z} \mathrm{SD}_i^2 \right)^{1/2} \tag{4}$$

Where SD_x is the standard deviation of the estimated GH-JRC locations in the *x*-direction among all six trials in each dataset. The same definition applies to the *y* and *z* directions.

The lower repeatability error means more repeatability for a method.

4.2.7. Accuracy of the methods

The accuracy of each method was accessed by calculation of the Euclidian distance (i.e. *d*, Table 4.2) between the estimated and the geometric GH-JRC, as was carried out by Lempereur *et al* (2010). To allow for a direct comparison between the estimated and geometric GH-JRC, they should be represented at the same coordinate system. Using the three scapular bony landmarks (AA, TS, and AI) on the CT-scan images and experimental data, the local coordinate system of the scapula was defined as the reference coordinate system. The direction of the scapular coordinate system axes was chosen similar to previous studies (Monnet et al, 2007; Stokdijk et al, 2000) with the *x*-axis pointing to the right, the *y*-axis pointing upward, the *z*-axis pointing backward, and the origin at AA. The scapular coordinate system obtained from the *in-vivo* measurements was aligned to the one derived from the CT images using the optimization method described by Veldpaus *et al* (1988). The AA point was selected as the basis point for transformations between the two local coordinate systems. The kinematic GH-JRCs were then transferred to the aligned coordinate system.

4.2.8. Statistical analysis

Two-tailed paired Student's t-Test was used for statistical analysis. The threshold for statistical significance was considered as 0.05. Post-hoc statistical power analysis for two-tailed Student's t-Test was carried out in order to evaluate the power of test with low number of subjects (n = 5).

4.3. Results

4.3.1. Repeatability of the methods

Comparison of the repeatability error (*e*) for the three datasets in each method and for all subjects showed that the minimum value for the average error was 0.62 and 0.43 cm for the IHA and SCoRE methods respectively (Table 4.1).

Table 4.1. The repeatability error (*e*) for the IHA and SCoRE methods. All values are in cm.

	IHA			SCoRE		
	Cir	**FE/Abd**	**FE/Abd/Cir**	**Cir**	**FE/Abd**	**FE/Abd/Cir**
S1	1.02	0.92	0.74	0.80	0.83	0.57
S2	0.81	0.77	0.51	0.57	0.44	0.29
S3	0.96	0.53	0.57	0.90	0.76	0.48
S4	0.78	0.84	0.55	0.53	0.56	0.47
S5	0.21	0.98	0.72	0.30	0.44	0.32
mean	0.76	0.81	0.62	0.62	0.61	0.43
(SD)	(0.32)	(0.17)	(0.10)	(0.24)	(0.18)	(0.12)

4.3.2. Accuracy of the methods

Differences up to 2.26 cm (TS point for S1, Table 4.2) appeared between the calibration positions of the *in-vivo* measured and CT-pointed bony landmarks. Although most data for subject S4 (Table 3.1, Chapter 3) were also available, however, these data had to be left out because of a large deviation between the *in-vivo* measured lay-out of the scapular landmarks and those as measured on the CT-scan. This amounted to a difference of more than 5 cm between the positions of AI in the two systems. We decided not to reconstruct this point because of the possible extra errors that this reconstruction might add.

The estimated kinematic GH-JRC for the IHA was on average 1.47 cm away from the geometric GH-JRC. For the SCoRE value this amounted to 2.07 cm (Table 4.2, Figure 4.3).

The closest GH-JRC predicted by IHA method had a distance of about 0.76 cm from the geometric GH-JRC while the best point estimated by the SCoRE method differed about 1.08 cm from the CT-estimated JRC, both related to S1 (Table 4.2).

The distance between the kinematic GH-JRCs calculated using the IHA and SCoRE methods for motion datasets Cir, FE/Abd, and FE/Abd/Cir was, respectively, 0.83 cm, 0.50 cm, and 0.78 cm. The same quantities were reported to be, respectively, 1.41 cm, 0.72 cm, and 0.46 cm in reference (Monnet et al, 2007). The mean difference between the two methods in the study by Lempereur *et al* (2010) was 0.48 cm.

4.3.3. Statistics

The difference between the IHA and SCoRE method for the distance to the geometrical GH-JRC (*d*) was significant (two-tailed *p*-value ~ 0.02, post-hoc power ~ 0.30, Table 4.3) for Dataset 3 (FE/Abd/Cir).

Table 4.2. The 3D positions of the scapular anatomical landmarks as well as the kinematic and geometric GH-JRC. All values are in cm. Kin.: kinematic, *d*: the Euclidian distance between the kinematic and the CT-based GH-JRC.

		Anatomical Landmarks						Geometric	Kinematic GH-JRC					
		AA		TS		AI		GH-RC	IHA			SCoRE		
		CT	Kin.	CT	Kin.	CT	Kin.	CT	Cir	FE/Abd	FE/Abd/Cir	Cir	FE/Abd	FE/Abd/Cir
S1	***x***	0	0	-9.13	-11.24	-11.12	-11.57	1.31	1.35	0.69	0.66	1.18	0.48	0.72
	y	0	0	0	0.78	-10.48	-9.96	-2.83	-3.19	-2.72	-2.69	-2.76	-2.9	-2.85
	z	0	0	0	-0.25	0	0.19	-3.12	-3.98	-3.55	-3.49	-4.19	-5.38	-4.99
	d	-	0	-	2.26	-	0.71	-	0.93	0.76	0.76	1.08	2.41	1.96
S2	***x***	0	0	-11.77	-10.85	-12.80	-11.94	-0.45	0.66	0.55	0.54	0.02	-0.05	-0.04
	y	0	0	0	1.48	-10.45	-11.00	-2.89	-3.8	-3.56	-3.63	-4.14	-3.06	-3.61
	z	0	0	0	-0.25	0	0.19	-2.45	-2.14	-3.24	-2.64	-2.96	-4.28	-3.64
	d	-	0	-	1.76	-	1.04	-	1.47	1.44	1.25	1.43	1.88	1.45
S3	***x***	0	0	-12.48	-12.45	-12.35	-12.05	-0.95	0.06	-2.01	-1.9	-1.13	-1.28	-1.23
	y	0	0	0	0.32	-15.02	-14.67	-3.29	-5.57	-4.24	-4.39	-6.78	-4.7	-5.4
	z	0	0	0	0	0	0	-3.43	-3.33	-2.6	-2.81	-4.73	-3.95	-4.21
	d	-	0	-	0.32	-	0.46	-	2.5	1.64	1.58	3.73	1.54	2.26
S4	***x***	0	0	-11.96	-11.13	-13.16	-13.26	1.39	0.46	0.44	0.46	0.62	1.24	1.04
	y	0	0	0	0.47	-11.47	-12.64	-2.82	-3.55	-4.5	-3.69	-3.47	-4.75	-4.33
	z	0	0	0	0	0	0	-4.22	-3.82	-4.3	-3.84	-3.54	-3.26	-3.36
	d	-	0	-	0.95	-	1.17	-	1.25	1.93	1.33	1.21	2.16	1.77
S5	***x***	0	0	-10.58	-10.00	-11.69	-11.62	-0.50	-1.72	-1.69	-1.69	-1.91	-1.43	-1.53
	y	0	0	0	1.20	-10.85	-12.10	-2.54	-5.36	-3.77	-4.61	-6.64	-4.55	-4.97
	z	0	0	0	0	0	0	-2.83	-2.29	-2.32	-2.30	-3.18	-1.23	-1.62
	d	-	0	-	1.33	-	1.25	-	3.12	1.78	2.44	4.35	2.73	2.90
mean	***x***	0	0	-11.18	-11.13	-12.22	-12.09	0.16	0.16	-0.40	-0.39	-0.24	-0.21	-0.21
	y	0	0	0	0.85	-11.65	-12.07	-2.87	-4.29	-3.76	-3.80	-4.76	-3.99	-4.23
	z	0	0	0	-0.10	0	0.08	-3.21	-3.12	-3.32	-3.06	-3.72	-3.67	-3.65
	d	-	0	-	0.86	-	0.45	-	1.85(0.92)	1.51(0.46)	1.47(0.62)	2.36(1.55)	2.14(0.46)	2.07(0.55)

Table 4.3. The results of the paired t-Test and post-hoc power analysis. (*e*: the repeatability error. *d*: the Euclidian distance between the kinematic and geometric GH-JRC)

	2-tailed *p*-value		**Post-hoc power**	
	d	***e***	***d***	***e***
Cir	0.16	0.11	0.08	0.10
FE/Abd	0.11	0.19	0.48	0.36
FE/Abd/Cir	0.02*	0.03*	0.30	0.68

*: significant difference ($p < 0.05$)

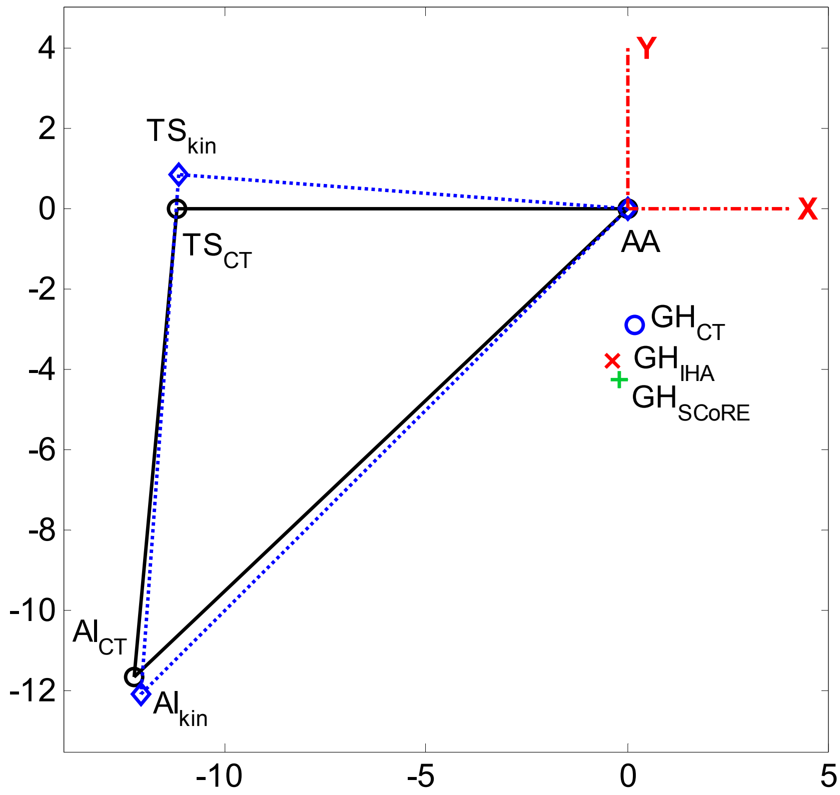

Figure 4.3. The kinematic and geometric GH-JRC as well as the scapular anatomical landmarks in the xy-plane. The mean values of the four subjects in Table 4.2 are used. The axes are in cm.

4.4. Discussion

This study compared two methods (SCoRE and IHA) for estimation of the GH-JRC for subjects with the shoulder hemi-arthroplastic endoprosthesis based on the distance to the geometric GH-JRC obtained from the subject-specific post-operative CT scans. The results for the IHA and SCoRE method were not the same: the IHA results were significantly closer to the geometrical rotation center than the SCoRE results. The difference between the estimated IHA and SCoRE centers was comparable to the similar studies on healthy adults (Lempereur et al, 2010; Monnet et al, 2007).

The comparison between the functional methods for estimation of the GH-JRC may be carried out based on either "repeatability" or "accuracy".

As for repeatability, Monnet *et al* (2007), found a lower repeatability error when using the SCoRE method (0.30 cm) as compared to the IHA method (0.43 cm), as we found in the current study, while Lempereur *et al* (2010) reported slightly higher repeatability error for the SCoRE method (4.36 mm vs. 4.11 mm for the IHA method). This means that there is not yet consensus about which method is more repeatable, even for the studies on healthy subjects. However, one should note that the results of the study by Monnet *et al* (2007) are statistically more reliable than the study by Lempereur *et al* (2010) due to its larger number of participants (10 vs 4). The difference between the results of the different studies may be related to the fixed error sources:

Both the SCoRE and the IHA methods start from the assumption that there is a GH-JRC with only three rotational degrees of freedom. This definition implies that translations within the joint are minimal. This assumption could potentially be a source of fixed errors. According to Graichen *et al* (2000) this is a valid assumption, since their MRI study of glenohumeral motions indicated mean glenohumeral translations during humeral elevation up to 1.2 mm. In our study translations were quite small and did not show a systematically changing position (Figure 4.4). Should, however, translations occur within the joint, this position would change with joint angle. In cases of a compromised joint in which more random translations are occurring, both positions and directions of the axes would change randomly. The fact that IHA method results can be interpreted as indication for the validity of the 3 DOF assumption, can be seen as a strong point of this particular method, which is in fact the exact opposite of the argument used by Monnet *et al* (2007) in their choice of the SCoRE over the IHA method.

Another source of fixed errors could be the assumption that there is a fixed relationship between the bony landmarks and the glenoid. Although the study by Meskers *et al* (1998a) has indicated that such a relationship exists and the assumption is therefore valid, it is, however, quite unlikely that there would be no interindividual variation at all.

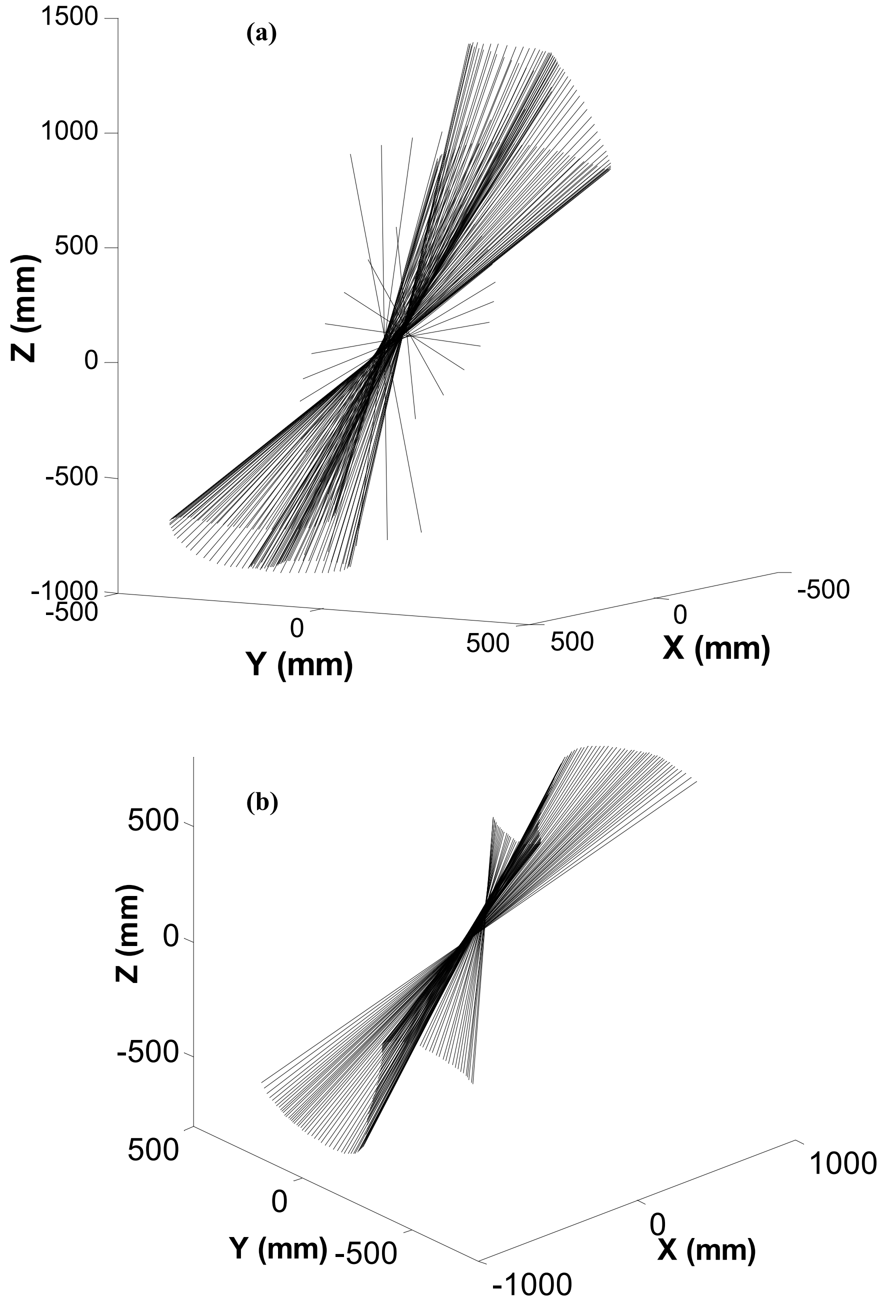

Figure 4.4. - The calculated instantaneous helical axes in space during (a) Abd, and (b) FE motion. Every 5 helical axes are plotted.

Regarding the accuracy, the reference point (the geometric GH-JRC) used for evaluating the accuracy of the two methods was similar in the current study (on patients) and the study by Lempereur *et al* (2010) (on healthy subjects). However, the results of the two studies are not identical. The difference between the studies may be due to the differences between the subjects (healthy vs patients with implants), which is not very likely, or related the random error sources. The potential sources for random errors could be the sampling errors of the motion capture system, the tissue artifact effects on motion of the technical markers (Cereatti et al, 2009), digitization errors of the flock of bird systems (Meskers et al, 1998b), treatment of the *in-vivo* measured data (e.g. filtering frequency, type of filter, etc.), errors in manual CT/MRI image processing, and inter-coordination transformation (from *in-vivo* measured to CT/MRI system or vice versa) errors (e.g. using the alternate examining basis point).

Accurate estimation of the GH-JRC is demanded for various applications. As a kinematic application, it is needed to define the local coordinate system of the upper arm as was stated in the ISB standardization protocol for the upper extremity (Wu et al, 2005). A more important application would be in subject-specific modeling. According to the recent studies (Nikooyan et al, 2010), it is now clear that to estimate reliable (muscle and joint reaction) forces, the musculoskeletal model should be scaled to subject-specific characteristics. Inaccuracies in estimation of the GH-JRC may cause considerable errors in calculation of some critical parameters (e.g. moment arms, origins and insertions of the muscles crossing the glenohumeral joint) in the scaled model.

4.5. Conclusions

This study aimed to validate two widely used functional methods (IHA and SCoRE) for estimating the GH-JRC *in-vivo*. Following conclusions can be drawn from this study:

- The SCoRE appeared to be a more repeatable method whereas the IHA method resulted in a more accurate estimation of the GH-JRC for patients with endoprostheses.
- The ISB standardization protocol recommends the IHA method for estimating the GH-JRC *in-vivo* in case of patients with shoulder implantation for whom the displaced rotation centers may occur. Assuming the geometric GH-JRC derived from the post-operative CT-data to be our reference, the IHA showed a significantly closer approximation for the most generalized combination of shoulder movements. We conclude that the IHA method can be recommended for estimation of GH-JRC for patients carrying shoulder implants.

4.6. References

Begon, M., Monnet, T., Lacouture, P., 2007. Effects of movement for estimating the hip joint centre. Gait & Posture 25 (3), 353-359.

Botha, C.P., Post, F.H., Hybrid scheduling in the DeVIDE dataflow visualisation environment, presented at Simulation and Visualization, Magdeburg, Germany, 2008.

Campbell, A.C., Lloyd, D.G., Alderson, J.A., Elliott, B.C., 2009. MRI development and validation of two new predictive methods of glenohumeral joint centre location identification and comparison with established techniques. Journal of Biomechanics 42 (10), 1527-1532.

Cereatti, A., Donati, M., Camomilla, V., Margheritini, F., Cappozzo, A., 2009. Hip joint centre location: An ex vivo study. Journal of Biomechanics 42 (7), 818-823.

Chang, L.Y., Pollard, N.S., 2007. Constrained least-squares optimization for robust estimation of center of rotation. Journal of Biomechanics 40 (6), 1392-1400.

Ehrig, R.M., Taylor, W.R., Duda, G.N., Heller, M.O., 2006. A survey of formal methods for determining the centre of rotation of ball joints. Journal of Biomechanics 39 (15), 2798-2809.

Gamage, S.S.H.U., Lasenby, J., 2002. New least squares solutions for estimating the average centre of rotation and the axis of rotation. Journal of Biomechanics 35 (1), 87-93.

Graichen, H., Stammberger, T., Bonel, H., Karl-Hans, E., Reiser, M., Eckstein, F., 2000. Glenohumeral translation during active and passive elevation of the shoulder -- a 3D open-MRI study. Journal of Biomechanics 33 (5), 609-613.

Halvorsen, K., 2003. Bias compensated least squares estimate of the center of rotation. Journal of Biomechanics 36 (7), 999-1008.

Halvorsen, K., Lesser, M., Lundberg, A., 1999. A new method for estimating the axis of rotation and the center of rotation. Journal of Biomechanics 32 (11), 1221-1227.

Lempereur, M., Leboeuf, F., Brochard, S., Rousset, J., Burdin, V., Rémy-Néris, O., 2010. In vivo estimation of the glenohumeral joint centre by functional methods: Accuracy and repeatability assessment. Journal of Biomechanics 43 (2), 370-374.

Meskers, C.G.M., van der Helm, F.C.T., Rozendaal, L.A., Rozing, P.M., 1998a. In vivo estimation of the glenohumeral joint rotation center from scapular bony landmarks by linear regression. Journal of Biomechanics 31 (1), 93-96.

Meskers, C.G.M., Vermeulen, H.M., de Groot, J.H., van der Helm, F.C.T., Rozing, P.M., 1998b. 3D shoulder position measurements using a six-degree-of-freedom electromagnetic tracking device. Clinical Biomechanics 13 (4-5), 280-292.

Monnet, T., Desailly, E., Begon, M., Vallee, C., Lacouture, P., 2007. Comparison of the SCoRE and HA methods for locating in vivo the glenohumeral joint centre. Journal of Biomechanics 40 (15), 3487-3492.

Nikooyan, A.A., Veeger, H.E.J., Westerhoff, P., Graichen, F., Bergmann, G., van der Helm, F.C.T., 2010. Validation of the Delft Shoulder and Elbow Model using in-vivo glenohumeral joint contact forces. Journal of Biomechanics 43 (15), 3007–3014.

Stokdijk, M., Nagels, J., Rozing, P.M., 2000. The glenohumeral joint rotation centre in vivo. Journal of Biomechanics 33 (12), 1629-1636.

van der Helm, F.C.T., Pronk, G.M., Veeger, H.E.J., van der Woude, L.H.V., 1989. The rotation center of the glenohumeral joint. Journal of Biomechanics 22 (10), 1092.

van der Helm, F.C.T., Veeger, H.E.J., Pronk, G.M., Van der Woude, L.H.V., Rozendal, R.H., 1992. Geometry parameters for musculoskeletal modelling of the shoulder system. Journal of Biomechanics 25 (2), 129-144.

Veeger, H.E.J., 2000. The position of the rotation center of the glenohumeral joint. Journal of Biomechanics 33 (12), 1711-1715.

Veldpaus, F.E., Woltring, H.J., Dortmans, L.J.M.G., 1988. A least-squares algorithm for the equiform transformation from spatial marker co-ordinates. Journal of Biomechanics 21 (1), 45-54.

Woltring, H.J., *Biomechanics of Human Movement, Applications in Rehabilitation, Sport and Ergonomics*. Washington, OH: Berlec Corporation, 1990.

Woltring, H.J., Huiskes, R., de Lange, A., Veldpaus, F.E., 1985. Finite centroid and helical axis estimation from noisy landmark measurements in the study of human joint kinematics. Journal of Biomechanics 18 (5), 379-389.

Woltring, H.J., Long, K., Osterbauer, P.J., Fuhr, A.W., 1994. Instantaneous helical axis estimation from 3-D video data in neck kinematics for whiplash diagnostics. Journal of Biomechanics 27 (12), 1415-1425.

Wu, G., van der Helm, F.C.T., Veeger, H.E.J., Makhsous, M., Van Roy, P., Anglin, C., Nagels, J., Karduna, A.R., McQuade, K., Wang, X., Werner, F.W., Buchholz, B., 2005. ISB recommendation on definitions of joint coordinate systems of various joints for the reporting of human joint motion-Part II: shoulder, elbow, wrist and hand. Journal of Biomechanics 38 (5), 981-992.

Modified from: A.A. Nikooyan, H.E.J. Veeger, P. Westerhoff, F. Graichen, G. Bergmann, F.C.T. van der Helm , 2010, "Validation of the Delft Shoulder and Elbow Model using *in-vivo* glenohumeral joint contact forces", Journal of Biomechanics 43(15): 3007–14.

Chapter 5

Quantitative validation of the Delft Shoulder and Elbow Model

The development of an instrumented shoulder endoprosthesis has now made the quantitative validation of the Delft Shoulder and Elbow Model possible. Motion data, EMG-signals, external forces, and *in-vivo* glenohumeral joint reaction forces (GH-JRF) were recorded for two patients with an instrumented shoulder hemi-arthroplasty, during dynamic motions (including abduction and anteflexion) and force tasks (with the arm held in a static position). Motions and external forces served as the model inputs to estimate the GH-JRF. In the modeling process, the effect of two different (stress and energy-based) optimization cost functions and uniform (size and mass) scaling were evaluated. Both the magnitude and the direction of the GH-JRF vector were compared. The model-estimated resultant GH-JRF followed the *in-vivo* measured one for dynamic tasks up to about 90° arm elevations, but generally underestimates the peak forces up to 31%; whereas a different behavior (ascending measured but descending estimated force) was found for angles above 90°. For the force tasks the model generally overestimated the peak GH-JRF for most directions of applying external loads (on average up to 34%). Applying the energy-based cost function improved model predictions for the dynamic anteflexion task (up to 9%) and for the force task (on average up to 23%). Scaling also led to improvement of the model predictions during the dynamic tasks (up to 26%), but had a negligible effect (< 2%) on the force task results. Uniform scaling did not considerably influence the position of the points of application of GH-JRF on the articular surface of the glenoid fossa while applying the energy-based cost function notably affected the force trajectory inside the glenoid. Although results indicated a reasonable compatibility between model and measured data, adjustments will be necessary to individualize the generic model with the patient-specific characteristics.

5.1. Introduction

To realistically replicate the behavior of the human locomotor system, a musculoskeletal model should be sufficiently complex (comprehensive, three-dimensional, and based on real anatomy). The complex models of the shoulder have been introduced in Chapter 2. Among these models, the Delft Shoulder and Elbow Model (DSEM) is the core of the current study.

As discussed before (Chapters 1 and 2), to validate the DSEM, the estimated muscle force-time curves were previously compared to measured EMG signals. This comparison showed good agreement (see reference (van der Helm, 1994) and Chapter 2). However, the agreement can only be seen as a qualitative validation (Inman et al, 1952) since it did not give information on the accuracy of predicted muscle force levels.

Recently, an implantable instrumented shoulder endoprosthesis (Westerhoff et al, 2009a) has been developed that is capable of *in-vivo* measuring contact forces and frictional moments in the gleno-humeral (GH) joint (see Chapter 3). The endoprosthesis has been tested and implanted in a number of patients for whom first data from activities of daily living have recently been published (Westerhoff et al, 2009b). Although measuring the muscle forces directly is not possible, the endoprosthesis allows for a generalized validation at the level of the summed muscle forces around the GH-joint.

Recent studies (Nolte et al, 2008; Rasmussen et al, 2007) have compared the analytical predictions with the published data from the first measured patient with the instrumented endoprosthesis (Bergmann et al, 2007). However, none of these studies used the simultaneous kinematic recordings of the same subjects, nor did they have the individual scapular motion available. To compensate for this, scapular motion pattern had to be used based on an assumed scapulohumeral rhythm. In general, we do know that this is not identical for controls and patients with endoprostheses (Veeger et al, 2006). In addition, comparisons were performed for a very limited kinematic motion range up to 45° humeral elevation angle.

In this chapter, GH-JRFs estimated by the DSEM are compared to forces from the instrumented shoulder endoprosthesis. The measured kinematics and external forces are used as model input. Since the DSEM traditionally uses a general (stress) cost function for the distribution of muscle moments and cadaver data as model parameters, the effects of the choice of a relatively new (energy-based) muscle load sharing cost function and uniform size and mass scaling on the model predictions are also taken into account. It is expected that the scaling to the subject's morphology and using an energy-based cost function will lead to a calculated contact force closer to the experimentally obtained contact force. Both the magnitude of the resultant GH-JRF and the direction of the GH-JRF vector will be compared between the model and experiment. For the direction of the GH-JRF vector, the trajectory of the GH-JRF vector inside the glenoid cavity (see Chapter 3) will be used as the reference for comparison.

5.2. Materials and Methods

5.2.1. Subjects

Two subjects with instrumented shoulder hemi-arthroplasty (S1 and S2, Table 3.1, Chapter 3) participated in the experiments. For the Ethics Statement and detailed descriptions about the participants see sections 3.2.1 and 3.2.2, Chapter 3.

5.2.2. Data recordings

Measured tasks comprised standard (unloaded) dynamic motions (including abduction and anteflexion) and quasi-static force tasks.

Subjects were asked to perform the dynamic tasks up to maximal possible arm elevation (see Table 3.2, Chapter 3).

Measurements comprised the collection of motion data, EMG, and external forces and moments (Figures 5.1 and 5.2), as well as *in-vivo* GH-JRF. For the detailed description about the motion, external loads, and *in-vivo* GH-JRF recordings see section 3.2.4, Chapter 3.

EMG signals of 12 muscles/muscle parts were gathered using a 16-channels Porti system (TMS International, Enschede, The Netherlands) at the sampling frequency of 1000 Hz. The measured muscles included the trapezius ascendens, transversum, and descendens, the infraspinatus, the deltoid anterior, medialis, and posterior, the pectoralis major clavicular and thoracic parts, the biceps short head, the triceps medialis, and the brachioradialis. The SENIAM recommendations (Merletti et al, 1999) were followed for the EMG sensor positioning. We visually checked the measured signals for possible crosstalk. To determine the maximum EMG values maximum voluntary contractions (MVCs) were also performed for each subject.

5.2.3. Kinematic data processing

Joint angles and local coordinate system definitions were determined following the ISB standardization protocol definitions (Wu et al, 2005), however direction was defined with the original DSEM axis (Veeger et al, 1997).

For S1, having the endoprosthesis on her left shoulder (Table 3.1, Chapter 3), all raw measured data was mirrored with respect to the sagittal plane in order to be represented in the right-handed coordinate system.

The glenohumeral joint rotation center, which is necessary for reconstruction of the local coordinate system of the humerus, was calculated using the Instantaneous Helical Axes (IHA) method (Veeger, 2000) (see Chapter 4 for detailed descriptions).

Since all three clavicular rotations are needed for DSEM input and only two landmarks are generally available for definition of clavicular orientation (SC and AC, Table 3.3, Chapter 3), the axial rotation of the clavicle was estimated by minimizing the rotations in the acromioclavicular joint as described in reference (van der Helm and Pronk, 1995).

5.2.4. Trajectory of the GH-JRF vector inside the glenoid

The *in-vivo* measured GH-JRF vector were transferred to the glenoid system by using the method described in section 3.2.6, Chapter 3. For the detailed description about the CT imaging and processing see sections 3.2.3 and 3.2.5, Chapter 3.

The intersection points of the GH-JRF vector through the articular surface of the glenoid were estimated from the compressive and shear components of the transferred forces on the glenoid.

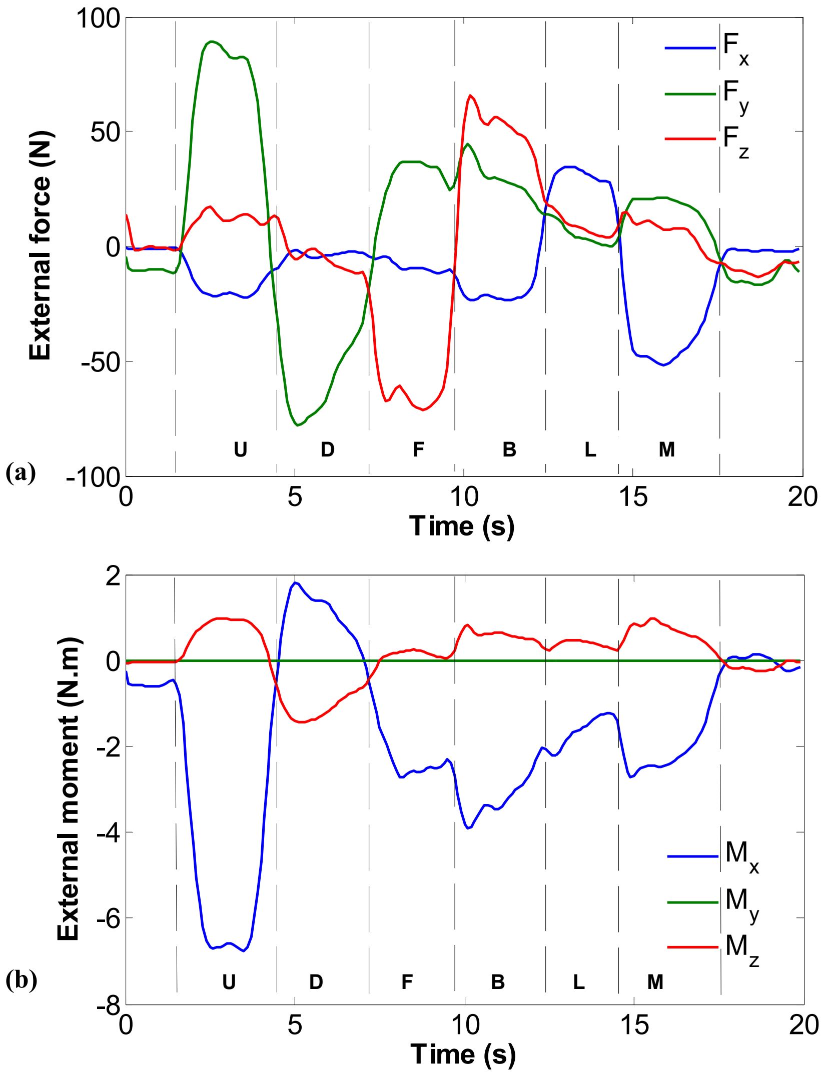

Figure 5.1. The measured external (a) forces and (b) moments, applied on the S1's hand during performing the force tasks in different directions. U= upward, D= downward, F= forward, B= backward, L= lateral, M= medial direction.

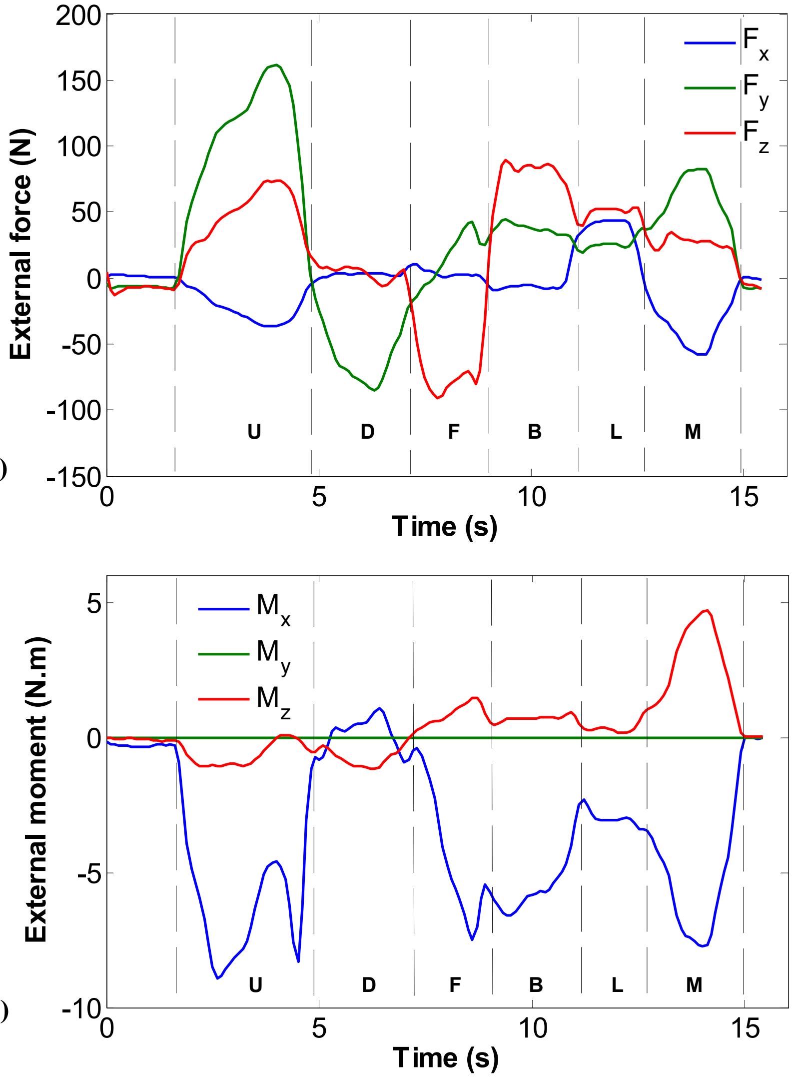

(a)

(b)

Figure 5.2. The measured external (a) forces and (b) moments, applied on the S2's hand during performing the force tasks in different directions. U= upward, D= downward, F= forward, B= backward, L= lateral, M= medial direction.

5.2.5. Estimating GH-JRF by the model

The Delft Shoulder and Elbow Model (DSEM) was extensively described in Chapter 2. The IDO model (see section 2.2.3, Chapter 2) is used here for modeling purposes. As an output of the IDO model, the GH-JRF is calculated by the summation of the model-estimated muscle forces around the glenohumeral joint.

As discussed previously (Chapters 2 and 3), stability of the model is addressed by constraining the direction of the GH-JRF vector inside the glenoid and prevents the glenohumeral joint dislocation.

As discussed in Chapter 2, the DSEM allows for the use of two different muscle load sharing cost functions namely a stress and an energy-based criteria which both are recruited in this study.

5.2.5.1. Uniform scaling

To include the anthropometry of a subject, *uniform* size and mass scaling is possible. In this study, the arm length ratio of the measured subject with respect to the cadaver used for the model (L10) was selected as the size scaling factor (Table 5.1). The arm length (l_{arm}) was calculated as follows:

$$l_{arm} = \left| \text{GH-}\left(\frac{\text{EL+EM}}{2}\right) \right| + \left| \left(\frac{\text{EL+EM}}{2}\right)\text{-}\left(\frac{\text{SR+SU}}{2}\right) \right| \quad (1)$$

Where GH, EL, EM, SR, SU are the spatial positions of the glenohumeral joint rotation center, lateral and medial epicondyle of the elbow and radial and ulnar styloid of the wrist in the global system, respectively.

To minimize the effect of a mass distribution difference between the cadaver and the subject, the ratio in Body Mass Index (BMI) (Keys et al, 1972) between the measured subject and the cadaver (Klein Breteler et al, 1999) was used as the mass scaling factor (Table 5.1).

Table 5.1. Uniform size and mass scaling parameters. BMI = Body Mass Index, SF = Scaling Factor. Cadaver: the cadaver from which the model parameters were obtained.

	Arm length (cm)	Height (cm)	Weight (kg)	BMI (kg/m²)	Size SF (arm length ratio)	Mass SF (BMI ratio)
S1	56	168	72	25.5	0.98	1.07
S2	49	163	85	32.0	0.86	1.35
Cadaver	57	168	67	23.7	-	-

5.2.5.2. Simulations

For each type of task and each subject, simulations were performed under three different conditions:

- the standard model (SM): the original model using the stress cost function (SCF),
- SM+ECF: the model using the energy cost function (ECF) for optimization, and
- SM+US: the uniformly scaled (US) model

5.2.6. EMG filtering and normalization

The measured EMGs were high-pass filtered, rectified, and subsequently low-pass filtered. For high- and low- pass filtering, second order Butterworth filter with cut-off frequencies of, respectively, 25 and 2 Hz were used. For each muscle, the measured EMG was normalized with respect to the maximum value from MVCs.

5.2.7. Measure of goodness of fit

5.2.7.1. Magnitude of the resultant GH-JRF

To evaluate model results, three sets of indicators were defined as follows:

1) The bivariate two-tailed Pearson Correlation Coefficient (R) and the Root Mean Squared Error (RMSE, Figure 5.3): indicates how well the model-estimated force pattern follows the measured GH-JRF.
2) The average offset (AO): the average value of the differences between the estimated and measured resultant GH-JRF at all points, indicating how the magnitude of the estimated GH-JRF differs from that of the measured GH-JRF.
3) The peak force error (PE): the difference between estimated and measured resultant GH-JRF normalized by the measured resultant GH-JRF (Table 5.2).
    a. For dynamic tasks, the PE is calculated at the point that the peak of the calculated force occurs (around 90° humeral elevation angle).
    b. For force tasks, the PE is calculated for all six directions. The average of these six values is considered to present the PE.

For both AO and PE, a minus value indicates underestimation of the model with respect to the experiments while a positive value indicates an overestimation.

5.2.7.2. Direction of the GH-JRF vector

The plots for the model-predicted trajectory of the GH-JRF vector inside the glenoid fossa were compared to the ones measured *in-vivo*.

5.3. Results

5.3.1. Magnitude of the resultant GH-JRF

5.3.1.1 Dynamic tasks

For abduction (Figures 5.4a and b) up to about 90° arm elevation, the in-vivo measured and model-predicted (by the standard model) GH-JRF showed good consistency (R = 0.9883 and 0.9907, AO = -57.7N and -7.9 N, for S1 and S2, respectively), although model estimates were generally lower (up to 31.3%, Table 5.2). It can be seen that for abduction motion, applying the ECF increases the underestimation by about 9% (Table 5.2).

For anteflexion (Figures 5.5a and b), the model predictions follow the measured forces up to about 90° arm elevation (R = 0.9682 and 0.9756, AO = -45.4N and -72.4N, for S1 and S2, respectively). In contrast to abduction, applying the ECF slightly reduced the differences between the model and the experiment (up to about 9%, Table 5.2).

In both abduction and anteflexion (Figures 5.4 and 5.5) the calculated and measured forces showed a different behavior for angles above 90° arm elevation; the calculated force started to decrease, while the measured force continued to increase.

Uniform scaling reduced the underestimations (up to 8% and 25% for S1 and S2, respectively) during dynamic tasks (Table 5.2, Figures 5.3, 5.4, and 5.5).

5.3.1.2. Force tasks

With the exception of the medial direction (two subjects) and upward direction (S2 only), the model predictions (Figures 5.6a, b) showed an overestimation compared to the measured forces (AO up to 477.8N, PE up to 33.6%).

Using the ECF led to less overestimation (up to 23%, Table 5.2). It reduced the overestimation up to 29% and 50% in the downward direction, up to 16% and 41% in the backward direction, and up to 14% and 29% in the lateral direction, for S1 and S2, respectively (Table 5.2, Figure 5.6).

Uniform scaling had a negligible effect (less than 2%) on the force tasks for both subjects (Table 5.2, Figures 5.3 and 5.6).

The model-predicted individual muscle forces (Figure 5.7 a, b, c, g, h) generally showed compatibility with the normalized measured EMG-signals of the superficial muscles (Figure 5.8).

5.3.2. Direction of the GH-JRF vector

The position of the model-predicted force trajectory inside the glenoid cavity was relatively close to the one measured *in-vivo* in case of S1 and S2 during abduction, and S1 during forward flexion (Figures 5.9 and 5.10). Nevertheless, the difference between the model-predicted and measured force trajectories in case of S2 during forward flexion, and S1 and S2 during force task was remarkable (Figures 5.9 and 5.10).

Applying the ECF notably changed the position of the force trajectory inside the glenoid (but not necessarily in the desired direction). Uniform scaling did not have considerable effect on the position of points of application of GH-JRF vector on the articular surface of the glenoid fossa.

Table 5.2. The peak force error (PE, in %) at all measured tasks and for two subjects. Plus/minus signs mean over/underestimation. SM = Standard Model, ECF = Energy Cost Function, US: Uniform Scaled

Motion task	Subject	SM	SM + ECF	SM + US
Abduction	S1	-18.6	-27.8	-10.3
	S2	-29.1	-36.3	-3.5
Anteflexion	S1	-21.6	-13.0	-14.7
	S2	-31.3	-23.6	-9.8
Force task	S1	+27.6	+14.4	+28.7
	S2	+33.6	+10.4	+31.8

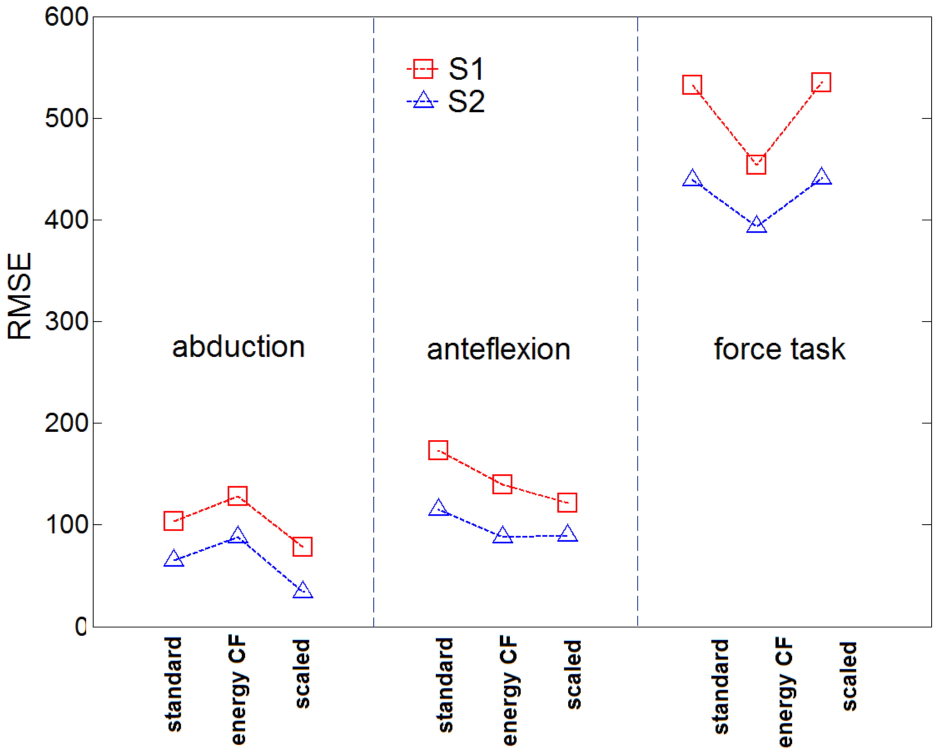

Figure 5.3. The Root Mean Squared Error (RMSE) calculated between the model-estimated and the measured GH-JRF: dynamic motions and forces tasks, three model assumptions (Table 2).

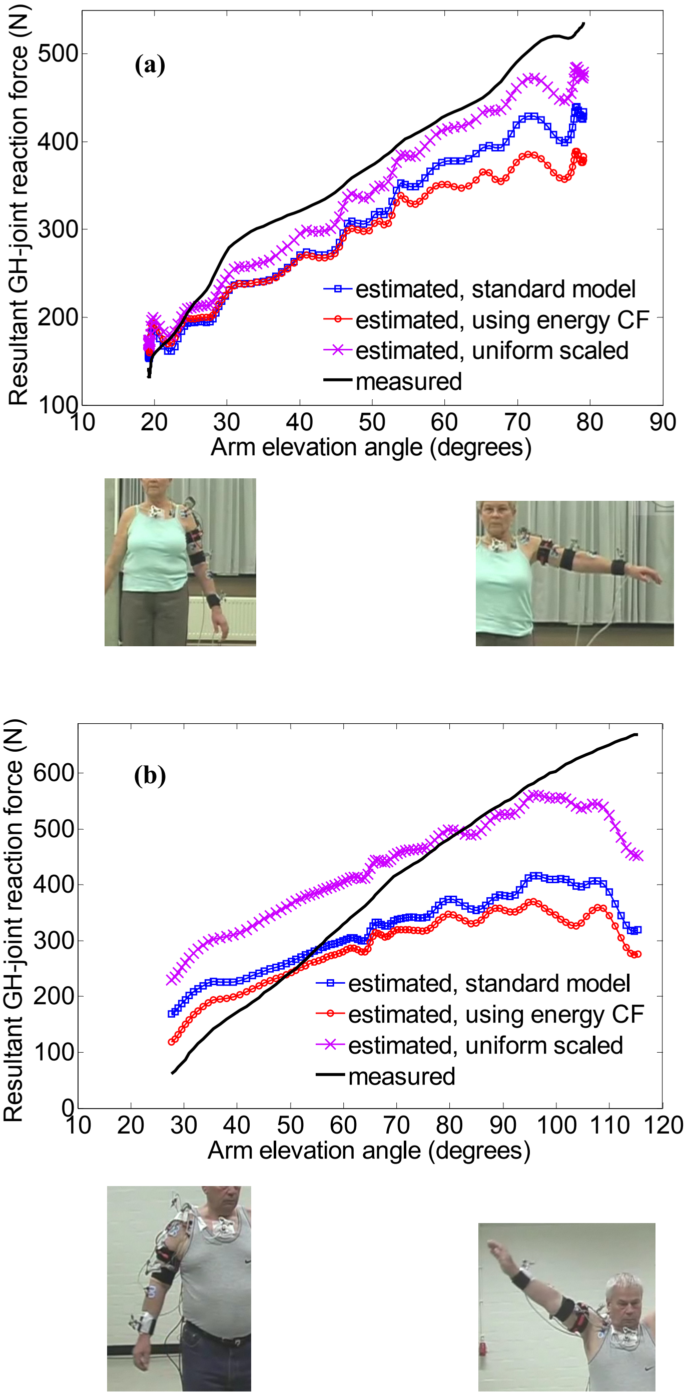

Figure 5.4. Comparison of measured and calculated GH-JRF during abduction. *In-vivo* measured (solid line), model-estimated standard model (blue line), applying the energy cost function (red line), and uniform scaled (purple line) GH-JRF vs arm elevation angle for (a) S1 (b) S2.

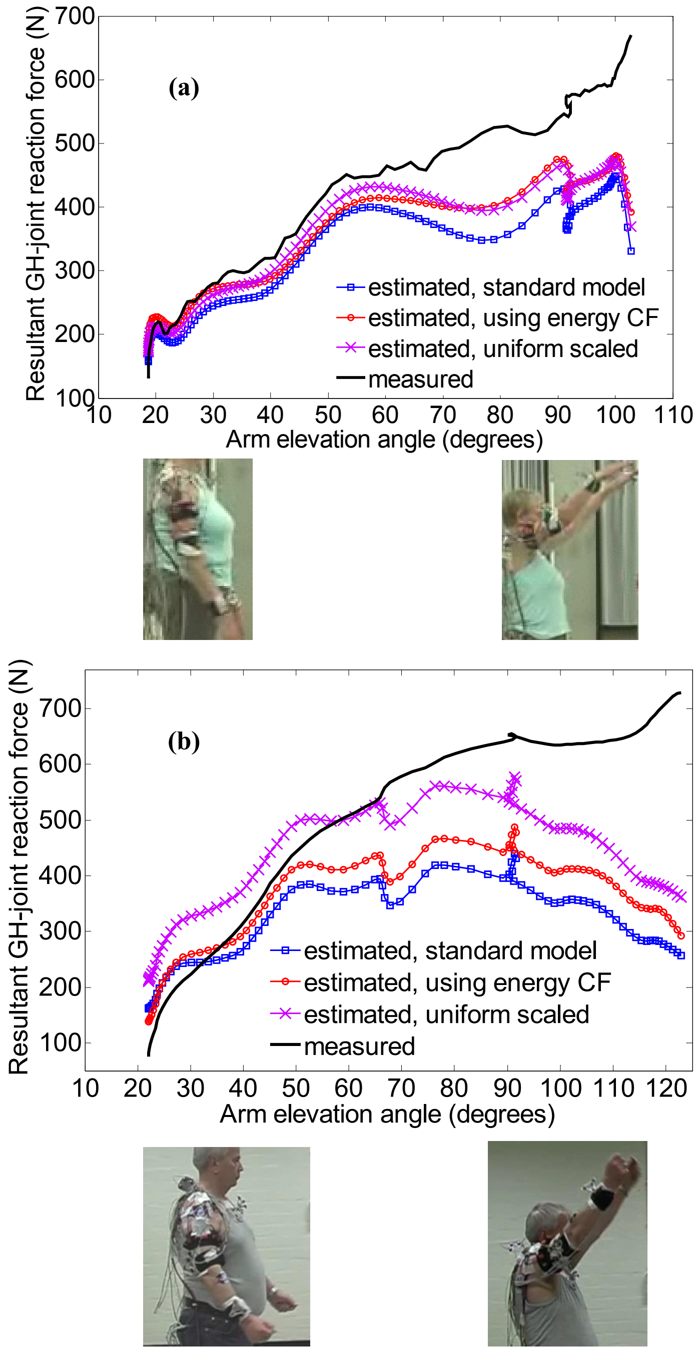

Figure 5.5. Comparison of measured and calculated GH-JRF during forward flexion. *In-vivo* measured (solid line), model-estimated standard model (blue line), applying the energy cost function (red line), and uniform scaled (purple line) GH-JRF vs arm elevation angle for (a) S1 (b) S2.

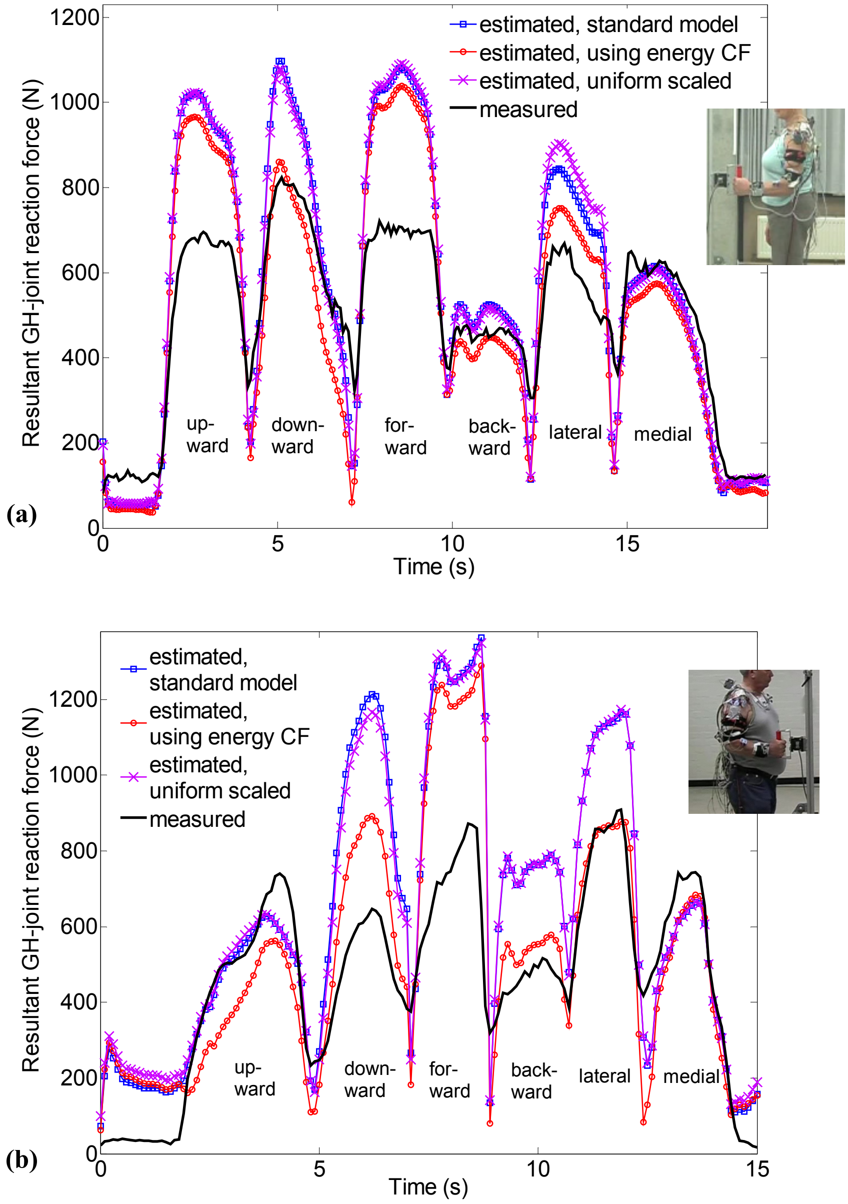

Figure 5.6. Comparison of measured and calculated GH-JRF during force tasks. *In-vivo* measured (solid line), model-estimated standard model (blue line), applying the energy cost function (red line), and uniform scaled (purple line) GH-JRF vs time in six different directions for (a) S1 (b) S2. The external force direction at the handles indicated.

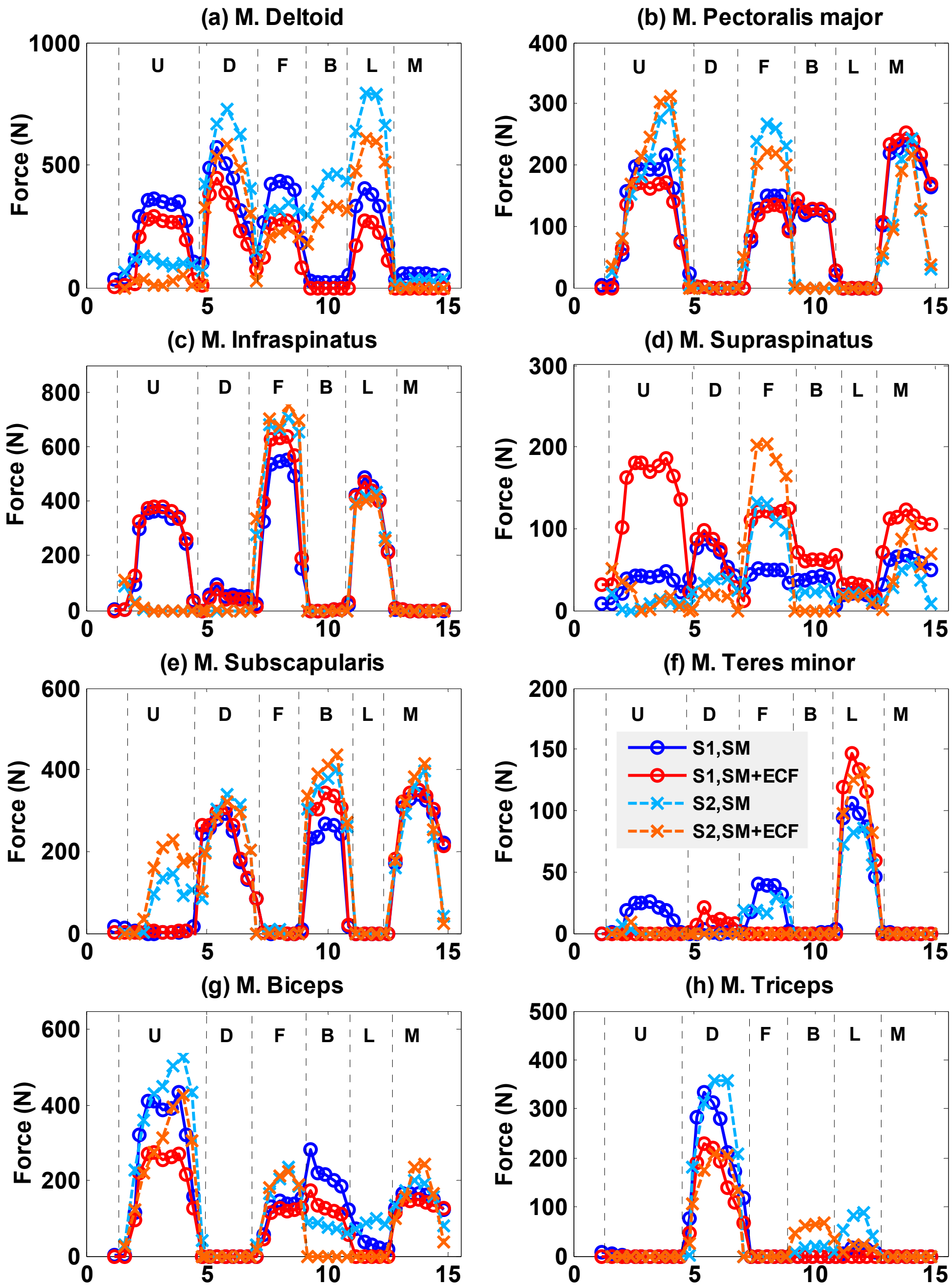

Figure 5.7. Model calculated individual muscle forces (with standard model and with model applying the energy cost function) during force tasks for two measured subjects. The force-time curves of S1 are resampled to those of S2 in order to show the results of two subjects in the same plot. U= upward, D= downward, F= forward, B= backward, L= lateral, M= medial direction.

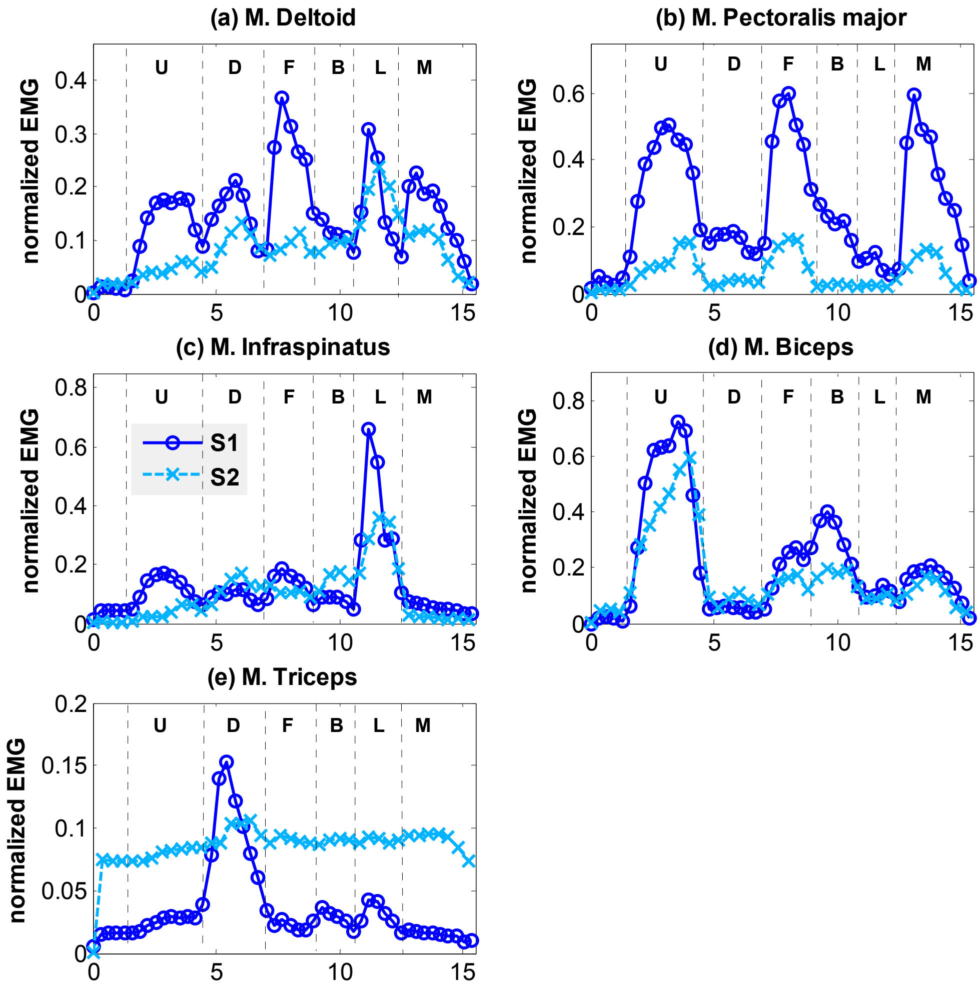

Figure 5.8. The measured EMG signals (of the superficial muscles) during force tasks for two measured subjects. The EMG signals for each muscle are normalized with respect to the maximum measured EMG for that muscle during the maximum voluntary contractions (MVC). U= upward, D= downward, F= forward, B= backward, L= lateral, M= medial direction.

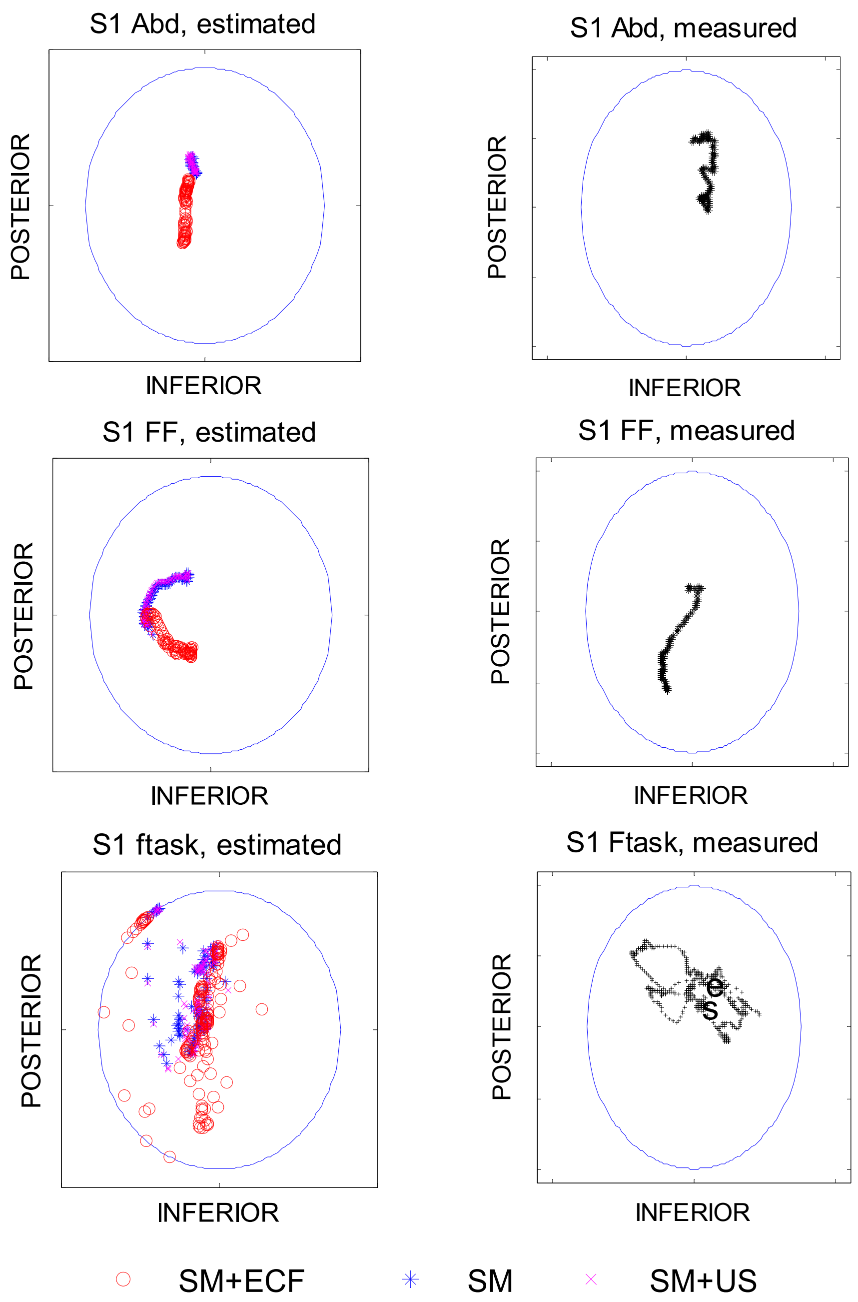

Figure 5.9. The model-estimated (estimated, left column) vs. *in-vivo* measured (measured, right column) trajectory of the GH-JRF vector inside the glenoid fossa for subject S1 during abduction (Abd), forward flexion (FF), and force task (Ftask). (SM: standard model; SM+ECF: model using energy cost function; SM+US: uniform scaled model)

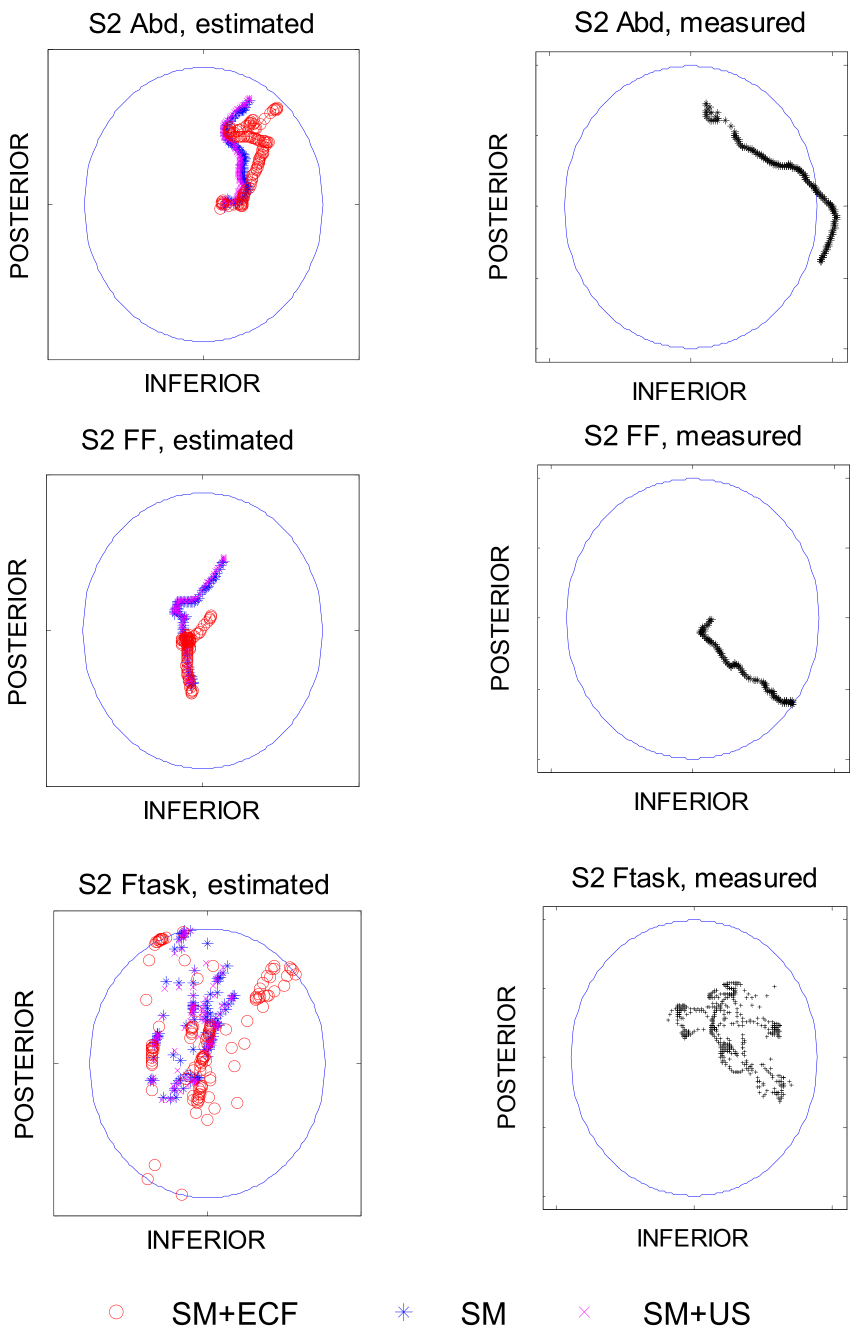

Figure 5.10. The model-estimated (estimated, left column) vs. *in-vivo* measured (measured, right column) trajectory of the GH-JRF vector inside the glenoid fossa for subject S2 during abduction (Abd), forward flexion (FF), and force task (Ftask). (SM: standard model; SM+ECF: model using energy cost function; SM+US: uniform scaled model)

5.4. Discussion

As results showed, the calculated and *in-vivo* measured GH-JRFs are not identical. Differences appeared between the both the magnitude and the direction of the GH-JRF vector. The calculated forces were lower than those measured for dynamic tasks, and too high for the force tasks.

In case of dynamic motions (Figures 5.4 and 5.5), the deviations between the model estimations and measured forces primarily occur at arm elevations above 60°. Since the previous studies (Nolte et al, 2008; Rasmussen et al, 2007) looked at arm elevations below this angle, and keeping in mind that the input was based on an assumed scapular motion pattern, results of those studies should be interpreted with some caution.

When performing dynamic tasks, the estimated and measured GH-JRF appeared to show a different behavior for angles above 90° arm elevation (Figures 5.4 and 5.5); the estimated force decreased, while the measured force continued to increase. The force drop above 90° elevations was previously assumed to be a general behavior of the musculoskeletal models of the shoulder, as it was reported by some other researchers (Poppen and Walker, 1978; Terrier et al, 2008), and was based on the fact that the lever of the external force/arm weight decreases after 90°, so that the muscular forces were expected to drop as well. The different behavior observed here may have been caused by muscle co-contraction in our subjects, based either on a 'standard' coordination pattern or on pathological motor control related to the endoprosthesis. A study by Favre *et al* (2005) introduced a method for estimating the GH-JRF in which muscles with higher mechanical advantage are favored. The method has been used to predict the GH-JRF during abduction motion (Favre et al, 2009) and the results showed that the predicted GH-JRF continued to increase after 90° arm elevation, as was observed in our experiments. The co-contraction was assumed to be the reason why the GH-JRF increased above 90° arm elevation. The results of the study by Favre *et al* state that the modeling approach allowing possible muscle co-contractions may lead to the different observed behavior for arm elevations higher than 90°. Thus, implementation of co-contraction might be essential for model improvement. One approach is to develop an EMG-driven model (see Chapter 6) in which the normalized measured EMG-signals provide additional constraints in the optimization procedure. Additionally, proprioceptive feedback has been proposed to be an alternative mechanism for postural stability (van der Helm and Rozendaal, 2000). Compared to co-contraction, proprioceptive feedback has both an advantage and a disadvantage: it does not cost energy but it has time delays. Implementing the proprioceptive feedbacks in the modeling process is an alternative solution for model improvement. However, there remains an uncertainty regarding which mechanism is used by the human body for (functional) stability in arm elevations above 90°, where the arm behaves like an inverted pendulum.

Another possible explanation for the discrepancies between the predicted and measured contact forces may be found in joint friction. A study by Bergmann *et al* (2001) on hip implants showed temperature elevations in gait (up to 43.1°C after one hour walking), indicating a considerable amount friction within the artificial joint. It is likely that friction also occurs in the shoulder hemi-prosthesis and that this friction causes extra work for the muscles. The instrumented prostheses measurement results showed in fact that these frictional moments were substantial with values up to 7Nm (Westerhoff et al, 2008). As a consequence, individualization of the shoulder model toward arthroplasty patient specific model versions might quite likely require implementation of these frictional moments into the model (see Chapter 8).

Detailed model calculations of the individual muscle forces may be useful to explain the discrepancies between the model-estimated and measured GH-JRF in some directions of applying the external forces when performing the force tasks. For example the model overestimates the GH-JRF in the upward direction for S1 (Figure 5.6a) and in the backward direction for S2 (Figure 5.6b). One can see in Figure 5.7 that in the upward direction the deltoid and infraspinatus muscles are favored by the model for S1 while subscapularis is favored for S2. Similarly, in the backward direction the model favors the pectoralis major for S1 and the deltoid for S2. The larger maximum muscle force for the deltoid muscle over those of both pectoralis major and the subscapularis muscles may explain the overestimations in the above-mentioned cases. This result may be generalized to the other directions. These overestimations may arise either from the muscle-load-sharing pattern or the differences between the model's and the subject's muscular anatomy. The former might lead to a favoring of the stronger muscles, which may not be the case for the patients, and the latter may estimate higher muscle forces than those that the patient is able to produce.

The energy criterion showed potential to simultaneously improve the model under- and over-estimations during the anteflexion motion and the force tasks. This criterion contains two weight factors to tune the linear and nonlinear terms (Praagman et al, 2006) which were theoretically derived. It is uncertain whether these factors are indeed optimal or could be further optimized (see Chapter 7).

In this study, a generic model was scaled to match few patients' anatomical parameters. As one can see in Figures 5.9 and 5.10, uniform scaling did not have sensible effect on the position of the points of application of the GH-JRF vector on the surface of the glenoid fossa. Giving that the magnitude of the resultant GH-JRF vector increased by scaling, one concludes that the uniform scaling only affected the compressive component (but not the shear component) of the GH-JRF vector. The applied scaling approach (uniform scaling) has, however, been shown to be inappropriate for patient specific modeling (Scheys et al, 2008) since it does not include the scaling of the subject's specific muscle strength parameters (e.g. PCSA). Significant interindividual variability (Figure 5.11) in bony and muscular anatomy, seems to be an important source of discrepancies between the experiments and the model, as this can change many parameters such as the muscle volume, PCSA, segment weights, shape of bony elements, moment arms and therefore most likely also the muscle forces. The direction of the force vectors toward the glenoid cavity is also highly dependent on the subject-specific geometry (see Chapter 3). Thus, for more extensive comparisons, the effect of full (subject-specific) scaling that also includes muscle parameters is a necessary next step.

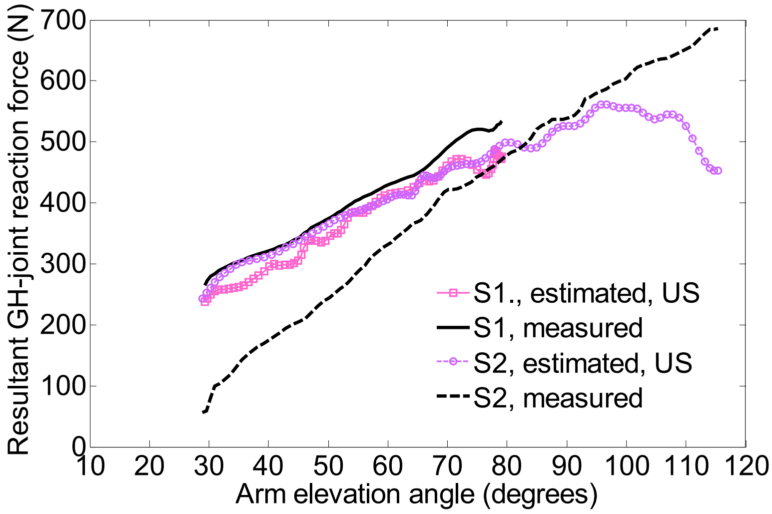

Figure 5.11. The effect of inter-individual differences. *In-vivo* measured and model-estimated uniform scaled (US) GH-JRF vs arm elevation angle during abduction motion for two measured subjects.

5.5. Conclusions

This work was the first attempt in quantitative validation of the shoulder part of the DSEM at the level of the GH-JRF. The *in-vivo* measured GH-JRF on two subjects was used as the basis of validation. Following conclusions can be drawn from this study:

- Compared with the magnitude of the resultant GH-JRF measured *in-vivo*:
    - The model generally underestimated the peak resultant GH-JRF for standard dynamic tasks like abduction and forward flexion.
    - The model generally overestimated the peak resultant GH-JRF for quasi-static force tasks.
- For dynamic tasks, the calculated and measured forces showed a different behavior for angles above 90° arm elevation; the calculated force started to decrease, while the measured force continued to increase.
- The model showed a relatively close prediction of the trajectory of the GH-JRF vector to the one measured *in-vivo* for abduction motion. However, the difference between the model predicted and *in-vivo* measured force trajectories was relatively remarkable during forward flexion and force tasks.
- Applying the energy-based cost function for inverse-optimization,
    - slightly increased the model underestimation during abduction.

    - slightly decreased the model underestimation during forward flexion.
    - considerably decreased the model overestimations in a few directions of applying external forces for the force tasks.
    - had no effect on the pattern of the model predicted GH-JRF for angles above 90° arm elevation.
    - had a considerable effect on the position of the force trajectory inside the glenoid for all shoulder tasks.
- Uniform size and mass scaling:
    - reduced the model underestimation during dynamic tasks.
    - had a negligible effect on the force tasks.
    - had no effect on the pattern of the model predicted GH-JRF for angles above 90° arm elevation.
    - had a negligible effect on the position of the force trajectory inside the glenoid for all shoulder tasks.
- Although, the model predictions showed compatibility with the measured data, improvements are still necessary to individualize the model with the patient specific characteristics. These improvements could include, but are not limited to:
    - implementation of the muscle co-contractions in the modeling process,
    - optimization of the muscle-load-sharing cost functions,
    - implementation of the friction-induced moments, measured in the instrumented shoulder implant, in the modeling process, and
    - the detailed patient-specific scaling of the model.

5.6. References

Bergmann, G., Graichen, F., Bender, A., Kaab, M., Rohlmann, A., Westerhoff, P., 2007. In vivo glenohumeral contact forces-Measurements in the first patient 7 months postoperatively. Journal of Biomechanics 40 (10), 2139-2149.

Bergmann, G., Graichen, F., Rohlmann, A., Verdonschot, N., van Lenthe, G.H., 2001. Frictional heating of total hip implants. Part 1. measurements in patients. Journal of Biomechanics 34 (4), 421-428.

Favre, P., Sheikh, R., Fucentese, S.F., Jacob, H.A.C., 2005. An algorithm for estimation of shoulder muscle forces for clinical use. Clinical Biomechanics 20 (8), 822-833.

Favre, P., Snedeker, J.G., Gerber, C., 2009. Numerical modelling of the shoulder for clinical applications. Philisophical Transactions of the Royal Society 367, 2095-2118.

Inman, V.T., Ralston, H.J., Saunders, J., Feinstein, B., Wright, E.W., 1952. Relation of human electromyogram to muscular tension. Electroencephalography and Clinical Neurophysiology 4 (2), 187-194.

Keys, A., Fidanza, F., Karvonen, M., Kimura, N., Taylor, H., 1972. Indices of relative weight and obesity. Journal of Chronic Diseases 25 (6), 329-343.

Klein Breteler, M.D., Spoor, C.W., Van der Helm, F.C.T., 1999. Measuring muscle and joint geometry parameters of a shoulder for modeling purposes. Journal of Biomechanics 32 (11), 1191-1197.

Merletti, R., Wallinga, W., Hermens, H., Freriks, B., *Guidelines for reporting SEMG data*: Roessingh Research and Development, 1999.

Nolte, A., Augat, P., Rasmussen, J., 2008. Analysis of the muscle and joint forces in the shoulder joint uisng the AnyBody simulation model. Journal of Biomechanics 41 (S1), S492.

Poppen, N.K., Walker, P.S., 1978. Forces at the glenohumeral joint in abduction. Clinical Orthopaedics and Related Research 135, 165-170.

Praagman, M., Chadwick, E.K.J., van der Helm, F.C.T., Veeger, H.E.J., 2006. The relationship between two different mechanical cost functions and muscle oxygen consumption. Journal of Biomechanics 39 (4), 758-765.

Rasmussen, J., de Zee, M., Tørholm, S., Damsgaard, M., 2007. Comparison of a musculoskeleal shoulder model with in-vivo joint forces. Journal of Biomechanics 40 (S2), S67.

Scheys, L., Van Campenhout, A., Spaepen, A., Suetens, P., Jonkers, I., 2008. Personalized MR-based musculoskeletal models compared to rescaled generic models in the presence of increased femoral anteversion: Effect on hip moment arm lengths. Gait & Posture 28 (3), 358-365.

Terrier, A., Vogel, A., Capezzali, M., Farron, A., 2008. An algorithm to allow humerus translation in the indeterminate problem of shoulder abduction. Medical Engineering & Physics 30, 710–716.

van der Helm, F.C.T., 1994. Analysis of the kinematic and dynamic behavior of the shoulder mechanism. Journal of Biomechanics 27 (5), 527-550.

van der Helm, F.C.T., Pronk, G.M., 1995. Three-dimensional recording and description of motions of the shoulder mechanism. Journal of Biomechanical Engineering 117, 27-40.

van der Helm, F.C.T., Rozendaal, L.A., "Musculoskeletal systems with intrinsic and proprioceptive feedback," in *Neural control of posture and movement*, J. M. Winters and P. Crago, Eds. NY: Springer Verlag, 2000, pp. 164-174.

Veeger, H.E.J., 2000. The position of the rotation center of the glenohumeral joint. Journal of Biomechanics 33 (12), 1711-1715.

Veeger, H.E.J., Magermans, D.J., Nagels, J., Chadwick, E.K.J., van der Helm, F.C.T., 2006. A kinematical analysis of the shoulder after arthroplasty during a hair combing task. Clinical Biomechanics 21, S39-S44.

Veeger, H.E.J., Yu, B., An, K.-N., Rozendal, R.H., 1997. Parameters for modeling the upper extremity. Journal of Biomechanics 30 (6), 647-652.

Westerhoff, P., Graichen, F., Bender, A., Halder, A., Beier, A., Rohlmann, A., Bergmann, G., 2009b. In vivo measurement of shoulder joint loads during activities of daily living. Journal of Biomechanics 42, 1840–1849.

Westerhoff, P., Graichen, F., Bender, A., Rohlmann, A., Bergmann, G., 2009a. An instrumented implant for in vivo measurement of contact forces and contact moments in the shoulder joint. Medical Engineering & Physics 31 (2), 207-213.

Westerhoff, P., Rohlmann, A., Bender, A., Graichen, F., Bergmann, G., 2008. In vivo shoulder joint forces at isolated motions. Journal of Biomechanics 41 (Supplement 1), S144-S144.

Wu, G., van der Helm, F.C.T., Veeger, H.E.J., Makhsous, M., Van Roy, P., Anglin, C., Nagels, J., Karduna, A.R., McQuade, K., Wang, X., Werner, F.W., Buchholz, B., 2005. ISB recommendation on definitions of joint coordinate systems of various joints for the reporting of human joint motion--Part II: shoulder, elbow, wrist and hand. Journal of Biomechanics 38 (5), 981-992.

Modified from: A.A. Nikooyan, H.E.J. Veeger, P. Westerhoff, B. Bolsterlee, F. Graichen, G. Bergmann, F.C.T. van der Helm, "An EMG-driven musculoskeletal model of the shoulder", under revision.

Chapter 6

An EMG-driven musculoskeletal model of the shoulder

This Chapter aims to develop an Electromyography (EMG)-driven model of the shoulder that can consider possible muscle co-contractions. A musculoskeletal shoulder model (the original model) is modified such that measured EMGs can be used as model-inputs (the EMG-driven model). The model is validated by using the *in-vivo* measured glenohumeral-joint reaction forces. Three patients carrying instrumented hemi-arthroplasty were asked to perform arm abduction and forward-flexion up to maximum possible elevation, during which motion data, EMG, and *in-vivo* glenohumeral-joint reaction forces were measured. The measured EMGs were normalized and together with analyzed motions served as model inputs to estimate the glenohumeral-joint reaction forces. All possible combinations of input EMGs ranging from a single signal to all EMG signals together were tested. The 'best solution' was defined as the combination of EMGs which yielded the closest match between the model and the experiments. Two types of inconsistencies between the original model and the measurements were observed including a general glenohumeral-joint reaction force underestimation and a glenohumeral-joint reaction force drop above 90° elevation. Both inconsistencies appeared to be related to co-contraction since inclusion of EMGs could significantly ($p < 0.05$) improve the predicted glenohumeral-joint reaction forces (up to 45% at the peak elevation angle). The developed model has shown the potential to successfully take the existent muscle co-contractions of patients into account. The developed model, therefore, can be used as a more reliable platform for prediction of the loads on the shoulder joint especially in clinical applications.

Nomenclature

θ	Joint angle
$\dot{\theta}$	Joint angular velocity
$\ddot{\theta}$	Joint angular acceleration
L_m	Muscle length
M	Net joint moment
F_m	Model-predicted muscle force
F_{min}	Minimum permissible muscle force in the inverse optimization
F_{max}	Maximum permissible muscle force in the inverse optimization
u	Hypothetical neural input
e	Neural excitation
a	Neural activation
L_{ce}	Length of contractile element
$nEMG$	Normalized EMG
F_{emg}	Predicted muscle force by the forward muscle model using the $nEMG$ as excitation
nEr	Normalized error

6.1. Introduction

Recent experimental findings confirmed that pathological muscle co-contraction occurs in patients with rotator cuff defects. Steenbrink *et al* (2009) showed that adductor (e.g. pectoralis major and latissimus dorsi) muscle co-contraction is a key factor to preserve the glenohumeral stability in patients with cuff lesions. It was also shown that adductor co-contraction is a possible cause of observed limitations in maximal arm elevation in those patients (Jost et al, 2000).

In Chapter 5 (Nikooyan et al, 2010), the glenohumeral-joint reaction forces (GH-JRF) estimated by the model (Delft Shoulder and Elbow Model) were compared to those simultaneously measured using an instrumented shoulder endoprosthesis. The comparison results showed two inconsistencies: 1) underestimation of the model predictions for abduction and flexion motions and 2) different behavior of the estimated and measured forces above 90° humeral elevations where the measured forces continued to increase while the model-predicted forces started to decrease. One may explain the differences between the model and experiments by muscle co-contraction which is generally not considered in the model. This is a common phenomenon: different studies have shown that the optimization-based inverse-dynamics musculoskeletal models (e.g. the Delft model) do generally neglect the antagonist muscle co-contractions (Cholewicki et al, 1995; Gagnon et al, 2001).

Researchers have introduced different methods to consider the muscle co-contraction in the modeling procedure such as developing advanced load sharing cost functions (Jinha et al, 2006). As an example of the possible effects of considering the muscle co-contraction on the modeling results one can refer to the study by Favre *et al* (2005) in which a method was introduced for estimating the GH-JRF taking the muscle co-contraction into account. The method has been used (Favre et al, 2009) to predict the GH-JRF during shoulder abduction and the results showed that the predicted GH-JRF continued to increase after 90° arm elevation as was observed in our experiments (Chapter 5). Favre *et al* (2009) also compared the GH-JRF calculated by their model to the one estimated by the Delft Shoulder and Elbow Model and pointed out that the former predicted generally higher GH-JRF during shoulder abduction.

An alternative to the use of different cost function is the addition of Electromyography (EMG) to the model input. The concept is to force the (neuro-) musculoskeletal model to follow the individual muscle activation patterns which are considered to be equal to the normalized measured EMG signals. A variety of EMG-driven models has been developed for static and/or dynamic tasks and at different anatomical sites such as knee and ankle (Buchanan et al, 2004; Buchanan et al, 2005; Gerus et al, 2010; Lloyd and Besier, 2003; Olney and Winter, 1985), spine (Cholewicki et al, 1995; McGill, 1992; van Dieen and Kingma, 2005), shoulder (Langenderfer et al, 2005; Laursen et al, 1998), elbow (Koo and Mak, 2005; Manal et al, 2002), and wrist (Buchanan et al, 1993).

Most of the existing EMG-driven models use the measured external joint moment as reference for validation. The congruity between the model-predicted net joint moments and the measured external moments has been defined as the measure of goodness-of-fit of the model. Based on our best knowledge, no model has been validated by directly comparing its predictions with the *in-vivo* measured muscle and/or joint reaction forces. Direct measurement of the individual muscle forces *in-vivo* has been hardly possible. However, a recently developed instrumented endoprosthesis (Westerhoff et al, 2009) now allows for *in-vivo* measurements at the level of summed muscle forces around a joint (joint reaction force). As for the shoulder joint, Praagman *et al* (2000) found a linear relationship between the magnitude of the model predicted net joint moment and the GH-JRF during static tasks. Nevertheless, one should note that using the same net joint moment but different load sharing criteria and/or constraints during inverse optimization would result in different predicted joint reaction forces (Chapter 5). Therefore, additional efforts for joint stabilization (e.g. co-contraction) during dynamic motions and specifically above 90˚ at which the arm behaves like an inverted pendulum, may appear in the pattern of the GH-JRF but not the net joint moment. Thus, to judge whether or not an EMG-driven model can account for the antagonist co-contraction at higher arm elevations, using the *in-vivo* measured GH-JRF as the validation reference is preferable over measured moments.

In this chapter, we will follow the EMG-driven modeling approach to consider the possible antagonistic co-contraction in the model. The Delft Shoulder and Elbow Model (DSEM) will be modified and used. The measured EMG signals of (a selection of) the superficial muscles of the shoulder and elbow will be normalized and used as the inputs to the EMG-driven model. All possible combinations of available EMGs, ranging from single muscle activity to all activities together, will be used as model inputs. As criterion for an improvement in model predictions, the calculated GH-JRFs will be compared to the *in-vivo* measured ones of patients with an instrumented shoulder endoprosthesis. The comparison results will also be used to find the most optimal combination(s) of the input-EMG signals. It is expected that including EMGs in the model input will lead to model predictions closer to the experimentally obtained joint contact forces.

6.2. Materials and Methods

6.2.1. Subjects

Three subjects with instrumented shoulder hemiarthroplasty (S1, S2, and S6, Table 3.1, Chapter 3) participated in the experiments. These three subjects were selected for this study because their maximal possible arm elevation (notably) exceeded 90º (see Table 3.2, Chapter 3).

For the Ethics Statement and detailed descriptions about the participants see sections 3.2.1 and 3.2.2, Chapter 3.

6.2.2. Motion, EMG, and force data collection

Measured tasks comprised standard (unloaded) dynamic motions including abduction and forward flexion. The subjects were asked to perform the tasks up to maximal possible arm elevation (see Table 3.2, Chapter 3).

Measurements included the collection of motion data and EMG as well as *in-vivo* GH-JRF. For the detailed description about the motion and *in-vivo* GH-JRF recordings see section 3.2.4, Chapter 3.

EMG signals of 12 superficial muscles (Table 6.1) were measured using Ambu N-00-S ECG surface EMG electrodes and recorded by a 16-channels Porti system (TMS International, Enschede, The Netherlands) at the sampling frequency of 1000 Hz. The SENIAM recommendations (Merletti et al, 1999) were followed for the EMG sensor positioning. We visually checked the measured signals for possible crosstalk. To determine the maximum EMG values maximum voluntary contractions (MVCs) were also performed for each subject.

Table 6.1. Recorded EMG signals

Muscle	# recording sites	Muscle part
trapezius	3	1. ascending (TRPA) 2. transversal (TRPT) 3. descending (TRPD)
infraspinatus (INF)	1	-
deltoid	3	1. anterior (DA) 2. medial (DM) 3. posterior (DP)
pectoralis major	2	1. clavicular (PMC) 2. thoracic (PMT)
biceps	1	short head (BS)
triceps	1	medial (TRM)
brachioradialis (BRC)	1	-

6.2.3. Kinematic data analysis

For the detailed description about the kinematic data analysis see section 5.2.3, Chapter 5.

6.2.4. EMG normalization

For EMG normalization, numerous methods have been introduced and used (Burden, 2010). Nevertheless, there is no consensus about which method is most appropriate for this purpose (Hug, 2010).

Starting with EMG normalization in the current study, we used the maximum measured EMG during MVCs as the reference value. However, for some muscles (e.g. deltoid anterior and brachioradialis) the EMG measured during dynamic trials exceeded the maximum EMG obtained from MVCs. To overcome this problem, we decided to scale the maximum EMG obtained from MVCs. Various studies reported the EMGs from cycling (Hautier et al, 2000), swimming (Clarys et al, 1983), and baseball pitching (Jobe et al, 1984) up to, respectively, 126%, 160%, and 226% of the maximum EMGs from MVCs. By using a scaling factor of 1.25, as was also found by Hautier *et al* (2000), no EMG from dynamic trials exceeded the scaled maximum EMGs.

The measured EMGs were high-pass filtered, rectified, and subsequently low-pass filtered. For high pass filtering, second order Butterworth filter with cut-off frequency of 25 Hz was used. Shiavi *et al* (1998) showed that a cut-off frequency of 25 Hz was appropriate for the removal of low-frequency artifacts in gait. However, for one subject (S6), due to the low quality of the measured EMGs, we used a high cut-off frequency for high-pass filtering. Studies showed that using very high (~ 250 Hz) filtering frequency can remove up to about 95% of the raw EMG signal power (Brown et al, 2010). Using a cut-off frequency of 250 Hz was considerably effective to eliminate the noises and to produce smoother signals for this subject. After rectification, signals were recursively low-pass filtered to obtain a linear envelope. To this end, a cut-off frequency of 2 Hz was used. Olney and Winter (1985) showed for gait that the cut-off frequencies should not exceed 3 Hz. In a biomechanical study of the trunk muscles (Staudenmann et al, 2007), a cut-off frequency of 2 Hz was used. In a more recent study, Yoshida and Terao (2003) showed that for the hand muscles the most suitable cut-off frequency would be a value between 1.7 and 2.8 Hz.

For each muscle, the measured EMG was normalized with respect to the scaled maximum value found for that muscle.

6.2.5. The EMG-driven model

The original inverse-forward dynamics optimization (IFDO, Figure 2.1b, Chapter 2) versions of the Delft Shoulder and Elbow Model was modified in order to include the measured EMGs in the input (Figure 6.1).

In the developed model, a three-element (contractile, series elastic, and parallel elastic elements) Hill-type model (Winters and Stark, 1985) is used (see section 2.9, Chapter 2 for a detailed description).

In the IFDO model (Chapter 2), at each time-step (i) the calculated optimal muscle forces in the inverse optimization procedure are constrained by maximum ($F_{max,i}$) and minimum ($F_{min,i}$) permissible values of the muscle forces estimated by a forward muscle model with use of the muscle states of the previous time-step ($e_{i\text{-}2}$, $a_{i,\text{-}1}$, $L_{ce,i\text{-}1}$, Figure 2.1b, Chapter 2). At the same time-step (i), an inverse muscle model is used to estimate the neural inputs ($e_{i\text{-}1}$, a_i, $L_{ce,i}$) that will be used as the inputs to the forward muscle model in the next step (i+1).

The EMG-signal can physiologically be interpreted as action potentials arriving at the muscle membrane and is therefore analogous to the excitation (*e*). In the EMG-driven model, for the muscles with recorded EMG activity (path I, Figure 6.1) instead of the excitation (e_{i-2}) predicted by the inverse muscle model the normalized EMG ($0 \leq nEMG \leq 1$) is used as input to the forward muscle. Therefore, instead of using the calculated maximum and minimum forces ($F_{max,i}$, $F_{min,i}$) as constraints for inverse optimization, the muscle forces calculated by using the input EMG ($F_{emg,i}$) with a chosen tolerance of 5% error is used. The other muscle forces (path II, Figure 6.1) are calculated in the normal inverse optimization procedure. For the inverse optimization an energy-based cost function (Praagman et al, 2006) was used as the muscle load sharing criterion.

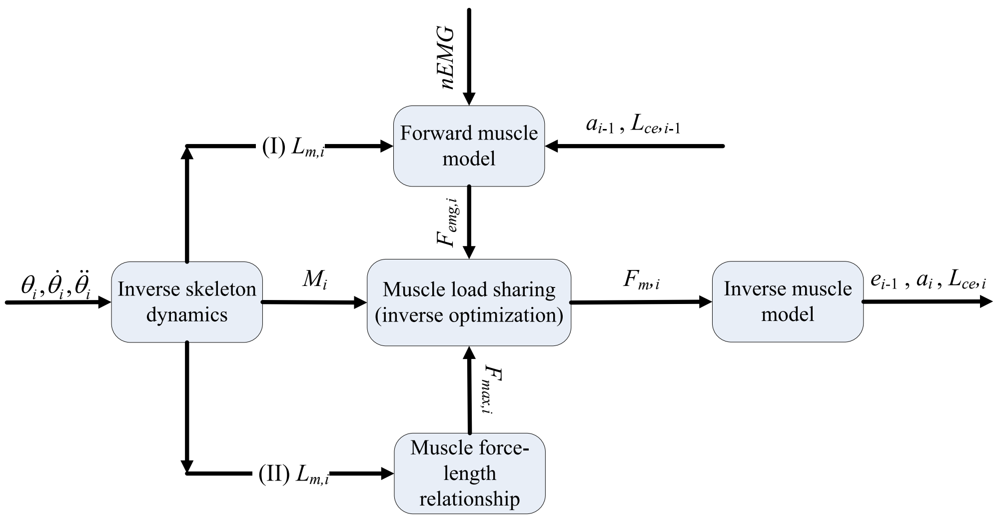

Figure 6.1. Schematic of the developed EMG-driven model

6.2.6. Mapping recorded EMGs to muscle elements in the model

To evaluate the developed EMG-driven model, the normalized recorded EMGs were used as inputs to the new developed model (Figure 6.1). Table 6.2 shows the process of mapping the recorded electrical activity to the different muscle elements in the EMG-driven model. For some muscles like trapezius and deltoid, the categorization of muscles in the DSEM is somewhat different from the measured ones. In the DSEM, the trapezius and deltoid muscles have been categorized based on their origins either on the scapula or clavicle (the scapular and clavicular parts, Table 6.2). However, the EMGs were recorded from the trapezius ascendens, pars transversum, and descendens parts (Table 6.1) and the deltoid anterior, medialis, and posterior parts (Table 6.1, Figure 6.2). In order to assign the measured EMGs from trapezius and deltoid muscles to the muscle elements in the model (Table 6.2), a geometrical distribution was applied in this study.

In the case of biceps brachii muscle, 75% of the recorded EMG from biceps short head was assigned to the biceps long head in the model (Table 6.2). The other measured EMGs were assigned to the similar muscles in the model (Table 6.2).

Table 6.2. Mapping the (normalized) recorded EMGs (Table 6.1) to the muscle elements in the EMG-driven shoulder model.

Muscle in the model	Element no.	% Normalized recorded EMG
Trapezius scapular part (TRPS)	1 to 6	100% TRPT
	7 to 8	50% TRPT + 50% TRPD
	9 to 11	100% TRPD
Trapezius clavicular part (TRPC)	1	100% TRPA
	2	75% TRPA + 25% TRPT
Deltoid scapular part (DS)	1 to 2	100% DP
	3 to 4	50% DP + 50% DM
	5 to 6	20% DP + 80% DM
	7 to 8	10% DP + 90% DM
	9	100% DM
	10	90%DM + 10% DA
	11	80% DM + 20% DA
Deltoid clavicular part (DC)	1 to 4	100% DA
Infraspinatus (INF)	1 to 6	100% INF
Pectoralis major clavicular part (PMC)	1 to 2	100% PMC
Pectoralis major thoracic part (PMT)	1 to 6	100% PMT
Biceps short head (B)	1 to 2	100% BS
Biceps long head (B)	1	75% BS
Triceps medialis (TRM)	1 to 5	100% TRM
Brachioradialis (BRC)	1 to 7	100% BRC

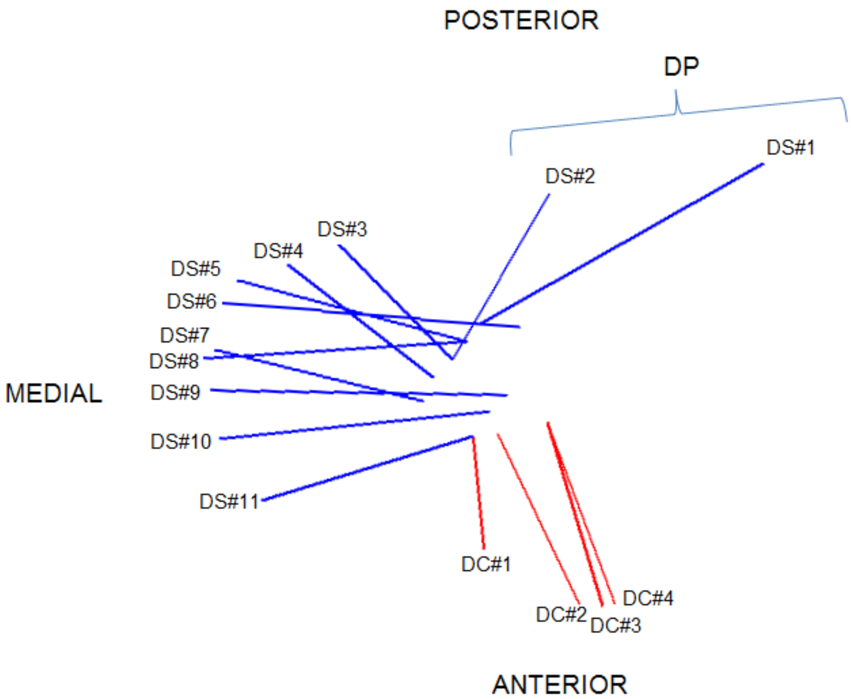

Figure 6.2. Top view of the (lines of action of) different elements of the deltoid muscle in the model. DS: deltoid scapular part, DC: deltoid clavicular part, DP: deltoid posterior part.

6.2.7. Model simulations

A schematic of the simulation procedure is depicted in Figure 6.3. For each muscle/muscle part in the 1st (left) column of Table 6.2, an ON/OFF situation for simulation was defined:

- ON for each muscle means that the input EMG for that muscle is used as input to the forward muscle model (i.e. Path I, Figure 6.1).
- OFF for each muscle means that the input EMG for that muscle is *not* used as input to the forward muscle model and, like non-measured muscles, the muscle force is calculated in the normal inverse optimization procedure (i.e. Path II, Figure 6.1).

At first (Step 1, Figure 6.3), the model simulation was carried out when input EMGs for all muscles were simultaneously used (i.e. all 10 signals in the 1st column of Table 6.2 were ON). However, the model crashed for this situation.

In the following step (Step 2, Figure 6.3), we tried to find out which muscle(s) caused the problem:

Firstly, we grouped the 10 signals in Table 6.2 into 7 groups (in order to reduce the number of simulations): TRP (S+C), D (S+C), PM (C+T), INF, B, TRM, and BRC.

It means that for example for deltoid (D) muscle, the scapular (DS) and clavicular (DC) parts should be simultaneously ON or OFF. For each subject and each motion, this led to 2^7 (=128) combinations of ON/OFF situations. The first round of model simulations showed that only those combinations of EMGs which included the EMG from TRP (either TRPS or TRPC) caused the model to fail. Therefore, subsequent simulations continued without using the EMG from trapezius (i.e. both TRPS and TRPC signals were switched OFF).

The remaining 8 signals in the 1st column of Table 6.2 (i.e. DS, DC, INF, PMC, PMT, B, TRM, and BRC) were used for the final round of simulations (Step 3, Figure 6.3). For each subject and motion, the model simulations were repeated when using either only one input EMG, all input EMGs together, or any combinations of different input EMGs (in total 2^8 =256 combinations of ON/OFF situations). For forward flexion motion, additional simulations were also carried out when using only the EMG of the DP muscle (Figure 6.2) as input to the model. Given the number of subjects (=3) and motions (=2), 1539 model simulations were, therefore, carried out.

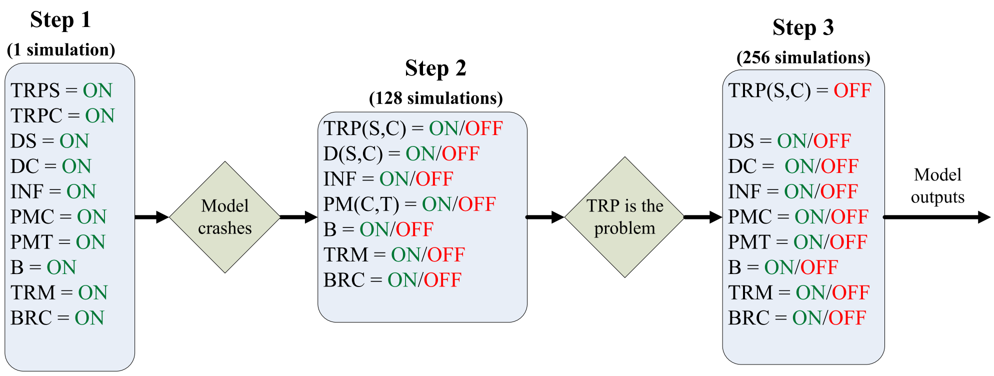

Figure 6.3. The modeling simulation procedure showing how different input EMGs were used at different stages. The number of simulations at each step is given for each subject and each measured shoulder motion. ON: the EMG signal is used as input to the forward muscle model; OFF: the EMG signal is not used as input to the forward muscle model.

6.2.8. Measure of goodness of fit

For all combinations of input EMGs, the model-predicted GH-JRF was calculated and compared to the *in-vivo* measured GH-JRF. To measure the goodness of fit four indicators were defined as follows:

1. The Root Mean Squared Error (RMSE) between the model-estimated and measured GH-JRF which indicates how well the model-estimated force pattern follows the measured force.

2. The average offset (AO) which is the average value of the differences between the estimated and measured GH-JRF at all points indicating how the magnitude of the estimated force differs from that of the measured force.
3. The force error at 90˚ humeral elevation angle (E_{90°) which is the difference between estimated and measured GH-JRF normalized by the measured GH-JRF and calculated at 90˚ humeral elevation.
4. The force error at the maximal humeral elevation angle ($E_{\alpha max}$) which is the difference between estimated and measured GH-JRF normalized by the measured GH-JRF and calculated at the maximal humeral elevation (α_{max}, Table 3.2, Chapter 3).

One should note that for AO, E_{90°, and $E_{\alpha max}$ (Figure 6.4), a minus value means underestimation of model with respect to the measured one while the positive value indicates an overestimation.

To find the most optimal combination of the input EMGs (the best solution), we defined a normalized error (nEr) for each set of simulation (*i*) considering all above mentioned indicators as follows:

$$\mathrm{nEr}_i = \frac{1}{2}\left\{\frac{1}{2}\frac{\mathrm{RMSE}_i}{\mathrm{RMSE}_{\mathrm{org}}} + \frac{1}{2}\left|\frac{\mathrm{AO}_i}{\mathrm{AO}_{\mathrm{org}}}\right|\right\} + \frac{1}{2}\left\{\frac{1}{2}\left|\frac{\mathrm{E}_{90^\circ,i}}{\mathrm{E}_{90^\circ,\mathrm{org}}}\right| + \frac{1}{2}\left|\frac{\mathrm{E}_{\alpha\max,\mathrm{i}}}{\mathrm{E}_{\alpha\max,\mathrm{org}}}\right|\right\} \tag{1}$$

Where the subscript ‘org’ for each indicator refers to the values found for that indicator when running the original model (with no EMG in the input). The normalized error (nEr, Table 6.3) will therefore be equal to 1 for the simulations with original model. For each subject and motion, the combination of simultaneously used input EMG signals which resulted to the minimum value for nEr among all simulations for that subject and motion was selected as the ‘best solution’ (Table 6.3).

6.2.9. Statistical analysis

To evaluate the significance of the effects of using the EMG as input on the modeling outputs a two-tailed paired *t*-Test was carried out. The force error at maximal elevation angle ($E_{\alpha max}$) between the EMG-driven model using the best solution and the original model were compared. The threshold (alpha-level) for statistical significance was considered as 0.05.

Table 6.3. The calculated normalized error (nEr) between the in-*vivo* measured GH-JRF and the one predicted by both the original model (no EMG in the input) and the EMG-driven model using the activity of individual muscles as well as the activities of the most optimal combination of simultaneously used muscles (the 'Best solution') as model inputs. (Abd: abduction; FF: forward flexion. For muscle names see Tables 6.1 and 6.2)

Motion task	Subject	no EMG (original model)	only DC as input	only DS as input	only DP as input	only INF as input	only PMT as input	only PMC as input	only B as input	only TRM as input	only BRC as input	'Best solution' as input	Muscles incorporating in the Best solution
Abd	S1	1.00	0.98	1.10	-	0.98	0.45	1.15	1.17	0.98	1.01	0.40	PMT+TRM
	S2	1.00	1.23	9.44	-	0.89	0.79	1.30	1.02	1.48	1.01	0.75	PMT+TRM
	S6	1.00	0.95	1.41	-	0.85	0.17	0.93	1.01	0.97	1.00	0.15	PMT+TRM
	mean	1.00	1.05	3.99	-	0.91	0.47	1.13	1.07	1.14	1.01	0.45	-
	(SD)	(0.00)	(0.16)	(4.73)	-	(0.07)	(0.31)	(0.18)	(0.09)	(0.29)	(0.01)	(0.32)	-
FF	S1	1.00	0.93	0.26	0.60	0.91	1.13	0.91	0.95	0.96	0.95	0.18	DS+DC+PMC+BRC
	S2	1.00	1.00	1.20	0.41	0.84	0.96	0.92	0.84	0.84	1.00	0.37	DC+PMC+B+BRC
	S6	1.00	1.00	0.43	0.55	0.97	0.35	0.75	1.03	0.98	0.99	0.21	DS+DC+PMC+BRC
	mean	1.00	0.98	0.63	0.52	0.91	0.81	0.86	0.94	0.93	0.98	0.26	-
	(SD)	(0.00)	(0.04)	(0.50)	(0.10)	(0.07)	(0.41)	(0.10)	(0.09)	(0.07)	(0.03)	(0.10)	-

6.3. Results

Representing the results of all modeling simulations (using all possible combinations of input EMGs) was not feasible; therefore, a selected number of results are shown here. In Table 6.3 and Figures 6.5-6.7 the effect of using the best solution as well as the activity of individual muscles as the inputs to the EMG-driven model on the modeling outcome were represented.

During abduction, the use of the input EMG of the PMT together with TRM led to the closest match between the model-estimated and the measured GH-JRF for three subjects (Table 6.3, Figures 6.4, 6.5a, 6.6.a, and 6.7a). The results, however, showed that using only the input EMG of the PMT muscle led to a very small increase (on average across three subjects ~ 3%) in the model underestimation of the GH-JRF when compared with the model driven by the best solution (i.e. PMT + TRM). Using only the input EMG of the DS muscle for abduction, caused a huge difference (on average across three subjects ~ 200%) between the model and the experiment, especially for subjects S2 and S6.

In case of forward flexion (FF, Figures 6.4, 6.5b. 6.6b, and 6.7b), the best solutions for subjects S1 and S6 (i.e. DS+ DC+PMC+BRC, Table 6.3) were comparable but a different optimal combination of input EMGs (i.e. DC+ PMC+ BRC, Table 6.3) was found for subject S2. Although using only the input EMG of the DS muscle led to considerable model overestimation for subjects S2 (Table 6.3, Figures 6.4 and 6.6b), however, it improved model predictions by more than 50% for subjects S1 and S6 (Table 6.3, Figures 6.4, 6.5b, and 6.7b). Adding only the EMG from DP as input to the model for flexion improved both the pattern above 90º arm elevation and the magnitude of model-predicted GH-JRF at the maximum arm elevation (on average across three subjects up to about 33%). Using the input EMG of the PMT muscle during forward flexion motion helped to some extent filling the gap between the model prediction and the experimental data (Table 6.3) but this failed in correcting the descending pattern of the predicted GH-JRF for above 90º arm elevation.

By using the optimal combination of measured EMGs (i.e. the best solution) as input to the EMG-driven model, the model predicted GH-JRF at maximal arm elevation significantly (two-tailed $p \sim 0.002$) improved (on average up to about 45%) in comparison to the original model (see Figures 5-7). Also, the pattern of the predicted GH-JRF for above 80-90˚ arm elevation got closer to what was *in-vivo* measured (Figures 6.5b, 6.6, and 6.7). The magnitude of the model predicted GH-JRF increased overall, meaning that the general model underestimation at higher (> 60˚-70˚) arm elevation angles decreased but caused model overestimation at lower (< 60˚-70˚) elevation angles.

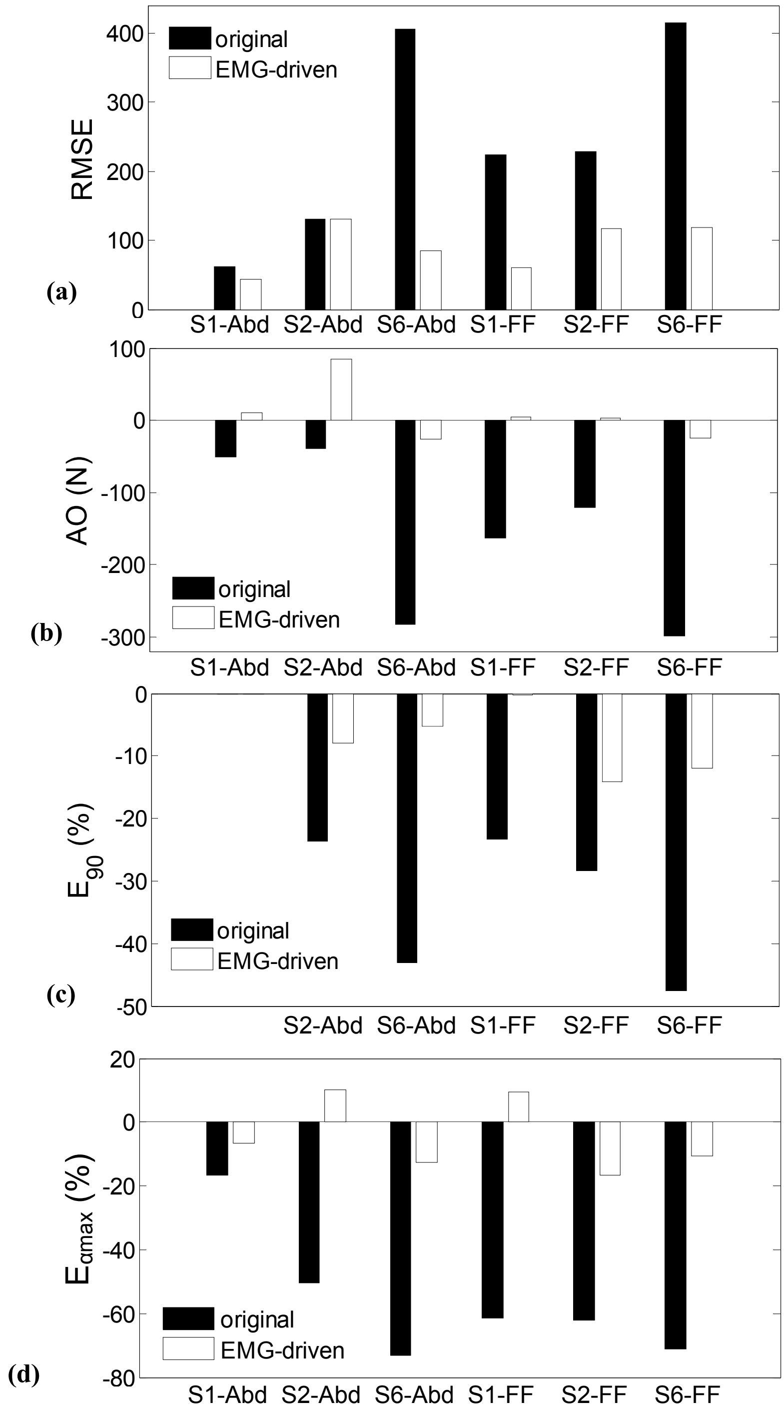

Figure 6.4. (a) RMSE, (b) AO, (c) $E_{90^{\circ}}$, and (d) $E_{\alpha max}$, between the GH-JRF estimated by the original and EMG-driven (using the best solution) models and the measured one.

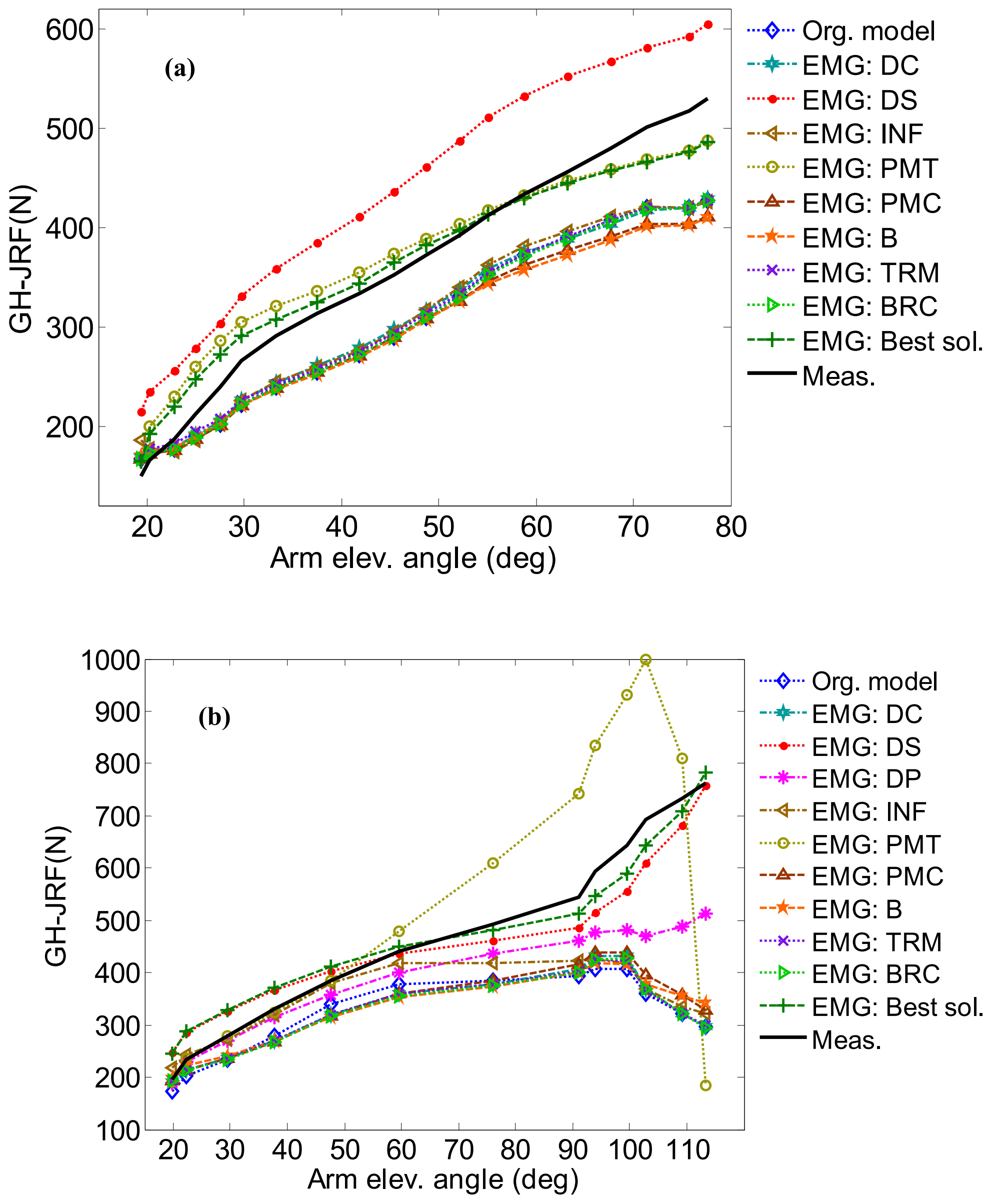

Figure 6.5. Comparison of measured and estimated GH-JRF for S1 during (a) abduction and (b) forward flexion. *In-vivo* measured (Meas.), original model-estimated (Org. model), and EMG-driven model-estimated GH-JRF using the EMG of individual muscles as well as the activities of the most optimal combination of simultaneously used muscles (Best sol.) as model inputs

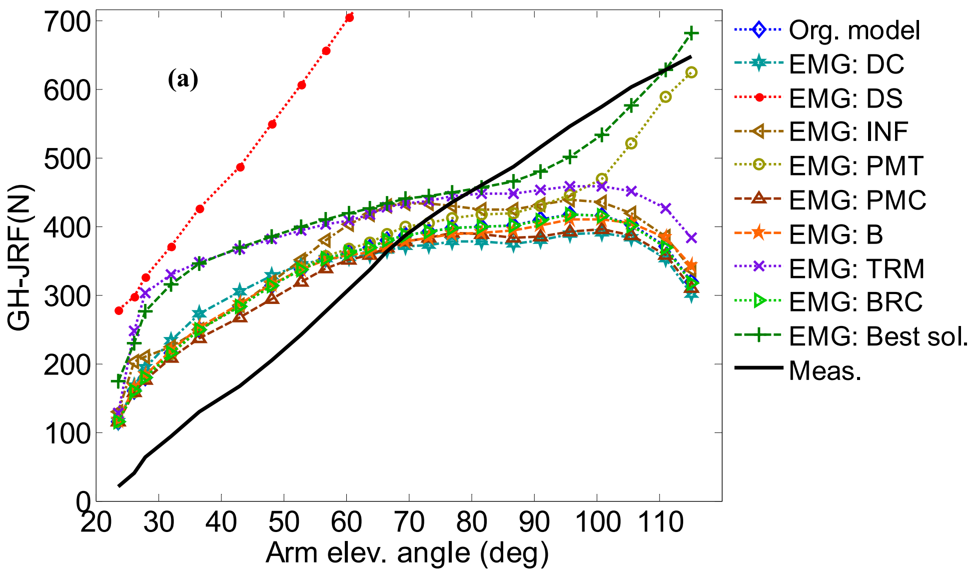

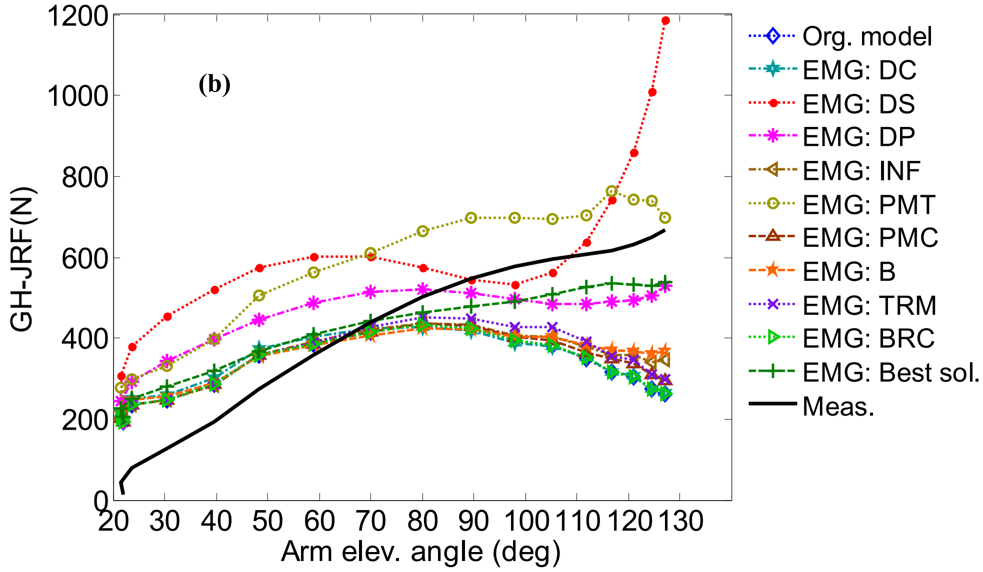

Figure 6.6. Comparison of measured and estimated GH-JRF for S2 during (a) abduction and (b) forward flexion. *In-vivo* measured (Meas.), original model-estimated (Org. model), and EMG-driven model-estimated GH-JRF using the EMG of individual muscles as well as the activities of the most optimal combination of simultaneously used muscles (Best sol.) as model inputs

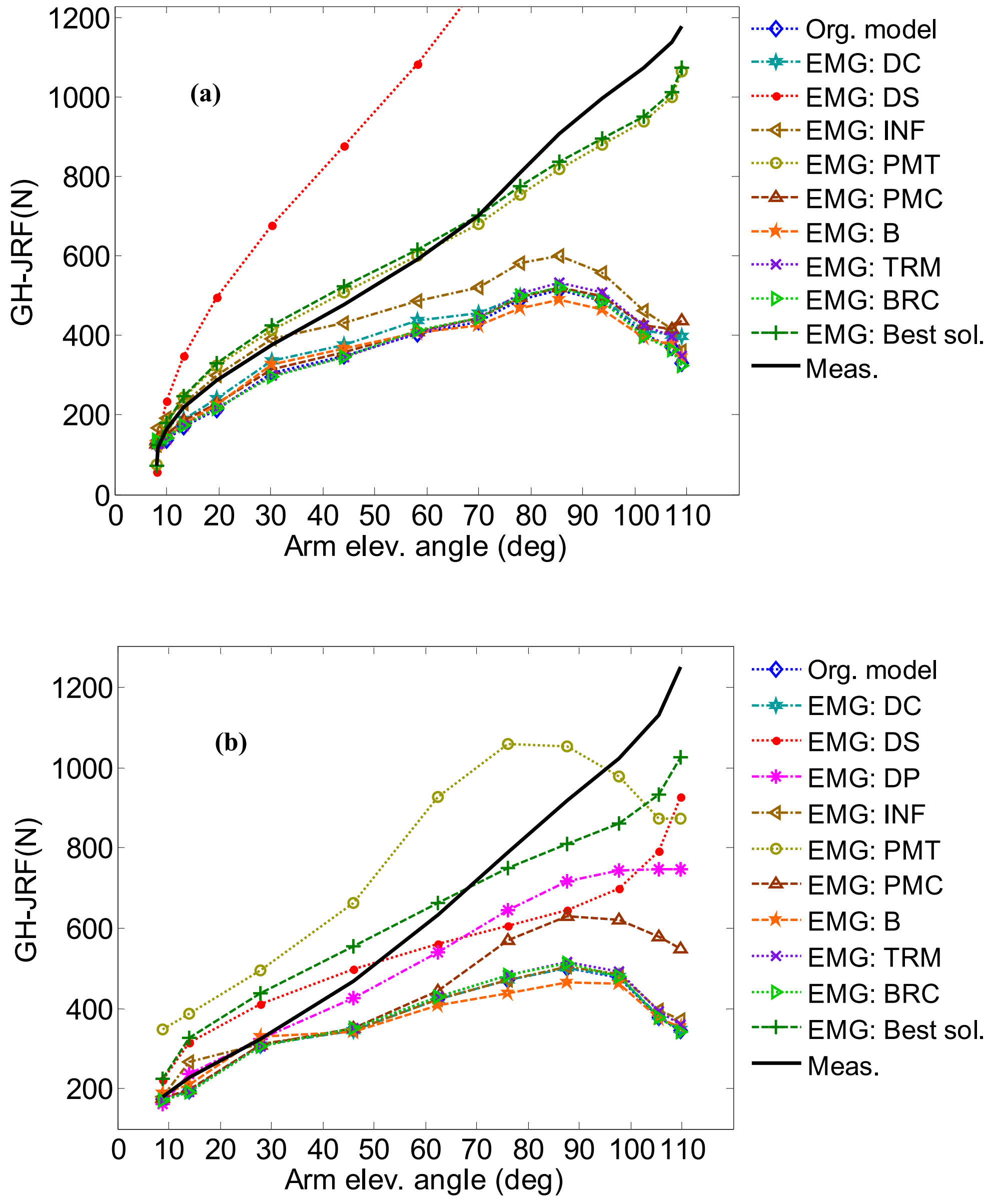

Figure 6.7. Comparison of measured and estimated GH-JRF for S6 during (a) abduction and (b) forward flexion. *In-vivo* measured (Meas.), original model-estimated (Org. model), and EMG-driven model-estimated GH-JRF using the EMG of individual muscles as well as the activities of the most optimal combination of simultaneously used muscles (Best sol.) as model inputs

6.4. Discussion

The predictions of the GH-JRF using an EMG-driven model of the shoulder were compared to those simultaneously measured on the patients with instrumented shoulder arthroplasty. Both types of inconsistencies between the original version of DSEM and the measurements, namely a general force underestimation and a force drop above 90° humeral elevation, seem to be related to antagonist co-contraction. That is because inclusion of EMGs in the model input could considerably improve both the magnitude (on average up to 45% at maximum arm elevation) and the pattern (for above 90° arm elevation) of the model-predicted GH-JRFs.

If only one measured EMG should be used as input to the EMG-driven model to account for the antagonist muscle co-contraction, our recommendations will be as follows:

For abduction motion, it is obvious from the results (Table 6.3, Figures 6.4, 6.5a, 6.6a, and 6.7a) that using only the input EMG of the PMT muscle caused a negligible difference compared with when simultaneously using the input EMG of the PMT and TRM muscles (i.e. the best solution). The PMT is generally known as an adductor and hence is an antagonist muscle during abduction motion. The original model predicts a low activation for PMT which is in contrast to what was observed in the EMG measurements (Figure 6.8a). Adding only the EMG from PMT as model input during abduction motion improved the model-predicted GH-JRF at maximum arm elevation on average up to about 37%. This means that the primary source of inconsistencies between the original model and the experiment is the antagonist PMT muscle co-contraction which was not considered in the original model. We, therefore, recommend using the input EMG from PMT muscle for abduction motion.

For forward flexion motion, as one can see in Table 6.3 and Figures 6.5b and 6.7b, for subjects S1 and S6 the difference between the best solution and using only the EMG of the DS muscle in the input is relatively small (on average e between two subjects ~ 4% as for the GH-JRF at maximal arm elevation). For these two subjects the differences between the model and experiment during forward flexion motion may be explained through the antagonist DS muscle co-contraction which was not considered in the original model (Figure 6.8b). However, using only the EMG of the DS muscle in the input for subject S2 caused an overestimation of the GH-JRF at maximal arm elevation of about 73%. For this subject (S2) the result of the best solution and using only the input EMG from DP (the posterior part of the DS muscle, Figure 6.2) were very close at higher (> 90º) arm elevation angles (Figure 6.6b). For subjects S1 and S6, using only the EMG from DP as input to the model improved both the pattern for above 90º arm elevation and the magnitude of model-predicted GH-JRF at the maximum arm elevation (on average between two subjects ~ 30%). These findings make it difficult to choose between using only the measured EMG of the DS (both the posterior and medial parts of the deltoid) or DP (only the posterior part of the deltoid) as the input to the EMG-driven model. Since, using the EMG from DS muscle led to considerable difference between the model and experiment for subject S2, we may recommend DP to be used during forward flexion motion.

Summarizing the last two paragraphs, if one wants to use only one input EMG to the model to account for possible antagonist co-contraction we recommend the PMT and DP muscles for abduction and forward flexion motions, respectively. Nevertheless, to be more decisive the effects of other antagonist muscles should be evaluated, specifically the rotator cuff muscles since they are the main stabilizers of the glenohumeral joint. In this study we could measure the infraspinatus muscle using the surface electrodes. In overall, adding the input EMG of the infraspinatus led to slight improvement (on average ~ 9%) in the magnitude of the model-predicted resultant GH-JRF (when compared with the in-*vivo* measured forces) during both abduction and forward flexion motions while did not have any effect on the pattern of the predicted forces for above 90º elevation. Regarding the other muscles in the rotator cuff, measuring the supraspinatus and subscapularis activity is not possible with surface EMG. To measure these two muscles, wire electrodes should be used (Meskers et al, 2004). The downside of using wire electrodes is however, that the EMG activity can only be recorded for a small range of motion. The teres minor is also very difficult to be measure even through wire electrodes. One should also take our recommendations with caution when applying them to young healthy subjects. Although for our patients no serious rotator cuff damage was reported, however, they are likely to have pathological motor control as can be concluded from their, sometimes strongly, limited elevation capacity.

A tolerance of 5% for the muscle forces calculated in the forward muscle model by using the normalized EMG as input was used in this study (see section 6.2.5). This threshold could be used in the input EMG signals to account for possible errors in calculating the normalized EMG. However, to prevent the problems caused in satisfying the joint equilibrium and considering the linear EMG-to-force relationship used in this study, we preferred to use this tolerance on the forces predicted by the forward muscle model. That tolerance was arbitrarily chosen, however, it seems to be an appropriate selection. Reducing the tolerance should make the model predict closer muscle activations to those experimentally measured although problems can be met in satisfying the equilibrium at the joints and, on the other hand, increasing it the model can predict lower co-contractions moving the results closer to those of a traditional optimization. We tried to quantify the effect of using different tolerances on the modeling results for a specific case: subject S6 during performing abduction motion and using only the activity for PMT as input to the model. We chose the tolerances of 1%, 5%, 10%, and 20% and compared the model-predicted GH-JRFs at maximal arm elevation angle. Results showed that the magnitude of the model-predicted resultant GH-JRF decreased (as expected) by about 3%, 7%, and 16% when changing the tolerance from 1% to, respectively, 5%, 10%, and 20%. Although changing the tolerance influenced the model-predictions, however, these changes were not considerable (~ 7%) in the range of 1% to 10% tolerance. This means that our choice for using a 5% tolerance was reasonably acceptable.

The developed model in this study was driven using the measured EMG signals from a selected number of superficial muscles. Using the measured activation as model input could potentially affect the activation pattern of non-driven (either not measured or not used) muscles. Considering that a large number of combinations of measured activities, ranging from single activity to all activities together, were used for modeling simulation, it would be hardly possible to quantify the changes in the activation pattern of the not-driven muscles for all modeling simulations. However, since in this study the model prediction of the GH-JRF was of major interest (and consequently the *in-vivo* measured GH-JRF was chosen as our 'golden standard' for validation of the modeling predictions), errors appearing in the model-predicted GH-JRF could be an indication of considerable alteration in the activation pattern of non-driven muscles surrounding the glenohumeral joint. That could be the case for trapezius muscle. As explained before, the model crashed when using any combination of input EMG signals which included the activity from trapezius muscle. This may be explained by considerably increasing the activity of the other muscles (e.g. deltoid) when including the EMG from trapezius muscle in the model input.

Although including the EMG as model inputs considerably improved the model predictions, one should note that using surface EMG is not the only model tuning option:

The morphological difference between the model and measured subjects seems to be a potential source of the inconsistency between the model and experiments, specially the general GH-JRF underestimation. The variability in the bony and muscular anatomy may change a lot of modeling parameters such as shape of bony contours, PCSA, and moment arms. Therefore, a full-scaling of the model including the size, mass, and strength scaling may have considerable effects on the modeling results.

Another potential source of discrepancies between the model and measurements could be the joint friction in patients. In addition to the joint reaction forces, the instrumented shoulder endoprosthesis is also able to measure the frictional moments in the glenohumeral joint. The measurements showed that these frictional moments were substantial with up to 7 Nm (Westerhoff et al, 2009; Westerhoff et al, 2008). Comparing to the net joint moments given in the literature (Giroux and Lamontagne, 1992; Hoozemans et al, 2004; Veeger et al, 2002), one can see that the frictional moment may reach 20% of the total net shoulder joint moment. Therefore, implementation of these frictional moments into the model may have notable effects (see Chapter 8).

Another potential factor affecting the modeling output is related to the optimization cost function. In Chapter 5 we used two inverse optimization cost functions including an energy-based (the one used in this study) and a quadratic stress cost function. The results of that study showed that the GH-JRF predicted by the original model by using the two cost functions were not identical (differences reached 10% of the peak GH-JRF). The major promising feature of the energy-based cost function is the adjustability of the tuning weight factors of the cost function which were hypothetically determined by Praagman (Praagman, 2008). It is, however, uncertain whether these factors are correct or still need optimization. Using alternative weight factors will certainly influence the model-estimated GH-JRF (see Chapter 7).

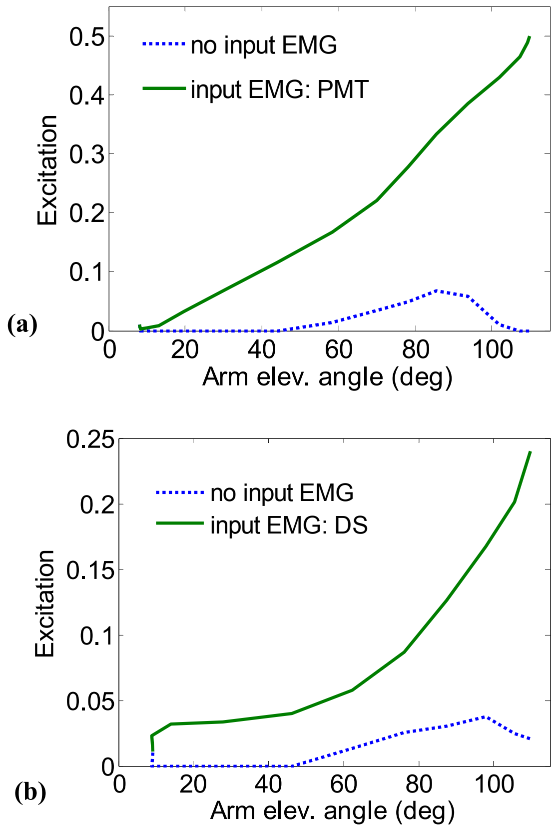

Figure 6.8. The model calculated neural excitation during (a) abduction and (b) forward flexion for S6.

As mentioned before, there is still no consensus about the best EMG normalization method (Burden, 2010; Perry, 1992). The European recommendations for surface EMG (the SENIAM project) (Merletti et al, 1999) suggests use of EMG from MVCs as the normalization reference. However, as observed in the current study, some researchers reported that using the MVC as reference may result in normalized EMGs exceeding 100% (Clarys et al, 1983; Hautier et al, 2000; Jobe et al, 1984). Clarys (2000) believed that the EMGs from MVCs are not appropriate for normalizing EMGs from dynamic tasks. Using the MVCs for normalization has also received criticism regarding its reliability (Yang and Winter, 1984). In the current study, we used a scaling factor in the range of scaling factors reported in the literature to keep the normalized EMGs from dynamic tasks below 100%. As a recommendation for the future, it would be interesting to quantify the effects of different normalization routines on the EMG-driven model outputs.

By comparing the developed model in the current study to the other existing EMG-driven models some differences may be discerned:

The detailed EMG-driven models developed for the lower extremity (Buchanan et al, 2004; Lloyd and Besier, 2003) included the EMGs of almost all muscles passing the joint and a fixed relationship between measured muscles and those that could not be measured. However, among the 31 muscles available in the DSEM, the EMG of only 12 muscles could be measured. It can be therefore said that our model, in contrast to those models, is ‘partially’ (but not fully) driven by the EMGs.

The second major difference, as mentioned before, is related to the reference for model validation. The vast majority of existing EMG-driven models including the ones developed for the shoulder (Langenderfer et al, 2005; Laursen et al, 1998) have been validated by using the measured external joint moment as the reference. The model developed here was validated at the level of summed muscle forces around the glenohumeral joint which were measured *in-vivo*. The force drop above 90° elevations as was observed for original model predictions in the current and previous studies (Terrier et al, 2008) is based on the fact that the moment arms of the muscles passing the glenohumeral joint start to decrease after 90° (Ackland et al, 2008). However, EMG measurements on both healthy (Inman et al, 1944) and patients (the current study) showed that the neural activity increases above 90°. Similar to EMG signals, the measured GH-JRFs also showed an incremental pattern after 90°. Increasing the muscular activity would be an indication of extra effort needed for stabilizing the shoulder joint which behaves like an inverted pendulum above 90°.

6.5. Conclusions

An EMG-driven model of the shoulder was developed and validated against *in-vivo* measured GH-JRF on three patients with an instrumented shoulder arthroplasty.

Following conclusions can be drawn from this study:

- In contrast to the original model, this model could successfully account for the muscle co-contractions occurring during standard dynamic tasks at higher arm elevations.
- The EMG-driven model can be used as a more reliable platform for prediction of the loads on the shoulder joint especially in clinical applications.
- As a recommendation for the future, the effects of different normalization routines on the EMG-driven model outputs can be quantified.

6.6. References

Ackland, D.C., Pak, P., Richardson, M., Pandy, M.G., 2008. Moment arms of the muscles crossing the anatomical shoulder. Journal of Anatomy 213 (4), 383-390.

Brown, S.H., Brookham, R.L., Dickerson, C.R., 2010. High-pass filtering surface EMG in an attempt to better represent the signals detected at the intramuscular level. Muscle & Nerve 41 (2), 234-239.

Buchanan, T.S., Lloyd, D.G., Manal, K.T., Besier, T.F., 2004. Neuromusculoskeletal modeling: estimation of muscle forces and joint moments and movements from measurements of neural command. Journal of Applied Biomechanics 20 (4), 367-395.

Buchanan, T.S., Lloyd, D.G., Manal, K.T., Besier, T.F., 2005. Estimation of muscle forces and joint moments using a forward-inverse dynamics model. Medicine and Science in Sports and Exercise 37 (11), 1911–1916.

Buchanan, T.S., Moniz, M.J., Dewald, J.P.A., Rymer, W.Z., 1993. Estimation of muscle forces about the wrist joint during isometric tasks using an EMG coefficient method. Journal of Biomechanics 26 (4-5), 547-560.

Burden, A., 2010. How should we normalize electromyograms obtained from healthy participants? What we have learned from over 25years of research. Journal of Electromyography and Kinesiology 20 (6), 1023-1035.

Cholewicki, J., McGill, S.M., Norman, R.W., 1995. Comparison of muscle forces and joint load from an optimization and EMG assisted lumbar spine model: Towards development of a hybrid approach. Journal of Biomechanics 28 (3), 321-331.

Clarys, J.P., 2000. Electromyography in sports and occupational settings: an update of its limits and possibilities. Ergonomics 43 (10), 1750-1762.

Clarys, J.P., Massez, C., van der Broeck, M., Piette, G., Robeaux, R., "Total telemetric surface of the front crawl," in *Biomechanics VIII-B. International Series on Biomechanics*, vol. 4B, H. Matsui and K. Kobayashi, Eds. Champaign, 1983, pp. 951-958.

Favre, P., Sheikh, R., Fucentese, S.F., Jacob, H.A.C., 2005. An algorithm for estimation of shoulder muscle forces for clinical use. Clinical Biomechanics 20 (8), 822-833.

Favre, P., Snedeker, J.G., Gerber, C., 2009. Numerical modelling of the shoulder for clinical applications. Philisophical Transactions of the Royal Society 367, 2095-2118.

Gagnon, D., Larivière, C., Loisel, P., 2001. Comparative ability of EMG, optimization, and hybrid modelling approaches to predict trunk muscle forces and lumbar spine loading during dynamic sagittal plane lifting. Clinical Biomechanics 16 (5), 359-372.

Gerus, P., Rao, G., Buchanan, T.S., Berton, E., 2010. A Clinically Applicable Model to Estimate the Opposing Muscle Groups Contributions to Isometric and Dynamic Tasks. Annals of Biomedical Engineering 38 (7).

Giroux, B., Lamontagne, M., 1992. Net shoulder joint moment and muscular activity during light weight-handling at different displacements and frequencies. Ergonomics 35 (4), 385-403.

Hautier, C.A., Arsac, L.M., Deghdegh, K., Souquet, J., Belli, A., Lacour, J.R., 2000. Influence of fatigue on EMG/force ratio and cocontraction in cycling. Medicine and Science in Sports and Exercise 32 (4), 839-843.

Hoozemans, M.J.M., Kuijer, P.P.F.M., Kingma, I., Van DieÃ«n, J.H., De Vries, W.H.K., Van Der Woude, L.H.V., Veeger, D.J.H.E.J., Van Der Beek, A.J., Frings-Dresen, M.H.W., 2004. Mechanical loading of the low back and shoulders during pushing and pulling activities. Ergonomics 47 (1), 1-18.

Hug, F., 2010. Can muscle coordination be precisely studied by surface electromyography? Journal of Electromyography and Kinesiology 21 (1), 1-12.

Inman, V.T., Saunders, J.B.D., Abbott, L.C., 1944. Observations on the function of the shoulder joint. Journal of Bone and Joint Surgery 26, 1-30.

Jinha, A., Ait-Haddou, R., Herzog, W., 2006. Predictions of co-contraction depend critically on degrees-of-freedom in the musculoskeletal model. Journal of Biomechanics 39 (6), 1145-1152.

Jobe, F.W., Moynes, D.R., Tibone, J.E., Perry, J., 1984. An EMG analysis of the shoulder in pitching: a second report. American Journal of Sports Medicine 12 (3), 218-220.

Jost, B., Pfirrmann, C.W.A., Gerber, C., 2000. Clinical outcome after structural failure of rotator cuff repairs. Journal of Bone and Joint Surgery-American Volume 82A (3), 304-314.

Koo, T.K.K., Mak, A.F.T., 2005. Feasibility of using EMG driven neuromusculoskeletal model for prediction of dynamic movement of the elbow. Journal of Electromyography and Kinesiology 15 (1), 12-26.

Langenderfer, J., LaScalza, S., Mell, A., Carpenter, J.E., Kuhn, J.E., Hughes, R.E., 2005. An EMG-driven model of the upper extremity and estimation of long head biceps force. Computers in Biology and Medicine 35 (1), 25-39.

Laursen, B., Jensen, B.R., Nemeth, G., Sjogaard, G., 1998. A model predicting individual shoulder muscle forces based on relationship between electromyographic and 3D external forces in static position. Journal of Biomechanics 31 (8), 731-739.

Lloyd, D.G., Besier, T.F., 2003. An EMG-driven musculoskeletal model to estimate muscle forces and knee joint moments in vivo. Journal of Biomechanics 36 (6), 765-776.

Manal, K., Gonzalez, R.V., Lloyd, D.G., Buchanan, T.S., 2002. A real-time EMG-driven virtual arm. Computers in Biology and Medicine 32 (1), 25-36.

McGill, S.M., 1992. A myoelectrically based dynamic three-dimensional model to predict loads on lumbar spine tissues during lateral bending. Journal of Biomechanics 25 (4), 395-414.

Merletti, R., Wallinga, W., Hermens, H., Freriks, B., *Guidelines for reporting SEMG data*: Roessingh Research and Development, 1999.

Meskers, C.G.M., de Groot, J.H., Arwert, H.J., Rozendaal, L.A., Rozing, P.M., 2004. Reliability of force direction dependent EMG parameters of shoulder muscles for clinical measurements. Clinical Biomechanics 19 (9), 913-920.

Nikooyan, A.A., Veeger, H.E.J., Westerhoff, P., Graichen, F., Bergmann, G., van der Helm, F.C.T., 2010. Validation of the Delft Shoulder and Elbow Model using in-vivo glenohumeral joint contact forces. Journal of Biomechanics 43 (15), 3007–3014.

Olney, S.J., Winter, D.A., 1985. Predictions of knee and ankle moments of force in walking from EMG and kinematic data. Journal of Biomechanics 18 (1), 9-20.

Olney, S.J., Winter, D.A., 1985. Selecting representative muscles for EMG analysis of gait: A methodology. Physiotherapy Canada 37 (4), 208-217.

Perry, J., *Gait analysis: normal and pathological function*. Thorofare, NJ: SLACK Inc., 1992.

Praagman, M., 2008. Muscle load sharing: An energy-based approach. PhD Thesis, Free University, Amsterdam.

Praagman, M., Chadwick, E.K.J., van der Helm, F.C.T., Veeger, H.E.J., 2006. The relationship between two different mechanical cost functions and muscle oxygen consumption. Journal of Biomechanics 39 (4), 758-765.

Praagman, M., Stokdijk, M., Veeger, H.E.J., Visser, B., 2000. Predicting mechanical load of the glenohumeral joint, using net joint moments. Clinical Biomechanics 15 (5), 315-321.

Shiavi, R., Frigo, C., Pedotti, A., 1998. Electromyographic signals during gait: Criteria for envelope filtering and number of strides. Medical and Biological Engineering and Computing 36 (2), 171-178.

Staudenmann, D., Potvin, J.R., Kingma, I., Stegeman, D.F., van Dieën, J.H., 2007. Effects of EMG processing on biomechanical models of muscle joint systems: Sensitivity of trunk muscle moments, spinal forces, and stability. Journal of Biomechanics 40 (4), 900-909.

Steenbrink, F., de Groot, J.H., Veeger, H.E.J., van der Helm, F.C.T., Rozing, P.M., 2009. Glenohumeral stability in simulated rotator cuff tears. Journal of Biomechanics 42 (11), 1740-1745.

Terrier, A., Vogel, A., Capezzali, M., Farron, A., 2008. An algorithm to allow humerus translation in the indeterminate problem of shoulder abduction. Medical Engineering & Physics 30, 710–716.

van Dieen, J.H., Kingma, I., 2005. Effects of antagonistic co-contraction on differences between electromyography based and optimization based estimates of spinal forces. Ergonomics 48 (4), 411-26.

Veeger, H.E.J., Rozendaal, L.A., van der Helm, F.C.T., 2002. Load on the shoulder in low intensity wheelchair propulsion. Clinical Biomechanics 17 (3), 211-218.

Westerhoff, Graichen, F., Bender, A., Rohlmann, A., Bergmann, G., 2009. An instrumented implant for in vivo measurement of contact forces and contact moments in the shoulder joint. Medical Engineering & Physics 31 (2), 207-213.

Westerhoff, P., Graichen, F., Bender, A., Halder, A., Beier, A., Rohlmann, A., Bergmann, G., 2009. In vivo measurement of shoulder joint loads during activities of daily living. Journal of Biomechanics 42, 1840–1849.

Westerhoff, P., Rohlmann, A., Bender, A., Graichen, F., Bergmann, G., 2008. In vivo shoulder joint forces at isolated motions. Journal of Biomechanics 41 (Supplement 1), S144-S144.

Winters, J.M., Stark, L., 1985. Analysis of fundamental human movement patterns through the use of in-depth antagonistic muscle models. IEEE Transactions on Biomedical Engineering 32, 826-839.

Yang, J.F., Winter, D.A., 1984. Electromyographic amplitude normalization methods: Improving their sensitivity as diagnostic tools in gait analysis. Archives of Physical Medicine and Rehabilitation 65 (9), 517-521.

Yoshida, M., Terao, M., "Suitable cutoff frequency of low-pass filter for estimating muscle by surface electromyogram," in *Engineering in Medicine and Biology Society, 2003. Proceedings of the 25th Annual International Conference of the IEEE*, vol. 2, 2003, pp. 1709-1711 Vol.2.

Chapter 7

Relative contribution of energy consumption processes in a load sharing cost function

The aim of this chapter is to quantify the relative contributions of two muscle energy consumption processes (detachment of cross-bridges and calcium-pumping) incorporated in a previously developed muscle load sharing cost function, namely the energy-based criterion, by using *in-vivo* measured glenohumeral-joint reaction forces (GH-JRF). Motion data and *in-vivo* GH-JRF were recorded for four patients carrying an instrumented shoulder implant while they were performing abduction and forward flexion motions up to their maximum possible arm elevations. Motion data were used as input to the Delft Shoulder and Elbow Model for estimation of the GH-JRF. The widely used stress as well as the energy-based cost functions were adopted as the load sharing criteria. For the energy-based criterion, simulations were run for a wide range of different weight parameters (determining the relative contribution of the two energy processes) in the neighborhood of the previously assumed parameters for each subject and motion. Model-predicted and *in-vivo* measured GH-JRFs were compared for all model simulations. Application of the energy-based criterion with new identified parameters resulted in significant (two-tailed $p < 0.05$, post-hoc power ~ 0.3) improvement (on average ~ 20%) of the model-predicted GH-JRF at the maximal arm elevation compared to when using either the stress or the pre-assumed form of the energy-based criterion. About 25% of the total energy consumption was calculated for the calcium-pumping process at maximal muscle activation level when using the new parameters. This value was comparable to the corresponding ones reported in the previous literature. The identified parameters are, therefore, recommended to be used instead of their predecessors.

List of abbreviations

SCF	The Stress Cost Function
ECF	The Energy-based Cost Function
DSEM	The Delft Shoulder and Elbow Model
GH-JRF	The Glenohumeral-Joint Reaction Force
RMSE	The Root Mean Squared Error
α_{max}	The maximal arm elevation angle
$E_{\alpha max}$	The normalized error at the α_{max}
E_{cb}/E_{ca}	The relative contribution of the two energy terms in the ECF
F/F_{max}	The muscle force ratio
wf_1	The first weight factor of the energy-based cost function
wf_2	The second weight factor of the energy-based cost function
ECF_{def}	The default from of the energy-based cost function
$ECF_{x,y}$	The energy cost function with $wf_1 =$ x, and $wf_2 =$ y.
Abd	Abduction motion
FF	Forward Flexion motion

7.1. Introduction

Inverse-dynamics musculoskeletal modeling faces an indeterminacy problem for calculation of individual muscle forces. More than one combination of muscle forces may produce the same given net moment around a joint. It is not yet understood how the central nervous system shares the loads among all muscles passing a joint. We try to approximate the load sharing of the human by minimizing a "cost function" to find a relatively arbitrary "optimal" solution. Several cost functions have been introduced (for an overview see reference (Tsirakos et al, 1997)) among which two are being used in this study. The first criterion, the quadratic stress cost function (SCF) (Crowninshield and Brand, 1981), is the most widely used criterion and minimizes the summed muscle stress around a joint. The second criterion is briefly called the energy-based cost function (ECF) (Praagman, 2008). This criterion is based on two main energy consuming processes in a muscle needed to produce a contraction, namely "*detachment of cross bridges*" and "*re-uptake of calcium*" (Praagman et al, 2006). Both cost functions have been implemented and used in the Delft Shoulder and Elbow Model (DSEM).

In a previous study (Praagman et al, 2006), the SCF and ECF were compared based on the muscle oxygen consumption using near infra-red spectroscopy where the ECF was favored due to its better qualitative consistency with the measured oxygen consumption, specifically for the elbow muscles. Later (Steenbrink et al, 2009), it was shown that in comparison with the SCF, the ECF results in a better consistency between experimental results and the DSEM predicted principal actions.

In Chapter 5 the glenohumeral-joint reaction forces (GH-JRF) estimated by the DSEM were compared to those simultaneously measured using an instrumented shoulder implant (Westerhoff et al, 2009). Both SCF and ECF were used in the optimization process to calculate the GH-JRF. As results showed, the model generally underestimated the GH-JRF for dynamic tasks like abduction and forward flexion, but also that model estimations using the two cost functions differed up to 9% (see Table 5.2, Chapter 5).

For the ECF, the relative contribution of the two processes was unknown, and the two terms were implemented based on the assumption of a 1:1 (cross-bridges to calcium pumping) contribution at 50% activation during an isometric contraction (Praagman et al, 2006). This assumption resulted in 1:2 ratio at 100% activation. There is no agreement either for techniques or results among various studies that tried to quantify these relative contributions for single muscles. *In-vitro* measurements were carried out for maximal (Barclay et al, 1993; Barclay et al, 2008; Homsher et al, 1972; Rome and Klimov, 2000; Stienen et al, 1995; Szentesi et al, 2001; Walsh et al, 2006) or submaximal isometric single fibre muscle contractions (Burchfield and Rall, 1985; Rall, 1979; Rall and Schottelius, 1973; Wendt and Barclay, 1980; Zhang et al, 2006). As for maximal isometric contractions, one may conclude from the literature that about 23-44% of the total energy consumption is related to the ion (Ca^{2+} and/or Na^{+}) pumping and the remainder is related to cross-bridges cycling. In a review study, Barclay *et al* (2007) concluded that regardless of muscle contractile properties, techniques used for measuring the energy consumption, and experimental condition, the contribution of the Ca^{2+} pumping is more or less the same (~30-40% of the total energy consumption) for muscles from mammals in isometric contraction.

In this chapter, we aim to identify the adjustable parameters of the ECF which can lead to:

1) a closer match between the model and the experiment as for the GH-JRF, and

2) a relative contribution of the two energy terms at maximum muscle activation which coincides with the corresponding values in the literature.

The kinematic data from four patients with an instrumented endoprosthesis are used as model input. The inverse-dynamic simulation is performed using the DSEM and by recruiting both SCF and ECF as the muscle load sharing criteria. For the ECF, the simulation process is repeated for a variety of different adjusting parameters of the ECF. All model simulated GH-JRFs are compared to the ones measured *in-vivo* to identify new parameter sets. The new identified parameter sets will then be applied to calculate the relative contribution of the two energy terms and the results will be compared to the corresponding values in the literature.

7.2. Materials and Methods

7.2.1. Subjects

Four subjects with instrumented shoulder hemi-arthroplasty (S1, S2, S5, and S6, Table 3.1, Chapter 3) participated in the experiments. For the Ethics Statement and detailed descriptions about the participants see sections 3.2.1 and 3.2.2, Chapter 3.

7.2.2. Data recordings

Measured tasks included (unloaded) abduction and forward flexion motions. The subjects were asked to perform the tasks up to maximal possible arm elevation (see Table 3.2, Chapter 3).

Measurements comprised the collection of motion data as well as *in-vivo* GH-JRF. For the detailed description about the motion and *in-vivo* GH-JRF recordings see section 3.2.4, Chapter 3.

7.2.3. The energy-based muscle load sharing cost function

Following a detailed cadaver study on the shoulder (Klein Breteler et al, 1999), information about muscle architecture and optimal fiber length was obtained which made it possible to implement the muscle dynamics in the inverse optimization process (see Chapter 2 for a detailed description).

The original form of the energy-based cost function (J_E) (Praagman et al, 2006) was, therefore, reformulated in order to take the muscle force-length relationship into account (Praagman, 2008) as follows:

$$J_E = \sum_{i=1}^{n} \left\{ \mathrm{E}_{\mathrm{cb}_i} + \mathrm{E}_{\mathrm{ca}_i} \right\} =$$

$$\sum_{i=1}^{n} \left\{ F_i l_{opt_i} + wf_1 m_i \left(\frac{F_i}{F_{i\max}(l)} + wf_2 \left(\frac{F_i}{F_{i\max}(l)} \right)^2 \right) \right\} \qquad (1)$$

where

i stands for the muscle element;

n is the total number of muscle elements;

E_{cb} and E_{ca} represent the two energy consumption processes including the detachment of cross-bridges and the calcium pumping, respectively.

F, l_{opt}, and m, are respectively the muscle force (N), the optimal muscle fiber length (cm), and the muscle mass (gr).

$F_{\max}(l)$ is the maximum muscle force (N) and is calculated as follows:

$$F_{\max}(l) = f(l_s).PCSA.\sigma_{\max} \qquad (2)$$

where $f(l_s)$ is the normalized muscle force-length relationship (Winters and Stark, 1985) and $PCSA$ is the muscle physiological cross sectional area (cm^2). $\sigma_{\max}$ is defined as 100 N/cm^2 (An et al, 1989) (see also section 2.2.3, Chapter 2).

wf_1 and wf_2 are adjustable weight factors. The wf_1 is an indication of the relative contribution of the two energy terms. The wf_2 determines the shares of the linear and nonlinear parts in E_{ca} but indirectly affects the relative contribution of the two energy terms as well. Due to lack of existing physiological knowledge, the weight parameters wf_1 and wf_2 were arbitrarily set as 100 and 4, respectively (Praagman, 2008).

7.2.4. Kinematic data processing

For the detailed description about the kinematic data analysis see section 5.2.3, Chapter 5.

7.2.5. Modeling simulations

The IDO version of the DSEM (see section 2.2.3, Chapter 2) was used for modeling purposes in this study. Calculated joint angles were used as model inputs. Model simulations were performed for abduction and forward flexion motions and for four subjects. Both SCF and ECF served as the muscle load sharing criteria during inverse-optmization. For each task and subject, for the ECF for optimization, simulations were repeated for different combinations of weight factors in the ECF (wf_1 and wf_2, Equation 1). The weight factors were changed in large ranges in the neighborhood of the default values (i.e. $wf_1 = 100$, $wf_2 = 4$) as follows:

$$\begin{cases} 1 \le wf_1 \le 200, \text{ step size} = 10 \\ 0 \le wf_2 \le 20, \text{ step size} = 1, \text{ and } wf_2 = 100 \end{cases} \tag{3}$$

The $wf_2 = 100$ was selected to study the effects of using a very high share of the nonlinear term in the E_{ca} on the modeling outcomes. The selected ranges led to 638 series of simulations for each motion and each subject. The GH-JRF was calculated as an output of the inverse-dynamics analysis.

7.2.6. Measure of goodness-of-fit

For evaluation of the results, the model-calculated and *in-vivo* measured GH-JRF were compared for all sets of simulations. To measure the goodness-of-fit we used two indicators including the Root Mean Squared Error (RMSE) between the model-estimated and measured GH-JRF at all points, and the error calculated at the maximal arm elevation angle (α_{max}, Table 3.2, Chapter 3) defined as the difference between estimated and measured GH-JRF normalized to the measured force ($E_{\alpha max}$). For $E_{\alpha max}$, a minus value means underestimation of model with respect to the measured one while a positive value indicates an overestimation.

For each subject and each motion the contour graphs for RMSE and $E_{\alpha max}$ were plotted for different values of the weight factors (Figures 7.1 and 7.2). To make the color consistency between the subplots, the positive values of $E_{\alpha max}$ ($|E_{\alpha max}|$) are plotted. Therefore, one should note that all values of $E_{\alpha max}$ in Figures 7.1 and 7.2 must be read as negative.

The combination of wf_1 and wf_2 that resulted in the minimum value of RMSE was selected as the best solution (ECF_{best}). Except for one case (i.e. S5 during forward flexion, Table 7.1), the best results were acquired when $1 \le wf_1, wf_2 \le 10$ (Table 7.1). Based on these results, three sets of weight factors were selected for more detailed follow-up comparisons as follows:

- The mean of the values presented in Table 7.1, i.e. $wf_1 = 4$, $wf_2 = 5$ (ECF_{mean}),
- The two extreme parameter sets, i.e. $wf_1 = 1$, $wf_2 = 10$ ($ECF_{1,10}$) and $wf_1 = 10$, $wf_2 = 1$ ($ECF_{10,1}$).

The RMSE and $E_{\alpha max}$ were calculated when using the three above mentioned combinations of weight factors for the ECF as well as the default form of the ECF ($wf_1 = 100$, $wf_2 = 4$, ECF_{def}) and the SCF during both abduction and forward flexion and for all subjects (Figure 7.3).

Table 7.1. The *best* solutions
the combinations of wf_1 and wf_2 that resulted in the minimum value of RMSE between the model estimated and measured GH-JRF for different subjects and motions.

	Abduction				Forward flexion				
	S1	**S2**	**S5**	**S6**	**S1**	**S2**	**S5**	**S6**	**mean**
wf_1	3	1	3	1	1	1	9	10	4
wf_2	2	6	1	1	3	9	19	1	5

7.2.7. Statistical analysis

For statistical analysis, a two-tailed paired Students' t-Test was used. The threshold for statistical significance was considered as 0.05.

Post-hoc statistical power analysis for two-tailed Student's t-Test was also carried out in order to evaluate the power of test with low number of subjects (n = 4).

7.2.8. Relative contribution of two energy terms

Having values for wf_1 and wf_2, the relative contribution of the two energy terms (E_{cb}/E_{ca}) was also calculated for different muscle elements at the maximum arm elevation angle for each motion. For each subject, motion, and force ratio (i.e. F/F_{max}, Equation 1), the calculated E_{cb}/E_{ca} was averaged over a selection of muscle elements and averaged across all subjects and motions (Figure 7.4).

7.3. Results

7.3.1. GH-JRF

The generic model generally underestimated the GH-JRF when compared to the *in-vivo* recordings ($E_{\alpha max}$, Figures 7.1 and 7.2).

The results (Figures 7.1 and 7.2) revealed that when the two weight factors simultaneously decreased, the magnitude of the RMSE and $|E_{\alpha max}|$ decreased indicating that the model estimations got closer to the measured data.

The highest deviations of the model calculations from the measurements occurred around the zone in which $10 \leq wf_1 \leq 80$ and $wf_2 = 20$ (Figures 7.1 and 7.2).

By increasing wf_2 from 20 to 100 (giving a higher share to the nonlinear part of the calcium pumping term), the RMSE and $|E_{\alpha max}|$ increased (on average ~ 12 % for $|E_{\alpha max}|$) for $wf_1 \leq 30$ but slightly decreased (on average ~ 3% for $|E_{\alpha max}|$) for higher values of wf_1.

By using the three selected sets of weight factors for the ECF (i.e. ECF_{mean}, $ECF_{1,10}$, and $ECF_{10,1}$), the model predicts of the GH-JRF significantly ($p < 0.05$, Post-hoc power ~ 0.3) improved (on average ~ 20% at α_{max}) in most cases compared to when using either the ECF_{def} or the SCF (Figure 7.3).

7.3.2. Relative contribution of the two energy terms

Regarding the relative contribution of different terms in the energy cost function (Figure 7.4), using the selected sets of weight factors led to E_{cb}:E_{ca} equal to, respectively, 2.3:1, 5.1:1, and 2.9:1 for ECF_{mean}, $ECF_{1,10}$, and $ECF_{10,1}$ at 100% muscle activation (i.e. $F/F_{max} = 1$). This implies that at maximum muscle activation, respectively, about 30%, 16%, and 25% of the total energy consumption is related to calcium pumping when using the ECF_{mean}, $ECF_{1,10}$, and $ECF_{10,1}$.

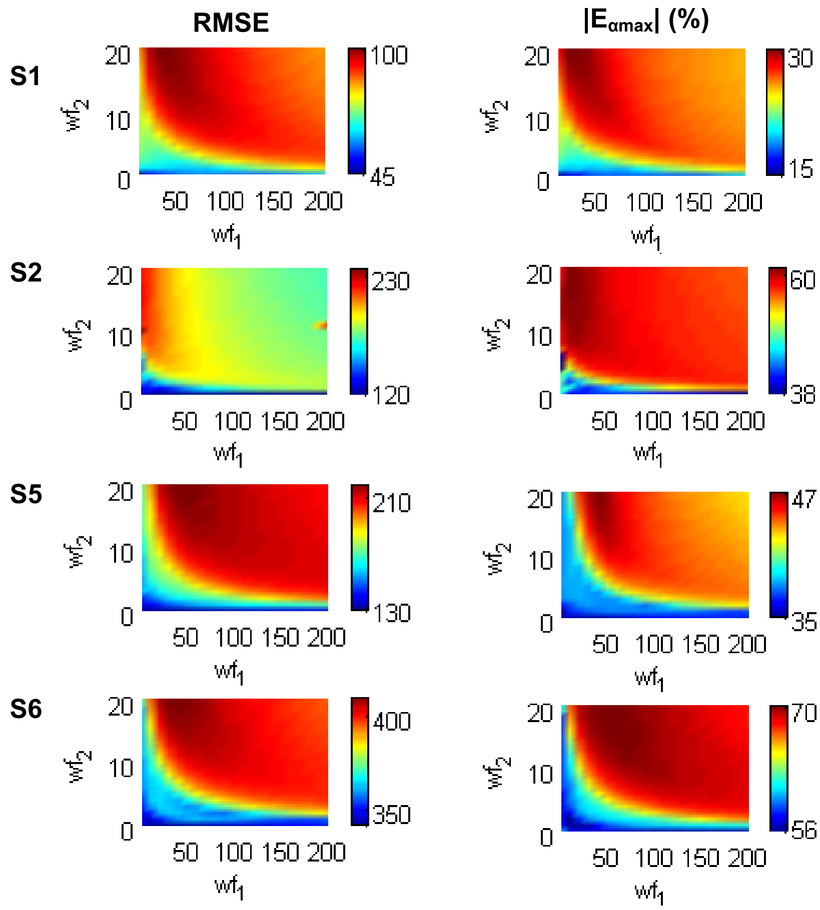

Figure 7.1. The Root Mean Squared Error (RMSE) and absolute error at maximal arm elevation ($|E_{\alpha max}|$) calculated between model-estimated and *in-vivo* measured GH-JRF at different combinations of the weight factors (wf_1 and wf_2) of the ECF and for the four measured subjects during performing abduction motion.

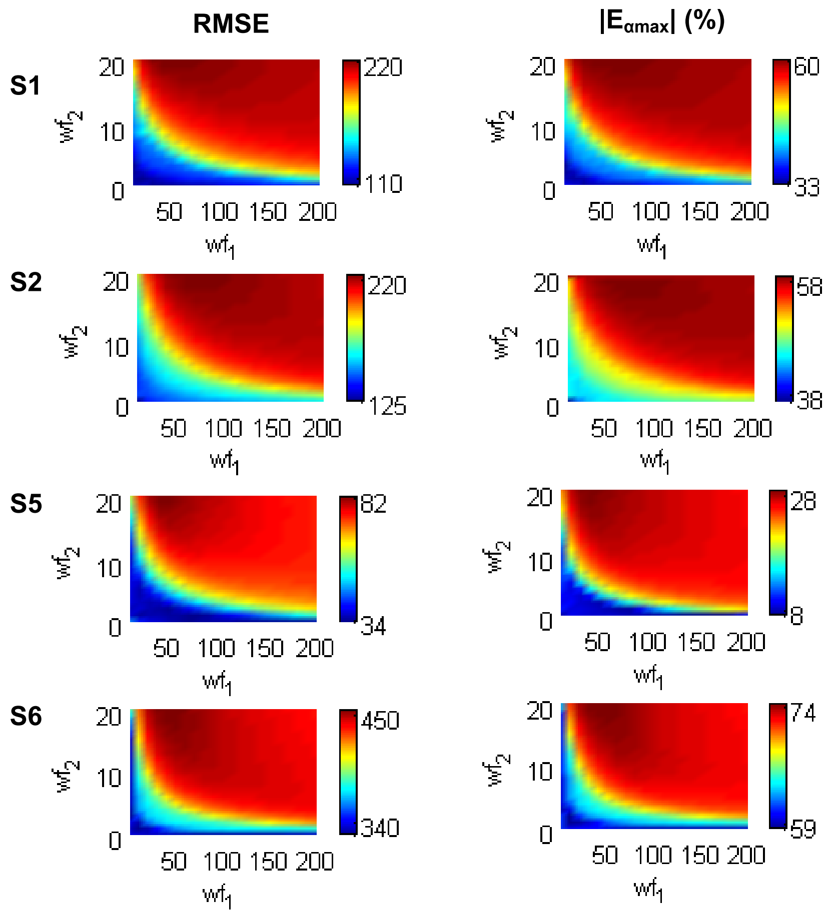

Figure 7.2. The Root Mean Squared Error (RMSE) and absolute error at maximal arm elevation ($|E_{\alpha max}|$) calculated between model-estimated and *in-vivo* measured GH-JRF at different combinations of the weight factors (wf_1 and wf_2) of the ECF and for the four measured subjects during performing forward flexion motion.

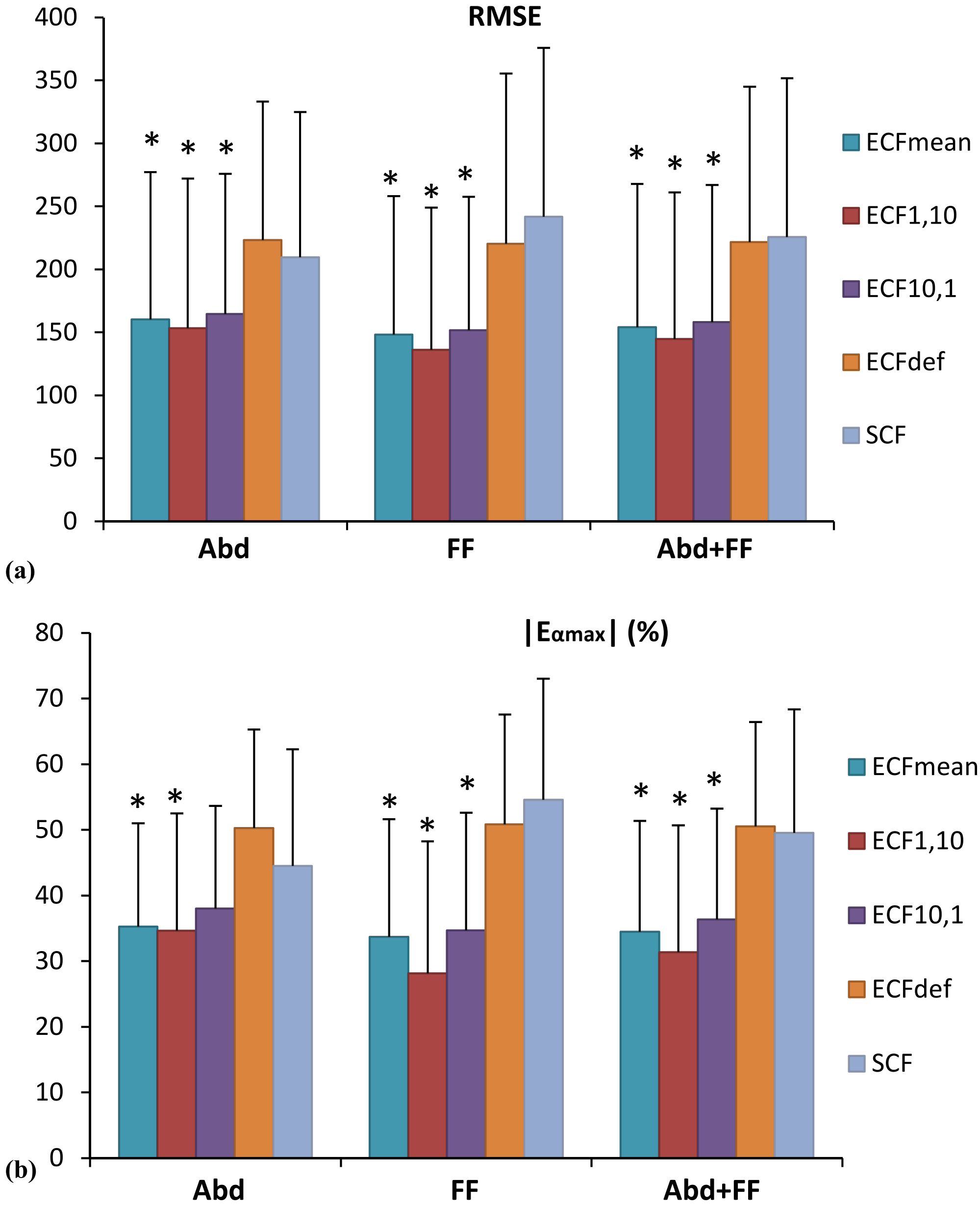

Figure 7.3. The (a) RMSE and (b) absolute $E_{\alpha max}$

Calculated for selected combinations of the weight factors of the ECF (ECF_{mean}, $ECF_{1,10}$, and $ECF_{10,1}$), the default form of the ECF (ECF_{def}) and the SCF averaged across all measured subjects during performing abduction (Abd), forward flexion (FF), and both abduction and flexion (Abd+FF) motions.

* Significant different from either ECF_{def} or SCF ($p < 0.05$)

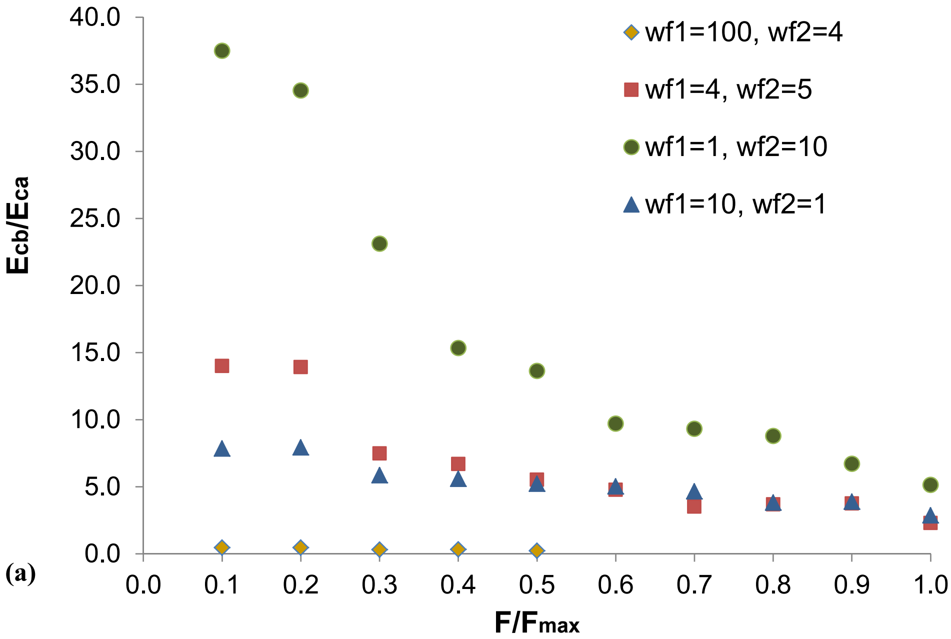

(a)

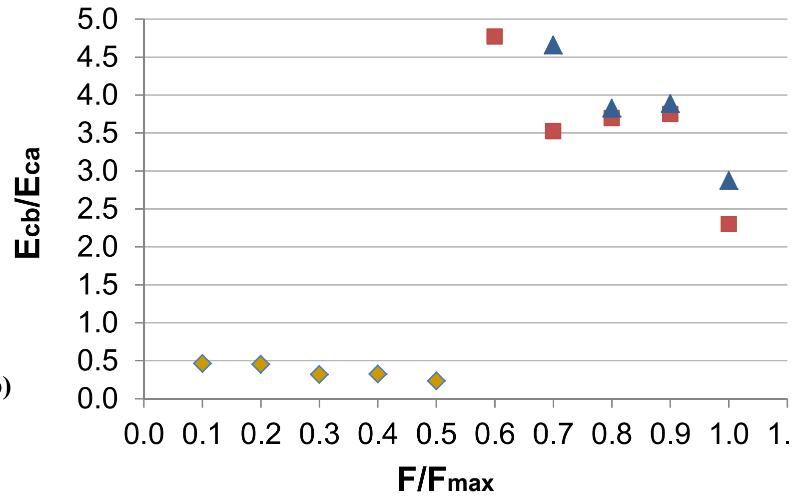

(b)

Figure 7.4. (a) The relative contribution (E_{cb}/E_{ca}) of the different energy terms in the ECF vs force ratio (F/F_{max}, Equation 1), for different sets of weight factors averaged across selected muscles and all subjects. (b) A zoomed-in view of the area in part-a in which $E_{cb}/E_{ca} \leq 5$.

7.4. Discussion

The *in-vivo* measured GH-JRF by instrumented shoulder endoprostheses were used to identify the weight parameters of a previously developed load sharing cost function. The new identified weight parameters were different from those that were originally used. By applying the new parameter sets the model could calculate the GH-JRF significantly closer (on average 20%) to what *in-vivo* measured.

Similar to our observations in Chapter 5 (Nikooyan et al, 2010), not only the generic model generally underestimated the GH-JRF compared to the *in-vivo* measurements but also the predicted GH-JRFs were not identical for the ECF_{def} and the SCF: when using the ECF_{def}, the model predicted GH-JRF was slightly lower (~ 6%) during abduction motion but not notably higher (~ 4%) during forward flexion motion.

Although using all selected parameter sets for ECF (i.e. ECF_{mean}, $ECF_{1,10}$, and $ECF_{10,1}$) resulted in significant improvements in the modeling calculations, however, one would expect a final recommended parameter set for future applications. The cost function with this selected parameter set not only should have the capability of considerably improving the model predictions but also should lead to a relative contribution of the energy terms which is in agreement with the corresponding values in the literature. Among the selected solutions, the $ECF_{1,10}$ had the lowest average values of both RMSE and $|E_{\alpha max}|$ (Figure 7.3). However, when using the $ECF_{1,10}$, the relative contributions of the energy terms at lower muscle activations (i.e. $F/F_{max} < 0.3$) do not seem feasible. Moreover, the contribution of the calcium pumping at maximum activation (~16%, Figure 7.4a) does not coincide with reported values for single muscles that range from 23% to 44% (Barclay et al, 2007; Barclay et al, 1993; Barclay et al, 2008; Homsher et al, 1972; Rome and Klimov, 2000; Stienen et al, 1995; Szentesi et al, 2001; Walsh et al, 2006). The other two parameter sets (ECF_{mean} and $ECF_{10,1}$) resulted in contributions for calcium pumping (30% and 25%) that were more in the range of these reported values. Although ECF_{mean} gave slightly better results (~ 3%) than the $ECF_{10,1}$ (Figure 7.3), however, $ECF_{10,1}$ showed a smoother pattern of the E_{cb}:E_{ca} at different muscle activations (Figure 7.4). We therefore recommend the $ECF_{10,1}$ as the new selected parameter set for the ECF.

The increase in magnitude of the model predicted GH-JRF when using the new parameter sets compared with the default form of the ECF and/or the SCF is related to the increase in model predicted individual muscle forces (Figure 7.5). For abduction, using the new identified parameter set mostly affected the model-prediction of the trapezius scapular part, serratus anterior, supraspinatus, biceps (long and/or short heads), and triceps medialis muscle forces. During forward flexion motion, the model prediction of the serratus anterior, supraspinatus, biceps short head, and triceps medialis muscle forces considerably increased when using the new identified parameter set.

As results showed (Figures 7.1 and 7.2), by either directly (wf_1) or indirectly (wf_2) decreasing the contribution of the calcium pumping with respect to the detachment of cross-bridges in the energy cost function, the model predicted GH-JRF increased. The role of wf_2 (i.e. a nonlinear quadratic term in the calcium pumping part) is more highlighted at the lower values of wf_1 (< 70). Although, Praagman *et al* (2008; 2006) found less false-negatives for model-estimated force to EMG comparisons when using a nonlinear quadratic term in the calcium pumping part, however, there is no (quantitative) proof about whether or not considering this nonlinear term leads to improvements in the model predictions. It has been stated that the linear muscle load sharing criteria generally favor discrete muscle action while the nonlinear criteria basically lead to synergism (Crowninshield and Brand, 1981; Dul et al, 1984b; Dul et al, 1984a). Nevertheless, considering that by increasing the share of the nonlinear term in the energy cost function the model predicted GH-JRF decreases, it seems that this nonlinear term does not play a major role in changing the synergism of muscle force sharing.

The results of Chapter 5 (Nikooyan et al, 2010) showed that in contrast to dynamic tasks, the DSEM overestimated the GH-JRF for static force tasks. The results of that study showed that using the ECF could considerably improve (up to 50%) the model prediction of the GH-JRF in a few directions of applying the external loads. Therefore, one would expect that including the static force tasks in the evaluation procedure may lead to find more generalized parameter sets for energy criterion.

Other than the general underestimation of the model, the previous study (Nikooyan et al, 2010) also showed that the estimated and measured GH-JRF behaved differently at arm elevation angles above 90º (increasing measured vs. decreasing model-estimated). As proposed before, the different behavior can be caused by muscle co-contraction based on either a standard or pathological (related to endoprosthesis) coordination pattern. Researchers have developed and used advanced muscle load sharing cost functions in order to consider the muscle co-contraction in the modeling procedure (Forster et al, 2004; Jinha et al, 2006). Among four measured subjects in the current study, two subjects (S2 and S6) were able to elevate their arms above 90º during both abduction and forward flexion while subject S1 could only do that during flexion motion. Using the new identified parameters in the current study showed the potential to improve the pattern of the model-predicted GH-JRF for above 90º in three cases (Figure 7.6). Nevertheless, this effect seems to be a bit random considering that the tuned criterion did not have any effect on the pattern of the model predicted GH-JRF above 90º for S2 during abduction (Figure 7.6 b) and S6 during forward flexion (Figure 7.6 d). The EMG-driven modeling (Laursen et al, 1998; Lloyd and Besier, 2003) is an alternative approach to account for possible antagonist co-contraction (Chapter 6). The results in Chapter 6 revealed that including the EMGs as input to the model could considerably improve (up to 45%) the model predictions of the GH-JRF especially for above 90º. The ECF_{def} was used as the muscle load sharing criterion in that study. One should, however, note the mechanisms that improve the pattern of the model predicted GH-JRF above 90º were not identical in the two approaches. In the EMG-driven model, the force behavior above 90º was improved by forcing the model to follow the recorded activation pattern of the major antagonist co-contractors like pectoralis major clavicular part (during abduction) or deltoid posterior part (during forward flexion). Using the tuned parameter set for the ECF (ECF_{best}), affected the model predictions of the GH-JRF by giving an incremental load share for above 90º to muscles like trapezius scapular part, serratus anterior, supraspinatus, and/or biceps short (Figure 7.5).

Other than the energy processes presenting in the current ECF, there are also some energy processes that have not been accounted for. An important process is the higher energy rate associated with shortening, sometimes called the Fenn effect (Alexander, 1997; Lichtwark and Wilson, 2005). Neglecting the Fenn effect may limit implementation of the ECF in high-speed dynamic movements. Given that some muscles are shortening at different rates during fast dynamic movements, it is likely to have an impact on the estimates of energy cost. Therefore, for application of the ECF in fast dynamic movements (e.g. throwing ball in baseball) the so-called Fenn effect should be taken into account.

7.5. Conclusions

The relative contribution of two muscle energy consumption processes including the detachment of cross-bridges and the calcium pumping incorporating in the energy-based criterion was quantified by using *in-vivo* measured GH-JRF on four patients carrying an instrumented shoulder implant. A set of new weight parameters which determines the relative contribution of the energy term was identified. Following conclusion(s) can be drawn from this study:

- The energy-based criterion with new identified parameter set resulted in not only significant improvements of the model calculated GH-JRF but also a relative contribution of the two energy terms at maximum muscle activation which coincides with the corresponding values in the literature for isometric contraction. The new identified parameter set is therefore recommended to be used instead of the previously used parameters.

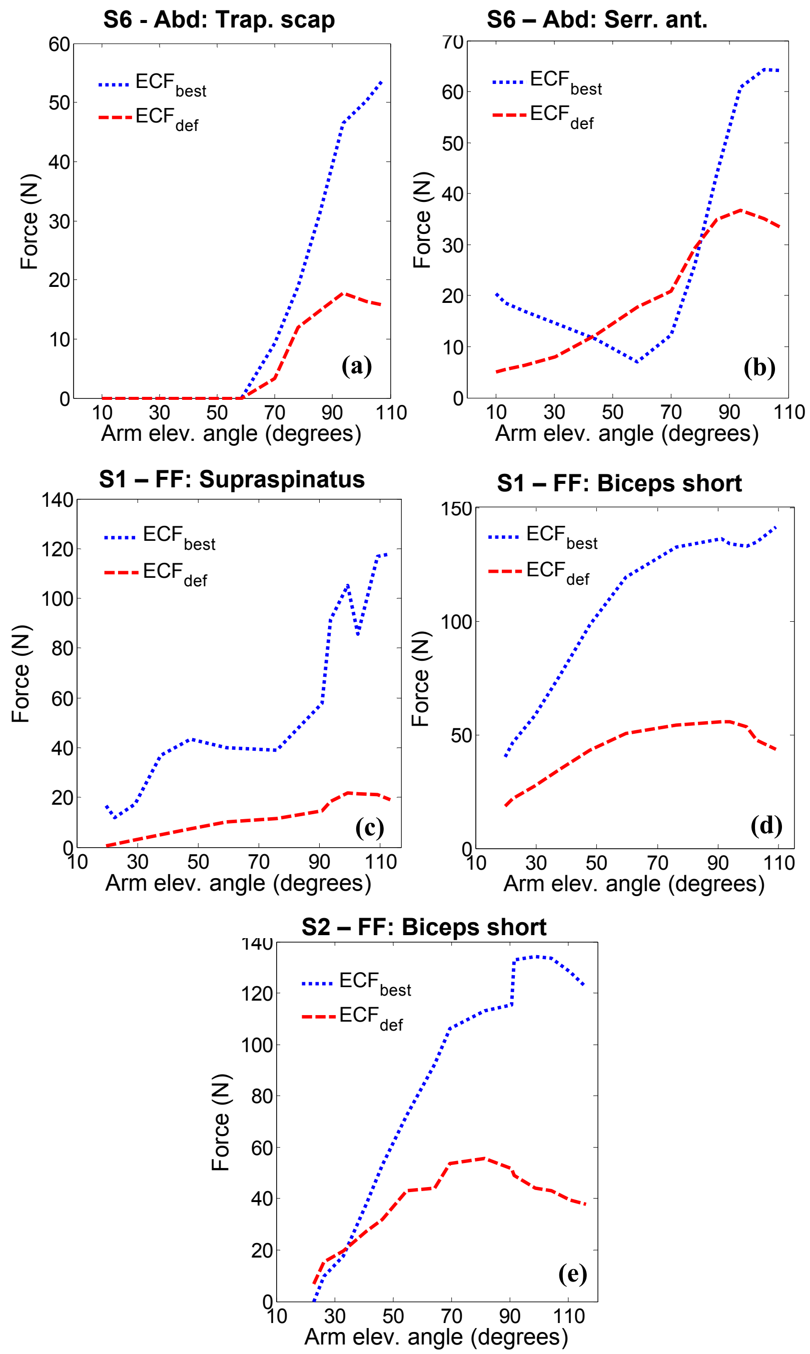

Figure 7.5. Comparing the model-estimated muscle forces using the best solution and the default set for the ECF vs arm elevation angle for subjects who could elevate their arm above 90º. trap. scap.: trapezius scapular part muscle, serr. ant.: serratus anterior muscle.

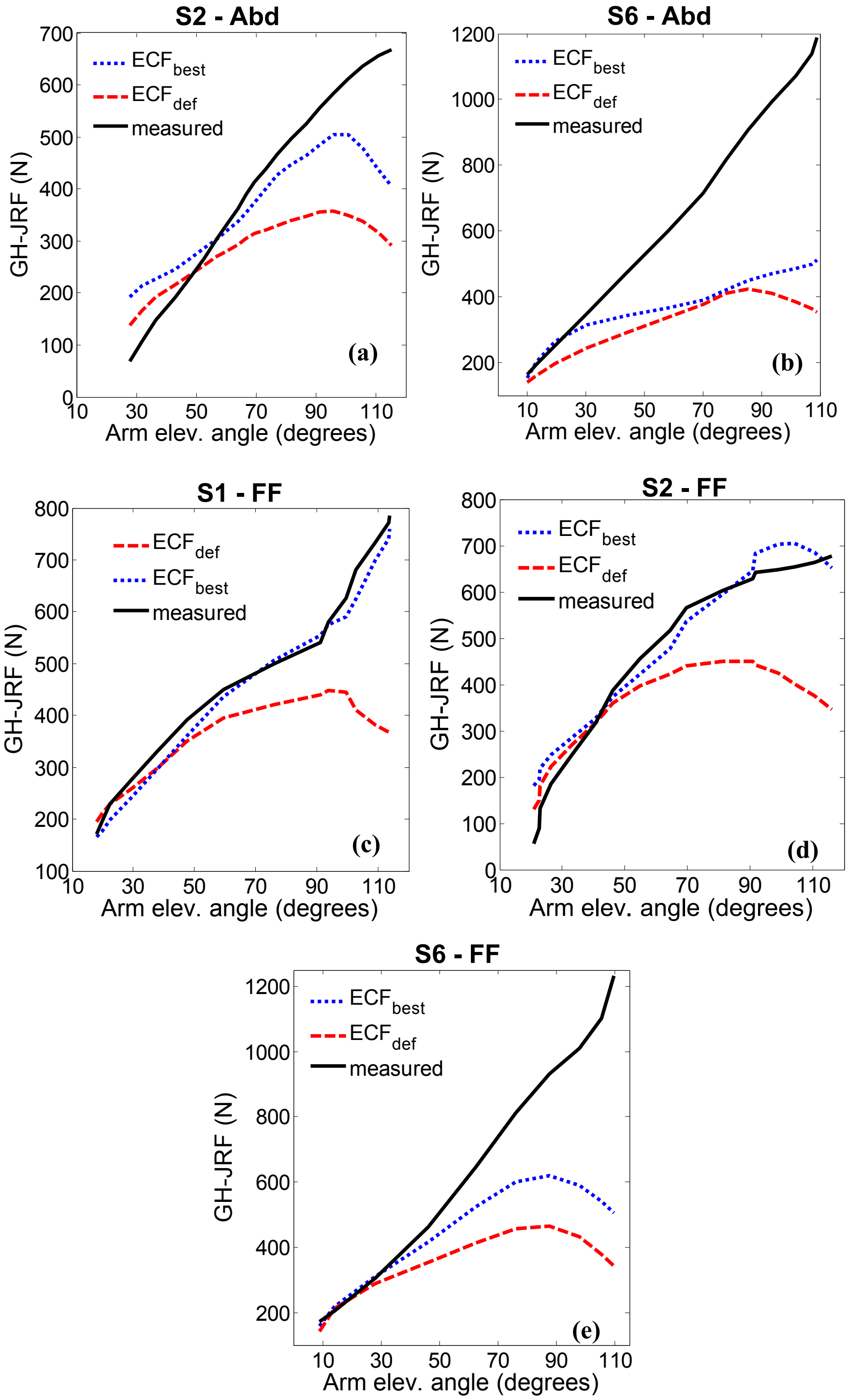

Figure 7.6. Comparing the model-estimated using the best solution (ECF_{best}, Table 2) and the default set (ECF_{def}) for the ECF and the measured GH-JRF vs arm elevation angle for subjects who could elevate their arm above 90º.

7.6. References

Alexander, R.M., 1997. Optimum Muscle Design for Oscillatory Movements. Journal of Theoretical Biology 184 (3), 253-259.

An, K.N., Kaufman, K.R., Chao, E.Y.S., 1989. Physiological considerations of muscle force through the elbow joint. Journal of Biomechanics 22 (11-12), 1249-1256.

Barclay, C., Woledge, R., Curtin, N., 2007. Energy turnover for Ca2+ cycling in skeletal muscle. Journal of Muscle Research and Cell Motility 28 (4), 259-274.

Barclay, C.J., Constable, J.K., Gibbs, C.L., 1993. Energetics of fast-twitch and slow-twich muscles of the mouse. Journal of Physiology-London 472, 61-80.

Barclay, C.J., Lichtwark, G.A., Curtin, N.A., 2008. The energetic cost of activation in mouse fast-twitch muscle is the same whether measured using reduced filament overlap or N-benzyl-p-toluenesulphonamide. Acta Physiologica 193 (4), 381-391.

Burchfield, D.M., Rall, J.A., 1985. Energetics of activation in frog skeletal muscle at sarcomere lengths beyond myofilament overlap. Biophysical Journal 48 (6), 1049-1051.

Crowninshield, R.D., Brand, R.A., 1981. A physiologically based criterion of muscle force prediction in locomotion. Journal of Biomechanics 14 (11), 793-801.

Dul, J., Johnson, G.E., Shiavi, R., Townsend, M.A., 1984b. Muscular synergism--II. A minimum-fatigue criterion for load sharing between synergistic muscles. Journal of Biomechanics 17 (9), 675-684.

Dul, J., Townsend, M.A., Shiavi, R., Johnson, G.E., 1984a. Muscular synergism--I. On criteria for load sharing between synergistic muscles. Journal of Biomechanics 17 (9), 663-673.

Forster, E., Simon, U., Augat, P., Claes, L., 2004. Extension of a state-of-the-art optimization criterion to predict co-contraction. Journal of Biomechanics 37 (4), 577-581.

Homsher, E., Wallner, A., Mommaert.Wf, Ricchiut.Nv, 1972. Activation heat, activation metabolism and tension-related heat in frog semitendinosus muscles. Journal of Physiology-London 220 (3), 601-&.

Jinha, A., Ait-Haddou, R., Herzog, W., 2006. Predictions of co-contraction depend critically on degrees-of-freedom in the musculoskeletal model. Journal of Biomechanics 39 (6), 1145-1152.

Klein Breteler, M.D., Spoor, C.W., Van der Helm, F.C.T., 1999. Measuring muscle and joint geometry parameters of a shoulder for modeling purposes. Journal of Biomechanics 32 (11), 1191-1197.

Laursen, B., Jensen, B.R., Nemeth, G., Sjogaard, G., 1998. A model predicting individual shoulder muscle forces based on relationship between electromyographic and 3D external forces in static position. Journal of Biomechanics 31 (8), 731-739.

Lichtwark, G.A., Wilson, A.M., 2005. A modified Hill muscle model that predicts muscle power output and efficiency during sinusoidal length changes. Journal of Experimental Biology 208 (15), 2831-2843.

Lloyd, D.G., Besier, T.F., 2003. An EMG-driven musculoskeletal model to estimate muscle forces and knee joint moments in vivo. Journal of Biomechanics 36 (6), 765-776.

Nikooyan, A.A., Veeger, H.E.J., Westerhoff, P., Graichen, F., Bergmann, G., van der Helm, F.C.T., 2010. Validation of the Delft Shoulder and Elbow Model using in-vivo glenohumeral joint contact forces. Journal of Biomechanics 43 (15), 3007–3014.

Praagman, M., 2008. Muscle load sharing: An energy-based approach. PhD Thesis, Free University, Amsterdam.

Praagman, M., Chadwick, E.K.J., van der Helm, F.C.T., Veeger, H.E.J., 2006. The relationship between two different mechanical cost functions and muscle oxygen consumption. Journal of Biomechanics 39 (4), 758-765.

Rall, J.A., 1979. Effects of temperature on tension, tension-dependent heat, and activation heat in twitches of frog skeletal muscle. Journal of Physiology-London 291 (JUN), 265-275.

Rall, J.A., Schottelius, B.A., 1973. Energetics of contraction in phasic and tonic skeletal muscles of the chicken. Journal of General Physiology 62 (3), 303-323.

Rome, L.C., Klimov, A.A., 2000. Superfast contractions without superfast energetics: ATP usage by SR-Ca2+ pumps and crossbridges in toadfish swimbladder muscle. Journal of Physiology-London 526 (2), 279-286.

Steenbrink, F., Meskers, C.G.M., van Vliet, B., Slaman, J., Veeger, H.E.J., De Groot, J.H., 2009. Arm load magnitude affects selective shoulder muscle activation. Med Biol Eng Comput 47 (5), 565-72.

Stienen, G.J.M., Zaremba, R., Elzinga, G., 1995. ATP utilization for calcium uptake and force production in skinned muscle fibres of Xenopus laevis. Journal of Physiology-London 482 (1), 109-122.

Szentesi, P., Zaremba, R., van Mechelen, W., Stienen, G.J.M., 2001. ATP utilization for calcium uptake and force production in different types of human skeletal muscle fibres. Journal of Physiology-London 531 (2), 393-403.

Tsirakos, D., Baltzopoulos, V., Bartlett, R., 1997. Inverse optimization: functional and physiological considerations related to the force-sharing problem. Critical Review of Biomedical Engineering 25, 371–407.

Walsh, B., Howlett, R.A., Stary, C.M., Kindig, C.A., Hogan, M.C., 2006. Measurement of activation energy and oxidative phosphorylation onset kinetics in isolated muscle fibers in the absence of cross-bridge cycling. American Journal of Physiology-Regulatory Integrative and Comparative Physiology 290 (6), R1707-R1713.

Wendt, I.R., Barclay, J.K., 1980. Effects of dantrolene on the energetics of fast- and slow-twitch muscles of the mouse. American Journal of Physiology 238 (1), C56-C61.

Westerhoff, P., Graichen, F., Bender, A., Rohlmann, A., Bergmann, G., 2009. An instrumented implant for in vivo measurement of contact forces and contact moments in the shoulder joint. Medical Engineering & Physics 31 (2), 207-213.

Winters, J.M., Stark, L., 1985. Analysis of fundamental human movement patterns through the use of in-depth antagonistic muscle models. IEEE Transactions on Biomedical Engineering 32, 826-839.

Zhang, S.J., Andersson, D.C., Sandstrom, M.E., Westerblad, H., Katz, A., 2006. Cross bridges account for only 20% of total ATP consumption during submaximal isometric contraction in mouse fast-twitch skeletal muscle. American Journal of Physiology-Cell Physiology 291 (1), C147-C154.

Modified from: A.A. Nikooyan, H.E.J. Veeger, P. Westerhoff, G. Bergmann, F.C.T. van der Helm , "The effect of articular friction on the estimation of glenohumeral joint reaction forces", waiting approval for submission.

Chapter 8

Articular friction in the artificial shoulder joint

The aim of this chapter is to implement the friction-induced moments measured by the instrumented shoulder hemiarthroplasty in the Delft Shoulder and Elbow Model and to explore the effects on the prediction of the glenohumeral joint reaction forces. Six patients with instrumented shoulder hemiarthroplasty capable of measuring joint loads *in-vivo* were measured. Motion data, *in-vivo* glenohumeral joint reaction forces, and *in-vivo* frictional moments were recorded simultaneously during performing unloaded abduction and forward flexion motions up to maximal arm elevation. The glenohumeral joint reaction forces estimated by the model with and without including frictional moments in the modeling process were compared to the recorded glenohumeral joint reaction force. Adding the measured frictional moments to the model input significantly (two-tailed $p \sim 0.01$) improved (on average ~ 9%) the model predicted glenohumeral joint reaction force at the maximal arm elevation. The Coulomb friction coefficient (μ) in the artificial shoulder joint was also estimated to be $\mu \sim 0.16 \pm 0.10$. This study concludes that friction moments in the shoulder endoprosthesis are considerable and do have a significant effect on the joint reaction forces of the shoulder and should therefore be included in the biomechanical analysis of artificial shoulder joints.

8.1. Introduction

Joint replacement is a well-known treatment for severe joint diseases like osteoarthritis (Franceschini et al, 2005). Some studies revealed that despite a design also aimed at minimization of internal friction, considerable friction still occurs within artificial joints. In a study on hip prostheses (Bergmann et al, 2001), the temperature rose up to 43.1°C after one hour walking. A similar and more recent study (Pritchett, 2006) on different types of knee implant showed a temperature rise of about 9°C in 40 minutes walking, indicating a notable friction.

Various techniques were developed to measure the moments induced by friction in artificial joints. The frictional moments (FM) were measured using hip joint simulators reached 1.2 Nm and 7.9 Nm, respectively, in studies by Saikko (2009) and Bishop *et al* (2008). The instrumented endoprosthesis of the hip (Damm et al, 2010) and the shoulder (Westerhoff et al, 2009a) joints have been developed such that *in-vivo* measurements the joint contact forces and moments is possible. As for the shoulder joint, studies on subjects carrying an instrumented shoulder endoprosthesis while performing dynamic and/or activity of daily living tasks showed that the FM could become as high as 7 Nm (Bergmann et al, 2007; Westerhoff et al, 2009b).

The importance of considering friction in the biomechanical studies of artificial joints is twofold:

Firstly, the potential damage that a rise in temperature in the joint may cause to the surrounding tissues (Lu et al, 1999). The excessive wear and production of debris in the bone-implant area can cause aseptic inflammation (Hallab and Jacobs, 2009).

Secondly, in- or excluding FM in musculoskeletal modeling process may affect the total joint moment and consequently the predicted muscle and joint reaction forces. Musculoskeletal models usually ignore the joint friction for patients with implant. In optimization-based models, the net joint moment is generally calculated through an inverse-dynamic analysis in which the equations of motions are solved using measured kinematics and external forces as inputs. Studies on shoulder loads during weight handling (Giroux and Lamontagne, 1992) and wheelchair propulsion (Veeger et al, 2002) revealed that the net joint moment in the shoulder joint reached 40 Nm. If net joint moment has the same magnitude in healthy joint as in artificial joints, an FM up to 7 Nm as measured in the instrumented implant, would therefore be slightly less than 20% of the total net joint moment. As a consequence, including FM in the modeling process will have notable effects on modeling results.

The aim of this study is to implement FM as measured *in-vivo* using an instrumented shoulder implant in the Delft Shoulder and Elbow Model (DSEM). The model-estimated GH-JRF with and without considering FM will be compared to forces measured *in-vivo* using an instrumented endoprosthesis. By applying some simplifying assumptions, we will also try to estimate the Coulomb friction coefficient in the artificial shoulder joint from the *in-vivo* measured data and compare it with the corresponding values in the literature.

8.2. Materials and Methods

8.2.1. Subjects

Six subjects with instrumented shoulder hemi-arthroplasty (S1 to S6, Table 3.1, Chapter 3) participated in the experiments. For the Ethics Statement and detailed descriptions about the participants see sections 3.2.1 and 3.2.2, Chapter 3.

8.2.2. Data recordings

Measured tasks included unloaded abduction and forward flexion motions. The subjects were asked to perform the dynamic tasks up to maximal possible arm elevation (see Table 3.2, Chapter 3).

Measurements comprised the collection of motion data as well as *in-vivo* glenohumeral-joint reaction forces (GH-JRF) and frictional moments (FM). The *in-vivo* measured forces and moments were synchronized and re-sampled with the motion recording frequency to allow for further processing. For the detailed description about the motion recordings see section 3.2.4, Chapter 3. For details about the *in-vivo* measurement of contact forces and moments in the instrumented implant see references (Bergmann et al, 2007; Westerhoff et al, 2009a).

8.2.3. Implementation of frictional moment in the modeling process

In a ball-and-socket joint, the resultant joint contact force vector should pass through the joint rotation center (i.e. $\mathbf{F}_N$, Figure 8.1). However, if the force does not pass through the humeral head center (i.e. $\mathbf{F}_r$, Figure 8.1) it will cause a moment (i.e. $\mathbf{M}_f$, Figure 8.1) around the joint center of rotation, which was also the point around which the recorded moments were calibrated. The only reasonable explanation for such moment would be the existence of a tangential force component (i.e. $\mathbf{F}_f$, Figure 8.1) between the articular surfaces which can be explained through joint friction.

The IDO version of the DSEM (see section 2.2.3, Chapter 2) was used for modeling purposes in this study.

In the DSEM, which is basically a finite element model, anatomical structures are modeled by mechanical elements: bones by beam, muscles by active truss, ligaments by passive truss, and joints by hinge elements. To include the measured FM between the humerus and scapula, a virtual 3-hinges system was added to the glenohumeral joint while the degrees-of-freedom of the model did not change. The FM was implemented as a rotational stress in the hinge elements, adding to the calculated net joint moments in the glenohumeral joint.

8.2.4. Transformations

In the DSEM, the calculated net moment are represented in the joint coordinate system. Values for the GH-JRF and FM were measured directly by the instrumented shoulder implant, and consequently transferred to the glenoid coordinate system. The same inter-coordinate transformations as in Chapter 3 (section 3.2.6) were used to transfer the *in-vivo* measured GH-JRF and FM to the glenoid side. At each measured time-frame (t), the rotation matrix ${}^{gl}\mathbf{R}^{i}(t)$ (Equation 4, section 3.2.6, Chapter 3) was used to rotate the measured GH-JRF and FM from the implant-based ($\mathbf{F}_i$ and $\mathbf{M}_i$) to the glenoid ($\mathbf{F}_{gl}$ and $\mathbf{M}_{gl}$, Figure 8.2) coordinate system as follows:

$$\begin{aligned} \mathbf{F}_{gl} &= -{}^{gl}\mathbf{R}\cdot{}^{i}\,\mathbf{F}_i \\ \mathbf{M}_{gl} &= -{}^{gl}\mathbf{R}\cdot{}^{i}\,\mathbf{M}_i \end{aligned} \tag{1}$$

Where the negative sign in Equation 1 means that the transferred force and moment are the "reaction force and moment" acting on the glenoid component.

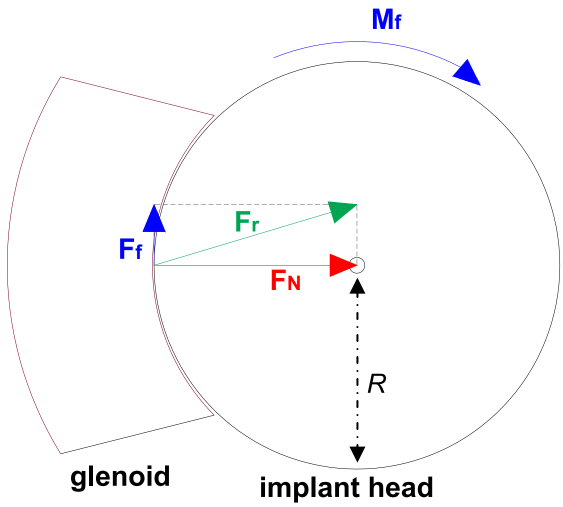

Figure 8.1. 2D scheme of the forces and moments acting at the implant head. $\mathbf{F}_f$: the friction force, $\mathbf{M}_f$: the frictional moment caused by the friction force, recorded by the instrumented implant; $\mathbf{F}_N$: the normal force, recorded by the implant; R: the implant head radius.

8.2.5. Kinematic data processing

Joint angles (inputs to the model) were calculated from measured motion data. For the detailed description about the kinematic data analysis see section 5.2.3, Chapter 5.

8.2.6. Modeling simulations

For each type of task and each subject, simulations were carried out for two different conditions including

1. the original model (and thus without friction), and
2. a model version considering FM in the modeling procedure (with friction).

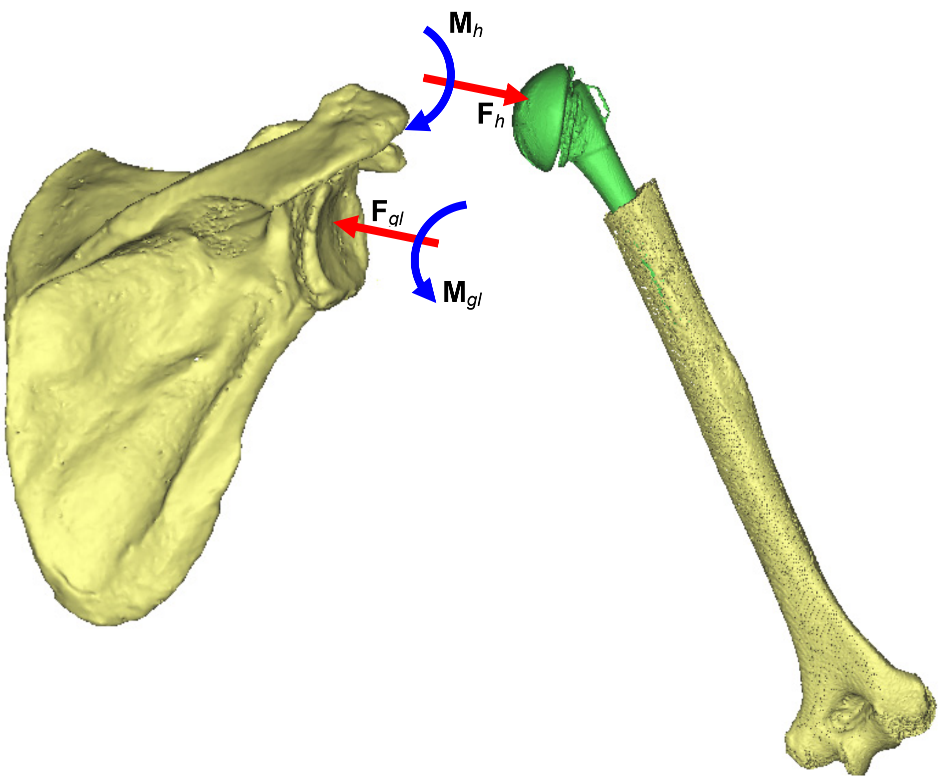

Figure 8.2. Schematic of the glenohumeral joint contact force and moment vectors acting on the humeral head ($\mathbf{F}_h$, $\mathbf{M}_h$) and the reaction force vector acting on the glenoid ($\mathbf{F}_{gl}$, $\mathbf{M}_{gl}$). Images are related to subject S6.

The GH-JRF was calculated through an inverse-dynamic simulation in the DSEM. Joint angles (section 8.2.5) were used as model inputs. The default form of the energy-based criterion (see Chapter 7) was used as the muscle load sharing cost function for inverse optmization. The model estimations of the GH-JRF were then compared to the ones *in-vivo* measured by the instrumented implant.

8.2.7. Measure of goodness-of-fit

To evaluate model results, three sets of indicators were defined as follows:

1. The Root Mean Squared Error (RMSE) between the model-estimated and measured GH-JRF which indicates how well the model-estimated force pattern follows the measured force.

2. The force error at 90˚ humeral elevation angle (E_{90°) which is the difference between estimated and measured GH-JRF normalized by the measured GH-JRF and calculated at 90˚ humeral elevation. E_{90° was calculated only for those subjects who could elevate their arms higher than 90˚ (Abd: N=2; FF: N=4; see Table 3.2, Chapter 3).
3. The peak force error ($E_{\alpha max}$) which is the difference between estimated and measured GH-JRF normalized by the measured GH-JRF and calculated at the maximal humeral elevation (α_{max}, Table 3.2, Chapter 3).

For E_{90° and $E_{\alpha max}$, a minus value means *underestimation* of the model predictions with respect to the measured one while a positive value indicates an *overestimation*.

8.2.8. Statistical analysis

To evaluate the significance of the effects of implementing the FM on the modeling outputs, a two-tailed paired Students' t-Test was used. The threshold for statistical significance was considered as 0.05. Post-hoc statistical power analysis for two-tailed Student's t-Test was also carried out in order to evaluate the power of test with low number of subjects (n = 6).

8.2.9. Estimation of friction coefficient

Different types of friction may exist in an artificial joint such as Coulomb and viscous friction. Considering that our patients had a hemi-arthroplasty, viscous-type friction may still exist because of the cartilage covering the surface of the glenoid fossa. Nevertheless, it is anticipated that the Coulomb friction has the largest contribution to the total frictional loads.

To estimate the Coulomb friction coefficient of the artificial shoulder joint, we made some simplifying assumptions:

1. There is only sliding and spinning motions between the articular surfaces, and
2. The friction and joint reaction forces are applied at one point.

The friction coefficient (μ) may be calculated from the friction ($\mathbf{F}_f$) and the normal ($\mathbf{F}_N$) force vectors (Figure 8.1) as follows:

$$\mu = \frac{|\mathbf{F}_f|}{|\mathbf{F}_N|} \tag{2}$$

Where $|\mathbf{F}_N|$ is equal to the measured resultant GH-JRF.

The friction force vector ($\mathbf{F}_f$) can be calculated from the measured moment (i.e. $\mathbf{M}_f$, Figure 8.1) and the implant head radius (i.e. R, Figure 8.1, for values see Table 3.1, Chapter 3).

The measured moment can be due to both sliding and spinning in the joint. The spinning occurs when a subject simultaneously rotates the arm (externally or internally) when performing an arm elevation task like abduction or forward flexion. Therefore, the sliding ($\mathbf{M}_{sl}$, perpendicular to the normal force) and spinning ($\mathbf{M}_{sp}$, parallel to the normal force) components of the measured moment vector (M_f) should be distinguished:

$$\theta = \cos^{-1}\left(\frac{\mathbf{M_f} \cdot \mathbf{F_N}}{|\mathbf{M_f}||\mathbf{F_N}|}\right) \tag{3}$$

$$\begin{aligned} |\mathbf{M_{sl}}| &= \sin(\theta)|\mathbf{M_f}| \\ |\mathbf{M_{sp}}| &= \cos(\theta)|\mathbf{M_f}| \end{aligned} \tag{4}$$

Where θ is the angle between the measured moment and force vectors. $\mathbf{M_f}.\mathbf{F_N}$ is the inner product of the moment and normal force vectors. When there is no spinning, the two vectors should be perpendicular to each other (θ = 90º).

The magnitude of the friction force ($|\mathbf{F_f}|$) is calculated from the perpendicular component of the measured moment (i.e. $|\mathbf{M}_{sl}|$) and the radius of the implant head as follows:

$$|\mathbf{F_f}| = \frac{|\mathbf{M_{sl}}|}{R} \tag{5}$$

8.3. Results

8.3.1. Original model-predictions

During both abduction (Abd, Figure 8.3) and forward flexion (FF, Figure 8.4) up to about 90° arm elevation, model-predicted (no friction) and the *in-vivo* measured GH-JRF showed good consistency (average Pearson correlation coefficient ~ 0.85). Although model estimations at the maximum arm elevation were generally lower (on average ~ 38%), however, the model generally overestimated the GH-JRF for subjects S3 and S4 during both abduction and forward flexion motions (Figures 8.3 and 8.4).

Similar to the observations in Chapters 5, 6, and 7, for angles above 90° arm elevation the calculated force started to decrease, while the measured force continued to increase.

8.3.2. Effect of including FM

Although in few cases the RMSE increased by implementing the frictional moments in the DSEM (i.e. S3-Abd and S3-FF, Figures 8.3, 8.4, and 8.5a), however, on average for all subjects and motions the RMSE between the model and experiments significantly ($p < 0.05$, Table 8.1) decreased by adding joint friction to the model.

Adding friction to the model generally increased the magnitude of the model-predicted GH-JRF at 90˚ and/or maximum arm elevation (Figures 8.3, 8.4, and 8.5b and c). On average, adding friction to the model led to non-significant ($p > 0.05$, Table 8.1) improvement (on average ~ 4%) of the model predicted GH-JRF at 90˚ arm elevation. Except one case (S3-Abd, Figure 8.5c), the model predicted GH-JRF at the maximum arm elevation was improved by adding the friction to the model. The statistical results showed that this improvement was significant ($p = 0.01$, Table 8.1).

Table 8.1. Comparing the model estimations of the GH-JRF before and after including the frictional moments in the modeling process. The two-tailed *p*-value (*p*) and post-hoc power (Power) for paired t-Test are given ($n = 6$).
* significant difference ($p < 0.05$)

	Abd+FF	
	p	Power
RMSE	0.03*	0.04
E_{90°	0.19	0.04
$E_{\alpha max}$	0.01*	0.08

8.3.3. Friction coefficient

High linear correlation ($R^2 \geq 0.75$, Figure 8.6) was found between the friction ($F_f = |\mathbf{F}_f|$) and normal ($F_N = |\mathbf{F}_N|$) forces. The estimated friction coefficient was found to be between 0.07 and 0.36 (0.16 ± 0.10). A good agreement between friction coefficient of abduction (0.18 ± 0.12) and forward flexion (0.15 ± 0.08) within individual subjects was also observed. The effect of spinning component of the measured moment on the calculated friction force was negligible (< 3%, $\theta \sim 87°$) for subjects S1, S2, S4, and S6 while was considerable (on average ~ 20%, $\theta \sim 63°$) for subjects S3 and S5.

8.4. Discussion

The FM measured by the instrumented shoulder endoprosthesis were implemented in the IDO version of the Delft Shoulder and Elbow Model. The results showed that implementation of the FM in the modeling procedure slightly improved (on average ~ 9%) the model calculation of the GH-JRF at the maximum elevation when using the *in-vivo* measured GH-JRF as the reference for quantitative evaluations.

Adding friction generally led to increase in model estimations of the GH-JRF (Figures 8.3 to 8.5). The importance of the load increase in the artificial shoulder joints due to the friction is twofold:

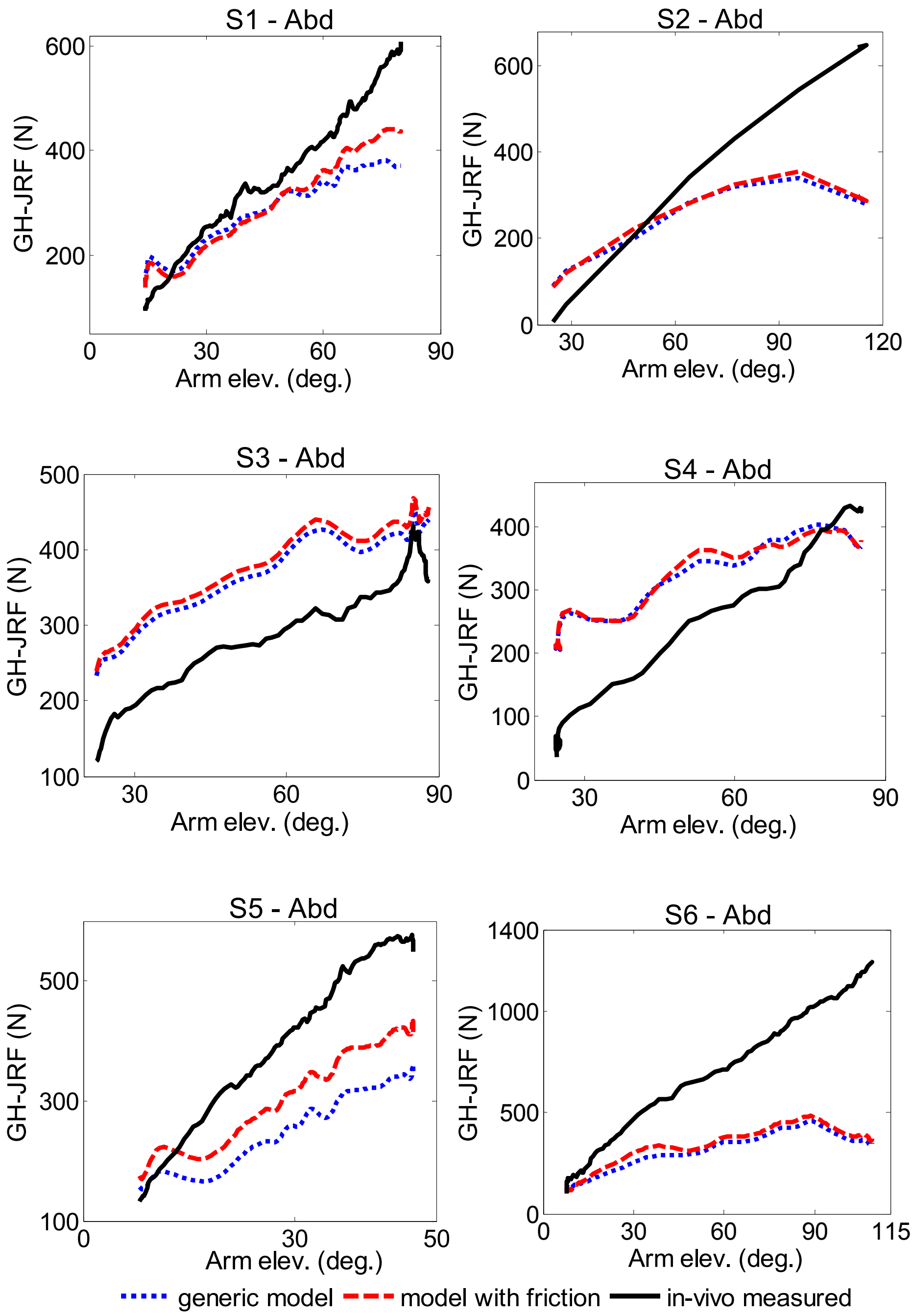

Figure 8.3. The measured and calculated GH-JRF with and without friction vs arm elevation angle for six measured subjects during abduction motion.

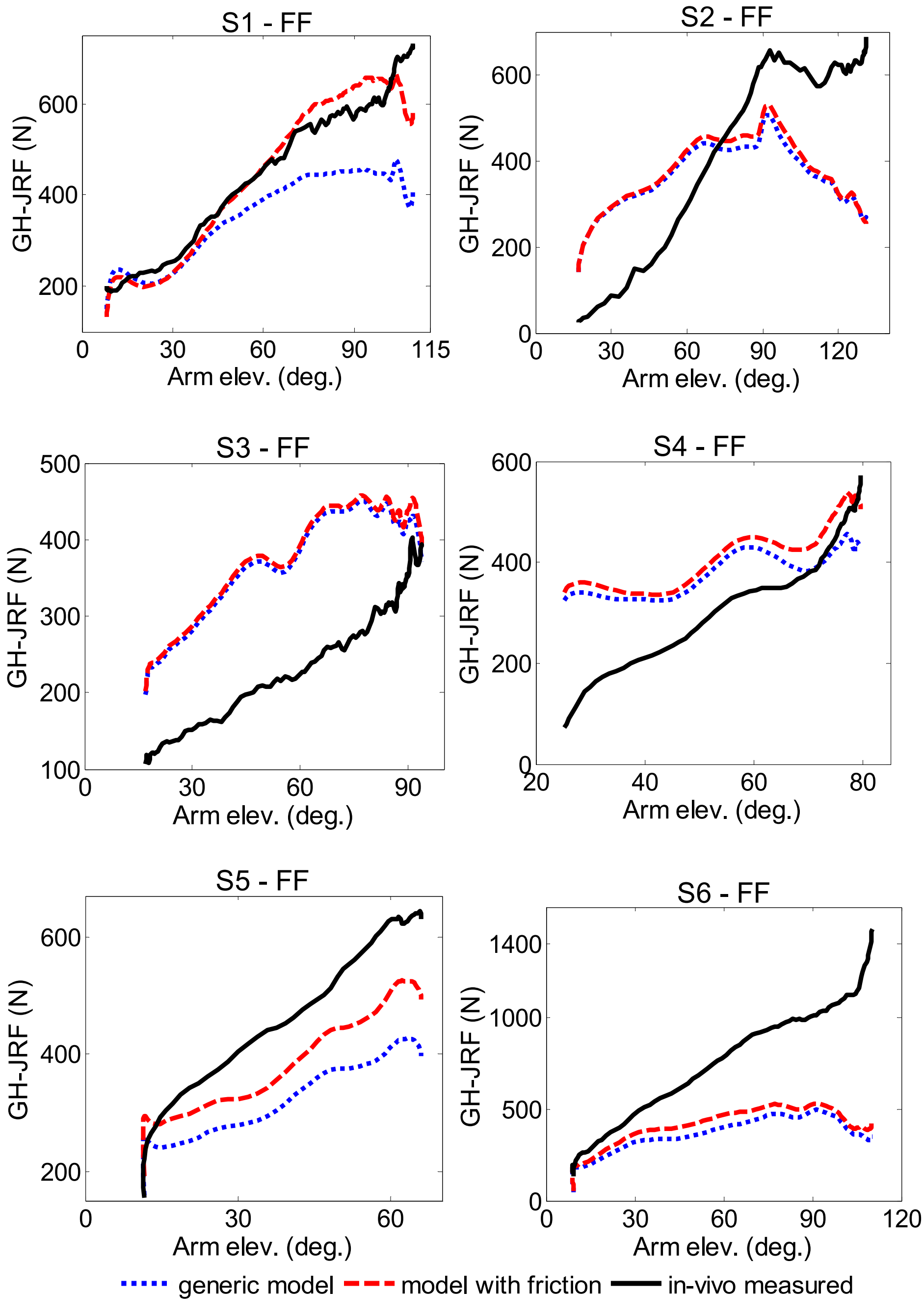

Figure 8.4. The measured and calculated GH-JRF with and without friction vs arm elevation angle for six measured subjects during forward flexion motion.

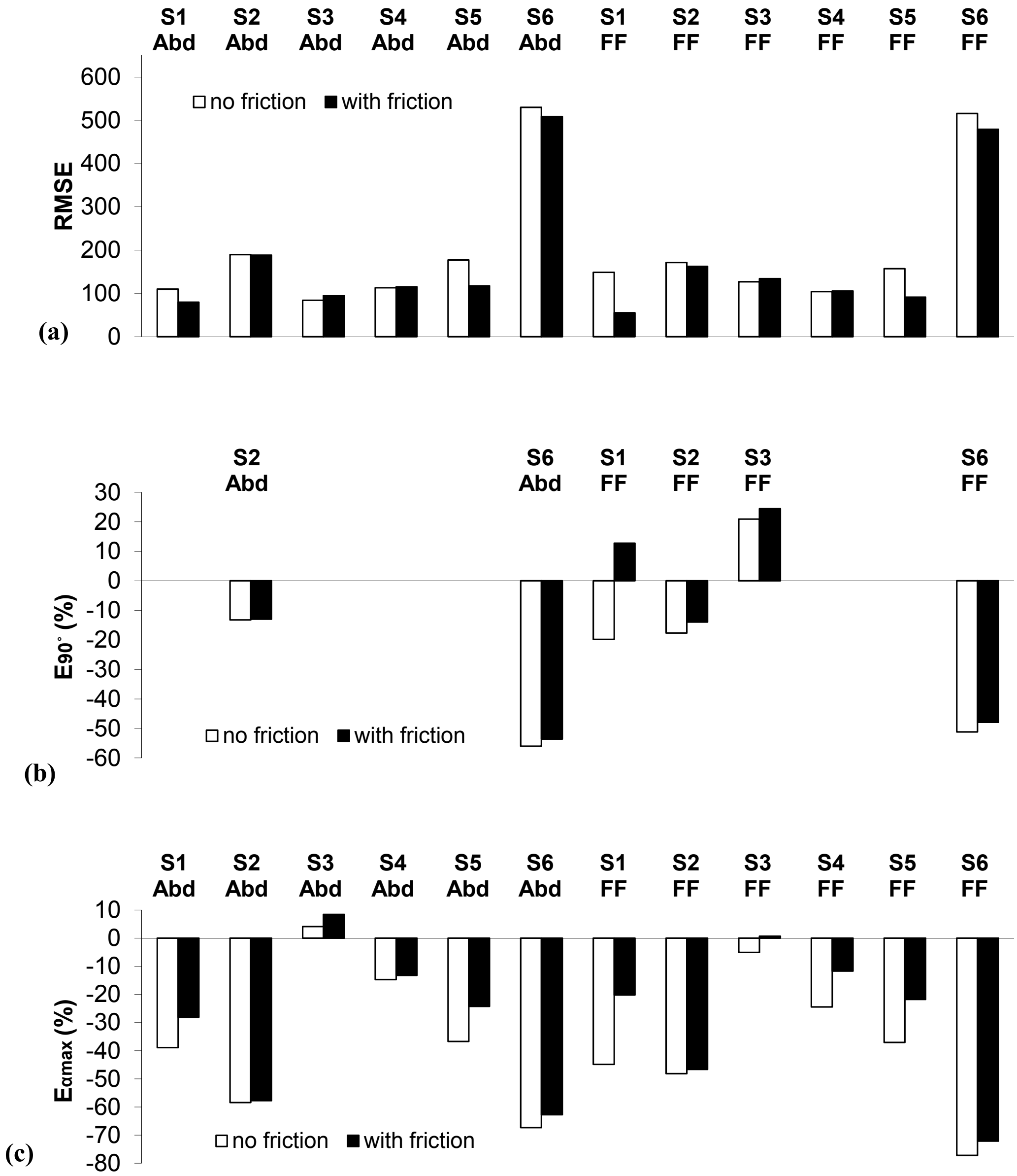

Figure 8.5. Difference between measured and calculated GH-JRF with and without friction during abduction (Abd) and forward flexion (FF) for six measured subjects.
The (a) RMSE, (b) error at 90º arm elevation (E_{90^o}), and (c) error at the maximum arm elevation ($E_{\alpha max}$).

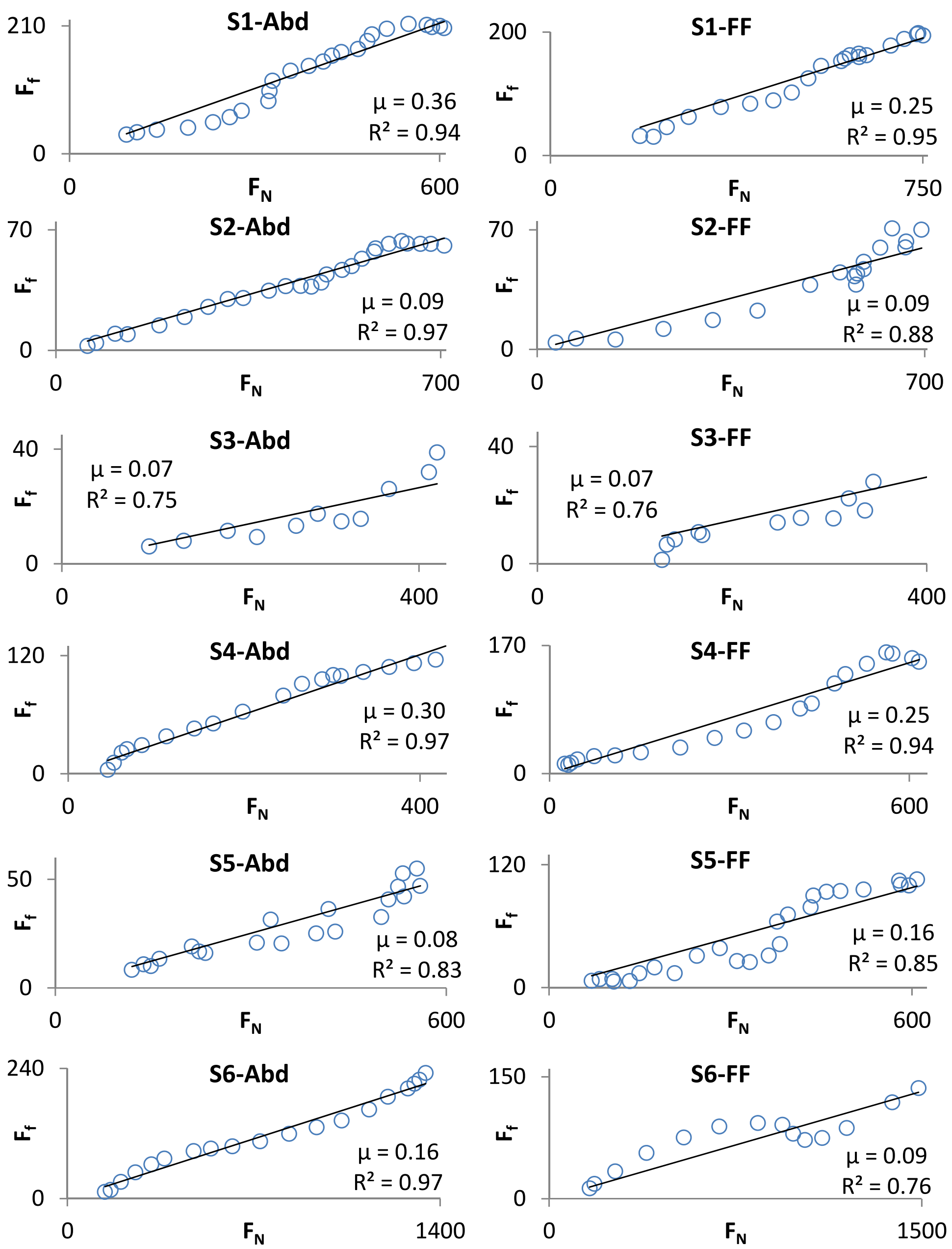

Figure 8.6. The friction force ($F_f = |\mathbf{F}_f|$) versus normal force ($F_N = |\mathbf{F}_N|$) for all subjects and motions. R^2: the coefficient of determination, μ: the friction coefficient ($= F_f/F_N$).

Firstly, a higher joint reaction force is an indication of extra muscle force around the glenohumeral joint. This extra force may cause fatigue during activities of daily living and therefore reduce the functionality of the shoulder joint after joint replacement.

Secondly, higher joint loads but especially also a higher tangential force due to friction may cause early loosening of the artificial joint compartments. In an in-*vitro* study, Andersson *et al* (1972) revealed that the FMs are not large enough to cause loosening. However, a later study by Morrey and Ilstrup (1989) on 6128 patients over 9 years showed that acetabular loosening rates were higher among patients with hip implants with larger implant radii, where the larger implant head radius was seen as an indicator of higher FM.

A large variability in measured FM (from 1.4 to 5.3 Nm) was observed among different subjects. This variability could be related to different implant head shapes, material, and/or radii. In case of our subjects, the shapes (spherical) as well as the material (cobalt-chrome-steel alloy) of the implants were the same but the radii were different (Table 3.1, Chapter 3). In line with Gandhe and Grover (2008), for our subjects S2 and S3, who had the smallest implant head radii (22 mm), the lowest max values for FM were found (1.47 and 1.40 Nm). Subjects S4 and S5, who had an implant with a larger radius (24 mm) indeed had higher FM (3.11 and 2.90 Nm). Subject S6 with the largest head radius (25 mm) had FM higher (3.82 Nm) than S2, S3, S4, and S5. The only exception to this size – friction relationship was subject S1 who had the largest FM (5.26 Nm) but had the second largest implant head radius (24 mm).

In a separate study, Westerhoff *et al* (2009b) observed large FM during performing the activities of daily living like hair combing or holding and lifting weights. In the current study only standard dynamic motions were analyzed. Given the low calculated statistical post-hoc power (~ 0.1), a more decisive conclusion about the significance of the effect of adding FM on the model outputs can be drawn by considering a wider range of tasks including the activities of daily livings.

A relatively high linear correlation ($R^2 = 0.88 \pm 0.09$) between friction and normal forces (Figure 8.6) showed that, as expected before, the contribution of Coulomb friction in the artificial joint is higher than the other types of friction (e.g. viscous friction, cohesion, etc.). Although there is no study on the friction coefficient of the shoulder hemiarthroplasty, the calculated friction coefficients in the current study ($0.07 \leq \mu \leq 0.36$) were comparable to the ones reported in the literature ($0.001 \leq \mu \leq 0.35$) for hip hemi-endoprostheses (Muller et al, 2004; O'Kelly et al, 1978; Patel and Spector, 1997; Roberts et al, 1982; Rydell, 1966; Stachowiak et al, 1994; Tsukamoto et al, 1992). One may need additional information to calculate the specific contribution of the other types of friction in the artificial joint. For example to estimate the viscous friction, the joint angular velocity should be calculated. Although it is possible in the current study to calculate the shoulder joint angular velocity from kinematic recordings, however, based on the obtained results the contribution of the viscous type friction will be negligible.

Although adding FMs to the model improved model predictions for patients with a shoulder endoprosthesis, however, large discrepancies between the model and experiments still remained (Figures 8.3 to 8.5). Therefore, one should think of adding other model features:

As extensively discussed in Chapter 6, a major source of discrepancies, especially for arm elevation angles above 90º (Figures 8.3 and 8.4) is the muscle co-contractions in our patients. For the subjects who could elevate their arm above 90º, implementation of the FM in the model did not have a major effect on the pattern of the model predictions of the GH-JRF above 90º arm elevation angle (Figures 8.3 and 8.4). As it was shown in Chapter 6, implementing muscle co-contraction in the model (i.e. by adding the measured EMG signals) could significantly improve the model predictions.

As stated before, the default form of the energy-based muscle load sharing cost function was used for inverse-optimization in this study. However, according to the results in Chapter 7, using the tuned parameters for the energy-based cost function may considerably improve the model predictions.

The morphological differences between the model and measured subjects seems to be a major source of inconsistency (under and/or overestimations) between model and experiments. The variability in the bony and muscular anatomy may change many modeling parameters (e.g. physiological cross-sectional area, moment arms, etc.). Therefore, a full-scaling of the model may have considerable effects on the modeling results.

Implementation of the *in-vivo* measured FM by the instrumented shoulder endoprosthesis in the Delft shoulder and Elbow Model improved the model predictions by about 10%. It is concluded that including the friction in the modeling procedure is important, at least for models of patients with shoulder endoprostheses. However, still two important questions remain unanswered: do the FM values and conclusions also apply to healthy joints? and, how should one add FM to the model if does not have an instrumented endoprosthesis?

To answer the first question, one assumes a larger friction coefficient in the implant than in the normal healthy joint considering that at least one part in artificial joint has lost the cartilage tissue. Giving that a relatively linear relationship between friction force and FM was found in this study, one would expect smaller magnitude of FM and consequently smaller effect on the model results for healthy subjects.

Adding FM directly to the model without having an instrumented endoprosthesis is hardly possible. By making several simplifying assumption (e.g. no spinning), having the radius of the implant head and (*in-vitro*) friction coefficient in the artificial joint, and using the model estimated GH-JRF by the original (no-friction) model, one would be able to approximate the magnitude of the resultant FM from Equations 2 and 5. However, it is not possible to calculate the components of FM vector (in the glenoid system) from such limited information. The predicted resultant FM can only be used to assess the overall effect of adding FM to the model, as can (partly) be seen in the results of the current study.

8.5. Conclusions

The *in-vivo* measured frictional moments by the instrumented shoulder endoprosthesis were implemented in the Delft shoulder and Elbow Model. The first time friction coefficient in the shoulder hemiarthroplasty was also estimated using the *in-vivo* measured data. Following conclusions can be drawn from this study:

- Adding the measured frictional moments to model improved the model predictions by about 10%. Such improvement was statistically significant. It is, therefore, concluded that when using the model for patients with shoulder arthroplasty, the friction should be considered in the modeling procedure.
- The estimated friction coefficient for the shoulder hemiarthroplasty using the *in-vivo* measured data was in the range reported in the literature for the hip hemiarthroplasty. It is, therefore, concluded that the method which was used in this study to estimate the friction coefficient is a valid method.

8.6. References

Andersson, G.B., Freeman, M.A., Swanson, S.A., 1972. Loosening of the cemented acetabular cup in total hip replacement. J Bone Joint Surg-Br Vol 54 (4), 590-599.

Bergmann, G., Graichen, F., Bender, A., Kaab, M., Rohlmann, A., Westerhoff, P., 2007. In vivo glenohumeral contact forces-Measurements in the first patient 7 months postoperatively. J Biomech 40 (10), 2139-2149.

Bergmann, G., Graichen, F., Rohlmann, A., Verdonschot, N., van Lenthe, G.H., 2001. Frictional heating of total hip implants. Part 1. measurements in patients. J Biomech 34 (4), 421-428.

Bishop, N.E., Waldow, F., Morlock, M.M., 2008. Friction moments of large metal-on-metal hip joint bearings and other modern designs. Med Eng Phys 30 (8), 1057-1064.

Damm, P., Graichen, F., Rohlmann, A., Bender, A., Bergmann, G., 2010. Total hip joint prosthesis for in vivo measurement of forces and moments. Med Eng Phys 32 (1), 95-100.

Franceschini, R., Franceschini, M., Romano, P., Busso, P., Caruso, E.M., De Amici, S., 2005. Joint replacement in osteoarthritis: State of the art. Semin Arthritis Rheum 34 (6), 73-77.

Gandhe, A., Grover, M., 2008. (i) Head size, does it matter? Current Orthopaedics 22 (3), 155-164.

Giroux, B., Lamontagne, M., 1992. Net shoulder joint moment and muscular activity during light weight-handling at different displacements and frequencies. Ergonomics 35 (4), 385-403.

Hallab, N.J., Jacobs, J.J., 2009. Biologic effects of implant debris. Bulletin of the NYU Hospital for Joint Diseases 67 (2), 182-188.

Lu, Z., McKellop, H., Liao, P., Benya, P., 1999. Potential thermal artifacts in hip joint wear simulators. J Biomed Mater Res 48 (4), 458-464.

Morrey, B.F., Ilstrup, D., 1989. Size of the femoral head and acetabular revision in total hip-replacement arthroplasty. J Bone Joint Surg-Am Vol 71 (1), 50-55.

Muller, L.P., Degreif, J., Rudig, L., Mehler, D., Hely, H., Rommens, P.M., 2004. Friction of ceramic and metal hip hemi-endoprostheses against cadaveric acetabula. Arch Orthop Trauma Surg 124 (10), 681-687.

O'Kelly, J., Unsworth, A., Dowson, D., Hall, D.A., Wright, V., 1978. A study of the role of synovial fluid and its constituents in the friction and lubrication of human hip joints. ARCHIVE: Engineering in Medicine 1971-1988 (vols 1-17) 7 (2), 73-83.

Patel, A.M., Spector, M., 1997. Tribological evaluation of oxidized zirconium using an articular cartilage counterface: A novel material for potential use in hemiarthroplasty. Biomaterials 18 (5), 441-447.

Pritchett, J.W., 2006. Heat generated by knee prostheses. Clin Orthop Rel Res 442, 195-198.

Roberts, B.J., Unsworth, A., Mian, N., 1982. Modes of lubrication in human hip joints. Ann Rheum Dis 41 (3), 217-224.

Rydell, N.W., 1966. Forces acting on the femoral head-prosthesis. A study on strain gauge supplied prostheses in living persons. Acta Orthop Scand 37, Suppl 88:1-132.

Saikko, V., 2009. Friction Measurement in the Biaxial Rocking Motion Hip Joint Simulator. J Tribol-Trans ASME 131 (1), 8.

Stachowiak, G.W., Batchelor, A.W., Griffiths, L.J., 1994. Friction and wear changes in synovial joints. Wear 171 (1-2), 135-142.

Tsukamoto, Y., Mabuchi, K., Futami, T., Kubotera, D., 1992. Motion of the bipolar hip prosthesis components. Friction studied in cadavers. Acta Orthop Scand 63 (6), 648-652.

Veeger, H.E.J., Rozendaal, L.A., van der Helm, F.C.T., 2002. Load on the shoulder in low intensity wheelchair propulsion. Clin Biomech 17 (3), 211-218.

Westerhoff, P., Graichen, F., Bender, A., Halder, A., Beier, A., Rohlmann, A., Bergmann, G., 2009b. In vivo measurement of shoulder joint loads during activities of daily living. J Biomech 42, 1840–1849.

Westerhoff, P., Graichen, F., Bender, A., Rohlmann, A., Bergmann, G., 2009a. An instrumented implant for in vivo measurement of contact forces and contact moments in the shoulder joint. Med Eng Phys 31 (2), 207-213.

Chapter 9

Conclusion, discussion, and recommendations

9.1. Conclusion

The research reported in this thesis focused on the most challenging issue in the area of musculoskeletal modelling: the *validity* of a musculoskeletal model.

The first time *in-vivo* shoulder joint loads measured in an instrumented shoulder endoprosthesis (Westerhoff et al, 2009) (originally measured on the humeral head) were represented on the glenoid side (Chapter 3). Within a wide range of motion of the shoulder movements and for most (~ 86 %) of the measured patients and tasks, the direction of the glenohumeral joint reaction force vector pointed towards the glenoid cavity. This finding supports the validity of a modeling stability assumption according to which the direction of the glenohumeral joint reaction force vector should be constrained inside the glenoid fossa to maintain the joint stability. Potential errors in CT image processing and/or motion recording are possible explanations for the 14% situations where the GH-JRF points outside the glenoid.

The glenohumeral joint rotation center is impossible to palpate *in-vivo* and, therefore, should be estimated. Two widely used functional methods including the Instantaneous Helical Axes (IHA) (Woltring et al, 1994) and Symmetrical Center of Rotation (SCoRE) (Ehrig et al, 2006) for estimating the glenohumeral joint rotation center *in-vivo* were compared and validated based on patient-specific CT data (Chapter 4). The IHA method resulted in a significantly more accurate approximation (i.e. closer to the geometric rotation center derived from the subject-specific CT-data) and is, consequently, recommended for estimation of glenohumeral joint rotation center *in-vivo* for patients carrying shoulder implants.

To assess the validity of a sophisticated musculoskeletal model of the shoulder, the Delft Shoulder and Elbow Model (DSEM), the *in-vivo* measured glenohumeral joint reaction forces and moments from the instrumented shoulder hemiarthroplasty were used as our '*golden standard*' (Chapter 5). In general, the agreement between predicted glenohumeral joint reaction forces by the 'generic' model (generic form and morphology) and the *in-vivo* measured one was not satisfactory.

We, consequently, identified a number of potential factors which might have caused the differences between the model and experiment including:

1. the morphological difference between the subject and the model,
2. the antagonist muscle co-contraction,
3. the type of muscle load sharing cost function being used for inverse optimization, and
4. the articular friction in the artificial joint.

To match few patients' anatomical parameters, the model was uniformly scaled to the subject's mass and size (Chapter 5) which led to improvement of the model predicted glenohumeral joint reaction force during the dynamic tasks (up to 26%), but had a negligible effect (< 2%) on the force task results. This approach, however, did not include the scaling of the subject's specific muscle strength parameters (e.g. PCSA).

To consider the possible antagonistic co-contraction in the model, an EMG-driven version of the DSEM was developed in which the measured normalized EMG signals of the superficial muscles of the shoulder could be used as the model inputs (Chapter 6). Both types of inconsistencies between the generic model and the measurements during performing dynamic motions, namely a general force underestimation and a force drop above 90° humeral elevation, were found to be related to antagonist co-contraction since inclusion of EMGs in the model input could considerably improve both the magnitude (on average up to 45% at maximum arm elevation) and the pattern (for above 90° arm elevation) of the model-predicted glenohumeral joint reaction forces. An important conclusion would be that antagonist muscle co-contraction should be considered in the modeling procedure specially when simulating the above head shoulder movements.

New adjustable parameters of an energy-based muscle load sharing cost function for inverse optimization (Praagman, 2008; Praagman et al, 2006) were identified in this research (Chapter 7) which led to a closer match (on average up to 20% at maximum arm elevation during performing dynamic motions) between the model and the experiment as for the glenohumeral joint reaction forces. The identified parameters are, therefore, recommended to be used instead of their predecessors (Praagman, 2008).

The friction-induced moments *in-vivo* measured by the instrumented shoulder hemi-arthroplasty were also implemented in the DSEM (Chapter 8). Such implementation led to about 10% improvement in the model prediction of the glenohumeral joint reaction forces when compared with the *in-vivo* measured forces. It is therefore concluded that the friction moments in the shoulder endoprosthesis are considerable and should be included in the biomechanical analysis of artificial shoulder joints.

9.2. Discussion

The validity issue can be discussed on the level of either the *kinematic* or the *dynamic* model. The validity of the model at these levels will subsequently be discussed below.

9.2.1. Validity of the kinematic model

9.2.1.1. Input motion

The validity of the methods/techniques being used in transition from measured kinematics to input motion is of great importance since they can notably influence the accuracy of the model inputs.

In-vivo palpated anatomical landmarks are used to determine the local coordinate system of the bony segments and also to find the joint angles which are the input motions to the DSEM. Anatomical landmarks which are impossible to palpate *in-vivo* should be approximated. An important example is the glenohumeral joint rotation center which needs to be estimated from the relative poses of the distal (humerus) and proximal (scapula) segments. In Chapter 4, two functional methods for the estimation of the glenohumeral joint rotation center including the IHA and the SCoRE methods were compared. The IHA method resulted in a significantly more accurate estimation of the glenohumeral joint rotation center for patients with endoprostheses. However, neither SCoRE nor IHA approximated the joint rotation center within 8 mm. Such deviation from the geometric rotation center, even for the best approximations, has been also observed in other studies (Campbell et al, 2009; Lempereur et al, 2010). This error might occur because CT landmarks were taken from the bony surface images and *in-vivo* landmarks were obtained by palpation. In a cadaver study on the hip, Cereatti *et al* (2009) concluded that the soft tissue artifact was a major parameter affecting the performance of the functional methods for estimation of the joint rotation center.

The impact of the inaccuracy in palpating the anatomical landmarks and/or estimating the rotation center *in-vivo* depends on the application of the obtained values. When used for the determination of the local coordinate system the effect will be quite small, if not negligible. Obtained values will also be useful for scaling etc. If, however, values are used to determine the moment arms of for instance deltoid, effect can be much larger, both on calculated muscle forces, or muscle length changes and ranges.

All three clavicular rotations are used for DSEM input. However, according to the ISB standardization protocol for upper extremity (Wu et al, 2005) only two anatomical landmarks on the clavicle (SC and AC, Table 3.3, Chapter 3) can be palpated *in-vivo*. Therefore, the axial rotation of the clavicle cannot be directly calculated from the recorded kinematics and should be approximated. van der Helm and Pronk (1995) developed an iterative Gauss-Newton method according to which the axial rotation of the clavicle could be estimated from the orientation of the scapula assuming minimized rotations in the acromioclavicular joint. This method was used in the current research to determine the axial rotation of the clavicle (see Chapters 2, 5, 6, 7, and 8). The assumption that the rotations in the acromioclavicular joint are minimized, however, still needs to be experimentally validated. Using bi-planar fluoroscopy technique may help in that regard.

9.2.1.2. Kinematic optimization

In the Delft Shoulder and Elbow Model, the shoulder girdle is modeled as a close-chain mechanism. Two major constraints of the close-chain mechanism (see section 2.8, Chapter 2) should be met:

1. the length of the conoid ligament must remain constant (= 1.83 cm), and
2. the distance between the surface of the thorax and the points TS and AI (Table 3.3, Chapter 3) must remain constant.

Force in the ligament depends only on the ligament length since the ligament is a passive element (Pronk et al, 1993). The length changes in the ligaments would cause huge changes in ligament forces, which would affect the muscle force during inverse optimization as well. The rigid conoid ligament, which has been modelled by TRUSS element in the current form of the DSEM, cannot be shortened/lengthened but can transmit muscle forces. The drawback of a rigid ligament is that it constraints the input motion. Alternative could be to allow length changes of the ligaments, and make the forces in the ligaments independent of the ligament length. This, however, may violate the physical laws (absence of a stress-strain relationship). A more detailed study of the ligament characteristics is possible through the forward dynamics simulations during which the ligaments play a major role in preventing excessive joint rotation (Pronk et al, 1993).

Although the scapula is constrained to glide over the thorax, there is no experimental proof about the validity of the second argument. Some preliminary calculations (Bolsterlee et al, 2011) show that at higher arm elevation angles (> 90º) this hypothesis may be violated. The effect of replacing this constraint with a soft constraint, however, has not yet been quantified but it is likely that using a soft constraint (like the one which is already implemented in the AnyBody modeling system and/or is already possible in the forward model version of the DSEM) would affect the scapular rotations like antero-posterior tilt. Using bi-planar fluoroscopy measurements could be extremely helpful to assess the validity of this assumption.

To accommodate for differences in the geometry between subject and model and to ensure that all recorded position inputs to the model can actually be attained by the model, the measured input angles are adjusted by minimization of the cost function defined as follows (see also Equation 2, section 2.2.2):

$$J = W_1\left((dC_x)^2 + \left(dC_y\right)^2 + (dC_z)^2\right) + W_2\left((dS_x)^2 + \left(dS_y\right)^2 + (dS_z)^2\right) \quad (1)$$

Where dC_x and dS_x are the differences between the measured and optimized angles for the clavicle and scapula around the x-axis, respectively. A similar definition is applied for angles around the y- and z- axes. W_1 and W_2 are weight factors. By using this cost function and tuning the weight factors, the errors spread over different joint angles. As discussed before (section 2.8, Chapter 2), the choice of the relative weight factors (W_1 and W_2) is very subjective. Therefore, a set of weight factors that results in the best match between the model-calculated and measured angles for one subject will not necessarily the best one for another subject with a completely different morphology and/or scapular motion pattern. As a conclusion, for future application, one should keep in mind not using the kinematic optimization cost function when fully scaling the model to the subject-specific geometry because of the possible extra errors that it might add.

9.2.2. Validity of the dynamic model

9.2.2.1. Load sharing

More than one combination of muscle forces may produce the same given net moment around a joint. The muscle load sharing is approximated by minimizing a cost function to find a unique solution.

The results of this thesis (Chapters 5 and 7) showed that the choice of a muscle load sharing cost function for inverse optimization (the IDO model, Chapter 2) can have a (relatively) considerable effect on the model predictions for individual muscles as well as for the glenohumeral joint reaction forces. As a general conclusion of this study, we recommend the use of the energy-based cost function instead of the traditional quadratic stress cost function for future applications. This recommendation is given based on the following reasons:

1. The energy-based cost function is more physiologically related since, in contrast to the stress cost function, it accounts for the muscle dynamics (i.e. muscle force-length relationship) in the inverse-dynamic optimization process.
2. In the study by Praagman *et al* (2008; 2006), a closer match (less false-negatives) was found between the DSEM predicted individual muscle forces and the measured EMG signals when using the energy-based cost function compared to the stress criterion. The study by Praagman *et al* can be seen as a qualitative validation of the energy-based cost function.
3. In the current study, the model predictions of the glenohumeral joint reaction forces generally showed a closer match to the *in-vivo* measured forces using the energy-based cost function compared to the stress criterion (Chapters 5 and 7). The current research can be seen as a quantitative validation of the energy-based cost function.

9.2.2.2. Joint stability

The glenohumeral stability was extensively discussed in Chapters 2, 3, and 5.

As mentioned before, the (*quasi-static*) stability of the model is being maintained by constraining the direction of the glenohumeral joint reaction force vector inside the glenoid to prevent the glenohumeral joint dislocation. In Chapter 3, it was proved that this is a valid assumption since for a wide range of motion of the shoulder, the trajectory of the *in-vivo* measured glenohumeral joint reaction force vector stayed inside the glenoid fossa.

The quasi-static stability is somewhat different from *functional* stability aiming to handle perturbations at arm elevations above 90° when the arm behaves like an inverted pendulum. Antagonist muscle co-contraction was proposed to be a potential candidate providing the functional stability (see Chapter 5). In Chapter 6, the effect of considering muscle co-contraction in the modeling process was evaluated which showed notable influence on the magnitude as well as the pattern (above 90º arm elevation) of the model predicted glenohumeral joint reaction force. Therefore, an important conclusion of the current study would be that antagonist muscle co-contraction should be considered in the modeling procedure specially when simulating the above head shoulder movements.

9.2.2.3. Input EMG signals

Through optimization of muscle forces in the DSEM, no co-contraction will be predicted, whereas the glenohumeral joint reaction force measurements indicate that co-contraction is present above 90 degrees humeral elevation (see Chapters 5 to 8).
To account for possible antagonist muscle co-contraction, an EMG-driven model was developed in this research (see Chapter 6). The measured EMG-signals were normalized and used as inputs to the forward muscle model in the EMG-driven model. The results of Chapter 6 revealed that including measured EMG signals in the modeling process could tremendously improve (up to 50%) the model predictions of the glenohumeral joint reaction forces.

The normalized EMG signal as inputs to the EMG-driven model determines the magnitude of the predicted muscle forces by the forward muscle model. The techniques being used to treat (i.e. normalize) the raw measured EMG signals will notably affect the magnitude of the EMG amplitude and most likely the outcomes of an EMG-driven musculoskeletal model. There is no consensus in the literature yet about the most appropriate normalization technique (Chapter 6). EMG-normalization based on the maximum EMG obtained from MVCs has a major limitation for usage during dynamic shoulder motions and for patients. As observed in Chapter 6, for some muscles the EMG measured during dynamic trials may exceed the maximum EMG obtained from MVCs. The choice of the most appropriate method for EMG normalization, especially during dynamic tasks, seems to be a major challenge for the future applications.

9.2.2.4. EMG-force relationship

In the developed EMG-driven model (Chapter 6), a Hill-type model was used for EMG to force (neural to muscle activation) transformation.

The Hill-type model considers a linear EMG-force relationship (line I, Figure 9.1). However, studies observed some nonlinearities in the EMG to joint moment relationship (Woods and Bigland Ritchie, 1983). A nonlinear (exponential) EMG-force relationship (line II, Figure 9.1) was used for prediction of muscle forces and joint moments from EMGs in spine (Potvin et al, 1996) and knee (Lloyd and Besier, 2003). Manal and Buchanan (2003) used a nonlinear exponential model for lower activations ($u < 0.3$) but a linear proportional for higher activations (line III, Figure 9.3). By implementing the two-phasic relationship in an EMG-driven Hill-type model, they found a better prediction of the measured elbow joint moment in comparing to when using a linear affinity. In the current study (Chapter 6), for all subjects and motions an overestimation of the measured glenohumeral joint reaction forces occurred at the lower elevation angles (lower activation). In case of our subjects, it seems that a better fit of the measured glenohumeral joint reaction forces will be acquired when using an EMG-force relationship completely in the reverse direction (line IV, Figure 9.1) of what the previous studies used. The effect of using a nonlinear EMG-force relationship on the modeling results still needs to be quantitatively evaluated for future applications.

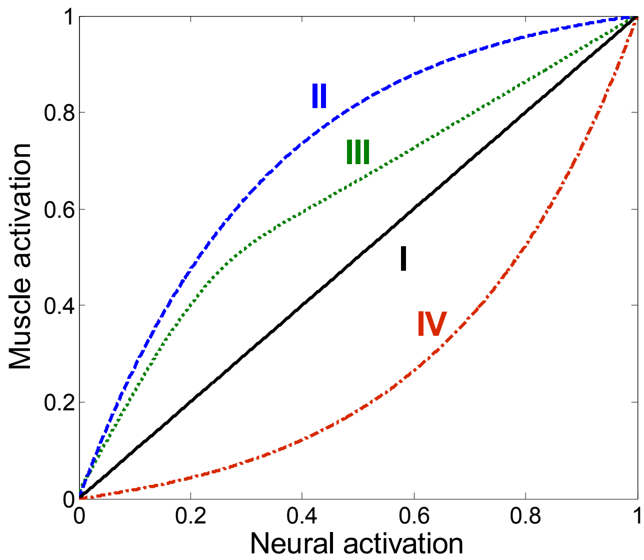

Figure 9.1. The neural-muscle activation (EMG-force) relationships.
(I) proportional, (II) nonlinear relation used in reference (Potvin et al, 1996) , (III) two-phasic (nonlinear and proportional) relation used in reference (Manal and Buchanan, 2003), and (IV) nonlinear relationship in the reverse direction of II.

9.2.2.5. Glenohumeral joint reaction forces

A main goal of this research was to *quantitatively* validate a comprehensive model of the shoulder i.e. the Delft Shoulder and Elbow Model (DSEM). The *in-vivo* measured glenohumeral joint reaction forces from an instrumented shoulder hemiarthroplasty were used as our '*golden standard*' for validation.

Results of the current study (Chapters 5 to 8) showed that the model-calculated (using the original version of the model) and *in-vivo* measured glenohumeral joint contact forces were not identical. The differences appeared in:

- the magnitude of the resultant force,
- the pattern of the resultant force for arm elevations above the horizontal level (> 90°), and
- the trajectory of the force vector inside the glenoid cavity.

For standard dynamic tasks (i.e. abduction and forward flexion), the original model generally underestimated the peak resultant force (on average across six subjects ~40%, Chapter 8), although few cases of overestimation (up to about 5% for one subject, Chapter 8) were also observed. For the quasi-static force tasks, the original model generally overestimated (on average across two subjects ~ 23%, Chapter 5) the peak resultant force for most directions of applying external loads. One may conclude that the DSEM in the original form (in the generic form and morphology and without any development/modification) is moderately accurate for the estimation of glenohumeral joint reaction forces.

The calculated and measured forces showed also a different behavior for angles above 90° arm elevation; the calculated force started to decrease, while the measured force continued to increase (Chapters 5 to 8). This finding violates the traditional shoulder modeling assumption (Poppen and Walker, 1978) according to which model-predicted joint reaction force for above 90º arm elevation should decrease because the lever of the external force/arm weight decreases after 90° (Ackland et al, 2008). As discussed in Chapter 5, the different behavior observed for our patients may has been caused by the existence of a pathological motor control, including excessive co-contraction, related to the use of a shoulder endoprosthesis. We do believe that this is only partially the case since co-contraction most likely also occurs in healthy subjects, and propose two arguments that underline our belief that the conclusion in this research (for implanted patients) can be generalized to healthy subjects:

1. For our patients no serious rotator cuff damage was reported (see Section 3.2.2, Chapter 3). Therefore, the chance of muscle tear/dysfunction is low. However, they are still prone to have pathological motor control as may be concluded from their limited elevation capacity (see Table 3.2, Chapter 3).
2. EMG measurements on both healthy (van der Helm, 1994) and patients (the current study) showed that the neural activity increases above 90°. Increasing the muscular activity would be an indication of extra effort needed for stabilizing the shoulder joint above 90° (see 9.2.2.2) for both patients and healthy subjects.

In general, the match between the position of the intersection of the joint reaction force vector and the glenoid predicted by the model and the one measured was not satisfactory (Chapter 5). The mismatch between the direction of the force vector in model and experiment was not notably improved by modeling developments and modifications (e.g. uniform scaling and using alternative cost function). As the results of Chapter 3 showed, the position of the points of application of the reaction force vectors on the articular surface of the glenoid fossa not only considerably changes from one subject to the other but also is very sensitive to either the accuracy of the recorded motion (e.g. lateral rotation of the scapula) or changes in the geometrical parameters for individual subjects (e.g. tilt angle between the scapula and the glenoid). Therefore, scaling the model to subject-specific geometry may considerably affect (and most likely in the right direction) the model predicted trajectory of the glenohumeral joint reaction force vector inside the glenoid cavity.

9.3. Recommendations

9.3.1. Which model version/modification and when should be used?

This study provided all aspects and developments of the Delft Shoulder Model since its original introduction in 1994 (Chapter 2). Some novel modifications in the model were also carried out in this research (Chapters 6 to 8).

Three different simulation architectures available in the DSEM including an inverse dynamics optimization - IDO, an inverse-forward-dynamics optimization - IFDO, and an inverse-forward-dynamics optimization with controller – IFDOC, were presented and qualitatively validated in Chapter 2.

The IDO and IFDO predicted similar forces indicating that the effects of considering the muscle force-velocity relationship in case of low-speed motions were not remarkable. Given that the IDO model is slightly faster than IFDO and has a simpler structure it is recommended to be used to study low- and/or medium- speed dynamic shoulder movements.

As the results in Chapter 2 showed, the IFDOC predicted higher glenohumeral joint reaction forces during dynamic motions like forward flexion compared with the IDO (and IFDO). Considering the general model underestimation of the resultant glenohumeral joint reaction forces (Chapters 5 to 8), the IFDOC could potentially be a better candidate for modeling dynamic tasks. However, relative muscle forces predicted by IFDOC for some major muscles (e.g. trapezius and deltoid, Chapter 2) do not seem to be realistic. This could be caused by excessive motions which can be improved by (small) modifications in the model. A rigorous validation of the IFDOC model is still required for a decisive conclusion about using IFDOC for future applications.

Uniform (size and mass) scaling showed capability to improve the model predictions, at least during performing dynamic shoulder tasks (up to 26%, Chapter 5). It is therefore concluded that the differences in morphology between the subject and the model could be a major source of discrepancies between the model calculations and experimental results. Thus, scaling the model to subject's morphology is strongly recommended for future application of the model. To do this, one would need data, especially MRI since that is feasible for patients (CT is better for the kinematic model). Scaling the muscle characteristics is expected to have a considerable effect.

By modifying the IFDO version of the DSEM (Chapter 2) a novel version of the model, i.e. the EMG-driven model, was developed (Chapter 6). Since the new model showed high capacity to improve both the magnitude (up to 50%) and the pattern (for above 90º arm elevation angle) of the model predicted resultant glenohumeral joint reaction forces, it is much recommended to use this new model for future applications. However, one should note that still a validation is needed at the level of EMG normalization and EMG-to-force relationship.

The result of Chapter 7 showed that the energy-based criterion with new identified parameter set resulted in not only significant improvements (up to 20%) of the model calculated glenohumeral joint reaction forces (compared with the ones *in-vivo* measured) but also a relative contribution of the two energy terms at maximum muscle activation which coincides with the corresponding values in the literature (*in-vitro* studies). It is, therefore, recommended to use the identified parameters for the energy-based cost function in this thesis (Chapter 7) instead of the previously assumed parameters (Praagman, 2008) for future modeling applications during standard dynamic shoulder motions like abduction and forward flexion.

The *in-vivo* measured frictional moments by the instrumented endoprosthesis were implemented in the modeling procedure (Chapter 8). Adding the frictional moments led to a general increase in the magnitude of the model-predicted resultant glenohumeral joint reaction force. Higher joint loads but especially also the tangential force due to friction may cause an unexpected earlier loosening of the artificial joint compartments. Also, extra force due to friction may cause fatigue during the activities of daily living and therefore reduce the functionality of the shoulder joint after joint replacement. Therefore, when using the model for implant design and estimating loads on the shoulder joint in the implanted patients, the effect of articular friction on the modeling results should be considered.

9.3.2. Recommendations for future research

Although several important aspects of the biomechanical modeling of the shoulder have been investigated in this research, some aspects still remained unexplored.

- One would anticipate the subject-specific modeling to be one of the most challenging issues in the future of musculoskeletal modeling. The morphological difference between the model and measured subjects seems to be a major source of the observed inconsistency between the model and experiments in this research. The results of EMG-driven modeling (Chapter 6) showed that how sensitive is the model to boundaries on the maximum permissible individual muscle forces. Therefore, a full (subject-specific) scaling which especially includes the muscle strength parameters (e.g. PCSA, volume, optimum fiber length, etc.) obtained by CT/MRI data must be a next step.
- As we saw, some modeling assumptions (e.g. the constant distance between the surface of the thorax and the points TS and AI, minimizing the rotations in the AC joint, etc.) in the DSEM still need to be experimentally validated in the future.
- The musculoskeletal model mainly used in this thesis was the DSEM. However, in Chapter 2 other available models of the shoulder were presented and compared with the DSEM. What really influences the predictions of a musculoskeletal model is related to the modeling assumptions. To keep the merits of the DSEM but also for a true comparison, the different modeling assumptions and developments from the other models could be implemented and evaluated in the DSEM. Examples

of these developments are listed below, however, one should not limit his/herself to this list.

- The effect of applying two different muscle load sharing cost functions (including the stress and energy-based criteria) on the model results has been studied. Rasmussen *et al* (2007) found considerably different (~ 40%) model-predicted (by the AnyBody shoulder model) glenohumeral joint reaction forces when applying the quadratic (stress) and min/max (Rasmussen et al, 2001) criteria as the muscle load sharing for inverse optimization. It would be, therefore, interesting to implement the min/max criterion in the DSEM and investigate the effects of using this cost function on the model estimations.
- Instead of a simple muscle wrapping method being used in the current version of the DSEM, a recently developed algorithm for exact multi-object muscle wrapping (Marsden et al, 2008) can be implemented and used. Using this new algorithm for wrapping of the larger muscles like deltoid may lead to considerable changes in the muscle moment arms. Therefore, it would be an important next step to implement the new algorithm for muscle wrapping in the DSEM.

- Despite the fact that development of the EMG-driven version of the DSEM led to remarkable improvements in the model predictions of the glenohumeral joint reaction forces, there is still much room for improvement of the EMG-driven model.
    - Current state-of-the-art EMG normalization techniques are far from perfect. To develop an appropriate method for EMG normalization will be a future challenge.
    - There is still a need to develop a physiologically-based method to distribute EMG signals from measured muscles between similar muscle elements in the model.
    - A nonlinear EMG-to-force relationship (Figure 9.1) can be implemented in the model and be evaluated the future applications.
- The effect of uniform scaling (Chapter 5), including the co-contraction in the model input (Chapter 6), using the energy-based cost function with tuned parameters (Chapter 7), and implementing the *in-vivo* measured frictional moments in the modeling process (Chapter 8) on the model result was separately studied in different chapters of this thesis. However, considering that none of these effects is linear, the effect of a combination of all these features on the modeling outcomes will not be necessarily a linear superposition of the individual effects. Thus, a multi-factorial effect study would be a future work.

9.4. References

Ackland, D.C., Pak, P., Richardson, M., Pandy, M.G., 2008. Moment arms of the muscles crossing the anatomical shoulder. Journal of Anatomy 213 (4), 383-390.

Bolsterlee, B., van der Helm, F.C.T., Veeger, H.E.J., Kinematic optimization to individualize scapular and clavicular kinematics in the closed-chain shoulder mechanism, presented at EUROMECH Colluquium 511, Azores, Portugal, 2011.

Campbell, A.C., Lloyd, D.G., Alderson, J.A., Elliott, B.C., 2009. MRI development and validation of two new predictive methods of glenohumeral joint centre location identification and comparison with established techniques. Journal of Biomechanics 42 (10), 1527-1532.

Cereatti, A., Donati, M., Camomilla, V., Margheritini, F., Cappozzo, A., 2009. Hip joint centre location: An ex vivo study. Journal of Biomechanics 42 (7), 818-823.

Ehrig, R.M., Taylor, W.R., Duda, G.N., Heller, M.O., 2006. A survey of formal methods for determining the centre of rotation of ball joints. J Biomech 39 (15), 2798-2809.

Lempereur, M., Leboeuf, F., Brochard, S., Rousset, J., Burdin, V., Rémy-Néris, O., 2010. In vivo estimation of the glenohumeral joint centre by functional methods: Accuracy and repeatability assessment. Journal of Biomechanics 43 (2), 370-374.

Lloyd, D.G., Besier, T.F., 2003. An EMG-driven musculoskeletal model to estimate muscle forces and knee joint moments in vivo. Journal of Biomechanics 36 (6), 765-776.

Manal, K., Buchanan, T.S., 2003. A one-parameter neural activation to muscle activation model: estimating isometric joint moments from electromyograms. Journal of Biomechanics 36 (8), 1197-1202.

Marsden, S.P., Swailes, D.C., Johnson, G.R., 2008. Algorithms for exact multi-object muscle wrapping and application to the deltoid muscle wrapping around the humerus. Proceedings of the Institution of Mechanical Engineers, Part H: Journal of Engineering in Medicine 222 (7), 1081-1095.

Poppen, N.K., Walker, P.S., 1978. Forces at the glenohumeral joint in abduction. Clinical Orthopaedics and Related Research 135, 165-170.

Potvin, J., Norman, R., McGill, S., 1996. Mechanically corrected EMG for the continuous estimation of erector spinae muscle loading during repetitive lifting. European Journal of Applied Physiology and Occupational Physiology 74 (1), 119-132.

Praagman, M., 2008. Muscle load sharing: An energy-based approach. PhD Thesis, Free University, Amsterdam.

Praagman, M., Chadwick, E.K.J., van der Helm, F.C.T., Veeger, H.E.J., 2006. The relationship between two different mechanical cost functions and muscle oxygen consumption. Journal of Biomechanics 39 (4), 758-765.

Pronk, G.M., Van der Helm, F.C.T., Rozendaal, L.A., 1993. Interaction between the joints in the shoulder mechanism: the function of the costoclavicular, conoid and trapezoid ligaments. ARCHIVE: Proceedings of the Institution of

Mechanical Engineers, Part H: Journal of Engineering in Medicine 1989-1996 (vols 203-210) 207 (48), 219-229.

Rasmussen, J., Damsgaard, M., Voigt, M., 2001. Muscle recruitment by the min/max criterion -- a comparative numerical study. J Biomech 34 (3), 409-415.

Rasmussen, J., de Zee, M., Tørholm, S., Damsgaard, M., 2007. Comparison of a musculoskeleal shoulder model with in-vivo joint forces. Journal of Biomechanics 40 (S2), S67.

van der Helm, F.C.T., 1994. Analysis of the kinematic and dynamic behavior of the shoulder mechanism. Journal of Biomechanics 27 (5), 527-550.

van der Helm, F.C.T., Pronk, G.M., 1995. Three-dimensional recording and description of motions of the shoulder mechanism. J Biomech Eng-T ASME 117, 27-40.

Westerhoff, P., Graichen, F., Bender, A., Rohlmann, A., Bergmann, G., 2009. An instrumented implant for in vivo measurement of contact forces and contact moments in the shoulder joint. Medical Engineering & Physics 31 (2), 207-213.

Woltring, H.J., Long, K., Osterbauer, P.J., Fuhr, A.W., 1994. Instantaneous helical axis estimation from 3-D video data in neck kinematics for whiplash diagnostics. J Biomech 27 (12), 1415-1425.

Woods, J.J., Bigland Ritchie, B., 1983. Linear and non-linear surface EMG/force relationships in human muscles. An anatomical/functional argument for the existence of both. American Journal of Physical Medicine 62 (6), 287-299.

Wu, G., van der Helm, F.C.T., Veeger, H.E.J., Makhsous, M., Van Roy, P., Anglin, C., Nagels, J., Karduna, A.R., McQuade, K., Wang, X., Werner, F.W., Buchholz, B., 2005. ISB recommendation on definitions of joint coordinate systems of various joints for the reporting of human joint motion--Part II: shoulder, elbow, wrist and hand. Journal of Biomechanics 38 (5), 981-992.

Summary

Detailed information about muscle forces in the human body musculoskeletal system are highly demanded for several applications such as the improvement of the design and preclinical testing of endoprostheses, a more detailed description of muscle- or joint-injuries, and design and improvement of the treatments of motor disorders. Unfortunately, the measurement of muscle forces *in-vivo* is hardly possible by noninvasive methods. Today, biomechanical models of the musculoskeletal system are best alternative for the direct measurement of these forces. A musculoskeletal model of the upper extremity may be useful in the estimation of forces in the shoulder.

The shoulder joint is a complex and extremely moveable joint system, comprised of three synovial joints between thorax and humerus. The interactions between the many degrees-of-freedom of the shoulder girdle limit the usefulness of simple 2D models and lead to complex 3D models. These models should be detailed enough to realistically replicate the behaviour of the musculoskeletal system. The musculoskeletal model mainly used in this thesis is the Delft Shoulder and Elbow Model (the DSEM), a comprehensive 3D model developed in the Biomechatronics & Biorobotics Group at the Faculty of Mechanical Engineering, Delft University of Technology. To date, the DSEM has been used in a variety of clinical and biomechanical applications.

A major concern in biomechanical modeling of the human body musculoskeletal system is model validity. We use biomechanical models because we cannot directly measure muscle forces. On the other hand, to validate a model we need to compare its predictions to real measured muscle forces. This conflict makes model validation one of the most challenging issues in the area of musculoskeletal modeling. The agreement between force patterns and EMG can only be seen as a qualitative validation since this agreement does not give information on the magnitude and accuracy of predicted force levels.

The main goal of this thesis is the validation of a comprehensive biomechanical model of the shoulder, i.e. the DSEM. Recently, an implantable instrumented shoulder endoprosthesis has been developed that is capable of measuring contact forces and moments inside the glenohumeral joint *in-vivo*. The endoprosthesis has been tested and implanted in a number of patients. Although direct measurement of muscle forces is still not possible by this instrumented implant, it does allow for a general validation at the level of the summed muscle forces in the glenohumeral joint. In this thesis the measured reaction forces in the shoulder joint using an instrumented endoprosthesis are used, as a ‘golden standard’, for the validation of the DSEM.

Aside from the introductory chapter, the other chapters of this thesis are organized into two major parts. Where the chapters of the first part deal with the validation of the DSEM at the level of kinematic and dynamic models, the second part explores the reasons for the differences between model predictions and experimental data and focuses on model adjustments to find a closer match between model and experiment.

In the first part, Chapter 2 comprises a review of the DSEM developments since its first introduction, describes the different simulation architectures available in the DSEM, and compares this model to the other sophisticated shoulder models. Different DSEM simulation architectures are qualitatively validated following an EMG-force comparison approach. In Chapter 3, the validity of a major stability constraint in the model is experimentally evaluated using the in-vivo measured glenohumeral joint reaction forces transferred to the glenoid. It is shown that within a wide range of shoulder movements and for most (~ 86 %) of the measured patients and tasks, the direction of the glenohumeral joint reaction force vector points towards the glenoid cavity. This supports the modeling stability assumption according to which the direction of the joint reaction force vector is constrained inside the glenoid fossa to maintain the joint stability. At the level of kinematic modelling, different methods, i.e. the Instantaneous Helical Axis (IHA) and Symmetrical Center of Rotation (SCoRE) methods for approximation of the glenohumeral joint rotation center are compared and validated based on patient-specific CT data (Chapter 4). As a conclusion of chapter 4, the IHA method is recommended for estimation of glenohumeral joint rotation center for patients carrying shoulder implants since it shows a significantly closer approximation to the geometric rotation center derived from the subject-specific CT-data. Regarding the dynamic model, , the *in-vivo* measured glenohumeral joint reaction forces in the shoulder joint using an instrumented shoulder endoprosthesis are used to quantitatively validate the model at the level of summed muscle forces around the glenohumeral joint (Chapter 5). Three types of differences appear between model and experiment:

1. difference in the magnitude of the resultant glenohumeral joint reaction force including a general model underestimation during standard dynamic tasks while a general model overestimation during quasi-static force tasks,
2. difference in the pattern (ascending measured vs. descending model-predicted) of the resultant glenohumeral joint reaction force for arm elevations above the horizontal level during standard dynamic tasks, and
3. difference in the position of the intersection of the glenohumeral joint reaction force vector with the articular surface of the glenoid fossa during both dynamic and force tasks.

In the second part of this thesis we try to explore the reasons for the differences between model predictions and experimental data that were observed and described in the first part. A selection of potential causes is identified among which three are explicitly presented and investigated.

To match the model to some extent to the patients' anatomical parameters, the model is uniformly scaled to the subject's mass and size leading to an improvement of approximately 25% in the magnitude of the model-predicted resultant glenohumeral joint reaction force during dynamic tasks (Chapter 5). Uniform scaling, however, does not show any notable effect on either the pattern of the model-predicted resultant force for arm elevations above the horizontal level or the trajectory of the force vector inside the glenoid cavity.

Antagonist muscle co-contraction is proposed to be a potential candidate explaining, especially, the difference in the pattern of measured and model-predicted resultant force for arm elevations above the horizontal level (> 90°). In Chapter 6, to account for muscle co-contraction in patients with arthroplasty an EMG-driven version of the DSEM is developed in which the muscle activation is set equal to the recorded EMG for some of the muscles. The influence of considering muscle co-contraction in the modeling process is found to be notable (on average up to 45%) on both the magnitude and the pattern above 90º arm elevation of the model predicted glenohumeral joint reaction force.

In Chapter 7 we try to identify the adjustable parameters of an energy-based muscle load sharing cost function. The new criterion has been shown to be promising but had previously not been fine-tuned. New adjustable parameters are identified in that chapter leading to a closer match (on average up to 20%) between the model and the experiment as for the glenohumeral joint reaction forces.

In Chapter 8, the friction-induced moments *in-vivo* measured by the instrumented shoulder hemiarthroplasty are implemented in the DSEM. This implementation leads to slight (but statistically significant) improvements (on average up to 10%) in the model prediction of the resultant glenohumeral joint reaction forces when compared with the *in-vivo* measured forces. It is concluded that friction moments in the shoulder endoprosthesis are considerable and should be included in the biomechanical analysis of artificial shoulder joints. In that chapter, the Coulomb friction coefficient in an artificial shoulder joint is also estimated using the *in-vivo* measured forces and frictional moments.

The final chapter (Chapter 9) evaluates progress and new challenges resulting from the undertaken research and highlights the main findings of the thesis. Some guidelines are also suggested and areas for future research are recommended.

Samenvatting

Gedetailleerde informatie over spierkrachten in het menselijk bewegingsapparaat is voor diverse toepassingen van groot belang, zoals voor de verbetering van het ontwerp en het preklinisch testen van endoprothesen, een meer gedetailleerde beschrijving van de spier- of gewrichtsblessures en het ontwerp en de verbetering van behandelingsmethoden voor motorische stoornissen. Helaas is het meten van spierkrachten *in-vivo* nauwelijks mogelijk via niet-invasieve methoden en zijn biomechanische modellen van het bewegingsapparaat het beste alternatief voor de rechtstreekse meting van deze krachten. Dit geldt ook voor modellen van de bovenste extremiteit en de schatting van krachten in de schouder.

Het schoudergewricht is een uiterst beweegbaar complex gevormd door drie synoviale gewrichten tussen de thorax en de bovenarm en het zogenaamde scapulothoracale glijvlak. De interacties tussen de vele graden-van-vrijheid in de schoudergordel beperken het nut van eenvoudige 2D-modellen en vereisen complexe 3D-modellen om een realistische schatting van spierkrachten in de schouder mogelijk te maken.

Het spierskeletmodel dat in dit proefschrift een predominante rol speelt is het Delft Shoulder and Elbow Model (de DSEM), een uitgebreid 3D-model ontwikkeld in de Biomechatronics & Biorobotics Groep van de faculteit Werktuigbouwkunde, Technische Universiteit Delft. Het DSEM wordt gebruikt in een breed scala van klinische en biomechanische toepassingen.

Een belangrijk aandachtspunt in de biomechanische modellering modelvaliditeit. We maken gebruik van biomechanische modellen, omdat we spierkrachten niet direct kunnen meten, terwijl de validiteit van de voorspellingen eigenlijk alleen te bepalen is via de directe meting van diezelfde krachten. Dit conflict maakt modelvalidatie een van de meest uitdagende vraagstukken op het gebied van spierskeletmodellering. De overeenkomsten tussen berekende krachten in de tijd en gemeten spieractiviteit of EMG kan helaas alleen worden gezien als een kwalitatieve validatie omdat EMG geen informatie bevat over de absolute grootte van de voorspelde krachten.

Het belangrijkste doel van dit proefschrift is de validatie van het DSEM met behulp van een recent ontwikkelde implanteerbare geïnstrumenteerde schouderendoprothese. Met deze prothese kan de contactkracht tussen humeruskop en het glenoid van de scapula *in-vivo* gemeten worden. Hoewel de directe meting van spierkrachten met deze geïnstrumenteerd prothese nog niet mogelijk is en er alleen een totaalkracht gemeten kan worden, maakt de prothese het mogelijk om het model op het niveau van de totaalkrachten die in het glenohumerale gewricht werken te valideren. In dit proefschrift worden de gemeten contactkrachten vergeleken met behulp van het DSEM berekende krachten.

Naast het inleidende hoofdstuk, is dit proefschrift georganiseerd in twee delen. Het eerste deel richt zich op de validatie van de DSEM op het niveau van kinematische en dynamische modellen, het tweede deel omvat een aantal studies waarin de verschillen tussen de modelvoorspellingen en de experimentele data nader onderzocht worden en waarin modelaanpassingen gepresenteerd worden die de afstemming tussen model en experimentele data verbeteren.

Het eerste deel wordt gevormd door hoofdstuk 2 tot en met 5. Hoofdstuk 2 geeft een overzicht van de DSEM ontwikkelingen sinds de introductie van het model en beschrijft de verschillende beschikbare simulatie-modes die in het DSEM beschikbaar zijn. Daarnaast wordt het model vergeleken met andere beschikbare schoudermodellen.

In hoofdstuk 3 wordt een van de belangrijkste aannames in het DSEM, namelijk dat de krachtsvector in het glenohumerale gewricht loodrecht op het vlak van het glenoid-oppervlak moet staan, nader ge-evalueerd. Uit de resultaten blijkt dat binnen een groot scala van schouderbewegingen en voor de meeste (~ 86%) van de patiënten gemeten en taken de reactiekracht op het glenoidoppervlak gericht is. Deze bevindingen ondersteunen de algemene modelaanname dat de reactiekracht binnen het glenoidoppervlak gericht blijft en moet blijven om gewrichtsstabiliteit te waarborgen.

In hoofdstuk 4 worden twee verschillende methoden om het glenohumerale rotatiepunt te bepalen met elkaar vergeleken. Op basis van patiënt-specifieke CT-gegevens zijn de “Instantaneous Helical Axis” (IHA) en “Symmetrical Center of Rotation” (SCoRE) methoden met elkaar vergeleken en gevalideerd aan het geometrisch bepaalde rotatiecentrum. Geconcludeerd wordt dat de IHA de aanbevolen methode is voor de schatting van het glenohumerale gewrichtsrotatie-centrum, in ieder geval voor patiënten met een schouder gewrichtsvervanging.

De modelresultaten voor wat betreft de berekende contactkrachten worden in Hoofdstuk 5 vergeleken met de *in-vivo* gemeten glenohumerale reactiekrachten. Op basis van deze vergelijking konden drie verschillen worden onderscheiden:

1. de berekende contactkracht gaf in het algemeen een onderschatting van de gemeten waarden tijdens arm elevatie, maar een overschatting voor de berekening van krachten voor de krachttaken;
2. er was een verschil in het verloop van de gemeten en voorspelde krachten afhankelijk van de mate van arm elevatie. Bij heffing van de arm boven horizontaal nam de gemeten reactiekracht nog steeds toe terwijl de berekende reactiekracht afnam;
3. De berekende en gemeten projectie van de reactie- of contactkracht op het oppervlak van het glenoid kwamen zowel voor de arm elevatietaken als de krachttaken niet geheel overeen.

In het tweede deel van dit proefschrift worden drie mogelijke oorzaken voor de verschillen tussen de modelvoorspellingen en experimentele resultaten geexploreerd.

Om het model enigermate overeen te laten komen met de anatomie van de gemeten patienten is het model geschaald. De gebruikte schalingsmethode was die naar proefpersoon-gewicht en –lengte. Deze methode leidde tot een verbetering van de berekende krachten van ongeveer 25% van het oorspronkelijke verschil (Hoofdstuk 5). Uniform schaling blijkt echter geen noemenswaardige invloed te hebben op het patroon van de reactie- of contactkracht of het verloop van de projectie van de krachtvector op het oppervlak van het glenoid.

Het verschil tussen modelresultaten en gemeten resultaten boven de 90° elevatie is mogelijkerwijs te verklaren uit de aanwezigheid van co-contractie die door patiënten daarenboven mogelijk meer gebruikt wordt dan bij gezonde proefpersonen het geval zou kunnen zijn. In hoofdstuk 6 is de co-contractie meegemodelleerd door gebruik te maken van EMG van een selectie van schouderspieren als additionele input. Hiervoor werd de "EMG-driven" versie van het DSEM gebruikt. De invloed van additionele spieractiviteit (en daarmee co-contractie) was aanzienlijk (gemiddeld tot 45% verbetering) op zowel de grootte als het verloop van de voorspelde reactiekracht.

In hoofdstuk 7 wordt geprobeerd een eerder ontwikkelde cost-functie te "tunen". Deze nieuwe, op energieverbruik gebaseerde cost functie is al eerder gebruikt en beschreven maar was tot nu toe alleen gebruikt met vooraf gekozen, beredeneerde parameters. In dit hoofdstuk blijkt dat met beter gekozen parameters en een betere verdeling van de weging van activatie en contractie de berekende resultaten ongeveer 20% meer overeenkomen met de gemeten resultaten voor de gewrichtsreactiekracht.

In hoofdstuk 8 wordt getracht de *in-vivo* gemeten momenten in de humeruskop te incorporeren in de mechanische analyse met behulp van het DSEM. Deze momenten zijn het gevolg van wrijving tussen plastiek-kop en glenoid. De implementatie van de wrijvingsmomenten als extra input leverde een kleine, doch statistisch significante verbetering op van de modelvoorspellingen ten opzichte van metingen (tot 10% verbetering). Geconcludeerd kan worden dat de wrijving in de schouderprothese aanzienlijk is en geïmplementeerd zou moeten worden in de biomechanische analyse van kunstmatige schoudergewrichten

Het afsluitende hoofdstuk (hoofdstuk 9) omvat een algemene bespreking van de reultaten van dit werk en de daaruit voortvloeiende nieuwe uitdagingen. Het wordt afgesloten met een bespiegeling omtrent vervolgonderzoek naar aanleiding van deze proefschrift.

Curriculum vitae

Ali Asadi Nikooyan was born in Shemiran, Iran, in 1978.

He finished his high school from Alborz High School (Tehran, Iran) in 1996. He subsequently started his Bachelor of Science study in the School of Mechanical Engineering at the Sharif University of Technology (Tehran, Iran).

In 2004, a few years after his B.Sc. graduation, he continued his Master of Science study in the Department of Biomedical Engineering at the Amirkabir University of Technology. He received his M.Sc. degree with honor in Biomechanical Engineering in 2006.

Since May 2007, Ali joined the Shoulder Group in the Department of Biomechanical Engineering at the Delft University of Technology to work on his PhD project on the "validation of musculoskeletal shoulder models" under the supervision of Prof. dr. Frans van der Helm and Prof. dr. Dirkjan Veeger. His PhD project was funded by the Dutch Technology Foundation STW.

List of publications

Journal papers

1. A.A. Nikooyan, F.C.T. van der Helm, P. Westerhoff, F. Graichen, G. Bergmann, H.E.J. Veeger, 2011, “Comparison of two methods for in-*vivo* estimation of the glenohumeral joint rotation center of the patients with shoulder hemiarthroplasty”, *PLoS ONE* 6(3): e18488.
2. A.A. Nikooyan, H.E.J. Veeger, P. Westerhoff, F. Graichen, G. Bergmann, F.C.T. van der Helm, 2010, “Validation of the Delft Shoulder and Elbow Model using in-*vivo* glenohumeral joint contact forces”, *Journal of Biomechanics* 43(15): 3007-3014.
3. A.A. Nikooyan, A.A. Zadpoor, 2011, “An improved cost function for modeling of muscle activity during running”, *Journal of Biomechanics* 44(5): 984-987.
4. A.A. Zadpoor, A.A. Nikooyan (joint first author), 2011, “The relationship between lower-extremity stress fractures and the ground reaction force: a systematic review”, *Clinical Biomechanics* 26(1): 23-28.
5. A.A. Zadpoor, A.A. Nikooyan (joint first author), 2010, “Modeling muscle activity to study the effects of footwear on the impact force and vibrations of the human body during running”, *Journal of Biomechanics* 43(2): 186-193.
6. A.A. Nikooyan, A.A. Zadpoor, 2009, "Application of virtual environments to assessment of human motor learning during reaching movements", *Presence: Teleoperators and Virtual Environment* 18(2): 112-124.
7. A.A. Zadpoor, A.A. Nikooyan (joint first author), 2009, “Development of an improved desiccant-based evaporative cooling system for gas turbines”, *Journal of Engineering for Gas Turbines and Power-Transactions of the ASME* 131(3): 034506 (5 pages).
8. A.A. Zadpoor, A.A. Nikooyan, A.R. Arshi, 2007, “A model-based parametric study of impact force during running”, *Journal of Biomechanics* 40(9): 2012-2021.
9. A.A. Zadpoor, A.A. Nikooyan (joint first author), 2006, “A mechanical model to determine the influence of masses and mass distribution on the impact force during running- A discussion”, *Journal of Biomechanics* 39(2): 388-390.
10. M. Omidi, H.R.D. Taher, A.A. Zadpoor, A.A. Nikooyan, 2006, “Free vibration of circular and annular plates with variable thickness and different

combinations of boundary conditions", *Journal of Sound and Vibration* 296(4-5): 1084-1092.

11. M.T. Ahmadian, A.A. Nikooyan (joint first author), 2006, "Modeling and prediction of soft tissue directional stiffness using in-vitro experimental data", *International Journal of Scientific Research* 16: 385-389.

Submitted journal papers

1. A.A. Nikooyan, H.E.J. Veeger, E.K.J. Chadwick, M. Praagman, F.C.T. van der Helm, "Development of a comprehensive musculoskeletal model of the shoulder and elbow", *Medical & Biological Engineering & Computing*, under revision.
2. A.A. Nikooyan, H.E.J. Veeger, P. Westerhoff, B. Bolsterlee, F. Graichen, G. Bergmann, F.C.T. van der Helm, "An EMG-driven musculoskeletal model of the shoulder", *Human Movement Scienc*e, under revision.

Journal abstracts

1. A.A. Nikooyan, H.E.J. Veeger, F.C.T. van der Helm, P. Westerhoff, F. Graichen, G. Bergmann, "Comparing model predicted GH-joint contact forces by in-vivo measured forces", *Journal of Biomechanics* 41: S145.
2. A.A. Nikooyan, Zadpoor, A.A., Sh. Jannesar, "Finite element 2D nonlinear analysis of human fingertip under static loading to asses a model of tactile sensation", *Journal of Biomechanics* 39: S639.
3. A.A. Nikooyan, A.A. Zadpoor, A.R. Arshi, "A bond graph approach to analysis of effects of Arteriosclerosis on cardiovascular system's performance", *Journal of Biomechanics* 39: S606.
4. A.A. Zadpoor, A.A. Nikooyan, "Forced vibration analysis of harmonically excited nonlinear viscoelastic biomaterials", *Journal of Biomechanics* 39: S641.
5. A.A. Zadpoor, A.A. Nikooyan, A.R. Arshi, "Development of a nonlinear viscoelastic model of human body for computation of impact force during running", *Journal of Biomechanics* 39: S180.
6. A.A. Zadpoor, A.A. Nikooyan, A.R. Arshi, "An empirical approach to assessment of human brain's capability in learning of polynomial functions", *Emirates Medical Journal* 23 (3): 69-70.

Conference papers/abstracts

1. A.A. Nikooyan, H.E.J. Veeger, P. Westerhoff, F. Graichen, G. Bergmann, F.C.T. van der Helm, "Development of an EMG-assisted musculoskeletal

model of the shoulder and elbow", *Proc. the Third Dutch BME Conference*, January 20-21, 2011, Egmond aan zee, the Netherlands.

2. P. Westerhoff, F. Graichen, A. Rohlmann, A. Bender, A.A. Nikooyan, Veeger, H.E.J., van der Helm, F.C.T., G. Bergmann, "*In-vivo* glenoid loads during external rotation and abduction measured in two patients", *Proc. Orthopaedic Research Society (ORS) Annual Meeting*, January 13-16, 2011, Long Beach, CA. USA.
3. A.A. Nikooyan, H.E.J. Veeger, P. Westerhoff, F. Graichen, G. Bergmann, F.C.T. van der Helm, "Development of an EMG-assisted model of the Shoulder and Elbow", *Proc. International Shoulder Group meeting (ISG 2010)*, pp. 86-87, July 25-27, 2010, Minneapolis, MN, USA.
4. A.A. Nikooyan, H.E.J. Veeger, P. Westerhoff, F. Graichen, G. Bergmann, F.C.T. van der Helm, "How well does a musculoskeletal model predicts GH-joint contact forces? comparison with in-vivo data", *Proc. the ASME 2009 International Design Engineering Technical Conferences (IDETC)*, DETC2009 4 (PART C), pp. 1575-1581, August 30-September 2, 2009, San Diego, CA, USA.
5. A.A. Nikooyan, A.A. Zadpoor, "A model-based study of the muscle tuning during running with different shoes", *Proc. the International Symposium on Computer Methods in Biomechanics and Biomedical Engineering (CMBBE2008)*, February 2009, Porto, Portugal.
6. A.A. Nikooyan, H.E.J. Veeger, P. Westerhoff, F. Graichen, G. Bergmann, F.C.T. van der Helm, "Comparing model predicted GH-joint contact forces by in-vivo measured forces", *Proc. the Second Dutch BME Conference*, pp. 133, January 22-23, 2009, Egmond aan zee, the Netherlands.
7. A.A. Nikooyan, H.E.J. Veeger, P. Westerhoff, F. Graichen, G. Bergmann, F.C.T. van der Helm, "Comparing model estimated GH-joint contact forces to those measured in-vivo by instrumented shoulder endoprosthesis", *Proc. International Shoulder Group meeting (ISG 2008)*, pp. 64-65, July 10-13, 2008, Bologna, Italy.
8. A.A. Nikooyan, H.E.J. Veeger, P. Westerhoff, Graichen,, F. G. Bergmann, F.C.T. van der Helm, "Validation of a large-scale musculoskeletal model of the shoulder mechanism by using in-vivo GH-joint contact force measurements", *Proc. the 54th Nordic Orthopaedic Federation Congress*, June 11-13, 2008, Amsterdam, the Netherlands.
9. A.A. Zadpoor, A.A. Nikooyan, "The effects of footwear on impact force during running: a model-based study", *Proc. the Sixth IASTED International Conference on Biomedical Engineering (BioMED 2008)*, pp. 240-245, February 13-15, 2008, Innsbruck, Austria.
10. A.A. Nikooyan, Zadpoor, A.A., "A model-based parametric study of soft tissue vibrations during running", *Proc. the IEEE-EMBS Benelux Chapter*

Annual Symposium, pp. 49-52, December 6-7, 2007, Heeze, the Netherlands.

11. A.A. Nikooyan, A.R. Arshi, C. Lucas, F. Tabatabai, "Assessment of motor learning and generalization during reaching movement in dynamic virtual environment" (in Persian), *Proc. the Iranian Conference on Biomedical Engineering (ICBME2007)*, February 2007, Tehran, Iran.
12. M.A. Shirzi, A.A. Nikooyan, M.R. Hairi Yazdi, A.A. Zadpoor, C. Lucas, "A neurofuzzy approach to identification of some classes of soft tissues utilizing experimental data", *Proc. the 1st IEEE International Conference on Engineering of Intelligent Systems (IEEE ICEIS'2006)*, pp. 442-447, April 22-23, 2006, Jinnah University, Islamabad, Pakistan.
13. A.A. Zadpoor, A.R. Arshi, A.A. Nikooyan, "A bond graph approach to the modeling of fluid-solid interaction in cardiovascular system's pulsatile flow", *Proc. the 27th Annual International Conference of the IEEE in Medicine and Biology Society (IEEE-EMBS05)*, September 1-4, 2005, Shanghai, China.

Awards

1. European Society of Biomechanics (ESB) Student Award for the paper presented at the ESB 2008, Lucerne, Switzerland, 2008.